

Application and Development of Fourier Transform Holography

vorgelegt von
Diplom-Physiker
Christian Michael Günther
aus Berlin

Von der Fakultät II - Mathematik und Naturwissenschaften
der Technischen Universität Berlin
zur Erlangung des akademischen Grades

Doktor der Naturwissenschaften
– Dr. rer. nat. –

genehmigte Dissertation

Promotionsausschuss:

Vorsitzender: Prof. Dr. Mario Dähne
1. Gutachter: Prof. Dr. Stefan Eisebitt
2. Gutachter: Prof. Dr. Dr. Wolfgang Eberhardt

Tag der wissenschaftlichen Aussprache: 24. Januar 2012

Berlin 2012

D83

Kurzfassung

Das Thema der vorliegenden Arbeit ist die Fourier-Holografie an Röntgenquellen der dritten und vierten Generation. Dieses linsenlose Abbildungsverfahren nutzt die Kohärenz der Lichtquellen, um eine Referenzwelle in ein Transmissions-Streuexperiment einzukoppeln. Dadurch wird bei der Detektion der von einem Objekt gestreuten Objektwelle die vollständige Welleninformation aufgezeichnet. Somit umgeht die Fourier-Holografie das Phasenproblem linsenloser Abbildungsverfahren und erzeugt ein Bild des Objektes.

In Kombination mit Röntgenstrahlen stehen der Fourier-Holografie sowohl eine hohe Ortsauflösung als auch spezielle Kontrastmechanismen zur Verfügung. Insbesondere der magnetische Zirkulardichroismus ermöglicht die Untersuchung magnetischer Multilagen mit senkrechter Anisotropie. An Synchrotrons können heute routinemäßig magnetische Domänenkonfigurationen mit einer Ortsauflösung unterhalb von 50 nm im angelegten Magnetfeld und bei variabler Temperatur elementspezifisch abgebildet werden.

Durch Nutzung all dieser Parameter ist es möglich die Replizierung von magnetischen Domänen in einem austauschgekoppeltem System zu untersuchen. Die magnetische Konfiguration einer magnetisch harten Co/Pd-Multilage kann über dipolare Streufelder erfolgreich durch eine 10 nm dicke und nichtmagnetische Pd-Schicht hindurch einer magnetisch weichen CoNi/Pd-Multilage aufgeprägt werden. Diese Duplizierung lässt sich sowohl durch die Variation eines externen Magnetfeldes als auch durch Änderung der Temperatur an der Probe auslösen.

Fourier-Holografie schränkt das Sichtfeld auf die Probe stark auf typischerweise weniger als $1 \mu\text{m}^2$ ein. Im Falle magnetischer Multilagen entspricht dies der Breite weniger Domänen. Hierdurch ist es möglich in Hysteresekurven von Co/Pd- und Co/Pt-Multilagen, gemessen durch Röntgentransmission an der Co- L_3 Absorptionskante, nicht reproduzierbare Magnetisierungssprünge zu erkennen. Diese werden sowohl bei einer Erhöhung des Sputterdrucks bei der Probendeposition, als auch beim Einbringen einer antiferromagnetisch gekoppelten Zwischenschicht beobachtet. Parallel dazu ermöglichen magnetische Fourier-Holografie Bilder der *identischen* Probenregion die Untersuchung der magnetischen Konfiguration. Für die Probe mit der antiferromagnetisch gekoppelten Zwischenschicht konnte so ein antiferromagnetischer Streifendomänenzustand (antiferromagnetic stripe domain state) direkt nachgewiesen werden.

Freie-Elektronen Laser erzeugen hochbrillante, ultrakurze Röntgenpulse und versprechen damit eine sehr hohe zeitliche und räumliche Auflösung. Gleichzeitig erfordern die hohe deponierte Energie oberhalb der Ablationsschwelle vieler Materialien sowie die statistische Natur dieser Quellen die Entwicklung neuer Untersuchungsmethoden. Fourier-Holografie unterstützt multiple Referenzen, welche in Verbindung mit einer „split-and-delay line“

mehrere Hologramme einer Probe auf dem gleichen Detektor überlagern können und somit zwei Bilder innerhalb eines Femtosekunden-Zeitabstandes generieren. Die räumliche Trennung der entstehenden Bilder in der Hologramrekonstruktion kodiert dabei den Zeitunterschied und ermöglicht somit eine ultraschnelle Sequenz zweier Bilder. Dies stellt einen ersten Schritt auf dem Weg hin zu Röntgenfilmen ultraschneller Prozesse auf der Nanometerskala dar.

Abstract

The thesis deals with Fourier transform holography at third and fourth generation x-ray sources. This lensless imaging technique exploits the coherence of the light sources to couple a reference wave into a transmission scattering experiment. As a result, the complete wavefront information of the object wave is recorded in the detection process. In this way Fourier transform holography solves the phase problem of lensless imaging methods and provides an image of the object.

Fourier transform holography in combination with x-rays features a high spatial resolution and special contrast mechanisms. Especially x-ray magnetic circular dichroism makes the technique suited for the investigation of magnetic samples with perpendicular anisotropy. Today, the element-specific imaging of magnetic domain patterns is routinely performed at synchrotrons with a spatial resolution below 50 nm in a variable magnetic field and temperature environment.

By exploiting all of these parameters it becomes possible to investigate the duplication of domains in an exchange-decoupled system. The magnetic configuration of a magnetically hard Co/Pd multilayer is successfully replicated through a 10-nm-thick Pd layer into a magnetically soft CoNi/Pd multilayer. This duplication can be triggered either by the variation of an external magnetic field or the environmental temperature.

Fourier transform holography reduces the field of view on a specimen to typically less than $1 \mu\text{m}^2$. In the case of magnetic Co/Pd and Co/Pt multilayers this area corresponds to the width of few domains. Due to this confinement it is possible to find sudden irreproducible magnetization jumps in local hysteresis loops measured in transmission at the Co- L_3 edge. It is shown that such steps in the local hysteresis loop are observed when using increased sputter pressure during samples deposition or by introducing an antiferromagnetically coupled interlayer. In addition, holography images on the *identical* sample region allow detailed investigation of the magnetic configuration. For the antiferromagnetically coupled sample system an antiferromagnetic stripe domain state could be directly imaged.

Free-electron lasers provide femtosecond x-ray pulses with unprecedented peak brightness and promise a high spatial and temporal resolution. At the same time, the source's statistic character and energy deposition above the ablation level of many materials require the development of new experimental techniques. Fourier transform holography supports multiple references which, in conjunction with a split-and-delay line, make this technique capable to superimpose two holograms on the same detector and deliver two images of a specimen within a femtosecond time delay. The concept maps the temporal information of the pulse arrival to a spatial information in the hologram reconstruction. The resulting two-image sequence constitutes a first step towards ultrafast x-ray movies at the nanoscale.

Contents

List of Figures	vii
List of Abbreviations	ix
1 Introduction	1
1.1 Structure of the Thesis	2
2 Theory	5
2.1 Geometry of Scattering Experiments	6
2.2 Coherence	8
2.2.1 Longitudinal Coherence	9
2.2.2 Transverse Coherence	10
2.3 Fourier Transform Holography	12
3 Quasistatic Experiments	19
3.1 Synchrotrons as Source for FTH	19
3.1.1 Coherent Flux from Synchrotrons	19
3.1.2 XMCD and Resonant Magnetic Scattering from Out-of-plane Domains	21
3.1.3 Instrumentation for Synchrotron FTH	27
3.2 Domain Replication	29
3.2.1 Dipolar-coupled Multilayers	29
3.2.2 Field-induced Replication at Low Temperature	33
3.2.3 Temperature-induced Domain Replication	35
3.2.4 Comparison of Field- and Temperature-induced Domain Replication	39
3.3 Steplike Domain Propagation in Co/Pt and Co/Pd Multilayer Films	43
3.3.1 Steplike Magnetic Reversal Caused by Increased Defect Concentration	45
3.3.2 Steplike Magnetic Reversal in an AF-coupled Multilayer System .	53
3.4 Soft X-ray Rotating Beamstop	62
3.4.1 Beamstops in X-ray Imaging Experiments	62
3.4.2 A Rotating Wire as Soft X-ray Beamstop	64
3.4.3 Design of the Rotating Beamstop	66
3.4.4 Performance of the Device	70
3.4.5 Future Improvements of the Rotating Beamstop	75

4	Ultrafast Sequential X-ray Imaging	79
4.1	Motivation — The “Molecular Movie”	79
4.1.1	X-ray Free-Electron Lasers	80
4.2	Sample Concept and Setup	82
4.2.1	Concept and Sample Design for Time-resolved X-ray FTH	84
4.2.2	Experimental Setup at FLASH	86
4.3	Results and Discussion	89
4.3.1	Single-shot Reconstruction	89
4.3.2	Two-beam “Movie”	90
4.3.3	Comparison to Complementary Ultrafast X-ray Techniques	93
4.4	Details of Image Formation and Artifacts	94
4.4.1	Coherent vs. Incoherent Hologram Superposition	94
4.4.2	Image Artifacts	101
4.5	Future Perspectives	106
4.5.1	Scaling to High Resolution	106
4.5.2	Multiple Timeframes	108
4.5.3	Separation of the Diffraction Patterns	108
5	Summary and Outlook	113
	Bibliography	117
A	Practical Reconstruction of Fourier Transform Holograms	131
B	Resonant Magnetic Scattering with Soft X-rays	137
	Publications	143
	Acknowledgment of the Work of Others	147
	Acknowledgments	149

List of Figures

2.1	In-plane momentum transfer \mathbf{q}	6
2.2	Scattering experiments in general	7
2.3	Longitudinal (temporal) coherence	9
2.4	Transverse (spatial) coherence	11
2.5	Common holography geometries	12
2.6	Lensless FTH setup geometry	13
2.7	FTH image formation	15
3.1	Coherence by filtering	20
3.2	XMCD spectra	22
3.3	Magnetic holography	26
3.4	The FTH-mask	27
3.5	The ALICE diffractometer	28
3.6	Interlayer magnetostatic interaction	30
3.7	Sample structure for the domain replication experiment	31
3.8	Macroscopic hysteresis loop of the hard/Pd/soft ML system	32
3.9	Domain replication with magnetic field	34
3.10	Macroscopic VSM measurement of temperature-induced domain replication	36
3.11	FTH images of temperature-induced domain replication	37
3.12	Sample drift for temperature-dependent FTH	38
3.13	Comparison of field- and temperature-induced domain replication	40
3.14	In-focus LHL measurements	44
3.15	MFM images of the 3 mTorr and 6 mTorr samples after demagnetization	46
3.16	SEM images of the 3 mTorr and 6 mTorr samples	47
3.17	Local hysteresis loops for the 3 mTorr and 6 mTorr samples	48
3.18	Switching reproducibility for the 3 mTorr and the 6 mTorr samples	49
3.19	Binary magnetic states for the 3 mTorr and 6 mTorr samples	50
3.20	Statistics consideration for sums of magnetic images	51
3.21	Multilayer structure of the AF-coupled sample	54
3.22	Element-specific XMCD hysteresis loops on the AF-coupled sample	55
3.23	Local hysteresis loops on the AF-coupled sample	57
3.24	Stepped loop on the AF-coupled sample	59
3.25	Magnetic images for the AF-coupled sample recorded during a stepped loop	59
3.26	Switching reproducibility of the AF-coupled sample	60

3.27	Binary magnetic states and statistical analysis for the AF-coupled sample	61
3.28	Geometrical consideration for the rotating beamstop	65
3.29	Photographs of the rotating beamstop	67
3.30	Temperature curves for the rotating beamstop	68
3.31	Rotating beamstop with simple wires	69
3.32	The rotating beamstop plate	70
3.33	X-ray holograms recorded with the rotating beamstop	71
3.34	Measured absorption profile of the rotating beamstop	73
3.35	Diatom hologram reconstruction with and without rotating beamstop	75
3.36	Transmission profiles for serial operation of rotating beamstops	76
3.37	Transmission profiles generated by rotating beamstops in serial operation	77
4.1	Microbunching and transverse coherence at XFELs	81
4.2	Imaging with separate detectors	83
4.3	Multiplexed reference arrangement for x-ray sequential imaging	86
4.4	The setup at FLASH	87
4.5	Schematic layout of the soft x-ray autocorrelator	87
4.6	SEM images of the sequential imaging sample	88
4.7	Single-shot FTH at FLASH	89
4.8	Magnifications of specific single-shot reconstructions	90
4.9	Two-image “movie”	92
4.10	Subimage created by a double-exposed reference	94
4.11	Simulation of coherent vs. incoherent hologram superposition	99
4.12	FLASH energy jitter in multi-pulse FTH	101
4.13	FLASH energy jitter in single-shot FTH	102
4.14	FLASH spatial jitter	103
4.15	Artificial two-beam hologram	105
4.16	Simulated incoherent two-beam hologram including a $\Delta\mathbf{q}$ -shift	110
4.17	Separation of the two-beam hologram	111
A.1	Magnetic contrast	135
B.1	Resonance factors F' and F''	140

List of Abbreviations

AC	AutoCorrelator
ADU	Analog-to-Digital Unit
AF	AntiFerromagnetic
BG	Brandenburg Gate
BS	BeamSplitter (also BeamSplitting)
CCD	Charge-Coupled Device
CDI	Coherent Diffraction Imaging
FEL	Free-Electron Laser
FLASH	Free-electron LASer in Hamburg
FOV	Field Of View
FTH	Fourier Transform Holography
HERALDO	Holography with Extended Reference by Autocorrelation Linear Differential Operator
LASER	Light Amplification by Stimulated Emission of Radiation
LCLS	Linac Coherent Light Source
LHL	Local Hysteresis Loop
LIGA	Lithografie, Galvanik, Abformung (<i>German</i>)
MFM	Magnetic Force Microscopy
ML	MultiLayer
MOKE	Magneto-Optical Kerr Effect
PEEK	PolyEther Ether Ketone
ROI	Region Of Interest
SASE	Self Amplification of Spontaneous Emission
SAXS	Small-Angle X-ray Scattering
SCSS	Spring-8 Compact Sase Source
SEM	Scanning Electron Microscopy or Microscope
SNR	Signal-to-Noise Ratio
SQUID	Superconducting QUantum Interference Device
URA	Uniformly Redundant Array
VSM	Vibrating Sample Magnetometry
XFEL	X-ray Free-Electron Laser
XMCD	X-ray Magnetic Circular Dichroism
XPCS	X-ray Photon Correlation Spectroscopy
XTM	X-ray Transmission Microscopy or Microscope

1 Introduction

In 1948 Denis Gabor was looking for a way to improve the image quality in electron microscopy. He identified the aberration of the electron lenses as the limiting factor for the image resolution of electron microscopy and consequently introduced the lensless “electron interference microscope” [Gab48]. This new concept, which is known today as holography, abandons the use of lenses for image generation and therefore does not suffer from their limitations. The sacrifice of the lenses becomes possible as holography exploits the interference with a reference wave to record the amplitude and phase information of a wave scattered by an object. This fact gives holography its name, which constitutes of the syllables *holo-* and *-graphy* which originate from the Greek language and translate into *complete* or *total* and *recording* [Goo05], respectively.

Based on the coherence of the light, holography profited from the invention of the laser in 1960 [Mai60]. This source provides monochromatic light with an enormous coherence length and therefore stimulated the improvement of holography. In 1963 Leith and Upatnieks successfully separated the object and the reference beam with the help of a prism. The created off-axis holography solved the twin-image problem of Gabor’s in-line geometry [LU63]. In the year to follow Leith and Upatnieks managed to create a hologram reconstruction from a 3D-scene by interfering the off-axis reference light with the light reflected from an object [LU64]. In the same year the base for Fourier transform holography (FTH) was laid [Lug64; SF64]. For this holographic recording scheme a typically point-like reference is introduced within the sample plane, e.g. by the focus of a lens. Its name originates from the fact that a single Fourier transformation constitutes the mathematical operation to calculate the hologram reconstruction.

From this starting point on holography was constantly developed especially in the optical regime where lasers were available leading to a variety of holography applications today. For example, holographic labels are widely used as certificates of authenticity. Holographic methods can be exploited in materials testing, for instance to visualize deformations or vibrations on the wavelength level. Finally, holograms are used in art for their appeal and true three-dimensional image generation.

Already at the beginning of this development process considerations existed to use holographic techniques in conjunction with x-rays to achieve a high spatial resolution. In the year of 1965 the idea of lensless Fourier transform holography has been formulated [Str65] as well as demonstrated [WW65]. This implementation of FTH does require neither lenses nor beam-splitting optical elements and was therefore regarded as a suitable way to transfer the technique to x-rays where such devices perform inefficiently. Since no coherent x-ray source was available during the next years only basic experiments were performed.

The first lensless Fourier transform holograms recorded with x-rays were reported in 1972 using Carbon K_α radiation [Kik72] as well as synchrotron radiation [AIK72]. For both experiments a 2.5- μm -wide slit served as reference to image an arrangement of three 2.8- μm -wide slits.

With the introduction of undulators at third generation synchrotron sources the x-ray radiation provided was bright enough to allow for the extraction of an appreciable coherent flux. The first high-resolution experimental realization of x-ray Fourier transform holography was demonstrated in 1992 with soft x-ray undulator radiation of 3.4 nm wavelength. McNulty et al. [McN92] created the necessary x-ray point source with a Fresnel zone plate and performed Fourier transform holography at 60 nm resolution surpassing the spatial resolution of visible-light microscopy. The complete lensless version of Fourier transform holography was conducted by Eisebitt et al. in 2004. This group combined the holography technique with the resonant magnetic contrast available in the soft-x-ray regime to image a magnetic domain pattern with 50 nm resolution [Eis04]. In the short time since then lensless x-ray FTH has developed to an established technique that enables material science investigations, especially in the area of magnetic thin films with perpendicular anisotropy. For this sample system FTH features some unique selling points in comparison to competing x-ray imaging techniques. Still, the development of FTH is under way.

Today, the first x-ray free-electron lasers (XFELs) are operational and provide user mode. With the help of the spontaneous self-amplification of a highly brilliant electron bunch these sources generate femtosecond long x-ray pulses with an unprecedented number of x-ray photons [Ack07; Emm10]. These properties predestine XFELs for the investigation of the ultrafast time regime via single-pulse imaging. The high energy stored in such x-ray pulses puts scientists in front of new challenges as samples and optics are quickly evaporated in the intense light. At the same time the radiation provided is fully transversely coherent. It is therefore reasonable to assume that imaging experiments that rely on coherence instead on lenses will play a fundamental role in conjunction with x-ray free-electron lasers.

To generate XFEL radiation very long undulators and accelerators are required which make these lightsources huge facilities that may extend over kilometers. Because of their size XFELs will probably not find their way into everyday life like it happened with the laser in the optical regime. Nevertheless, in terms of the properties of the generated radiation these new x-ray sources of the fourth generation may trigger a comparable revolution for x-ray science as the laser did in (visible) optics. Fourier transform holography is definitely one of techniques that benefits from this development.

1.1 Structure of the Thesis

Subsequent to this introduction, chapter 2 gives a short overview on the basic theory necessary for coherent scattering. Sec. 2.1 introduces the basic parameters of scattering experiments in general, which are described in reciprocal space by the in-plane momentum

transfer q . Holography is an imaging method based on the coherence properties of the light. Sec. 2.2 defines these properties such as the coherence length. Sec. 2.3 describes the mechanism of the image formation in Fourier transform holography, which takes place by the convolution of the object with a reference defined by a small aperture.

The experimental part is divided into two chapters. First, chapter 3 reports on quasistatic experiments performed at third generation synchrotrons. Sec. 3.1 illustrates how Fourier transform holography is conducted at these partly coherent light sources. The effects of x-ray magnetic circular dichroism (XMCD) and resonant magnetic scattering is explained, which allow to probe magnetic materials via the polarized light that synchrotrons can deliver. Furthermore, details on the experimental realization are given in this section.

Section 3.2 introduces the scenario of domain replication under the influence of different external parameters. An exchange-decoupled magnetic multilayer system is examined at low temperature and under an applied external magnetic field. The element specificity of x-rays allows to distinguish between the domain patterns of the two multilayer stacks and reveals domain duplication induced by interlayer dipolar interaction.

Section 3.3 illustrates the effect of the reduced field of view typical for FTH. The investigated magnetic specimen is confined to the size of a few magnetic domains. Thus, it is possible to observe microscopic features in the resulting local hysteresis loops (LHLs), which are typically lost in averaging macroscopic measurements. Hereby, the integrated sample design of FTH allows to collect magnetic images on that identical sample region for comparison.

Section 3.4 makes a short excursus to the instrumentation development. The concept, design and performance of a beamstop optimized for scattering experiments is presented. A rotating wire produces a q -dependent absorption profile which allows for a faster data acquisition with less noise.

After the experiments with established methodology using synchrotron light from a storage ring source, the second experimental part of the thesis deals with the potential of FTH at new x-ray sources. Coherent imaging techniques profit tremendously from the increase in *coherent* photon flux of x-ray free-electron lasers. At the same time the unprecedented number of coherent x-ray photons compressed to femtosecond pulses as well as the stochastic light generation by the SASE process demands for new experimental methods. Chapter 4 discusses a new imaging approach, which is capable to record an ultrafast x-ray image sequence.

The characteristics of XFELs are described in Sec. 4.1. These facilities are built to provide short-wavelength x-ray radiation in short pulses of femtosecond duration, i.e. to combine a high resolution in space as well as in time. One goal of these fourth generation x-ray sources is to observe the dynamics of chemical and biological reactions, which can be described as the recording of a “molecular movie”.

In Sec. 4.2 the experimental details are specified. The layout of the sample structure is heavily based on reference multiplexing to collect multiple independent images. Together

with a soft x-ray autocorrelator, a split-and-delay line for x-rays, it becomes possible to record an ultrafast image sequence generated by a single XFEL pulse. The mathematical framework describing image formation in FTH is extended to the general case of an arbitrary number of references each with different amplitude and phase. Furthermore, the experimental setup for sequential x-ray imaging is described.

The experimental results for sequential x-ray imaging are presented in Sec. 4.3. First, the feasibility to reconstruct single-shot holograms is demonstrated. Afterwards, a two-beam hologram recorded with split XFEL pulses is presented. The independent images of the object in this reconstruction correspond to different points in time. The properties of such a holographic image sequence are analyzed in detail in Sec. 4.4. The image formation of a two-beam hologram reconstruction is discussed dependent on a coherent or incoherent hologram superposition. In addition, the effect of the statistical nature of the FEL pulses on the hologram reconstruction is investigated.

In Sec. 4.5 future aspects for the presented ultrafast imaging approach are shown. Possibilities for the scaling to high spatial resolution are discussed as well as the the recording of multiple time frames. A possible path for the separation of superimposed diffraction patterns is outlined.

Chapter 5 summarizes the conclusions drawn in the previous chapters and presents an outlook to future developments of FTH.

2 Theory

Holographic imaging is a two-step process. First, the hologram is recorded as interference pattern of the object and the reference wave. The recording can be realized by exposure of a photographic plate or a digital camera. The latter directly converts the resulting intensity pattern to a digital matrix. Second, the object wave is reconstructed from the hologram. Depending on the type of the detector the reconstruction is realized either optically, by illumination of the hologram with the reference wave, or analytically, by mathematical inversion of the digital hologram matrix. The much easier and faster data analysis makes the digital reconstruction superior compared to the optical one, especially as scientific-grade digital cameras are widely available by now.

In this chapter the basic definitions for the recording and the reconstruction of holograms are discussed. Emphasis is put on lensless Fourier transform holography (FTH), which is the imaging method of choice throughout this thesis. The setup geometry for FTH is very similar to a transmission scattering experiment and shares the basic definitions, which are explained in Sec. 2.1.

Scattering experiments do provide information on the investigated sample but usually not in form of an image. The reason is found in the phase problem. Light is an electromagnetic wave characterized by amplitude and phase. During the detection process of light the amplitude squared, i.e. the intensity, is recorded. The phase information is completely lost. The intensity pattern of the light scattered by a specimen alone is not sufficient to provide a unique solution for the real-space map of the specimen under consideration.

The situation is different when coherent light is used for sample illumination. In that case the recorded intensity pattern exhibits speckles, which are caused by interference of the light scattered at different sample locations. Under certain conditions, the so-called constraints, such speckle patterns can be inverted to real-space images via iterative phase retrieval algorithms. Another possibility is the introduction of a reference wave, which interferes with the scattered light and preserves the relative phase information in the interference pattern. Thus, with the help of coherence it is possible to invert scattering patterns to real-space images. Coherence in general is discussed in Sec. 2.2.

In holography the image of the sample is encoded by the reference wave. For the special case of Fourier transform holography a spherical-wave reference is used realized here by a small aperture. The hologram reconstruction is performed by a single two-dimensional Fourier transformation. Hereby, the image of the sample is generated by convolution of the object with the reference. This mechanism of image formation is explained in Sec. 2.3.

2.1 Geometry of Scattering Experiments

Fourier transform holography with x-rays is basically a small-angle x-ray scattering (SAXS) experiment in transmission geometry, sharing its properties and restrictions. Beyond classical SAXS the experiment exploits coherent x-rays and couples in a reference wave. These two measures solve the phase problem and allow to directly invert the x-ray scattering pattern to obtain an image of the object.

Photons carry a momentum determined by the product of the reduced Planck constant \hbar and the wave vector \mathbf{k} . The magnitude of the wave vector \mathbf{k} is determined by the wavenumber $k = 2\pi/\lambda$ and its direction is parallel to the light's propagation direction. X-ray photons traveling through matter interact with the present electrons. The interaction mechanisms are manifold but have in common that the radiation behind the sample carries information about the propagated material. The interactions are described by Maxwell's equations in the presence of matter. From this starting point formalisms for light-matter interaction like scattering, absorption and fluorescence can be derived like it is done in many text books [Att00; Pag06; LC96; SS06].

This thesis focuses on the analysis of elastic scattering patterns in the soft x-ray regime. Soft x-ray photons are influenced by the core electrons of the atoms. These electrons, more precisely the electron charge density, act as scattering centers and transfer a recoil to the photons. Consequently, the momentum and thus the wave vector of the incident photons \mathbf{k}_{in} is changed. For elastic scattering the wavenumber of the incident and scattered photon is identical ($k_{\text{in}} = k_{\text{out}} = k$), but the propagation direction differs. This directional change corresponds to the inner structure of the sample.

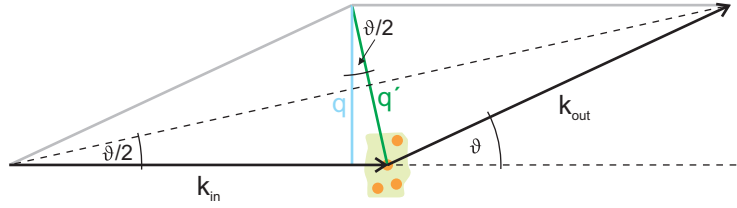


Figure 2.1: Passing through matter light is scattered into angle ϑ carrying the in-plane momentum transfer \mathbf{q} .

Fig. 2.1 illustrates the scenario. A photon is scattered into angle ϑ , while the wavenumbers of the photon before and after the interaction remain identical. The momentum transferred to the photon \mathbf{q}' during the scattering process is given by $\mathbf{q}' = \mathbf{k}_{\text{out}} - \mathbf{k}_{\text{in}}$. The magnitude of the momentum transfer \mathbf{q}' is given by

$$q' = 2k \sin\left(\frac{\vartheta}{2}\right). \quad (2.1)$$

The basic statement this equation is that a charge density with periodicity d scatters

light of wavelength λ into the scattering angle ϑ . The equivalent statement is made by Bragg's law: $n_{\text{order}}\lambda = 2d_{\text{lat}} \sin(\theta)$. Consequently Eq. 2.1 can be converted to the first order ($n_{\text{order}} = 1$) of Bragg's law by substituting $k = 2\pi/\lambda$ and $q' = 2\pi/d_{\text{lat}}$ with d_{lat} being the crystal periodicity [Att00]. Note that Bragg scattering is usually described in terms of a scattering angle chosen such that $2\theta = \vartheta$.

For the detection of the scattering signal in transmission geometry the component of \mathbf{q}' in the plane perpendicular to the incident radiation is of interest. This in-plane momentum transfer is denoted \mathbf{q} and its absolute value q . The ratio of q and q' is given by the cosine of the included angle, thus $q = q' \cos(\frac{\vartheta}{2})$. The insertion of Eq. 2.1 yields

$$q = 2k \sin\left(\frac{\vartheta}{2}\right) \cos\left(\frac{\vartheta}{2}\right) = \frac{2\pi}{\lambda} \sin(\vartheta). \quad (2.2)$$

This central equation connects the magnitude of the in-plane momentum transfer q to the wavelength λ of the incident light and the scattering angle ϑ . As in the comparison to Bragg's law q relates to the real-space periodicities of the sample in the plane normal to k_{in} via

$$q = \frac{2\pi}{d} \implies d = \frac{\lambda}{\sin \vartheta}. \quad (2.3)$$

That means smaller structures scatter into larger angles. At the same time a decrease of the light's energy (increase in λ) causes an increase of the scattering angle ϑ .

The recording of a scattering pattern of an object requires a suitable spatially resolving detector. Such a device is characterized by its number of pixels n in one dimension and their edge length s . Their product defines the detector size $D = n \cdot s$, which might differ along the two dimensions of the detector plane. The distance L between the sample and the detector plane sets the q -scaling on the detector as illustrated in Fig. 2.2. At distance

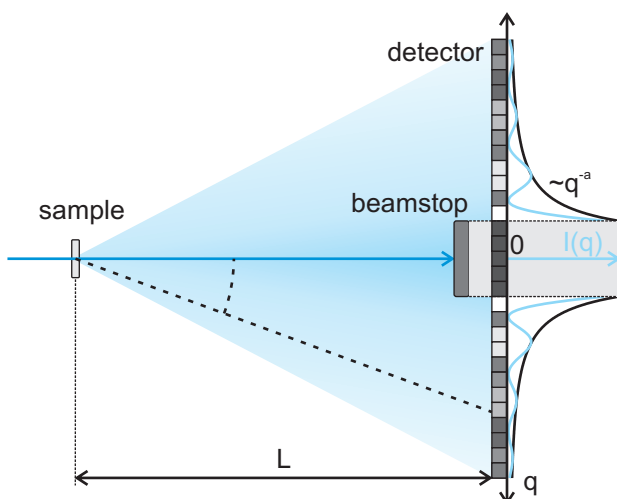


Figure 2.2: Basic layout of a scattering experiment. A detector consisting of n pixels collects the scattering pattern generated by an object. The intensities recorded in each pixel correspond to a certain spatial frequency of the sample.

L the outermost pixel records the maximum scattering angle, which corresponds to the smallest resolvable sample structure. Therefore, the position of the detector defines the diffraction-limited resolution d_{res} :

$$\tan \vartheta_{\text{max}} = \frac{D/2}{L} \quad \implies \quad d_{\text{res}} = \frac{\lambda}{\sin \vartheta_{\text{max}}}. \quad (2.4)$$

Within the small-angle approximation usually applicable for soft x-rays the tangent and sine of an angle can be approximated with the angle itself and Eq. 2.4 simplifies to

$$d_{\text{res}} = \frac{2\lambda L}{D}. \quad (2.5)$$

Smaller features are not resolvable since they scatter into larger angles missing the detector.

A similar boundary exists set by the pixel size s . A pixel detector can only sample frequencies corresponding to a periodicity of two pixels. This fact is also known as the Nyquist theorem. Fast oscillations in reciprocal space are created by large structures in real space. Note that for FTH this largest structure will usually be the object-reference distance. That means the scattering originating from sample features above a certain size in real space is lost to the pixel size s . Combining both limitations the number of pixels n of a detector defines a resolution ratio of $n/4$ for scattering experiments. Typical x-ray detectors feature a pixel number n of 2000, which results in a ratio of 500 for smallest versus largest structures resolvable. The exact values are defined by the sample detector distance L and the wavelength λ . For example, if the setup is tuned to a diffraction-limited resolution of 50 nm, the corresponding largest structure resolvable is 25 μm for a detector featuring $n = 2000$ pixels (see also [Pfa10a]). Note that the resolution window is defined by the number of pixels and not their size. The latter can be compensated by adjusting L and λ .

The signal of the intensity pattern recorded in the detector plane drops quickly for larger q . Depending on the sample structure the exponent of the corresponding power law varies between -3 and -6 [SBT04]. Due to this fast drop of the scattering signal and the limited dynamic range of CCD x-ray detectors a central beamstop is often integrated in x-ray scattering setups. This device blocks the bright forward scattering and possibly residual transmitted x-rays and enables a faster detection of the high-angle scattering corresponding to high-resolution information.

2.2 Coherence

Light is described as an electromagnetic wave with amplitude and phase. The important requirement for the recording of a hologram is interference, i.e. the ability of two wave-like states overlapping in time and space to add constructively or destructively depending on their phase shift. This particular property of the light is known as coherence quantifying the correlation of emitted wavefronts. Real light sources have a finite size and emit within

a bandwidth. As a result, the generated waves are different in energy and propagation direction. This fact degenerates the correlation and thus the coherence. Outside of the coherence regime wave interaction is described by adding their real-valued intensities only. The phase is neglected and interference cannot be observed anymore. Coherence is often described by two parameters measured along and perpendicular to the light's propagation direction.

2.2.1 Longitudinal Coherence

The parameter measured along the propagation direction of the electromagnetic wave is called longitudinal coherence. It quantifies the spectral properties of the light source and is also known as spectral or temporal coherence. Longitudinal coherence considers to which extent all photons emitted by a light source are of the same wavelength. Real light sources always emit within a bandwidth, i.e. the radiated wavelength λ carries a spectral uncertainty $\Delta\lambda$. Fig. 2.3 considers two waves originating from one source and exhibiting the maximum spectral uncertainty within the bandwidth. These two waves with wavelengths λ and $\lambda + \Delta\lambda$ are emitted into the same direction at the same time. Due to their wavelength difference both waves acquire a phase shift of 180° after some distance, thus they are completely anti-phase at this location. The waves emitted from the source may carry any intermediate spectral uncertainty $\Delta\lambda$. Considering all these waves emitted by the source, that means from this point on all phases are present in the emitted wave packet and consequently the light must be regarded as completely uncorrelated. The corresponding distance is called the longitudinal coherence length ξ_1 . It can be derived from the two exemplary waves with maximum spectral uncertainty. At ξ_1 the wave with the shorter wavelength λ has completed half an oscillation less than the other wave. Solving

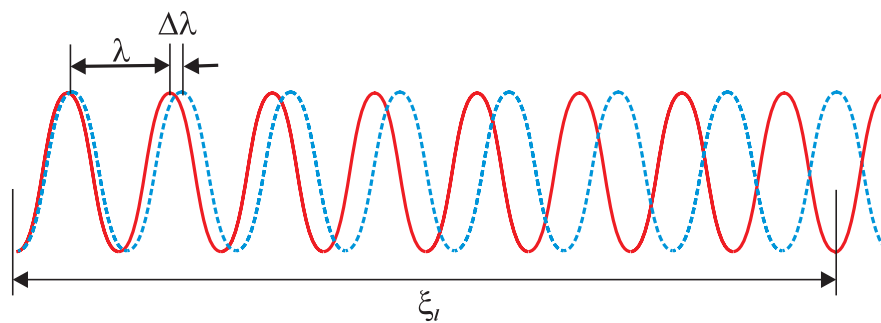


Figure 2.3: Two waves with slightly different wavelengths acquire a phase shift of π after propagating a distance larger than the longitudinal coherence length ξ_1 along the same direction.

$N\lambda = (N - 1/2)(\lambda + \Delta\lambda)$ for N yields the longitudinal coherence length [Att00]

$$\xi_1 = N\lambda \approx \frac{\lambda^2}{2\Delta\lambda}. \quad (2.6)$$

ξ_1 is inversely proportional to the bandwidth $\Delta\lambda$. The prefactor in Eq. 2.6 may vary upon assumptions for the spectral power density of the source (compare [VP04; Goo00]). The longitudinal coherence length defines the coherence time of a light source via $\tau_c = c \xi_1$ with c being the speed of light.

Waves originating from one source will not significantly contribute to an interference pattern in the detector plane if they show a path length difference larger than the longitudinal coherence length. That means in coherent scattering experiments the width of a sample perpendicular to the beam and ξ_1 together limit the maximum scattering angle ϑ under which interference can be observed

$$\frac{\lambda^2}{\Delta\lambda} > a \sin \vartheta. \quad (2.7)$$

Eq. 2.7 can be directly translated in terms of the achievable diffraction-limited resolution as derived in Ref. [VP04]:

$$\frac{\Delta\lambda}{\lambda} < \frac{d_{\text{res}}}{a}. \quad (2.8)$$

Here, d_{res} is the diffraction-limited resolution and a the width of the object. A ratio of $\Delta\lambda/\lambda$ of 1000 directly translates to the same resolution relative to the object width.

2.2.2 Transverse Coherence

Transverse or spatial coherence quantifies the correlation of wavefronts perpendicular to the light's propagation direction. It can be described as the degree to which a beam of light appears to have originated from a single point source. Thus, transverse coherence is inversely proportional to the apparent source diameter b . Following the derivation in the book by D. Attwood [Att00] a perfect transversely coherent beam with no divergence is impossible due to Heisenberg's uncertainty principle

$$\Delta\mathbf{x} \cdot \Delta\mathbf{p} \geq \frac{\hbar}{2} \iff \Delta\mathbf{x} \cdot \Delta\mathbf{k} \geq \frac{1}{2}, \quad (2.9)$$

which states that location and momentum of a photon cannot be measured with arbitrary accuracy at the same time. $\Delta\mathbf{x}$ is the spatial uncertainty in one dimension. The corresponding momentum uncertainty is expressed in terms of the wave vector $\Delta\mathbf{k}$. Assuming a small relative bandwidth $\Delta\lambda/\lambda = \Delta k/k$ the uncertainty of \mathbf{k} originates mainly from the uncertainty of direction Θ . If the small-angle approximation holds, $\Delta\mathbf{k}$ can be expressed

with $k\Delta\theta$ [Att00]:

$$\Delta x \cdot \Delta\theta = \frac{\lambda}{4\pi}. \quad (2.10)$$

Finally, $2\Delta x$ is identified with the source's diameter b and $\Delta\theta$ with the half angle of divergence Θ

$$b \cdot \Theta = \frac{\lambda}{2\pi}. \quad (2.11)$$

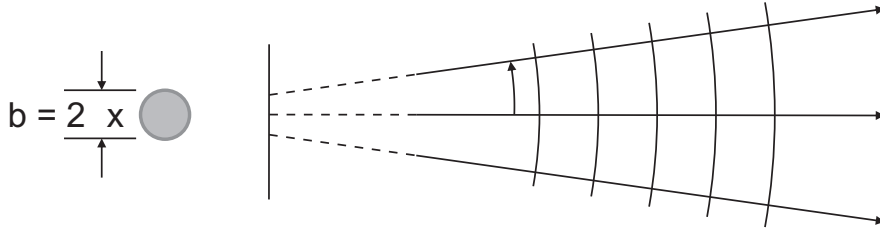


Figure 2.4: (Adapted from Ref. [Att00].) A light source of size b can only emit correlated wavefronts of wavelength λ into the divergence half angle Θ .

This relation determines the divergence half angle Θ into which a source of size b can emit correlated wavefronts of wavelength λ . In analogy to the longitudinal coherence length one can define a transverse coherence length ξ_{tr} . Note that $\xi_{\text{tr}} = L \cdot \Theta$ is a property that includes a dependence on the distance between the light source and the detector L :

$$\xi_{\text{tr}} = \frac{\lambda L}{2\pi b}. \quad (2.12)$$

In essence, the coherence of a light source can be determined by its spectral bandwidth $\Delta\lambda$ as well as its divergence half angle Θ and its size b . Eq. 2.6 and Eq. 2.11 define the two criteria in whose area of validity phase-sensitive interference experiments are possible. This regime is also described by the coherence volume V_c spanned by the longitudinal coherence length and the coherence area A_{tr} [Len01]

$$V_c = \xi_l A_{\text{tr}} = \xi_l \pi \xi_{\text{tr}}^x \xi_{\text{tr}}^y. \quad (2.13)$$

A_{tr} is the elliptical area defined by the two orthogonal coherence lengths ξ_{tr}^x and ξ_{tr}^y perpendicular to the light propagation direction.

The difference between incoherent and coherent x-ray scattering experiments directly manifests itself in the recorded pattern. If the sample area is illuminated incoherently, the sum of the scattered intensities is recorded at the detector and the scattering pattern contains statistical information on the spatial frequencies within the specimen. Upon coherent illumination the scattered light interferes and the squared sum of the scattered amplitudes is recorded. As a result, the scattering pattern corresponds to a fingerprint of the sample's real-space map and therefore allows to follow e.g. equilibrium fluctuations

on the wavelength scale within the sample [Shp07]. Furthermore, the coherent diffraction pattern allows for a solution of the phase problem either by iterative methods or holographic references [Mia99; McN92; Eis04].

2.3 Fourier Transform Holography

Holography is an imaging method based on the coherence of the light. The wave field scattered by an object, the object wave, is brought to interference with a reference wave. During the detection process the phase of the object wave is encoded relative to the phase of the reference wave in the intensity pattern. With this complete wave field information a reconstruction of the object wave, and thus ultimately of the object itself, is possible.

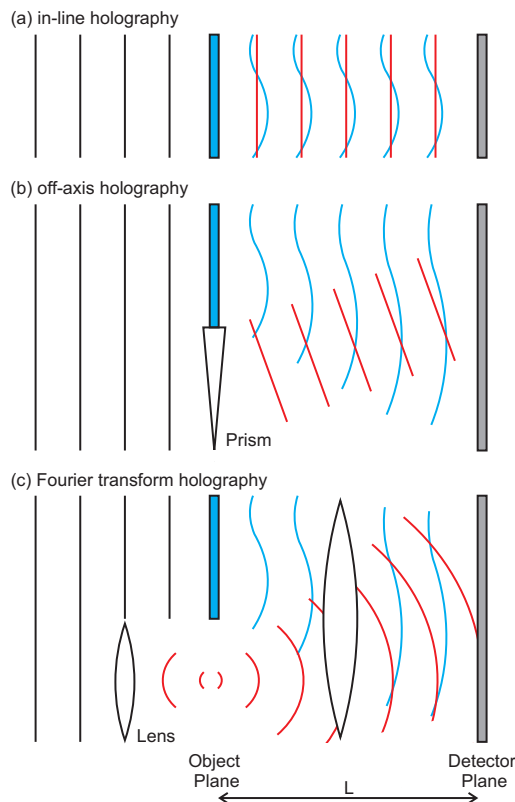


Figure 2.5: Three common geometries for hologram recording. The light is incident from the left (black). Behind the sample plane the scattered object wave (blue) and the reference wave (red) are distinguished. Interference takes place at the detector (gray). Visualized are the following setups:

- (a) in-line holography (D. Gabor)
- (b) off-axis (Leith-Upatnieks)
- (c) Fourier transform holography.

Various schemes for hologram recording do exist. Three of the most common setups are illustrated in Fig. 2.5. In-line holography as originally performed by D. Gabor [Gab48] is shown in panel (a). Here, the residual light directly transmitted through the sample serves as reference wave. This is probably the simplest setup, but it suffers from the twin-image problem. In the hologram reconstruction both parts of the twin-image reconstruct superimposed, which causes a blurring as only one part of the twin-image can be sharp at the same time.

The twin-image problem is solved by off-axis holography (Fig. 2.5(b)) first demonstrated by E. N. Leith and J. Upatnieks [LU63]. The reference beam is separately guided around the object and brought to interference with the object wave under an angle. As a result, the two parts of the twin-image reconstruct at separate locations without blurring.

For Fourier transform holography a spherical reference wave is exploited with its origin in the sample plane (Fig. 2.5(c)). In the initial setup the point source is realized by the focal spot of a lens. Furthermore, an additional lens is placed in between the sample and the detector plane such that both planes coincide with the front and back focal planes of this intermediate lens [Lug64]. The interesting point of this holography setup is that the mathematical connection between a wave exiting the sample plane and arriving at the detector plane is a single Fourier transformation. Consequently, this mathematical operation reconstructs the Fourier transform hologram. All three hologram recording geometries work well in the visible-light regime, where they have been initially demonstrated. Details on calculations of the wave fields for the mentioned holography setups can be found for instance in [Har02].

When it comes to soft x-rays the problem arises that light of this energy is strongly absorbed by essentially any kind of matter. The realization of optical elements like lenses or beamsplitters requires much more effort compared to the optical regime. For FTH an equivalent lensless implementation exists. This scheme illustrated in Fig. 2.6 was demonstrated in 1965 with visible light, but already with the application for x-rays in mind [WW65; Str65].

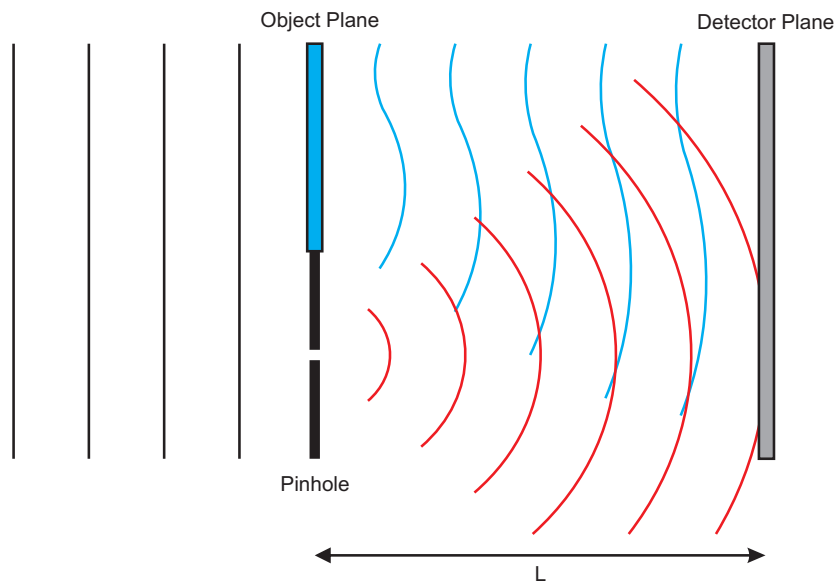


Figure 2.6: Schematic setup for the recording of a lensless Fourier transform hologram.

Instead of a lens a pinhole generates the spherical reference wave directly in the sample plane. The intermediate lens can be removed if the created scattering pattern is detected in

the far-field. Here, the far-field condition is fulfilled if the product of the lateral dimensions of the sample structures ($x_{\text{object}}, y_{\text{object}}$) in the sample plane and the wavenumber k is small compared to the sample detector distance L [Goo05]

$$L \gg \frac{k(x_{\text{object}}^2 + y_{\text{object}}^2)_{\text{max}}}{2}. \quad (2.14)$$

The exchange of lenses with x-ray transmissive apertures makes this holography setup suited for soft x-rays. The first demonstration of x-ray FTH surpassing the spatial resolution of visible-light microscopy was performed in 1992 by I. McNulty et al. [McN92]. The group exploited a Fresnel zone plate, a diffractive optical element which constitutes a lens equivalent for x-rays, to create the point reference and imaged gold test objects with a resolution of 60 nm. In 2004 S. Eisebitt et al. demonstrated the complete lensless implementation of FTH [Eis04]. The geometry was realized by an integrated nanostructured gold mask, which defined the object aperture as well as the reference pinhole. Exploiting magnetic contrast via x-ray magnetic circular dichroism Eisebitt et al. imaged the worm domain structure of a perpendicular anisotropy multilayer with 50 nm resolution.

Both x-ray FTH approaches have successfully proved the capability for high-resolution imaging [McN92; Eis04]. However, the integrated mask-sample approach suggested by Eisebitt et al. (see Sec. 3.1.3) has the advantages that (i) relative drift of reference and object is ruled out and (ii) the space in the direct vicinity of the sample remains free for additional experimental instrumentation such as, for instance, magnetic poles. As a result, a variety of experiments exploiting lensless FTH were performed since 2004 establishing the method as standard synchrotron imaging technique [Hel06; Tie10a; Tie10b; Tie10c; SN09; Sti10; Awa10; Pfa11; Pfa10b; Gue10; Gue09; Gü08; Gü10; Hel11].

The coherence properties discussed in the previous section enable FTH to encode the relative phase of an object wave in a diffraction pattern and thus to yield an image in the hologram reconstruction. For the discussion of the image formation in FTH the light wave transmitted by the sample and recorded on the detector needs to be considered. In accordance with Fig. 2.6 the exit wave emitted from the sample plane after interaction is denoted as sample function $s(\mathbf{r})$. The term sample is somewhat ambiguous as it can refer exclusively to the physical specimen under investigation as well as to the combination of the specimen with the nanostructured holographic mask. The meaning is usually clear from the context. Throughout this thesis $s(\mathbf{r})$ always designates the complete exit wave including the reference part. It considers absorption as well as phase shifts originating from the whole sample structure and is consequently complex-valued. The sample function is defined in real space as the sum of the object function $o(\mathbf{r})$ and a reference function $r(\mathbf{r})$

$$s(\mathbf{r}) = o(\mathbf{r}) + r(\mathbf{r}) = o(\mathbf{r}) + \delta(\mathbf{r} - \mathbf{r}_1). \quad (2.15)$$

The object function $o(\mathbf{r})$ describes the exiting wave transmitted only through the actual

specimen. This part of the sample function describes the (usually circular) shape of the object aperture as well as any structure contained therein. The goal of the FTH process is to reconstruct the object function $o(\mathbf{r})$, i.e. the image of the object. For convenience the center of the object function is identified with the origin of the coordinate system. In the sample plane the reference function is realized by a small aperture, which can be approximated by a delta function $\delta(\mathbf{r} - \mathbf{r}_1)$ at position \mathbf{r}_1 . In reality reference apertures feature limited transmission and a finite size. The reference reproduces the object function by convolution with itself in the hologram reconstruction.

An example for $s(\mathbf{r})$ is given in Fig. 2.7(a). The object is represented by the letter “F” with a line width of 7 pixels and the reference by a circle approximation consisting of 26 pixels overall. The color white and black correspond to pixel values of 0 and 1 representing the light transmission through the two apertures. The simulation assumes plane-wave illumination with a constant phase of zero over the entire field of view (FOV). The sample function in reciprocal space is denoted with $S(\mathbf{q})$ depending on the in-plane momentum transfer \mathbf{q} . The mathematical operation connecting the variables \mathbf{r} and \mathbf{q} is the Fourier transformation switching between real and reciprocal space

$$S(\mathbf{q}) = \mathcal{F}\{s(\mathbf{r})\} \quad \text{and} \quad \mathcal{F}^{-1}\{S(\mathbf{q})\} = s(\mathbf{r}). \quad (2.16)$$

In the far-field the detector, which is sensitive to intensities only, records the square of the Fourier transform of the real-space sample function $s(\mathbf{r})$. The simulation of such a pattern is visualized in Fig. 2.7(b) on a logarithmic intensity scale. This pattern constitutes the Fourier transform hologram. The hologram reconstruction is performed by applying an inverse Fourier transformation yielding the so-called Patterson map P . Instead of the inverse operation it is also possible to use a forward Fourier transform for the practical reconstruction of the real-valued intensity pattern. The only difference is a change of the sign of the phase during the transformation, which results in a switching of image and

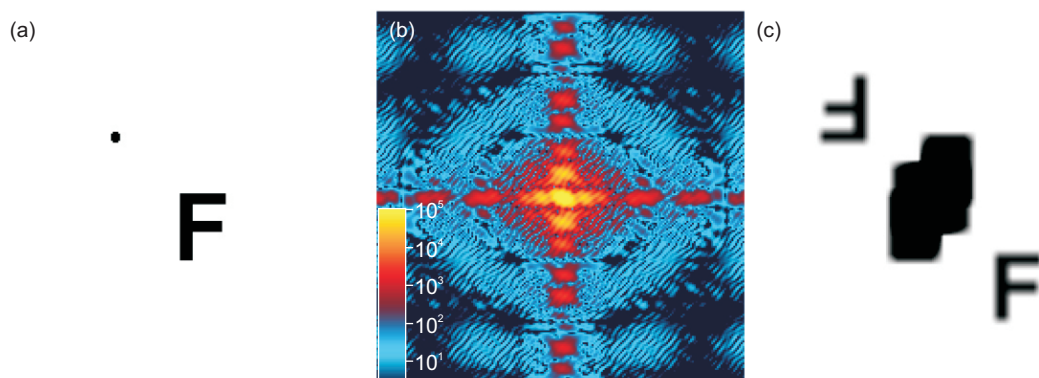


Figure 2.7: Image formation in Fourier transform holography: (a) Sample structure. (b) Simulated hologram on logarithmic intensity scale. (c) Hologram reconstruction.

twin-image in the reconstruction. The information on the object itself is not altered:

$$\begin{aligned}
P &= \mathcal{F}^{-1} \left\{ |S(\mathbf{q})|^2 \right\} = \mathcal{F}^{-1} \left\{ |\mathcal{F} \{s(\mathbf{r})\}|^2 \right\} = \mathcal{F}^{-1} \left\{ (\mathcal{F} \{s(\mathbf{r})\})^* \mathcal{F} \{s(\mathbf{r})\} \right\} \\
&= \mathcal{F}^{-1} \left\{ (\mathcal{F} \{s(\mathbf{r})\})^* \right\} * \mathcal{F}^{-1} \left\{ \mathcal{F} \{s(\mathbf{r})\} \right\} \\
&= s^*(-\mathbf{r}) * s(\mathbf{r}).
\end{aligned} \tag{2.17}$$

The operator $*$ denotes the convolution operation. In Eq. 2.17 the convolution theorem is used, which states that the Fourier transform of a product function equals the convolution of the Fourier transforms of its factors. As a result, the Patterson map P equals the autocorrelation of $s(\mathbf{r})$. For clarity, the convolution term in Eq. 2.17 can be written as the autocorrelation of $s(\mathbf{r})$

$$s(\mathbf{r}) \star s(\mathbf{r}) = s^*(-\mathbf{r}) * s(\mathbf{r}). \tag{2.18}$$

with the \star symbolizing the cross-correlation operation. For consistency, throughout the thesis only the convolution notation is used. Eq. 2.17 is expanded by inserting the real-space sample function:

$$\begin{aligned}
P &= s^*(-\mathbf{r}) * s(\mathbf{r}) \\
&= o^*(-\mathbf{r}) * o(\mathbf{r}) + \underbrace{o^*(-\mathbf{r}) * \delta(\mathbf{r} - \mathbf{r}_1)}_{P_1^*} + \underbrace{\delta(-\mathbf{r} - \mathbf{r}_1) * o(\mathbf{r})}_{P_1} + \delta(-\mathbf{r} - \mathbf{r}_1) * \delta(\mathbf{r} - \mathbf{r}_1).
\end{aligned} \tag{2.19}$$

The Patterson map consists of four convolution terms illustrated in the reconstruction of the simulated hologram in Fig. 2.7(c). The autocorrelations of the object function $o(\mathbf{r})$ and the reference function $\delta(\mathbf{r} - \mathbf{r}_1)$ form in the center of the Patterson map. In addition, two cross-correlation terms between the two functions are observed displaced from the center by $\pm \mathbf{r}_1$ [Pag06]. These two cross-correlations constitute the actual images of the object denoted here as P_1^* and P_1 . As inherent for holography methods one reference always creates a pair of complex-conjugated twin-images, which carry only redundant information. In Fig. 2.7(c) The Patterson map is thresholded to an intensity value of 26 for optimum visibility of the object image. This value equals the size of the reference and consequently defines the maximum overlap of the reference with the object. FTH can be used with multiple references creating independent images [Sch06]. This concept is taken up again in Sec. 4.2.1 where the independent images created by different references carry a time information.

Ideally the reference is a delta function reproducing the object without any artifacts. However, in reality reference apertures have a certain size and finite transmission. As the image P_1 is created by convolution of the reference with the object function, the reference shape directly influences the image. In the simulation the reference had a diameter close to six pixels. Comparing the original letter “F” in Fig. 2.7(a) and its reconstruction in panel (c) the blurring of the object due to the large reference becomes directly evident. Thus, the

size of the reference constitutes a second limit to the resolution in lensless FTH in addition to the diffraction-limited resolution defined by the scattering geometry discussed in Sec. 2.1. In case that the reference size reduces the resolution of a hologram reconstruction below the recorded momentum transfer \mathbf{q} , additional phase retrieval methods can restore the higher diffraction-limited resolution set by \mathbf{q}_{\max} . This procedure is demonstrated in [Sta08]. In general, FTH is optimized if both resolution-limiting conditions, the reference size and recorded momentum transfer, are balanced.

3 Quasistatic Experiments

Synchrotrons of the third generation feature undulator insertion devices. These alternating magnetic structures define a sinusoidal trajectory for the electron beam. The electrons start to radiate upon the acceleration experienced. Due to the repetitive emission process along the sinusoidal trajectory, the light emitted by a single electron is compressed into harmonics at specific wavelengths and emission angles. This fact plus the high number of photons generated by third generation synchrotrons allow to extract a significant coherent flux from these light sources. Consequently, coherence-based imaging experiments in the x-ray regime are performed at undulator beamlines of synchrotron sources.

Beyond their coherence capabilities in the x-ray regime, synchrotron radiation offers some unique features in comparison with standard laboratory sources. (i) The flux is orders of magnitude higher. (ii) The energy of the x-rays is continuously tunable, which allows e.g. to measure in resonance with electronic transitions. (iii) Undulators enable polarization control of the generated light and thus to observe polarization-based effects. In particular these effects include the sensitivity of the polarized x-rays to the magnetization of a sample, which is heavily exploited in this section. (iv) Finally, synchrotrons are pulsed sources. The intrinsic time structure of synchrotron light can be exploited for the investigation of repetitive dynamics via pump-probe experiments.

In this section two magnetic FTH experiments are presented. At the beginning, the properties of a synchrotron as source for coherent magnetic imaging are briefly discussed and the corresponding experimental setup is introduced. The first experiment illustrates FTH at variable temperature. The integrated mask-sample design provides stability to perform FTH under low environmental temperature and in applied magnetic field. The second experiment introduces the measurement of local hysteresis loops in conjunction with FTH. Such measurements contain information on the microscopic reversal behavior of magnetic systems and, here, show Barkhausen jumps. In both experiments the element specificity of x-rays enables the investigation of buried layers. The last section documents the design and performance of a rotating beamstop allowing to optimize x-ray scattering and FTH experiments.

3.1 Synchrotrons as Source for FTH

3.1.1 Coherent Flux from Synchrotrons

Synchrotrons generate light by the acceleration of electrons. For synchrotrons of the third generation this task is performed by undulators which consists basically of a magnet

structure generating an alternating magnetic field in a straight section. An electron traveling through the field of the undulator is forced on a sinoidal path in the plane perpendicular to the magnetic field. Because of its highly relativistic speed the electron emits light into a small cone in the forward direction. The parameters of the undulator are adjusted in such way, that the light emitted in each of the undulator periods is in phase and thus the synchrotron light emitted by one single electron passing through the undulator is coherently amplified. Usually several hundred bunches each containing a number of electrons on the order of 1×10^{10} are maintained in the storage ring of a synchrotron [Att00]. Neither the electrons in different bunches nor the electrons contained in a particular bunch are emitting light in phase, but incoherently. Consequently, the extraction of a coherent flux from a synchrotron source requires coherent filtering. This process which may be performed on any light source is illustrated in Fig. 3.1. A spectral filter transmits only a certain bandwidth of wavelengths and improves the monochromaticity and thus the spectral coherence of the light generated by the light source. A reduction of the angular acceptance angle, e.g. by introducing a pinhole, improves the transverse coherence. Both filtering processes can be combined to generate a coherent but strongly reduced photon flux.

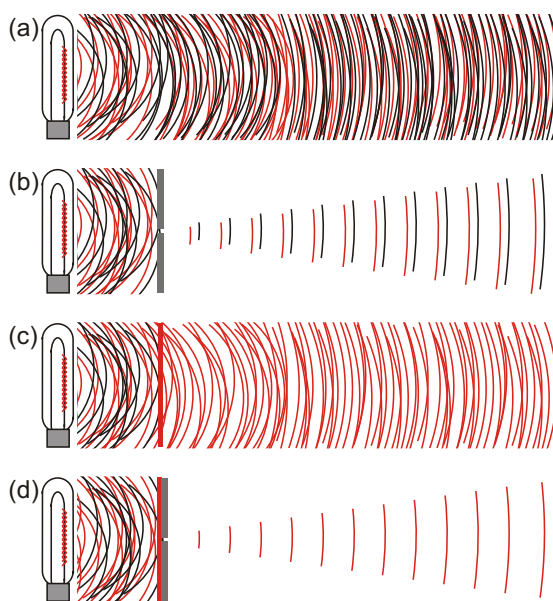


Figure 3.1: (Adapted from Ref. [Sch68].) By filtering of an incoherent light source illustrated in (a) a coherent photon flux can be extracted. (b) Pinholes reduce the apparent size of the source and increase the spatial coherence. (c) Energy filtering directly corresponds to an improvement of the longitudinal coherence. (d) The combination of both yields coherent light at a strong reduction of photon flux.

The coherence of a light source can be characterized by the degeneracy parameter Δ_c , which quantifies the average number of photons in each mode or in the coherence volume V_c which was introduced earlier in Eq. 2.13 [Len01]

$$\Delta_c = Br \frac{\lambda^3}{\pi c}. \quad (3.1)$$

Δ_c is proportional to the wavelength cubed, which means it becomes increasingly difficult to operate a highly coherent light source at short wavelengths. Furthermore, it is proportional to the brilliance (or spectral brightness) Br of a light source, which states the number of photons per unit time, per unit solid angle, per unit source area and per unit bandwidth. A high brilliance is a prerequisite for the filtering process illustrated above. The brilliance of synchrotron sources is on the order of 1×10^{19} ph/s mm² mrad² BW for a bandwidth BW of 0.1 %, which is sufficiently high to extract a significantly coherent x-ray flux [Att00]. The undulator radiation is further prepared by the beamline optics for the experiment. The optical elements such as gratings, mirrors or lenses may further affect the coherence of the light. The loss of radiation power due to the coherent filtering process can be quantified according to [Att00] in the following way:

$$P_{\text{coh},\lambda/\Delta\lambda} = \underbrace{\eta}_{\text{beamline efficiency}} \underbrace{\frac{(\lambda/2\pi)^2}{(d_x\Theta_x)(d_y\Theta_y)}}_{\text{spatial filtering}} \underbrace{N\frac{\Delta\lambda}{\lambda}}_{\text{spectral filtering}} \cdot P_{\text{cen}}. \quad (3.2)$$

$P_{\text{coh},\lambda/\Delta\lambda}$ is the reduced radiation power obtained by coherent filtering of the central radiation cone with power P_{cen} . η is the beamline efficiency considering insertion loss due to finite efficiency of the monochromator and optical elements. $d_{x,y}$ are the lateral dimension of a spatial filtering pinhole and $\Theta_{x,y}$ the corresponding beam divergences. N is the number of undulator periods [Att00].

The availability of coherent x-rays allowed for new experiments in that energy range. In x-ray photon correlation spectroscopy or speckle metrology the coherent scattering patterns of a specimen are analyzed in terms of correlation. Since each scattering pattern corresponds to a direct fingerprint of the sample state it is possible to obtain information on fluctuations in the sample [Shp07]. Especially imaging experiments may benefit from coherent x-rays. On one hand samples which are weakly absorbing can be investigated using phase contrast. On the other hand lensless, coherence-based experiments like coherent diffraction imaging [Mia99] or holography [Eis04] become possible. A short overview of this class of experiments in the x-ray regime can be found in [Len01; VP04].

3.1.2 XMCD and Resonant Magnetic Scattering from Out-of-plane Domains

Beyond the high photon flux at tunable photon energy APPLE-II undulators [Sas94] enable a sophisticated control over the polarization of the light generated. This way, resonant as well as polarization-dependent effects of the light-matter interaction (or their combination) can be observed at synchrotrons.

An example for such an effect is the x-ray magnetic circular dichroism (XMCD) first observed by Schütz et al. [Sch83; Sch87]. The group found an intensity difference in the spectra of an absorption experiment with left and right circularly polarized x-rays tuned to the iron K -edge (7112 eV) passing through magnetized iron. This dependence of the absorption coefficient on the sample magnetization and the x-ray helicity has later been

observed for different materials and at different absorption edges. Especially in the soft x-ray range at the $L_{2,3}$ absorption edges of d -metals XMCD has been found to be much stronger compared to the K -edge.

An example for XMCD at the Co- $L_{2,3}$ edges is given in Fig. 3.2. A Co layer of 40 nm thickness grown on a 50-nm-thick Si_3N_4 membrane constitutes the sample. Ta serves as buffer layer (5 nm) and as anti-oxidation cap (3 nm). The measurement signal recorded by a photodiode is the energy-dependent transmission of the x-rays through the sample. The Co-film features an in-plane anisotropy, thus the spectra are collected under an angle of 45° between the x-ray propagation direction and the sample plane. The incident synchrotron light features a circular polarization with positive helicity. A magnetic field applied along the in-plane direction of the Co-film ensures the magnetic saturation of the sample. The magnetic field can be inverted in order to change the sample saturation into the opposite direction.

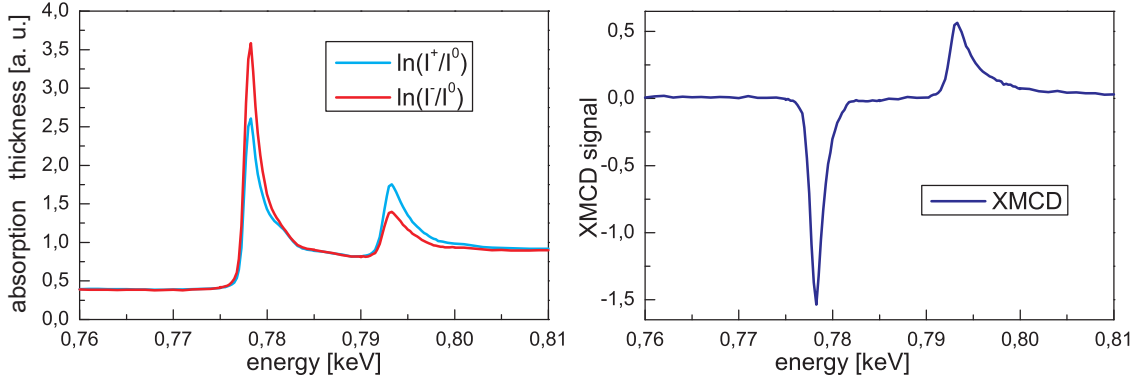


Figure 3.2: (Courtesy of Stefan Schaffert.) XMCD effect: (a) Absorption difference of circularly polarized x-rays (σ^+) at the Co- $L_{2,3}$ edges upon opposite magnetization of the sample. (b) XMCD (difference) signal.

The x-ray transmission is detected through the sample with positive (I^+) and negative (I^-) magnetic field applied as well as with the sample removed (I^0). Each of the three signals is normalized to the mirror current of the beamline to remove the influence of the decreasing beam current. In Fig. 3.2(a) the logarithm of the magnetic transmission curves normalized by I^0 is plotted. This signal is proportional to the absorption coefficients ($\mu^\pm \sim \ln(I^\pm/I^0)$). Note that μ^\pm is integrated over the sample thickness, including the contributions of the substrate, buffer and cap layers, which need to be removed for a quantitative analysis. The dependence of the absorption on the magnetization direction is already clearly visible in Fig. 3.2(a). In panel (b) the difference of the absorption coefficients μ^\pm is illustrated following the convention of a negative dichroic effect at the L_3 absorption edge [SS06]. This XMCD signal is divided by $\cos(45^\circ)$ and 0.9 to compensate for the sample tilt and the beamline polarization degree, respectively. Maximum XMCD is found at 778.3 eV and 793.3 eV for L_3 and L_2 , respectively. Since most of the synchrotron work in this thesis relies on the XMCD effect it is briefly discussed in this section.

Absorption at core-level electrons is the dominant mechanism of the light-matter interaction for soft x-rays. The cross-section for scattering is orders of magnitude lower in this energy range. Both mechanisms are closely related, a fact that manifests itself, for instance, in the Kramers-Kronig relation. This mathematical connection links the real and imaginary parts of the scattering factor $F(\mathbf{q}, E)$, which represent the refractive and absorptive contributions of the light-matter interaction near resonances (see Eq. 3.5). As a result, it is possible to derive both resonant contributions from the absorption cross-section, which is convenient from the experimentalist's point of view, although in practice this task may turn out to be difficult [SS06]. A comprehensive overview about magnetic x-ray absorption and scattering can be found in the text books by J. Stöhr & H.C. Siegmann or S.W. Lovesey [LC96; SS06]. A brief summary of the theoretical framework describing (soft) x-ray scattering as it is found in the book by J. Stöhr & H.C. Siegmann is given in appendix B. Within this framework x-ray scattering and absorption are treated uniformly in terms of the scattering length $f(\mathbf{q}, E)$ from which the differential cross-section for scattering $\frac{d\sigma}{d\Omega}$ and the cross-section for absorption σ^{abs} can be derived

$$\left(\frac{d\sigma}{d\Omega}\right)^{\text{scat}} = |f(\mathbf{q}, E)|^2 \quad \text{and} \quad \sigma^{\text{abs}} \sim \text{Im}\{f(\mathbf{q}, E)\}. \quad (3.3)$$

Absorption depends on the imaginary part of the scattering amplitude while scattering depends on the real and imaginary part. The general form of the scattering amplitude describing resonant scattering of photons at the electron system of an atom is

$$f(\mathbf{q}, E) = \underbrace{r_0 (\boldsymbol{\epsilon} \cdot \boldsymbol{\epsilon}')}_{\text{single } e^-} F(\mathbf{q}, E). \quad (3.4)$$

The first two factors, r_0 the classical electron radius and the product of the unit vectors of the incident and scattered light $\boldsymbol{\epsilon} \cdot \boldsymbol{\epsilon}'$, correspond to the scattering length from a single free electron. All additional effects originating from multielectron systems (atoms) or resonance effects at characteristic binding energies are contained in the scattering factor $F(\mathbf{q}, E)$. Within a semi-classical picture (see appendix B) describing resonant scattering as absorption and adjacent emission of a photon with the same energy the scattering factor $F(\mathbf{q}, E)$ consists of the following terms:

$$F(\mathbf{q}, E) = F^0(\mathbf{q}) + \underbrace{F'(E)}_{\text{refractive}} - i \underbrace{F''(E)}_{\text{absorptive}}. \quad (3.5)$$

$F^0(\mathbf{q})$ is the form factor describing the distribution of the scattering electrons. $F'(E)$ and $F''(E)$ are resonance factors, which consider the resonance effects if the incident light is tuned to the atom's binding energies. These functions are heavily energy-dependent and enhance the cross-sections for both absorption and scattering near the resonance. Still, for soft x-rays absorption clearly dominates the overall cross-section. The resonance factors are illustrated in the appendix in Fig. B.1.

While the scattering factor in Eq. 3.5 describes resonance effects it does not consider resonant *magnetic* scattering. The scattering factor for this process has the following form

$$F(\hbar\omega) = \frac{\hbar\omega^2\alpha_f\mathcal{R}^2}{2cr_0} \left[\underbrace{(\boldsymbol{\epsilon}'^* \cdot \boldsymbol{\epsilon}) G_0}_{\text{charge}} + \underbrace{i(\boldsymbol{\epsilon}'^* \times \boldsymbol{\epsilon}) \cdot \hat{\boldsymbol{m}} G_1}_{\text{XMCD}} + \underbrace{(\boldsymbol{\epsilon}'^* \cdot \hat{\boldsymbol{m}})(\boldsymbol{\epsilon} \cdot \hat{\boldsymbol{m}}) G_2}_{\text{XMLD}} \right] \quad (3.6)$$

with $\alpha_f = 1/137.04$ being the fine-structure constant and $\boldsymbol{\epsilon}$ and $\boldsymbol{\epsilon}'$ the polarization unit vectors of the incident and scattered radiation. $\hat{\boldsymbol{m}}$ is the unit vector along the sample magnetization direction. The derivation of the resonant magnetic scattering factor considers not only the binding energy, but introduces an initial state $|i\rangle$ and a final state $|f\rangle$, which both contain an electronic and a photon part. The transition between these states is described by the perturbation of the electromagnetic field. Consequently, the factors G_0, G_1 and G_2 contain the sums over transition probabilities between these states. Their analytical values as well as \mathcal{R}^2 are listed in the appendix. Within this model absorption is described as a first order process, the direct transition from $|i\rangle$ to an excited state $|f\rangle$. In contrast, (elastic) scattering is a second order process in which the evolution to the final state takes place via an excited intermediate state $|n\rangle$ from which the scattered photon is emitted. Hereby the intermediate state does not need to fulfill energy conservation laws until $|f\rangle$ is reached¹. The corresponding mathematical equations describing the first and second order processes go by the names of ‘‘Golden Rule No. 2 and No. 1’’ [SS06]. The latter, describing scattering, is better known as Kramers-Heisenberg relation [LC96]. The exact derivation of Eq. 3.6 is a longer one and the interested reader is referred to the books by Stöhr & Siegmann or Lovesey [LC96; SS06] again.

As already indicated in Eq. 3.6 the three terms containing G_0, G_1 and G_2 exhibit a different dependency on the unit polarization vectors of the x-rays and the sample magnetization direction. The first term is independent of the magnetization. G_0 describes the resonant scattering from a spherical charge distribution and the polarization dependence is the same as for Thomson scattering. The second term corresponds to XMCD and is linear in $\hat{\boldsymbol{m}}$. The third term is quadratic in $\hat{\boldsymbol{m}}$ and describes x-ray magnetic linear dichroism (XMLD). Thus, the interaction of x-rays with a magnetized sample depends on the sample orientation, the x-ray polarization and an external magnetic field, which acts on the sample magnetization.

All magnetic imaging experiments in this thesis are performed in transmission geometry with the sample plane being perpendicular to the light propagation direction (see Fig. 2.2). At the same time, the samples under investigation feature out-of-plane domains pointing normal to the sample plane. Thus, the magnetization is oriented collinear to the propagation direction of the light and perpendicular to the polarization vectors. According to the

¹ Within the bounds given by the energy-time uncertainty relation.

magnetic resonant scattering factor in Eq. 3.6 that means that the XMLD contribution equals zero while XMCD is maximized. Consequently, the magnetic contrast observed in the Fourier transform holograms and their reconstructions is caused by magnetic moments oriented perpendicular to the sample plane.

The origin of XMCD contrast can be explained in an intuitive two-step model, which is here illustrated for a d -metal as used in the experiments. First, an initially unpolarized electron from a spin-orbit split level, for instance $2p_{3/2}$ (L_3) absorbs a circularly polarized photon. In this process the angular momentum of the photon needs to be conserved and may be transferred to the spin due to spin-orbit coupling. As a result, the excited electrons are spin-polarized, that means photons with positive (negative) helicity have a higher probability to excite a spin-up (spin-down) photoelectron at the L_3 edge. At the L_2 edge the situation is vice versa.

In the second step the photoelectrons with opposite spin have different transition probabilities into the magnetically split $3d$ valence shell, i.e. the different densities of unoccupied states for different spin orientations serve as detectors for the spin-polarized photoelectrons. Since for d -metals the magnetization is mainly carried by the spins in the d -band, the circularly polarized light thus directly probes the sample magnetization [Sch87].

X-ray scattering experiments provide information on a certain length scale which is determined by the energy of the incident light. For example, scattering experiments in conjunction with hard x-rays can provide information on the distances between atoms in matter. The wavelength in the soft x-ray regime is typically larger than 1 nm which is not sufficient to resolve these distances. Instead, soft x-ray scattering tuned to the L -edges of d -metals gains sensitivity to the sample magnetization. Under these circumstances the scattering contains a significant part which originates from the periodicity of the comparably large domains, here with a domain width on the order of 100 nm. The derivations for general x-ray scattering remain valid for such a scenario.

In Fig. 3.3 an example for magnetic scattering is given. Panel (a) illustrates the magnetic scattering pattern generated by positive helicity x-rays at the Co- and Ni- L_3 absorption edges. The magnetic sample is described in detail in Sec. 3.3.2, its structure can be found in Fig. 3.21 and the holograms correspond to the reconstructions shown in Fig. 3.22. The sample consists of a Co/Pt multilayer containing an integrated amount of Co of 20 nm thickness and featuring a perpendicular anisotropy. In addition, a CoNi/Pd interlayer is integrated, which adds a small amount of 2 nm Ni. In Fig. 3.3 the image halves recorded at 778 eV correspond to the magnetization of the Co while the part recorded at 854 eV corresponds to the Ni magnetization. The magnetic signal recorded is directly proportional to the magnetization and thus weak for the small Ni-interlayer. The main contribution in the right half of Fig. 3.3(a) is the Airy pattern caused by a circular pinhole aperture. In addition, interference fringes are visible originating from the reference aperture. Both contributions can be attributed to the charge term (G_0) in the magnetic resonant scattering factor in Eq. 3.6. The magnetic scattering is almost not observable here. In contrast, the left half presents a hologram of the same magnetic state but with the photon energy tuned

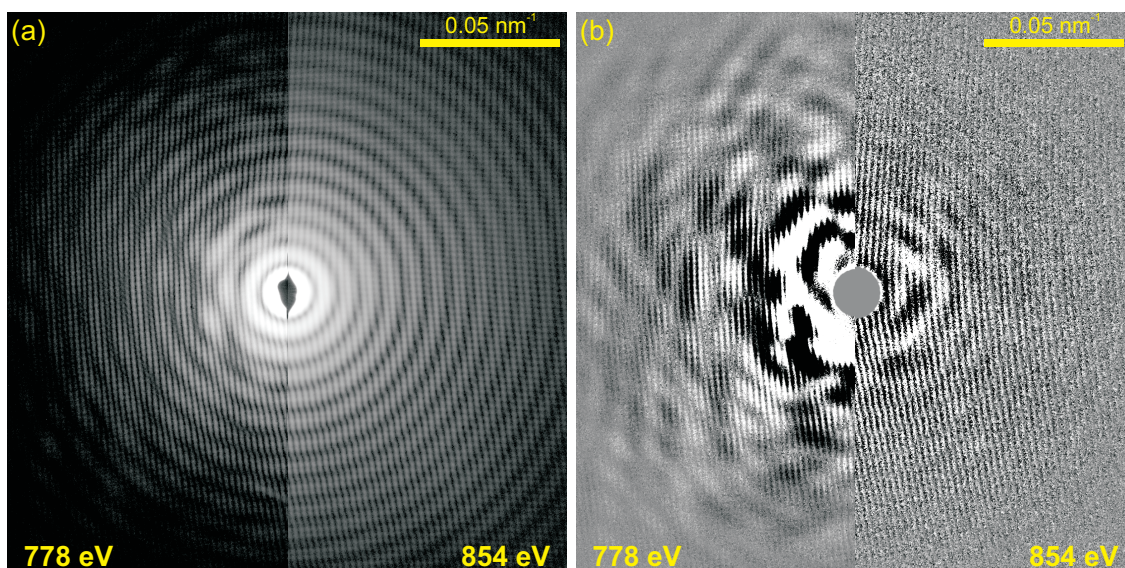


Figure 3.3: Magnetic scattering: all scattering patterns are shown up to a momentum transfer of 0.1 nm^{-1} . (a) Fourier transform holograms recorded with positive helicity on a \log_{10} -intensity scale ranging from 0 to 2.5 for 778 eV and 3.5 for 854 eV. (b) Difference holograms on linear grayscale. Black and white represent the z-scaling from -5 to 5 photons for both photon energies.

to the Co edge. The fringes of the Airy pattern exhibit a strong modulation, which is caused by the scattering from the out-of-plane domain pattern of the sample and thus corresponds to the second term in Eq. 3.6 (G_1). The contrast in the XMCD spectrum showed in Fig. 3.2(b) at the beginning of this section is generated by taking the difference of two spectra recorded for an oppositely saturated sample. For magnetic scattering from domains this procedure does not work as a magnetization inversion would hardly reproduce an identical domain pattern. The dichroic effect depends on the relative orientation of sample magnetization and the polarization state of the incident photons. That means the same contrast inversion can be achieved by changing the helicity of the incident light leaving the domain state unchanged.

Fig. 3.3(b) shows the difference of the holograms recorded with opposite helicity at the two absorption edges. Similar to the absorption spectra only the magnetic contribution changes sign upon helicity (or magnetization) inversion. That means all charge contribution cancels out in the hologram difference and the magnetic signal is strongly emphasized. Note that the holograms in panel (a) are plotted on a logarithmic intensity scale while for panel (b) a linear intensity scale is sufficient to reveal the magnetic scattering even for the small amount of scattering Ni. A more detailed discussion on magnetic scattering with circular and linear light can be found in [Eis03; Lö04].

3.1.3 Instrumentation for Synchrotron FTH

Fourier transform holography is a coherent imaging technique, which is able to deliver images from a recorded intensity pattern due to the conservation of the relative phase information through interference. In Fourier transform holography a point source within the object plane acts as a spherical reference. Although this point source may be realized by the focus of a zone plate [McN92], the integrated mask-sample design of lensless FTH is favorable in terms of stability. Here, a small aperture delivers the spherical reference wave.

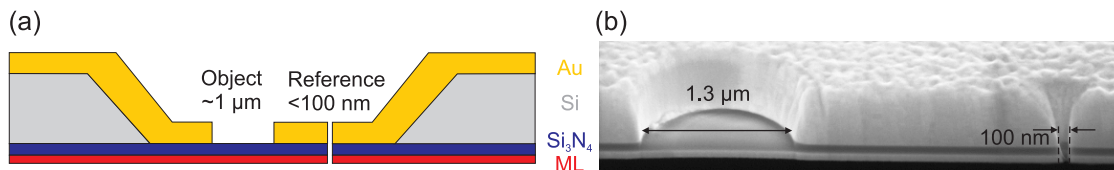


Figure 3.4: (SEM image reproduced from Ref. [Sch07b].) (a) The schematic illustrates the integrated mask-sample design of the FTH-mask. (b) Cross-section of an FTH-mask produced by focused ion beam (FIB) with a sputter-deposited magnetic thin film as sample.

For resolution in the sub-micrometer regime the optical aperture arrangement is realized via an integrated mask-sample design manufactured by nanostructuring processes. Si_3N_4 membranes are commercially available with a broad range of parameters regarding the thickness or the open area. A membrane of 100 nm thickness offers an x-ray transmission around 80% at the Co-L_3 edge and serves here as the basic substrate for FTH-mask manufacturing. On one side of this membrane the sample is deposited. For the present chapter these are magnetic multilayers with perpendicular anisotropy which are sputter-deposited over the complete membrane area. One exception is made in Sec. 3.4 where a reference sample based on absorption contrast is used. The second side of the membrane serves for the preparation of the apertures that define the FTH geometry. For that purpose this membrane surface is covered with a gold layer of about 1 μm thickness, which makes the structure opaque to soft x-rays. The circular apertures are defined by focused ion beam (FIB) milling. For the object hole the gold is removed within a radius of typically 500 nm down to the silicon nitride, but leaving the membrane and the sample on the opposite side intact. This aperture defines the field of view on the specimen. Reference apertures need to be made as small as possible to provide high resolution. For the given aspect ratio high-quality references have a diameter of less than 50 nm. Fig. 3.4 illustrates the schematic layout as well as a FIB cross-section through an FTH-mask.

This mask-sample structure is illuminated with coherent x-rays provided by undulator beamlines of the BESSY-II synchrotron in Berlin, Germany. Except for the in-focus hysteresis measurements shown in Figs. 3.17, 3.22 and 3.23, which have been recorded at UE56-1-SGM, all measurements involving synchrotron radiation were conducted at the UE52-SGM beamline [Sen01]. As the name suggests the beamline features an APPLE-II undulator [Sas94] with a magnetic period of 52 mm capable of delivering light with linear

as well as circular polarization. For all measurements the third undulator harmonic is monochromatized by a spherical grating with 1200 lines per millimeter providing a photon flux on the order of 1×10^{11} ph/s. At these settings the degree for circular polarization is 90%. The focus of the beamline is $17.4 \mu\text{m}$ times the size of the exit slit which can be adjusted in the range from $20 \mu\text{m}$ to $120 \mu\text{m}$. The beam divergence is 1 mrad in the vertical direction times 6 mrad in the horizontal direction. Additional information on the beamlines such as their layout can be downloaded from [HZBa].

FTH requires a micro- and nanostructuring effort for the sample preparation. As a result, the requirements on the imaging setup are comparably little demanding (except for a scientific-grade CCD) and do not necessarily ask for a dedicated apparatus. All synchrotron experiments reported here are performed with the ALICE diffractometer operated by the university of Bochum [GNZ03; Gra05]. The main purpose of this chamber is to perform soft x-ray scattering and diffraction experiments in reflection as well as in transmission. Therefore, it is easily adapted for Fourier transform holography.

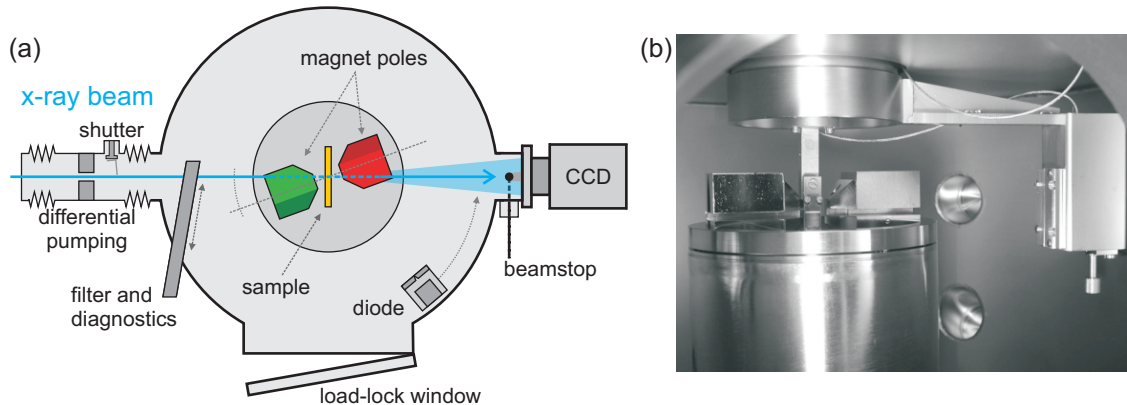


Figure 3.5: (Photograph from Ref. [Gra05].) (a) Schematic top view and (b) inside photograph of the ALICE diffractometer (side view).

Fig. 3.5 shows a schematic layout from the top as well as a photograph of the inside of the ALICE diffractometer. Soft x-ray experiments must be performed under vacuum to avoid the strong absorption by air at this wavelength. FTH experiments are typically performed at a pressure lower than 3×10^{-7} mbar. This pressure is sufficient for soft x-ray measurements as well as for the operation of the cooled charge-coupled device (CCD) camera. To meet the ultra-high vacuum (UHV) requirements of the beamline, a differential pumping stage consisting of an 1.5-mm-diameter pinhole and an additional turbo-molecular pump is installed upstream.

The (x, y, z, θ) -sample manipulator comes in from the top of the vacuum chamber. A GaAs photodiode on a 2θ rotation axis may be inserted on the beam axis behind the sample for fast, integrating intensity measurements. This detector scans the angle in the scattering plane. Filters and beam diagnostics are provided through linear feedthroughs

at the beam entrance into the main chamber. Magnetic poles are located in the direct vicinity of the sample and are capable to apply a continuously variable magnetic field of up to 7kOe provided by an ex-vacuum electromagnet. The magnet is rotatable in the scattering plane around the same angle as the sample manipulator (θ). The sample holder is connected to a He-cryostat for temperature-dependent measurements in the range from 4.2K to about 380 K.

For the spatially resolved recording of scattering patterns as required for FTH a charge-coupled device (CCD) camera is connected to the downstream port of the chamber. For the experiments either a PI-SX or a PI-MTE CCD camera from Princeton instruments is used. Both are based on the same silicon chip featuring 2048×2048 square pixels of $13.5 \mu\text{m}$ edge length. Via thermoelectrical cooling the PI-SX is operated at -75°C and the PI-MTE at -50°C . A shutter controlled by the CCD is installed directly downstream of the differential pumping pinhole to block the light during camera readout. Directly in front of the camera a beamstop blocks the forward scattering and residual x-rays directly transmitted through the sample. It consists of a spherical drop of epoxy adhesive on a $10\text{-}\mu\text{m}$ -thick, gold-coated tungsten wire that is mounted on a frame movable in the CCD-chip plane.

3.2 Domain Replication

The magnetic properties of multilayered magnetic thin films strongly depend on the layer parameters such as the layer thickness, the number of repeats or the material composition. Today, multilayers with an out-of-plane anisotropy play an important role as they are model systems for magnetic storage media. More complex systems like e.g. bilayers consisting of a magnetically hard and soft ML stack separated by a non-magnetic spacer allow to tune the magnetic coupling effects depending on the system parameters. Such coupled ML systems are of interest for the research in magnetic data storage [HTT09; HTT11] as well as in fundamental nanomagnetism [Fer08; Gru08; ZFDS04]. For a thorough understanding of the magnetic properties of such complex magnetic systems it is advantageous to be able to obtain information on the separate ML stacks. The present and the subsequent sections illustrate the application of x-ray Fourier transform holography in this context.

3.2.1 Dipolar-coupled Multilayers

In Fig. 3.6 an exemplary bilayer system consisting of two magnetic multilayers with perpendicular anisotropy separated by a non-magnetic spacer is illustrated. Thick spacers can prevent magnetic interlayer exchange-coupling between the two stacks¹. Such magnetic

¹ Direct exchange coupling is dominant only on the order of atomic distances. Oscillating interlayer exchange coupling with nonmagnetic spacers is typically observed for spacer thicknesses on the order of 10 \AA [Par91].

systems in conjunction with pre-patterned media have been suggested for multilevel recording to increase the information density in magnetic data storage [Alb05]. Two prerequisites need to be fulfilled. First, some kind of patterning is required with structure sizes below the typical domain width of the magnetic multilayers such that single-domain islands are realized, which represent the bits. Second, the coercivities of the two stacks have to be sufficiently different in order to selectively reverse only the magnetically weak or both multilayer stacks depending on the strength of an externally applied magnetic field. Given that these conditions are met each patterned bit exhibits four remanent magnetic states (up-up, up-down, down-up and down-down) for data storage instead of two. In reference [Alb05] multilevel recording is demonstrated with a pattern of 150 nm islands on 300 nm periodicity. The Co/Pt multilayer stacks featuring perpendicular anisotropy are separated by a spacer of 5 nm Pd. For this system the four remanent magnetic states could be prepared, but the interlayer magnetostatic interaction favors a parallel alignment of the two ML stacks in each bit.

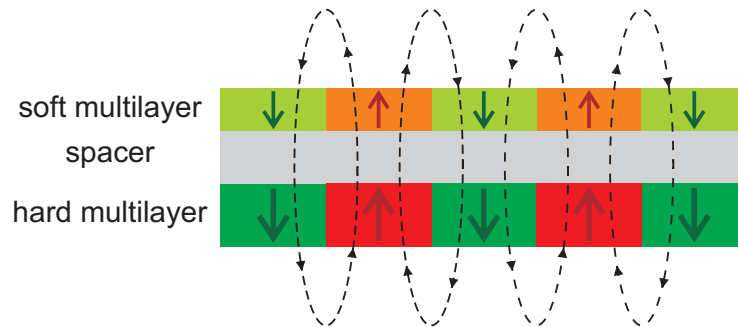


Figure 3.6: The interlayer magnetostatic interaction between two otherwise decoupled multilayer stacks favors a parallel alignment and may thus replicate domain patterns from one stack into the other.

In general, the influence of interlayer dipolar stray fields in perpendicular Co/Pt systems is observed for spacer thicknesses up to the order of 100 nm [Bal07]. This behavior is schematically illustrated in Fig. 3.6. For such a configuration the magnetization reversal of the soft stack strongly depends on the magnetic configuration in the hard stack. A domain state trapped in the hard stack generates strong local stray fields that favor a parallel orientation of the magnetic moments at a certain location in both stacks. That means the stray fields contribute to the energy required to overcome the barrier E_B for domain nucleation in the soft stack or to propagate existing domain walls. As a result, the specific state of the hard stack tends to get replicated to the soft one. In contrast, for a uniform magnetization of the hard stack almost no stray fields are sensed by the soft stack [RBD06]. Thus, the reversal of the soft stack in minor hysteresis loops may significantly change for different magnetic configurations of the hard stack. This behavior can be exploited by investigating the hard stack's configuration via minor loops of the soft stack [RBD06; Zha10]. In in-plane systems it was observed that the repeated reversal of

the soft stack can change the magnetic configuration of the hard stack even if the applied magnetic fields are below its coercivity [Gid98].

Magnetostatic interactions in multilayer systems are often investigated by established sample averaging methods like magnetic force and Kerr microscopy as well as by extraordinary Hall effect at room temperature [RBD06; Wie05; Zha10]. X-ray FTH is capable to image the domain replication in a dipolar-coupled multilayer system triggered by an external magnetic field as well as by temperature changes. The latter possibility might provide useful information in the context of thermal assisted recording [Mos02; HMW04; TMF03].

In order to investigate the dipolar coupling a hard/Pd/soft multilayer system, namely the layer sequence Pd(30) / [Co₃₀Ni₇₀(2)/Pd(15)]₃₀ / Pd(100) / [Co(3)/Pd(8)]₂₀ / Pd(12), is prepared by dc magnetron sputter deposition on Si wafers and Si₃N₄ membranes. All numbers correspond to the layer thickness perpendicular to the substrate plane in angstrom. The sample structure is visualized in Fig. 3.7(a). Two magnetic multilayer stacks are separated by 100 Å of Pd. 30 Å of Pd serve as seed layer while 12 Å of Pd prevent oxidation of the sample. The layer sequence of the magnetically hard stack is [Co(3)/Pd(8)]₂₀ deposited at 7 mTorr Ar pressure. For the magnetically soft stack the pure Co is replaced by an alloy with a composition of 30% Co and 70% Ni grown at a sputter deposition pressure of 3 mTorr, namely [Co₃₀Ni₇₀(2)/Pd(15)]₃₀. Because of the added amount of Ni in the soft stack it becomes possible to exclusively follow its reversal via soft x-ray element contrast.

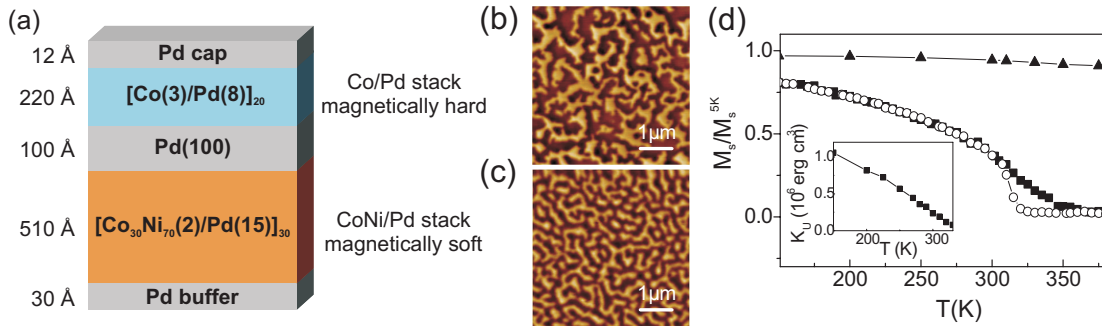


Figure 3.7: (a) Multilayer sequence for the domain replication experiment. (b,c) MFM images corresponding to a $(5 \mu\text{m})^2$ region of the demagnetized magnetic state of the (b) hard and (c) soft multilayer. (d) Temperature dependence of the normalized magnetization of the hard (triangles) and soft multilayer stacks. The soft stack was measured in remanence (open circles) and in an magnetic field of 1 kOe applied perpendicular to the sample plane (solid squares). The inset shows the temperature dependence of the soft stack's anisotropy.

In addition to the complete sample system, each ML stack is prepared separately on individual substrates for comparison. Both stacks exhibit a perpendicular anisotropy and show the formation of labyrinth domains in remanence as illustrated by MFM in Fig. 3.7(b,c). Fourier transformations of MFM images featuring a FOV of $(5 \times 5) \mu\text{m}^2$ reveal

that the majority of the domains exhibit a width from 190 nm to 360 nm for the hard Co/Pd stack while the majority of the domains in the soft CoNi/Pd stack lies in the range from 140 nm to 280 nm. Panel (d) compares the temperature dependence of the magnetization for both MLs as obtained by vibrating sample magnetometry (VSM) measurements. The magnetic field was applied normal to the sample plane. The hard Co/Pd stack exhibits an almost constant magnetization in the range between 150 K and 360 K. In contrast, the Curie temperature T_c of the CoNi/Pd system is tuned to a value close to 350 K. That means its magnetization as well as its anisotropy decrease continuously within this temperature region. Thus, it is possible to investigate the temperature dependence of the soft stack without influencing the hard stack. At 350 K the CoNi/Pd ML turns paramagnetic [Men96]. For the soft system the magnetization measurement is repeated in an external magnetic field of 1 kOe applied perpendicular to the sample plane. In the range from 310 K to 350 K this measurement differs from the one performed in remanence. This fact indicates that the out-of-plane anisotropy competes with an in-plane anisotropy closely below T_c .

A normalized macroscopic hysteresis loop of the combined [CoNi/Pd]/Pd/[Co/Pd] sample measured by VSM at 300 K with perpendicularly applied external field is presented in Fig. 3.8(a). The major loop reveals two distinct steps. These correspond to the reversal of the soft and the hard ML stack at ± 350 Oe and ± 4 kOe, respectively. That means the magnetic configuration of the hard multilayer system is only affected by external magnetic fields larger than 4 kOe. Consequently, minor hysteresis loops below that value correspond completely to the magnetization reversal within the soft ML.

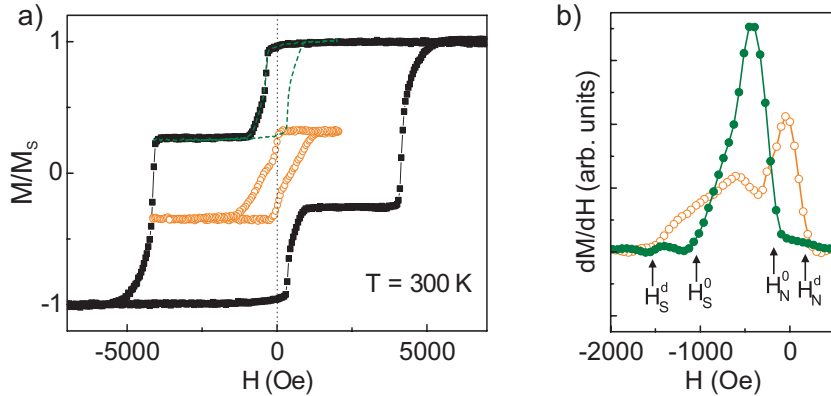


Figure 3.8: (a) Major loop (black solid symbols) of the magnetically hard/Pd/soft multilayer sample. The two minor loops correspond to the soft ML system with the hard layer in saturation (green dashed line) and with a 50%/50% up/down domain state (orange open symbols). (b) Derivatives of the descending branch of the minor loops without (green solid symbols) and with (orange open symbols) domains trapped in the hard ML stack [Hau08].

To reveal the presence of interlayer magnetostatic interactions two minor hysteresis loops between ± 2 kOe but with different initializing field sweeps are compared in Fig. 3.8(a).

For the first minor loop (green dashed line) the sample is brought to positive saturation in advance. The minor loop does not exhibit a residual bias field, which indicates the lack of direct exchange coupling between the hard and soft multilayer due to the Pd(100 Å) intermediate layer. A second minor loop (orange open symbols) is started after a field sweep from 8 kOe to -4.2 kOe which prepares a domain state with about 50% of the domains magnetized up and 50% magnetized down in the hard multilayer stack. Both minor loops of the soft layer differ significantly in terms of the nucleation field (H_N) and saturation field (H_S). This behavior is visualized by the derivatives of the descending branches in Fig. 3.8(b). The nucleation of domains in the soft layer starts at a lower nucleation field value H_N^d of 130 Oe compared to $H_N^0 = -250$ Oe for the saturated hard stack. At the same time the saturation field increases from $H_S^0 = -1.1$ kOe to $H_S^d = -1.55$ kOe. Thus, a broadening of the switching behavior for the soft stack is observed if domains are present in the hard stack. Such changes of the soft hysteresis loop were observed on similar systems and attributed to the dipolar fields of the hard multilayer influencing the soft system [RBD06]. The derivative of the minor loop under influence of dipolar fields (orange symbols) exhibits a dip at -300 Oe. At this point the complete domain state of the hard ML has been replicated into the soft ML. This was confirmed by element-specific imaging via x-ray transmission microscopy (XTM) at room temperature (see [Hau08]).

3.2.2 Field-induced Replication at Low Temperature

In a next step the evolving domain pattern in the soft stack is monitored during a minor hysteresis loop. The experiment is conducted at an arbitrary temperature of 150 K. Compared to room temperature, at 150 K the saturation magnetization and the anisotropy constant of the soft stack are larger by factors of two and four, respectively (see Fig. 3.7(d)).

Regarding temperature-dependent measurements the integrated mask-sample design of FTH rigidly couples the reference apertures to the field of view defined by the object aperture. Thus, relative drift between these optical elements is ruled out. Only movement of the complete sample within the x-ray beam may occur, which causes a corresponding lateral displacement of the detected hologram. For FTH a noticeable lateral displacement corresponds to a shift on the order of half a pixel, e.g. $0.5 \times 13.5 \mu\text{m}$ for the Princeton Instruments CCD camera used in the experiments. This stability needs to be maintained for at least one readout cycle of the CCD camera (typically on the order of 10 s) to prevent a smearing of the recorded diffraction pattern. Drift of more than half a pixel over *several* exposures can be compensated by later realignment of the individual holograms upon summation. While this stability criterion does not seem too demanding it turned out that sample drift could be observed, especially after temperature changes. A short note on this behavior is given at the end of this section.

To illustrate the domain replication from the hard into the soft stack element-specific FTH imaging is performed during the magnetic reversal in the soft stack. In Fig. 3.9 the corresponding macroscopic major and minor hysteresis loops measured by VSM at 150 K are presented. Note that a domain state with about half the domains pointing up

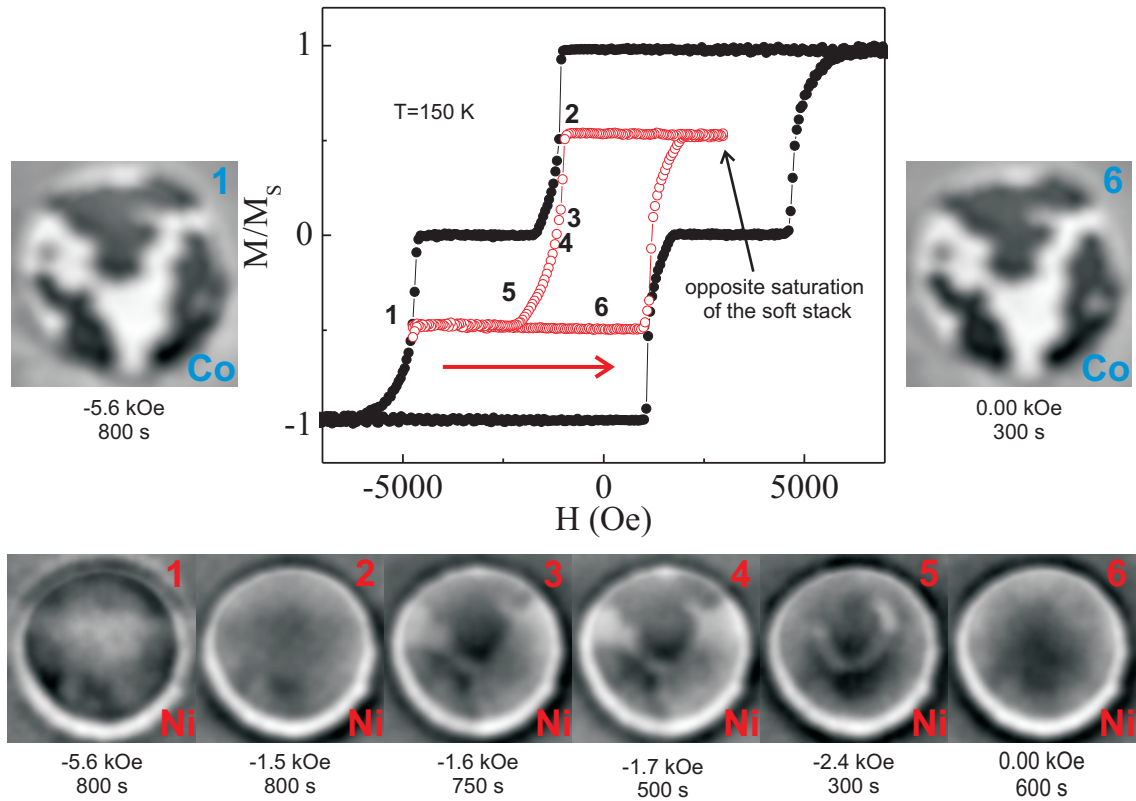


Figure 3.9: (Hysteresis loops by courtesy of Thomas Hauet.) Domain replication with magnetic field at 150 K. The red curve visualizes a minor hysteresis indicating the field points for FTH imaging. For each image the corresponding absorption edge, the applied magnetic field and the hologram exposure time is given.

and half pointing down in the hard stack was prepared before starting the minor loop on the soft stack. The comparison with the loops in Fig. 3.8(a) directly reveals the higher coercivity of the soft stack at 150 K. At this temperature the reversal of the soft stack takes place in the intervals between ± 1 kOe and ± 2 kOe. In addition, x-ray FTH images along an analogue minor hysteresis performed at the same temperature are shown. The FOV of the magnetic images features a diameter of $1.4 \mu\text{m}$. The bright and dark areas within these images correspond to an (anti-)parallel orientation of magnetic moments along the propagation direction of the x-ray beam. The images were recorded at the maximum absorption at the Co- L_3 (779 eV) and Ni- L_3 (852.75 eV) edges, which allows to monitor the magnetization within each stack separately. Images recorded at the Ni- L_3 edge correspond exclusively to the magnetization of the soft CoNi/Pd system as no Ni

is contained in the hard ML stack. Images recorded at the Co- L_3 edge in principle do correspond to the contribution of both ML systems. The different coercivity of both stacks allows to saturate the soft multilayer without changing the domain state of the hard one, e.g. by applying external magnetic fields with a magnitude in the interval of ± 2.5 kOe and ± 4 kOe at 150 K. Within these intervals the soft stack contributes only a uniform contrast due to its uniform magnetization and consequently any domain pattern observed corresponds to the magnetization of the hard Co/Pd system. In other words, for magnetic fields higher than H_s of the CoNi/Pd system FTH images recorded at the Co edge reveal the magnetic state of the hard stack only.

As before for the macroscopic measurement at room temperature a domain configuration is prepared in the hard stack. At 150 K a magnetic-field value of -5.6 kOe is chosen for this purpose. The resulting magnetic state is visualized by the FTH image number 1 at the Co- L_3 edge. At this field value the soft stack is saturated as the corresponding Ni-image number 1 reveals. From this starting point on the magnetic field is swept to 3.4 kOe saturating the soft stack in the opposite direction without changing the hard stack. Afterwards the magnetic field values -1.5 kOe, -1.6 kOe, -1.70 kOe, and -2.4 kOe are approached. For each of these field values FTH images are recorded at the Ni edge, revealing the magnetic domain state of the soft CoNi/Pd system. The hologram exposure time for each image is given in Fig. 3.9 below the value of the external magnetic field.

The formation of domains can first be observed in the Ni-image recorded at -1.6 kOe. Two domains form at positions and with shapes that are correlated, but not identical to the magnetic state of the hard stack in Co-image number 1. At -2.4 kOe most of the magnetic material within the FOV is reversed leaving only a small bow-like domain. Again this remaining domain is located at a position with the same magnetization orientation in the hard layer. Judging from the available FOV, the magnetic field necessary to replicate the domain pattern template of the hard stack lies between image number 4 and 5, thus between -1.7 kOe and -2.4 kOe. This value is significantly higher than for the case of 300 K (see Fig. 3.8(b)). At the end of the experiment the soft layer is brought to saturation again with a magnetic field of -4.5 kOe, afterwards the sample is put in remanence. The Ni-image number 6 supports the fact that the soft CoNi/Pd layer is saturated while the corresponding Co-image reveals the identical domain state as in number 1. The similarity of the two Co-images proves that no disturbance of the hard system has taken place during the minor hysteresis loop.

3.2.3 Temperature-induced Domain Replication

After imaging domain replication triggered by an external magnetic field it is possible to perform the replication via temperature changes. Macroscopic VSM measurements deliver the first indications of an irreversible change of the systems magnetization upon heating.

The experiment is started at a temperature of 150 K (see Fig. 3.10). As for the field-induced replication a magnetic field prepares a domain state with half of the hard stacks magnetization reversed while the soft stack is completely saturated. Afterwards, the

sample is put into remanence, which preserves the prepared magnetic state. From this starting configuration the sample is heated to different temperatures T_{\max} . No external magnetic field is applied during the heating and cooling cycle. The goal for this experiment is to observe that with rising temperature the energy barrier for magnetization reversal can be overcome and domain nucleation starts in the soft ML stack. The plot in Fig. 3.10 corresponds to a heating of the sample from $T = 150$ K to a certain T_{\max} with a subsequent cooling down back to the initial 150 K. During the temperature changes the magnetization of the complete sample is measured and plotted normalized to the magnetization of the start configuration at 150 K. After each cooling down the magnetic start configuration is restored by saturation of the soft stack.

For the first cycle the sample is heated to a T_{\max} of 250 K marked in the plot by the white triangle pointing down. The magnetization curve for heating and the subsequent cooling do coincide. That means the sample returns into its initial magnetic state without any changes. For the second cycle the sample is heated to a $T_{\max} = 300$ K. This value is

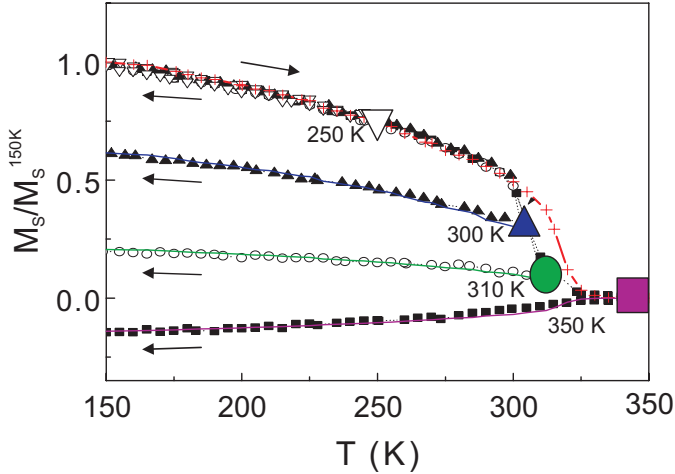


Figure 3.10: Magnetization vs temperature curves measured in remanence: Heating the sample above a certain T_{\max} changes the magnetization of the complete sample due to domain nucleation in the initially saturated soft ML stack. As a result, the sample's magnetization drops below its starting value.

indicated by the blue triangle pointing up. In this case the magnetization curve measured for the cooling branch does not follow the heating branch but stays below it. The sample only reaches about 60 % of its initial magnetization. From this fact it can be derived that part of the sample did reverse its magnetization direction. It is reasonable to assume that the magnetization change originates from the soft CoNi/Pd system, since its T_c lies closely above the approached temperature values, whereas the T_c of the hard Co/Pd system is much higher (see Fig. 3.7(d)). For two other heating cycles up to 310 K and 350 K, marked by the green circle and the purple square, the sample returns to magnetic states with a further reduced magnetization. For the latter the overall magnetization changes its sign upon cooling back to 150 K. As comparison the curve consisting of red crosses corresponds to a heating up to 350 K, but without any domains present in the hard stack.

To support the thesis that the magnetization reversals takes place in the soft ML stack only FTH imaging is performed during a heating cycle of the sample. The sample is

cooled down to 153 K and a similar start configuration as for the macroscopic measurement is generated with the help of an external magnetic field. The soft CoNi/Pd stack is saturated while a domain state with about half of the domains reversed is prepared in the hard stack. Again the sample is put to remanence afterwards and the external magnetic field is left switched off during the heating & cooling cycle. That means that similar to the macroscopic VSM measurement shown in Fig. 3.10 any change of the sample's domain configuration is caused by the temperature change. In contrast to the macroscopic measurement, the element-specific imaging of the two separate stacks allows to confirm that (i) the magnetic reversal takes places in the soft stack only and (ii) the dipolar stray fields originating from the domain pattern in the hard stack influence the domain formation in the soft stack.

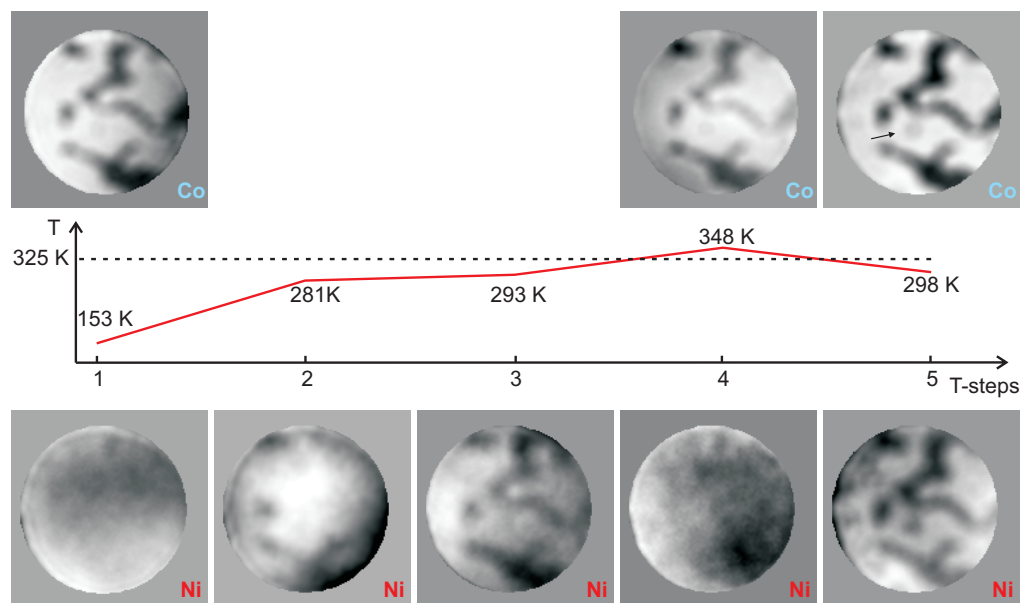


Figure 3.11: Magnetic FTH images recorded at the Co edge (upper row) and Ni edge (lower row) along a heating cycle. The corresponding temperature values are given in the central diagram.

In Fig. 3.11 images recorded at the Co and Ni edges are shown in the upper and lower row, respectively. Each column corresponds to a specific temperature setpoint whose value is given in the central diagram. There, the dotted line marks a temperature of 325 K where the soft stack does not exhibit any out-of-plane magnetization in remanence anymore according to Fig. 3.7(d). The overall exposure times for the FTH images are 1200 s, except for the Ni-image at 281 K, which was recorded during 2000 s and the Co-images at 153 K and 298 K, which each feature an exposure time of 600 s. The maximum XMCD contrast was found at 779.75 eV for the Co- L_3 resonance and at 853.6 eV for the Ni- L_3 resonance.

The first column illustrates the start configuration. The Ni-image exhibits no contrast

due to saturation, which means the domain pattern observed at the Co edge corresponds to the hard stack only. After the characterization of the initial magnetic state the temperature is raised. No domain nucleation in the soft stack is observed up to a temperature of 270 K (not shown). At the next temperature setpoint of 281 K the first domains become visible in the CoNi/Pd system. Comparing the generated individual soft-stack domains to the ones in the hard ML stack one finds that their shape is reproduced. It appears that without the influence of an additional external magnetic field a domain nucleated in the soft stack directly expands to the boundaries set by the corresponding domain in the hard stack, but not significantly beyond. Consequently, each individual domain is replicated as a whole. This observation is corroborated during further heating to $T = 293$ K where the complete domain pattern of hard ML stack is replicated to the soft one.

In a next step the temperature is raised above the T_c of the soft ML stack to a temperature of $T = 348$ K. Here, no clear contrast is observed in the FTH reconstruction in resonance with the Ni edge. That means the heating above T_c successfully puts the soft ML stack in a paramagnetic state without domain formation. At the same time a FTH image at the Co edge reveals the stable initial magnetic state within the hard-layer system. Finally, the temperature is set to 298 K (room temperature) where the soft ML system becomes ferromagnetic again. The corresponding FTH images reveal a matching of the domain states in both layers, thus the domains are completely replicated into the soft ML stack. In this configuration, with domains in both stacks, the Co-edge image contains information on both ML stacks simultaneously. For such a case it would be possible to observe areas with gray contrast, corresponding to an anti-parallel alignment of both stacks. In fact this seems to be true for the small, faintly visible domain marked by the arrow in the Co-image for the final 298 K. The corresponding Ni-image reveals a fully developed domain at the same location. In this case the contrast is ambiguous. The two Co-images recorded at 153 K and 348 K reveal a similar, but even fainter, contrast at the specific location whereas no contrast is observed in the corresponding Ni-images. Therefore, the contrast is attributed to the hard ML stack. It might be a local defect with an irregular magnetization orientation away from the perpendicular anisotropy. Nevertheless, this location is sufficient to trigger a domain nucleation in the soft stack after exceeding T_c .

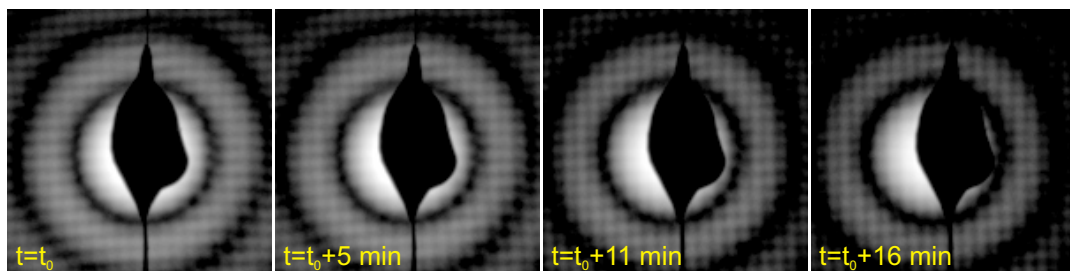


Figure 3.12: Four Fourier transform holograms recorded 45 min after a temperature raise of 50 °C over a time span of 16 min illustrate the resulting sample drift.

During the measurements of heating cycles the thermal drift of the experimental setup turned out to be a problem. The ALICE chamber features a long (~ 1 m) sample holder, which contracts and expands significantly upon temperature changes. For example after the initial cooling from room temperature to 153 K a drift of the hologram caused by thermal stabilization of the sample holder could be observed for several hours. To get an idea about the magnitude of this drift, the central part of a series of four holograms recorded with an intermediate time delay of ~ 5 min each is presented in Fig. 3.12. Here, the first hologram is recorded 45 min after raising the sample temperature from 310 K to 360 K. The exposure time of each hologram is $10 \text{ frames} \times 1.5 \text{ s}$ which corresponds roughly to a total recording time of 1 minute considering the detector readout time of 4.2 s. All images magnify the identical part of the detector illustrated by the fixed beamstop position. The drift of the sample holder causes a movement of the scattering pattern across the detector. In the fourth image recorded 16 min after the first one the center of the hologram has moved by 7 pixels in the horizontal and 1 pixel in the vertical direction¹. That means during the recording of one hologram within the 1 min recording time the diffraction pattern moves less than half a pixel on the detector. Thus, hologram recording with these parameters is possible 45 min after a temperature raise 50°C above room temperature. Afterwards the drift of the holograms can be compensated during the reconstruction process by shifting the image matrices upon summation with the corresponding offset in the horizontal and vertical direction. Alternatively, since only relative sample distances matter in the hologram reconstruction, it might be easier to separately reconstruct each hologram and perform the summation in real space.

In practice it was more convenient to avoid the sample drift by allowing for a sufficient temperature stabilization time. For the image series in Fig. 3.11 the experiment was paused for at least 1.5 hours after each temperature change. With this stabilization time it was possible to add the holograms for one temperature measurement without further consideration of the drift. Although this procedure worked, it is necessary to note that for temperature-dependent measurements, FTH would benefit from a dedicated and more adapted cryostage.

3.2.4 Comparison of Field- and Temperature-induced Domain Replication

The investigated sample features a perpendicular magnetic anisotropy. Consequently, in the magnetic images recorded each pixel can be assigned to one of the two magnetic orientations normal to the layer planes. To quantify the matching of the domain configurations contained in the hard and soft stack such idealized binary magnetic states are derived from the hologram reconstructions obtained during field-induced (Fig. 3.9) and temperature-induced (Fig. 3.11) domain replication.

¹ Note that the camera image is rotated by 90° , which means the horizontal direction in the images corresponds to the vertical direction in the chamber, along the length of sample holder.

In FTH the position and pixel resolution of the actual image depends on the energy of the incident light. First, in order to be able to compare Co-edge and Ni-edge images the pixel resolution of the complete Co-edge hologram reconstruction is increased by a factor of 1.09, which corresponds to the ratio of the Ni- L_3 and the Co- L_3 edges. Furthermore, the radius of the circular FOV is reduced to neglect the ringing which is observed at the circumference of the object aperture in some of the reconstructions. As compensation for an irregular, curved background the images are treated with the built-in histogram equalization function (`ImageHistModification`) of the IGOR Pro [Igo] software package. The resulting magnetic states are shown in the upper row of Fig. 3.13. From these images the binary states are derived by application of a manual threshold such that the characteristic shape of the domains is reproduced. These images approximating the pure magnetic information of the sample are arranged in the lower row of Fig. 3.13.

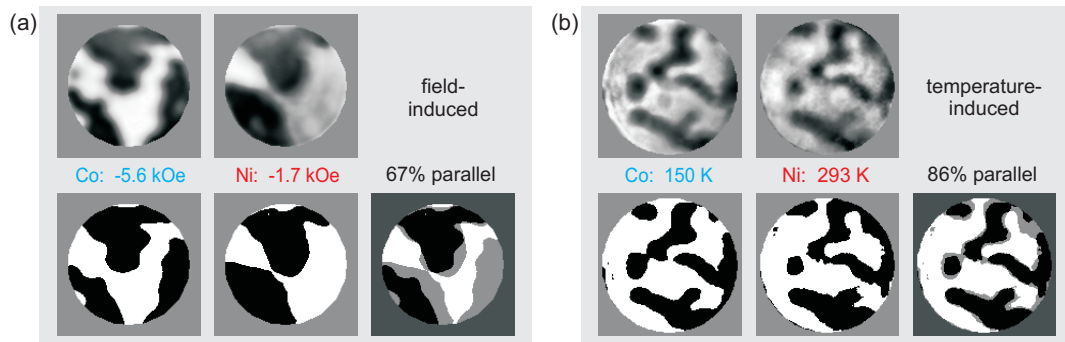


Figure 3.13: Comparison of the magnetic states contained in the hard (blue) and soft (red) multilayer stacks for (a) field- and (b) temperature-induced domain replication as measured in the experiment. The magnetic images with histogram equalization (upper row) and the derived binary magnetic states (lower row) are shown. The right column visualizes the direct comparison of the hard and the soft ML during each replication process.

Panel (a) and (b) of Fig. 3.13 correspond to the field- and temperature-induced domain replication, respectively. For both experiments the prepared magnetic template of the hard stack (left columns, blue) is compared to the most similar pattern of the soft stack's magnetic images recorded (middle columns, red). In all these images each pixel was assigned to represent either magnetization up or down with the help of the procedure described above. The images in the right column represent the pixel by pixel "summation" of the binary magnetic states of the hard and soft ML stacks. The summation is understood such that two white or black pixels result again in a pixel with the respective color. In contrast, the sum of pixels representing opposite magnetization is marked in gray. For the two comparison pictures the percentage of non-gray pixels is given quantifying the amount of parallel oriented magnetic moments within the FOV. According to that analysis correlation values of 67 % and 86 % are observed for field- and temperature-induced domain replication. An error of 5 % is estimated due to the simple manual domain recognition process and the partly ambiguous magnetic contrast. Obviously the hard stack's magnetic

configuration gets replicated, at least to a certain degree, to the soft stack by dipolar coupling. At the same time, this fact is an indicator that both stacks feature a similar intrinsic domain width as a strong difference of this parameter would lead to magnetic frustration during the replication of the hard stack's configuration.

Comparing both trigger variants a higher correlation was found for the temperature-induced domain replication. This appears reasonable as for thermal activation no external magnetic field needs to be applied and therefore the dipolar stray fields of the hard stack are the only additional influence on the soft system. That means once the raised temperature supplies sufficient energy to trigger domain nucleation at a specific location in the soft ML stack this domain can expand up to the boundaries set by the hard-layer domain. As the domain pattern in the hard stack corresponds to a net remanent magnetization and both ML systems feature a similar domain width, the replicated domain configuration in the soft stack is stable as well.

In contrast, for field-induced replication the problem arises that one has to know the field value, which successfully copies the domain pattern of the hard stack to the soft one. Raising the external field above this value may destroy the replicated pattern by forcing additional magnetic material in the soft stack in the reversed direction. In Fig. 3.13(a) the hard stack's configuration is compared to the Ni-image recorded at -1.7 kOe yielding a correlation value of 67%. The complete image set from Fig. 3.9 suggests that the optimum field value for field-induced domain replication at the given experimental parameters lies between -1.7 kOe and -2.4 kOe. In fact the correlation factor for the Ni-image recorded at -2.4 kOe (not shown) is less than 1% below the one for -1.7 kOe. It can be assumed that field-induced domain replication is in principle capable of reaching similar correlation factors as temperature-induced domain replication if the respective magnetic field value is sufficiently well known. That means, while both approaches can be used for domain replication, field-induced replication requires fine-tuning of the external applied magnetic field.

Finally, combining the results of the two replication experiments allows to give an estimate on the strength of the stray field \mathbf{H}_S originating from the hard Co/Pd stack. The energy barrier E_B that needs to be overcome to nucleate domains in the soft CoNi/Pd stack is set by its anisotropy K_u times a certain volume V considered. Domain nucleation in the soft stack will happen at a localized spot from which the domain will expand. That means the considered volume V can be very small compared to the typical domain size. Within a small volume the stray field \mathbf{H}_S as well as the magnetization \mathbf{M} is assumed to be constant:

$$\begin{aligned} E_B(T) &= K_u(T) \cdot V \approx \mathbf{M}(T) \cdot \mathbf{H}_S + \mathbf{M}(T) \cdot \mathbf{H}_{\text{ext}} \\ &\approx V \cdot \mathbf{m}(T) \cdot \mathbf{H}_S + V \cdot \mathbf{m}(T) \cdot \mathbf{H}_{\text{ext}} . \end{aligned} \quad (3.7)$$

This energy barrier E_B is strongly temperature-dependent in the range between 150 K and 350 K. The required energy to overcome E_B is provided by the stray field \mathbf{H}_S of the hard ML stack and the external magnetic field \mathbf{H}_{ext} if applied. The energy of a dipole in

these magnetic fields is given by its magnetic moment \mathbf{M} (or $\mathbf{m} \cdot V$ with \mathbf{m} being the magnetization per volume) times the magnetic field. Even without knowing the exact orientation of \mathbf{H}_S , once the domain nucleation starts within the CoNi/Pd stack, Eq. 3.7 does hold and can serve as an upper estimate for \mathbf{H}_S .

Two experiments have been performed in this section. In the first one, the reversal of the soft stack started at $T = 150$ K supported by the external magnetic field $\mathbf{H}_{\text{ext}} = -1.55$ kOe¹. In the second experiment the barrier E_B is constantly lowered by an temperature increase. No external magnetic field is applied. Switching in the CoNi/Pd stack is first observed in the image recorded at $T = 281$ K, while at 270 K the stack is still saturated. Here, 275 K is taken as onset. Eq. 3.7 can be evaluated for both nucleation points. The ratio of both equations allows to derive an expression for \mathbf{H}_S :

$$\frac{K_u(150 \text{ K}) \cdot \mathcal{V}}{K_u(275 \text{ K}) \cdot \mathcal{V}} \approx \frac{\mathcal{V} \cdot \mathbf{m}(150 \text{ K}) \cdot \mathbf{H}_S + \mathcal{V} \cdot \mathbf{m}(150 \text{ K}) \cdot \mathbf{H}_{\text{ext}}}{\mathcal{V} \cdot \mathbf{m}(275 \text{ K}) \cdot \mathbf{H}_S}. \quad (3.8)$$

The equation is solved for the stray field \mathbf{H}_S originating from the magnetically hard Co/Pd stack

$$\mathbf{H}_S \approx \frac{K_u(275 \text{ K}) \cdot \mathbf{m}(150 \text{ K})}{K_u(150 \text{ K}) \cdot \mathbf{m}(275 \text{ K}) - K_u(275 \text{ K}) \cdot \mathbf{m}(150 \text{ K})} \cdot \mathbf{H}_{\text{ext}}. \quad (3.9)$$

The ratios for $K_u(150 \text{ K})/K_u(275 \text{ K}) \approx 2.95$ and $m(150 \text{ K})/m(275 \text{ K}) \approx 1.7$ are obtained from Fig. 3.7. The insertion of these values yields:

$$\mathbf{H}_S \approx 1.36 \mathbf{H}_{\text{ext}} \approx 2.1 \text{ kOe} \approx 1.68 \times 10^5 \text{ A/m}. \quad (3.10)$$

Here, for the external magnetic field \mathbf{H}_{ext} an absolute value of 1.55 kOe was inserted derived from Fig. 3.9. A simulation using the Object Oriented MicroMagnetic Framework (OOMMF, [DP99]) finds a value of 1×10^5 A/m for the demagnetization field H_{demag} at the top of a Co/Pt multilayer system. This value agrees on a level of order of magnitude with the estimate from above.

In summary in this section a dipolar-coupled multilayer system consisting of a magnetically hard and a magnetically soft multilayer stack was characterized. Macroscopic VSM measurements varying the external magnetic field as well as the sample temperature revealed an influence of the magnetic configuration in the hard stack on the magnetic reversal behavior of the soft one. To separately image the magnetic configurations of each ML stack temperature-dependent x-ray FTH was performed in the interval from 150 K to 350 K. Hereby, the rigidly coupled FTH-mask provided the necessary relative stability of reference and object apertures. As a result, it was possible to record Fourier transform

¹ In Fig. 3.9 the image recorded at -1.5 kOe shows saturation of the soft stack while at -1.6 kOe a domain pattern first appears. The absolute value in between is taken as onset of the magnetic reversal.

holograms even though drift of the *complete* sample structure was observed. This drift resulted from temperature changes and compared slow to the typical hologram exposure times, i.e. the holograms could be reconstructed successfully.

The element specificity of x-rays allowed to separately probe the magnetic configurations of the two ML stacks. It was possible to follow the replication of domains trapped in the magnetically hard stack to the soft one via dipolar fields. The replication was triggered by an external magnetic field as well as by thermal activation. In both cases, the domain pattern nucleated in the soft stack could be correlated to the template generated beforehand in the hard stack. This fact directly proves the dipolar coupling of the two stacks and indicates a similar intrinsic domain width for the two ML.

Higher correlation of the copied domain state to the template was achieved for the temperature-induced duplication. For this process only one parameter, the temperature, needs to be varied. The experiment revealed a broad temperature range (from 293 K to ~ 325 K) suitable to trigger the duplication. In contrast, field-induced duplication asks for tuning of the external magnetic field for a given temperature. Deviations from this optimum value degrade the correlation of the copied state. Consequently, a lower correlation was found for field-induced domain duplication in the experiment.

3.3 Steplike Domain Propagation in Co/Pt and Co/Pd Multilayer Films

Ferromagnetism is an effect, which can be easily experienced in everyday life, i.e. on a macroscopic level. Its origin, however, is to be found on a microscopic level. The magnetic moments of electron spins and their orbital moments do align uniformly in the so-called Weiss domains and their sum determines the net magnetization of a ferromagnet. The domains can be aligned in an external magnetic field. Measuring the magnetization response dependent on changes of the magnetic field yields the hysteresis loop. From the hysteresis loop the coercivity and the remanence, which are characteristics for ferromagnetic materials, can be determined (see Ref. [Ber98] for an overview on magnetic reversal).

Understanding the macroscopic parameters of magnetism as average of a microscopic ensemble raises the question in how far the magnetic configurations have a correspondence between microscopic and macroscopic properties. For example, hysteresis loops measured on macroscopic samples do often exhibit an identical shape in subsequently repeated measurements apart from deviations caused by the measurement process. The return of the magnetic system to its initial magnetic state after the performance of a minor hysteresis loop is denoted return-point memory (RPM) [Pie07]. However, this considers the macroscopic observation only and does not necessarily mean that the microscopic system returns to its identical initial configuration as the same macroscopic magnetization can be generated by microscopically different domain patterns. To answer questions about *microscopic* RPM it is necessary to obtain information on the microscopic configuration of a ferromagnet during the magnetization reversal.

One possibility is to directly image the domain pattern of the sample during the

magnetic reversal. The requirements to be fulfilled are a sufficiently high spatial resolution to resolve the domains and the compatibility with in-field measurements. In fact a variety of magnetic imaging techniques exists today based on the interaction of light or electrons with magnetized matter or directly measuring the magnetic force. An overview over the various methods can be found in the book by Hopster & Oepen [HO05]. While a series of magnetic images provides an optimum characterization, high-resolution magnetic imaging is time-consuming and the recording of a set at closely spaced magnetic field values might turn out to be impractical. However, if such an image set is available, local hysteresis loops (LHLs) can be extracted from arbitrary sample locations within the FOV.

Alternatively, it is possible to measure fingerprints of the domain configuration by indirect methods. Speckle metrology, an elegant indirect approach was demonstrated with x-rays by Pierce et al. [Pie03]. This group analyzed the coherent x-ray scattering patterns for magnetic Co/Pt films with perpendicular anisotropy. Interference of magnetically scattered x-rays at the detector generates a unique speckle pattern, i.e. a fingerprint of the microscopic magnetic state of a large ensemble. By correlation of such scattering patterns in different subsequent hysteresis loops Pierce et al. found a dependency of the microscopic RPM on the defect density within the sample [Pie03; Pie05; Pie07].

Although FTH and speckle metrology do have a lot in common, FTH is capable to directly image a sample's domain pattern, mainly because of the nanostructured FTH-mask. This mask defines a microscopic FOV typically below $1\ \mu\text{m}^2$. In case of Co/Pt or Co/Pd multilayers this size corresponds to the width of few magnetic domains only. For such a small ensemble, "macroscopic" measurement methods from this sample area start to exhibit microscopic features, which are otherwise averaged out. For example, in the optical regime such local hysteresis loops are often measured by magneto-optical Kerr effect (MOKE) magnetometry in conjunction with a small laser spot to achieve high resolution [Cow98]. That means in addition to the high-resolution magnetic images FTH provides, *local* hysteresis loops with a high sample rate can be obtained by measuring the transmitted intensity through the FTH-mask. With this fast integrating measurement it is possible to identify interesting points within the magnetic reversal, which can be afterwards characterized in detail by FTH imaging.

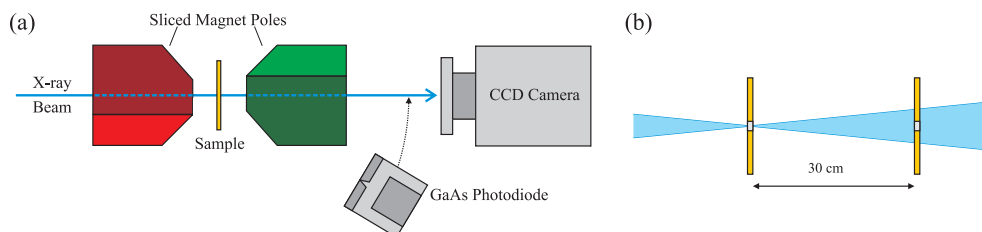


Figure 3.14: FTH can combine fast integrating measurements and high-resolution imaging on magnetic samples. (a) For the measurement of local hysteresis loops the 2D-detector is replaced by a faster, integrating photodiode. (b) In addition, the sample is moved into the beamline focus for better statistics.

For fast integrating measurements the sample can be placed in the beamline focus to maximize the SNR since no transverse coherence is required. In addition, a photodiode replaces the CCD and acts as a fast integrating detector (see Fig. 3.14). In practice the combination of the ALICE chamber and the BESSY-II UE52-SGM beamline, which is used for all imaging experiments, is not compatible with an in-focus position of the sample. Therefore, the in-focus local hysteresis loops presented in this section are measured at the UE56-1-SGM beamline at BESSY-II. Still, the FTH-mask ensures the stability of the FOV. Note that both measurements can exploit the advantages of soft x-rays such as their element specificity. In this section LHLs on Co/Pd and Co/Pt systems are presented that directly correspond to the microscopic reversal behavior of magnetic multilayers.

3.3.1 Steplike Magnetic Reversal Caused by Increased Defect Concentration

The reversal of a ferromagnetic material is strongly influenced by the structure of the material. Structural defects may act as nucleation centers or magnetic pinning sites hindering the propagation of domain walls. In magnetic thin films of Co/Pt an increase of the defect concentration was found to induce partial microscopic return point memory (RPM) [Pie03; Pie05; Pie07]. Such an onset might also be observable in *local* hysteresis loops (LHLs) measurements.

To investigate the effect of an increased defect concentration in combined LHLs and x-ray FTH images two magnetic multilayers (ML) are fabricated by magnetron sputter deposition. Twenty repeats of Co(4 Å)/Pd(8 Å) are grown on top of a Pd(30 Å) seed layer and capped by Pd(12 Å) to prevent oxidation. Thus, the complete layer sequence is Pd(30) / [Co(4)/Pd(8)]₂₀ / Pd(12) with all numbers corresponding to the vertical thickness in angstrom. Two samples are grown with identical ML composition, but at different Argon pressures during deposition. The first sample is sputtered at the standard Ar pressure of 3 mTorr, while for the second sample the deposition pressure is increased to a value of 6 mTorr.

Co/Pd multilayers with such parameters exhibit a strong magnetic anisotropy perpendicular to the layer planes [Hel03a; Dav04; Hel07]. The resulting strong stray fields give excellent contrast in magnetic force microscopy (MFM) measurements. In Fig. 3.15 typical remanent domain patterns after demagnetization are presented for the two samples. Both samples exhibit alternating up and down domains at all locations within the (5 μm)² observation area. In detail the patterns of both samples do differ. The intrinsic typical domain width is smaller for the 3 mTorr sample. In addition, the remanent domain patterns of the 6 mTorr sample exhibit more irregular domains compared to the 3 mTorr sample, which can be a first indicator for an increased defect concentration.

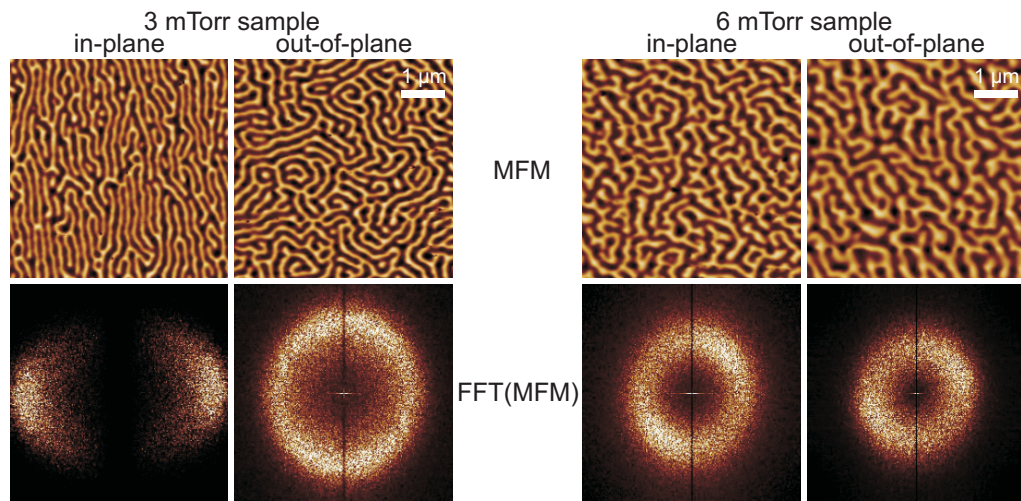


Figure 3.15: MFM images visualizing the domain structure of a $(5\ \mu\text{m})^2$ area of the 3 mTorr and 6 mTorr sample after in-plane and out-of-plane demagnetization. The Fourier transforms of a $(20\ \mu\text{m})^2$ area of the domain pattern reveal preferred magnetization directions, if present.

The magnetic configuration of Co/Pd multilayers strongly depends on their magnetic history. In Fig. 3.15 both samples are demagnetized in two different ways. First, an alternating external magnetic field with decreasing amplitude is applied along an in-plane axis. For in-plane demagnetization an alignment of the domains parallel to the field axis is expected (stripe domains). In the second case the field is applied along the easy axis pointing perpendicular to the layer interfaces. Out-of-plane demagnetization favors no in-plane direction. Thus, a domain pattern isotropic within the layer planes should show up. To clearly visualize any preferred magnetization directions present in the MFM-images the corresponding Fourier transforms are added to Fig. 3.15. For better statistics the FOV used for these Fourier transformations correspond to a somewhat larger sample area of $(20\ \mu\text{m})^2$ including the domain pattern part shown above. The typical domain width for each sample state is derived from the radial integration of the Fourier transforms. The width of the frequency ring is determined by the intensity drop to a value of $1/e$ of its maximum.

In this analysis the 3 mTorr sample follows the expectations. An alignment into stripe domains is observed for in-plane demagnetization and a domain pattern without preferred directions for out-of-plane demagnetization. The typical domain widths for both scenarios are (165 ± 90) nm and (155 ± 60) nm, respectively. In contrast, for the 6 mTorr sample no preferred in-plane direction can be imprinted into the system. The increased density of magnetically active defects caused by the increased sputter deposition pressure prevents the alignment into the magnetostatically lowest-energy configuration of parallel stripes. The domain widths for in- and out-of-plane demagnetization are (205 ± 90) nm and (280 ± 155) nm.

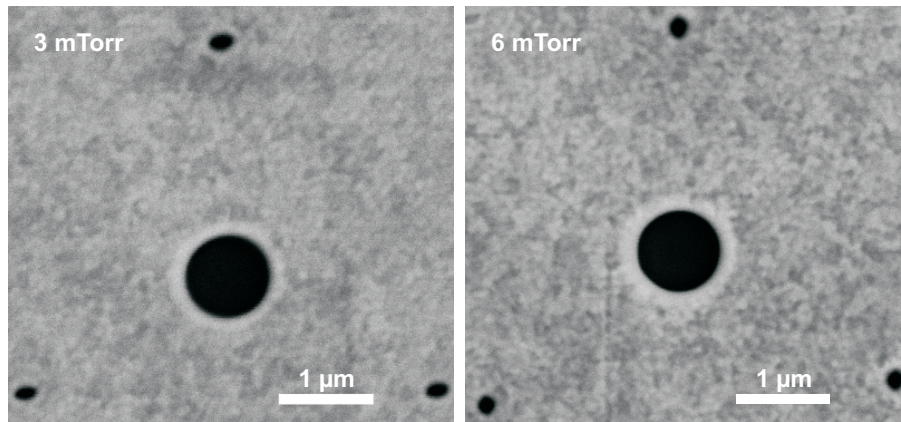


Figure 3.16: SEM images of both samples prepared for FTH measurements by FIB-nanostructuring.

For combined magnetic imaging and LHL measurements both samples are prepared with FTH-masks. In Fig. 3.16 SEM images of the integrated holographic masks defined by focused ion beam milling (FIB) into an 1- μm -thick gold film are presented. For both samples the diameter of the circular object aperture is 850 nm, corresponding to an area of $0.57 \mu\text{m}^2$. Considering the typical domain width from the MFM images this field of view leaves space for roughly six domains with alternating magnetization orientation for the 3 mTorr sample and about three domains for the 6 mTorr sample. Three reference apertures are milled equally spaced on the circumference of a circle with $2.5 \mu\text{m}$ radius. Their opening diameters at this side of the gold film approach 200 nm. On the other side of the gold film SEM images reveal diameters closely above 100 nm due to the conical narrowing of the holes' cross-sections as illustrated in Fig. 3.4(b).

The open area of each object aperture defines the part of the corresponding sample that is exposed to the x-ray radiation. The magnetic material in the area obscured by the gold film is not measured, but may certainly influence the reversal behavior of the sample within the FOV. Local hysteresis loops are measured with circularly polarized soft x-rays at the Co- L_3 absorption edge around 778 eV in the focus of the BESSY-II undulator beamline UE-56. Fig. 3.17 compares 3 LHLs with a hysteresis obtained by vibrating sample magnetometry (VSM) on a macroscopic ensemble for both samples.

In panel (a) LHLs are plotted for the 3 mTorr sample, which reveal a low coercivity of ~ 400 Oe. This sample nucleates domains before reaching remanence at a field value of ± 1 kOe as illustrated in the inset. All three LHLs as well as the macroscopic VSM loop look very similar to each other. In contrast, the 6 mTorr sample features full magnetic moment at remanence and a significantly larger coercivity of ± 1.1 kOe, i.e. the increased sputter pressure changes the general shape of the hysteresis loop significantly. The macroscopic hysteresis loop exhibits a smooth reversal once nucleation has started. In contrast, all three LHLs differ from the macroscopic measurement as well as from each other. All local measurements on the 6 mTorr sample exhibit a steplike reversal behavior.

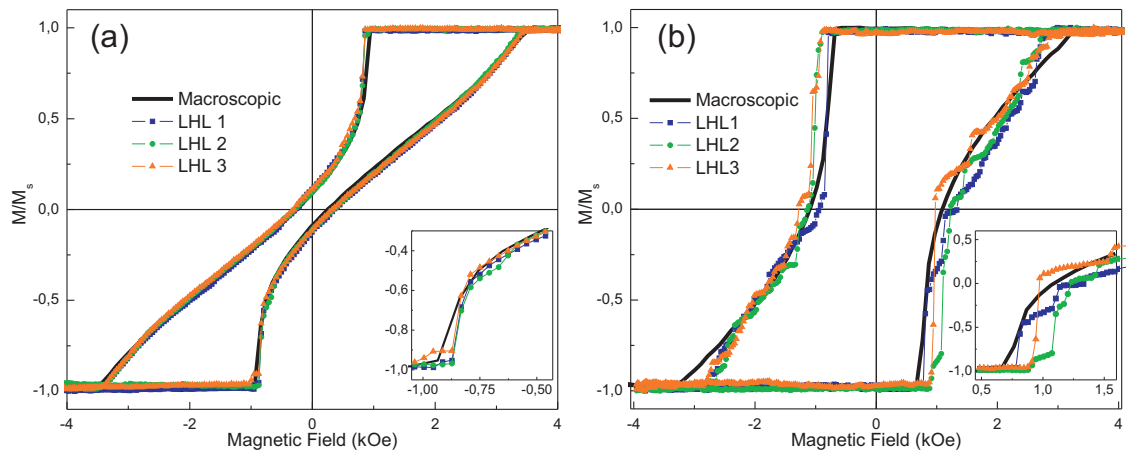


Figure 3.17: Comparison of three local hysteresis loops with a macroscopic VSM measurements for the multilayer compositions sputtered at (a) 3 mTorr and (b) 6 mTorr, respectively. The insets magnify the nucleation regions. The data can also be found in [Gü08].

These sudden jumps of the magnetization are irreproducible in their nature and can be interpreted as result of random spin-flip avalanches similar to observations in Barkhausen noise measurements [DZ06; KCS03; KS04]. In a simple picture, within the 3 mTorr sample domain walls may move relatively undisturbed. As a result, small changes of the magnetic field cause the magnetic reversal of a correspondingly small part of the sample. For the 6 mTorr sample the increased number of defects is obviously magnetically active and hinders a continuous propagation of domain walls upon field reversal. The domain walls get pinned at these defects and resist the increasingly higher magnetic field. Thus, the sample cannot react on small increases of the magnetic field, but remains in its pinned configuration. Once the value of the magnetic field gets sufficiently large to overcome the pinning, a comparably large amount of the sample magnetization reverses at once. Thus, on a microscopic level it is possible to observe a transition from a smooth hysteresis loop to a steplike reversal. Hereby, the fact that each LHL looks different proves that the domain configuration is different in each reversal. In contrast, the smooth LHLs for the 3 mTorr sample alone do not prove that the reversal takes place via similar microscopic magnetic configurations.

Apart from the reduced field of view defined by the FTH-mask, reference apertures are milled into the gold film for FTH imaging. To investigate the switching reproducibility of both samples a set of Fourier transform holograms of magnetic states with about 50 % of the sample area magnetized in opposite directions is collected. The holograms are recorded 30 cm downstream of the BESSY-II UE52-SGM beamline focus at field values of 0.4 kOe and 0.9 kOe for the 3 mTorr and 6 mTorr samples, respectively. Between the images the samples are saturated by a magnetic field of -7 kOe. The procedure is repeated 24 and 30 times for the two samples, respectively. Due to the integrated FTH-mask design the

magnetic images provide data on the *identical* sample region as the LHLs.

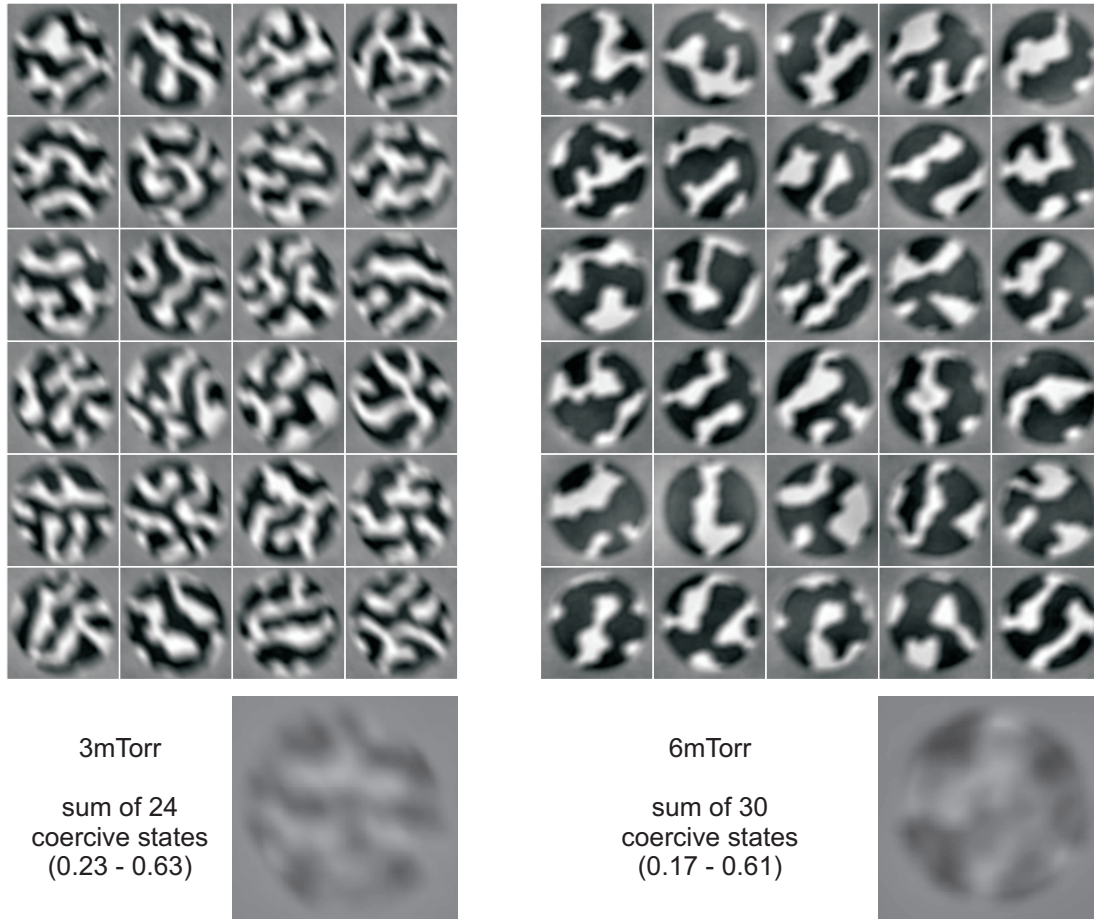


Figure 3.18: Switching reproducibility for the 3 mTorr (left) and 6 mTorr (right) sample, respectively. The enlarged images represent the sum of the magnetic-state images shown above. The values in brackets state the minimum and maximum z-values for these image sums.

In Fig. 3.18 24 magnetic images are shown for the 3 mTorr sample and 30 magnetic images for the 6 mTorr sample. In these images the black and white contrast corresponds to a magnetization direction parallel and antiparallel to the x-ray beam. These magnetic-state images corroborate the domain width of (155 ± 60) nm for the 3 mTorr sample and the more varying domain width of (280 ± 155) nm for the 6 mTorr sample as determined from the out-of-plane demagnetization MFM images. An important point is that for both samples all domain states shown appear significantly different. On first glance no specific pinning sites are visible within the FOV.

The presence of such a specific magnetic pinning site in these images would manifest in locations with a preferred magnetization orientation, i.e. it would appear more often black

than white or the other way round. For the identification of these locations the contrast in the individual images is normalized to the interval of 0 (black) and 1 (white) set by the minimum and maximum intensities. Afterwards an average image is calculated via pixel by pixel summation of all the individual domain states available. These two average images are shown enlarged in Fig. 3.18 on the same z-scale (0–1) as each individual FTH image. The minimum and maximum z-values of these images range from 0.23 to 0.63 and from 0.17 to 0.61 for the 3 mTorr and 6 mTorr sample, respectively. That means the direct summation of the individual magnetic states does not reveal any pixel which exhibits the same magnetization orientation in all the magnetic states recorded and thus could be directly considered as pinning site.

In addition, a circular region of interest (ROI) is defined considering only the pixels within the circular object aperture. The sum of all pixel values within this ROI divided by the number of pixels contained in this ROI results in the average sample magnetization. This value is 0.42 for the 3 mTorr sample and 0.38 for the 6 mTorr sample. Obviously a perfect remanent state was not generated for both samples. Instead a slight favor for the “black” domains is observed.

For a more profound analysis about the significance of the obtained coercive states the magnetic information is extracted from the images. This is possible as the investigated samples feature a perpendicular magnetic anisotropy, which means each pixel can be assigned to a “white” or “black” domain. Similar to the previous chapter that fact is taken into account by mapping the magnetic information of each hologram recorded to a binary image. The images presented in this chapter exhibit a better signal-to-noise ratio compared with the images from chapter 3.2. As a result, they can be directly converted to binary states using the IgorPRO built-in `ImageThreshold` function [Igo].

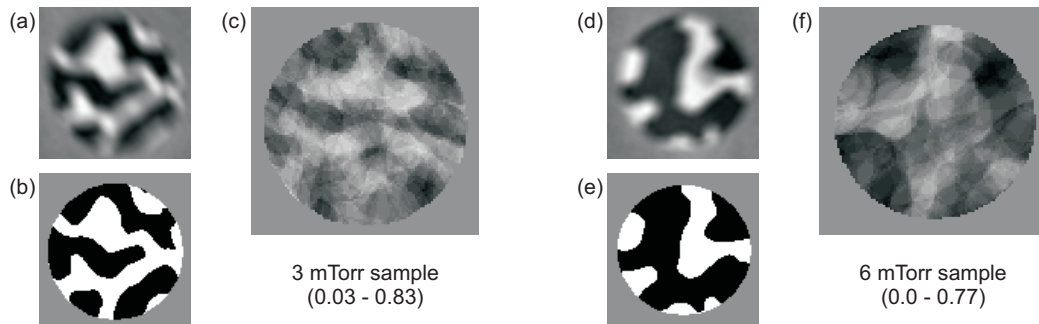


Figure 3.19: Exemplary reconstructed (a,d) and derived binary (b,e) magnetic states for the 3 mTorr and 6 mTorr samples. The corresponding image sums of all recorded binarized states are shown in panels (c) and (f). The values in brackets state the resulting minimum and maximum z-levels.

As an example, in Fig. 3.19 the first magnetic-state images from Fig. 3.18 are compared to the derived binary magnetic states for both samples. The characteristic shapes of the domains are reproduced. At the same time, the approximation of binary magnetization

orientation at every sample location removes any area of intermediate contrast such as at the borders of two opposite domains. As a result, the image sums in Fig. 3.19(c,f) of these binary states feature an increased contrast. The extreme z-values observed increase to the interval $[0.03-0.83]$ and $[0.0-0.77]$ for the 3 mTorr and 6 mTorr sample, respectively. That means pixels are found for the 6 mTorr sample that return to the “black” magnetization orientation in all 30 states recorded. The average magnetization for each sample determined from the two resulting sum-images is 0.44 and 0.35 for the 3 mTorr and the 6 mTorr sample. Both values deviate by less than 0.03 from the average magnetization values found in the sum-images in Fig. 3.18.

The question remains in how far the sums of the independent magnetic states are meaningful in revealing locations with preferred magnetization orientation, i.e. possible pinning or domain nucleation sites. To answer that question it is necessary to consider the statistics of the independent magnetic states recorded. The following simulation is conducted with the help of two MFM images of the two samples featuring a FOV of $(10\ \mu\text{m})^2$. Because of the large sample area investigated these MFM images can serve as a source to create random domain configurations corresponding to the reduced FOV of FTH. First, the MFM images are made binary, again by thresholding. The threshold is determined such that the average magnetization of the images resembles the values measured on the holograms. Afterwards, a square region of interest with 40^2 pixels, which corresponds to $(0.76\ \mu\text{m})^2$, is randomly chosen from the complete MFM image.

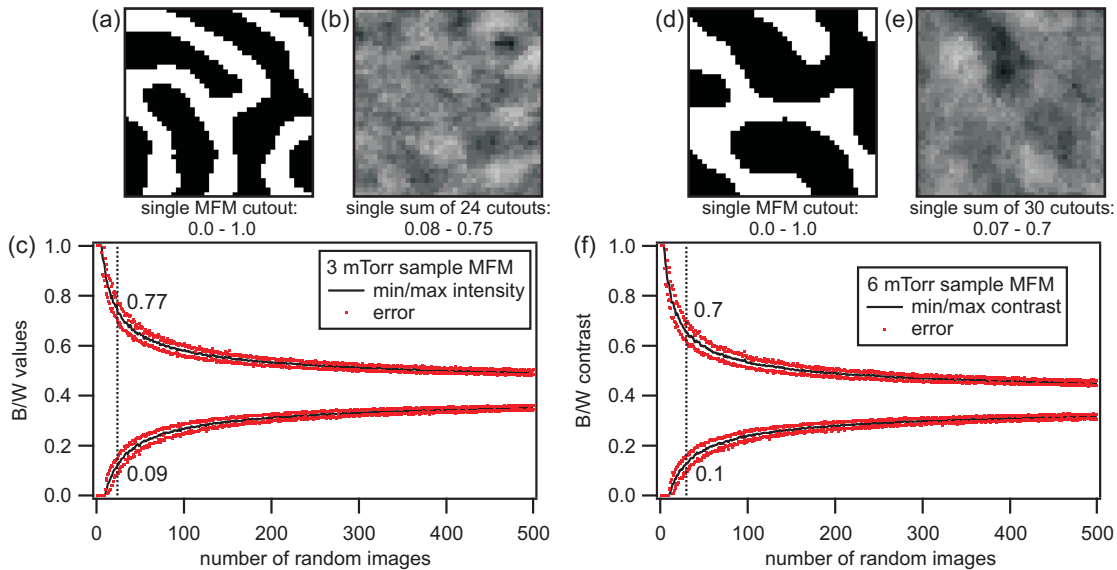


Figure 3.20: Statistics consideration for the average magnetization images of the 3 mTorr (left) and 6 mTorr (right) sample. (a,d) Exemplary magnetic state randomly chosen from the MFM image. (b,e) Single sum over 24 (30) randomly chosen states. (c,f) Plot of the minimum and maximum gray levels dependent on the number of random magnetic states added up.

Examples for such randomly chosen magnetic patterns are presented in panel (a) and (d) of Fig. 3.20. Next to these states in panel (b) and (e) the sums of 24 (30 for the 6 mTorr sample) of such randomly chosen states are shown including their minimum and maximum z -values. These two specific artificial image sums exhibit a slightly smaller contrast than the sums of the measured and binarized magnetic states from Fig. 3.19(d,f). The calculation is extended up to a sum of 500 random states to visualize the development of the contrast in the resulting image sums. These plots are shown in Fig. 3.20(c) and (f) for the two samples. For each data point the calculation is repeated 50 times to obtain the mean values (black lines) and the standard deviations (red dots) of the minimum and maximum z -values. Since random magnetic states have been generated from the MFM images for this calculation, these plots mark the boundaries for the z -values of sum images of uncorrelated magnetic states, i.e. magnetic states without pinning sites. If sample locations with preferred magnetization orientation would be present, the sum of a number of magnetic states is expected to exhibit z -values outside of the interval determined in Fig. 3.20(c,f). The black vertical line marks the expected contrast values for the 3 mTorr sample (24 states) and the 6 mTorr sample (30 states). According to that estimate a z -scaling ranging from 0.09–0.77 and 0.10–0.70 is expected for the two sample considering one sigma of the standard deviation.

A comparison with Fig. 3.19(c,f) reveals that the image sums of the measured binary states exceed these values. In principle this fact indicates the presence of locations with preferred magnetization orientation compared to a defect-free sample. However, the z -values from the averaged binarized measured magnetic states, which represent a single event in terms of statistics, are nominally just outside of the envelope determined in the statistical analysis. In addition, the binarization of the FTH and MFM images may introduce deviations in the average sample magnetization, which would finally lead to different expected z -values in the statistical estimate.

For the experiment that means, the contrast found in the sum-images of the magnetic states does not yet justify to clearly identify magnetic pinning. For that an increased number of magnetic states needs to be recorded. Judging from the plots in Fig. 3.20 a number on the order of 100 seems appropriate to clearly identify locations with a preferred magnetization orientation.

In summary, an increased Ar pressure during sputter deposition strongly affects the magnetic properties of an otherwise identical multilayer sequence due to the introduction of additional defects. These defects are magnetically active, which is evident in a significant change of the macroscopic hysteresis loop. Furthermore, it is not possible to use in-plane demagnetization to align the 6 mTorr sample into the magnetostatically lowest-energy state of parallel stripe domains. Further information on the magnetic reversal behavior are obtained by the measurement of XMCD-based local hysteresis loops on a reduced ensemble of the specimen in conjunction with magnetic FTH images on the identical sample region. While macroscopic and local hysteresis loops are very similar in the case of the 3 mTorr sample, for the 6 mTorr sample the increased defect density triggers a steplike reversal observed in the LHLs. These sudden jumps of the magnetization are attributed

to magnetic pinning which hinders a uniform domain wall motion in the 6 mTorr sample. At the same time the stepped loops are irreproducible in their nature. In that context the magnetization jumps can be interpreted as spin-flip avalanches such as observed in Barkhausen noise measurements. Finally, FTH images reveal an irreproducible domain configuration after sample saturation for both samples. While an indication for locations with preferred magnetization orientation exist, the number of recorded magnetic states is not sufficient for a reliable identification of specific pinning sites within the FOV. It is also important to note that such pinning sites could have an influence on the measured domain configurations if they are located just outside, but in the vicinity of the FOV.

Apparently, the 6 mTorr sample falls into a transition regime. Magnetic domains get trapped by structural defects and irreproducible spin-flip avalanches are present. On the other hand the defect density is not large enough to define deterministic domain nucleation and propagation channels. This is consistent with earlier observations on Co/Pt ML, where no return point memory (RPM) behavior was found below sputter deposition pressures of 7 mTorr [Pie03; Pie05; Pie07]. It is expected that a further increase of the sputter pressure would lead to reproducible LHLs and thus to microscopic RPM. Such reproducible, deterministic spin-flip avalanches have been observed in grain-based magnetic recording media and were suggested as fingerprint-like identification marks making individual recording devices distinguishable [IMO99; IMM99].

3.3.2 Steplike Magnetic Reversal in an AF-coupled Multilayer System

In the previous section perpendicular anisotropy Co/Pd multilayers have been investigated regarding their magnetic reversal behavior upon an increased defect concentration. The separate Co layers in such Co/Pd or similar Co/Pt multilayer stacks are vertically (perpendicular to the layer planes) correlated and consequently all Co layers reverse their magnetization as one. The beauty of layered magnetic thin films is that various coupling mechanisms exist and can be favored by controlling the ML parameters, which makes them valuable prototypes in the study of magnetic reversal processes. For example, stacks of perpendicular Co/Pd or Co/Pt multilayers can be antiferromagnetically (AF) coupled in the vertical direction by the introduction of Ru or Ir interlayers. In extended studies of such AF-coupled Co/Pt and Co/Pd multilayers [Hel03b; Hel07] two phases have been identified denoted mode 1 and mode 2 in Ref. [Hel03b]. Mode 1 corresponds to a vertically anticorrelated, horizontally correlated magnetic reversal. That means each complete Co/Pt stack switches as a whole one after the other if the multilayer system is exposed to an external magnetic field. In contrast, mode 2 describes a vertical ferromagnetic coupling of the multilayer. The magnetic reversal takes place via vertically correlated and horizontally anticorrelated labyrinth domain formation. The transition between these two phases can be controlled via the multilayer parameters such as the number of repeats or the layer thickness, but also via temperature changes [THH08].

For AF-coupled Co/Pt stacks with identical parameters a coexistence of the two phases next to each other was observed. In contrast it was not possible to combine both phases

and realize an antiferromagnetic stripe domain state. Such a state was predicted for AF-coupled ML systems [Kis07; RB04]. Because of the arrangement of alternating domains in the lateral as well as in the vertical direction (see Fig. 3.22(b)) this magnetic state of antiferromagnetic stripe domains has also been designated as checkerboard (or chessboard) state [Hel11]. In this context the necessity of depth-resolving characterization methods was emphasized.

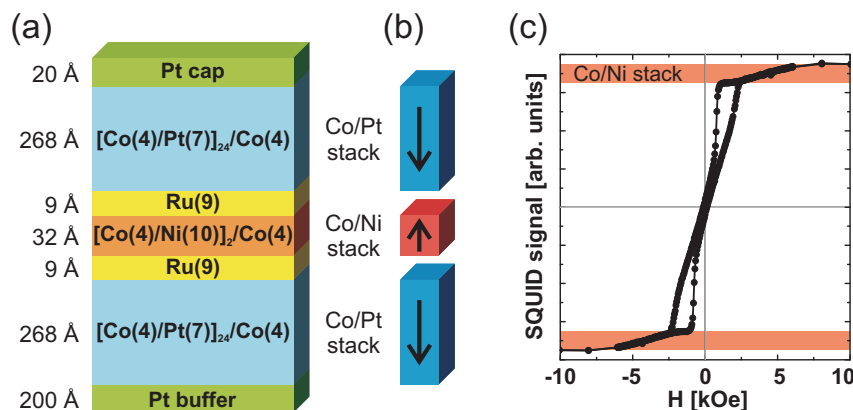


Figure 3.21: AF-coupled sample: (a) multilayer structure of the AF-coupled sample, the numbers give each stack thickness in angstrom. The resulting preferred magnetic orientation is visualized in the corresponding stacks next to the sample structure. (b) SQUID hysteresis loop of the AF-coupled sample.

To prepare and characterize such an antiferromagnetic stripe domain state the layer sequence Pt(200) / [Co(4)/Pt(7)]₂₄/Co(4) / Ru(9) / [Co(4)/Ni(10)]₂/Co(4) / Ru(9) / [Co(4)/Pt(7)]₂₅ / Pt(13) was grown by magnetron sputter deposition at an argon (Ar) pressure of 3 mTorr. All numbers correspond to the vertical layer thickness in angstrom. The layer sequence is schematically illustrated in Fig. 3.21(a). The sample was grown on silicon nitride (Si₃N₄) membranes for transmission x-ray experiments as well as on Si wafers for macroscopic magnetometry and MOKE measurements. Pt(200 Å) serves as buffer layer and Pt(20 Å) as cap for oxidation prevention. The sample consists of three multilayer stacks with perpendicular anisotropy: two stacks of [Co(4 Å)/Pt(7 Å)]₂₄/Co(4 Å) and one stack of [Co(4 Å)/Ni(10 Å)]₂/Co(4 Å). Similar to the two samples in the previous section each of these stacks exhibits a perpendicular anisotropy and can be thought of as one entity with an easy axis perpendicular to the layer planes. The Ru(9 Å) interlayers cause an antiferromagnetic (AF) coupling between the three ML stacks [Hel03b; Hel07]. Thus, the two Co/Pt stacks favor a parallel alignment to each other and an antiferromagnetic alignment to the central Co/Ni stack. This behavior is schematically illustrated for a uniform magnetization of the complete stacks in Fig. 3.21(b). The central Co/Ni stack features less repeats compared to the adjacent Co/Pt stacks to reduce the magnetostatic interaction at these interfaces [Bro92; Hel11] and thus favor the formation of ferrimagnetic stripe domains. In addition, Pt has been exchanged with Ni for the central stack to allow

for an exclusive monitoring of this stack at the Ni- L_3 absorption edge.

As a first characterization a hysteresis loop obtained by superconducting quantum interference device (SQUID) measurements of the complete AF-coupled sample is shown in Fig. 3.21(c). The magnetic field is applied perpendicular to the layer planes. In the interval of $H_s(\text{Co/Pt}) = \pm 2.5 \text{ kOe}$ the hysteresis loop exhibits the typical shape of a Co/Pt multilayer establishing ferromagnetic stripe domains during its reversal. The domain nucleation starts at $\pm 1 \text{ kOe}$. In this low-field part of the hysteresis loop the two Co/Pt stacks reverse their magnetization via stripe domain formation. At $H_s(\text{Co/Pt})$ the magnetic configuration of the sample corresponds to the illustration in Fig. 3.21(b): the Co/Pt stacks are completely saturated pointing in the same direction while the Co/Ni ML is uniformly magnetized into the antiparallel direction. Higher magnetic fields start to reverse the Co/Ni stack, but only a high external magnetic field $H_s(\text{CoNi})$ of 8 kOe is sufficient to overcome the AF-coupling and magnetize all three stacks into one direction. In panel (c) this contribution of the Co/Ni ML to the hysteresis loop at high magnetic fields is marked in red.

X-ray measurements in resonance with the Co- L_3 and Ni- L_3 absorption edges allow to study the reversal behavior of the two types of ML stacks separately. In Fig. 3.22(a) XMCD hysteresis loops are presented obtained at the two edges, respectively. While the loop recorded at the Co edge (778 eV) corresponds to the complete sample structure, the main signal contribution originates from the two thick Co/Pt stacks where most of the Co is contained. In contrast, the loop recorded at the Ni edge (853.9 eV) exclusively reveals the magnetization reversal of the intermediate Co/Ni stack. The loops were measured on a macroscopic Si_3N_4 membrane of $(2 \text{ mm})^2$ size located in the focus of the BESSY-II undulator beamline UE56-1. A field of up to $\pm 7 \text{ kOe}$ is applied, which is not sufficient to achieve complete sample saturation, but large enough to overcome the AF-coupling and to almost saturate all three ML stacks in one direction. The magnetic state of the complete sample structure during the hysteresis is schematically illustrated in panel (b).

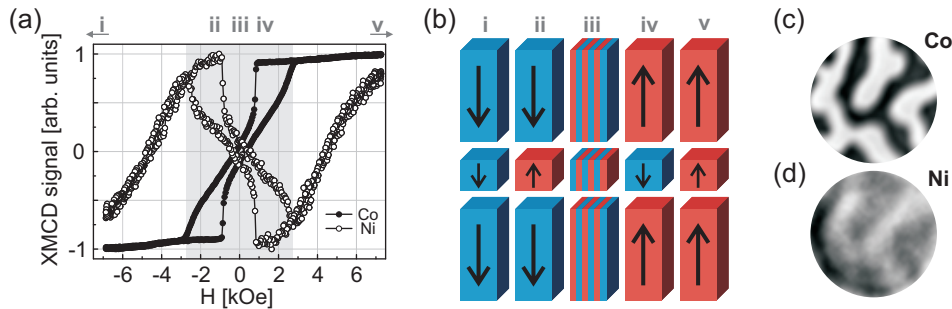


Figure 3.22: (a) XMCD hysteresis loops measured at the Co and Ni edges, respectively. For visibility both signals are normalized in y to the same scale. The Co/Ni stack is found to reverse its magnetization three times within one field sweep. (b) Schematic illustration for the magnetic configurations of the regions i–v marked in the hysteresis plot. (c) Co- and (d) Ni-edge FTH images of the remanent state.

Following the ascending branch of the two hysteresis loops starting from -7 kOe at negative saturation (marked i in Fig. 3.22(a,b)) the Co/Ni stack directly starts to inverse its magnetization via uniform reversible rotation. Approaching a field value of -1 kOe the sample is left in an uniform ferrimagnetic down-up-down state (ii). At this field value domain nucleation starts within the Co/Pt stacks. As domains appear in the Co/Pt stacks, the AF-coupling causes a second inversion of the Co/Ni magnetization back to the starting orientation as indicated by the opposite hysteretic reversal observed at the Co and Ni edges around remanence. Thus, the reversal in the region around remanence happens via the formation of lateral anti-phase domains with a vertically ferrimagnetic (up-down-up) structure (iii), the so-called checkerboard state. At 2.5 kOe the Co/Pt stacks are completely inverted, whereas the Co/Ni layer is magnetized uniformly antiparallel again (iv). A continued increase in external magnetic field starts the third inversion of the Co/Ni stack against the AF-coupling into the new magnetization direction, again via uniform reversible rotation. At 7 kOe the complete system has (almost) inverted its magnetization direction (v). Because of the antiferromagnetic coupling the central Co/Ni stack inverts its magnetization direction three times during a field sweep from one saturation to the opposite one.

To directly prove the preparation of a magnetic checkerboard state the AF-coupled sample is prepared on a holography mask for domain-pattern imaging via FTH. Panel (c) and (d) of Fig. 3.22 correspond to reconstructions obtained from holograms recording the sample's remanent state at the Co and the Ni edges, respectively. The overall hologram exposure times are 800 s for the Co-edge image and 3200 s for the Ni-edge image. The holograms for these two reconstructions have been shown earlier as examples for magnetic scattering in Fig. 3.3. The diameter of the field of view defined by the circular object hole measures $0.83 \mu\text{m}$. Two references with a diameter below 100 nm each are located at a center-to-center distance of $3 \mu\text{m}$ as shown in the inset of Fig. 3.23(a). The Co-hologram provides a high-contrast domain pattern of the sample magnetization averaged over all stacks. Again the signal is dominated by the two Co/Pt stacks. The magnetic scattering at the Ni edge is much weaker and does not collect signal up to the same q as for the Co edge due to the small amount of only 2 nm of buried Ni present in the sample. Consequently, the corresponding hologram reconstruction shows reduced contrast and resolution. Still, the domain pattern is clearly recognizable as being anticorrelated to the domain pattern at the Co edge. That means a domain pattern strongly similar to the one in the Co/Pt stacks but with opposite magnetization forms in the Co/Ni stack. Thus, a remanent antiferromagnetic stripe domain state has been prepared.

The holographic mask allows the measurement of local hysteresis loops to obtain information on the microscopic reversal behavior as in the previous section. The reduced FOV of $0.83 \mu\text{m}$ leaves space for about six domains judging by Fig. 3.22(c). The LHLs shown in Fig. 3.23 were measured in the focus of the BESSY-II undulator beamline UE56-1-SGM at the Co edge. A steplike magnetic reversal is observed although the AF-coupled sample has been sputtered at a deposition pressure of 3 mTorr. The magnification of the nucleation region in Fig. 3.23(b) gives evidence of an irreproducible nucleation onset. In

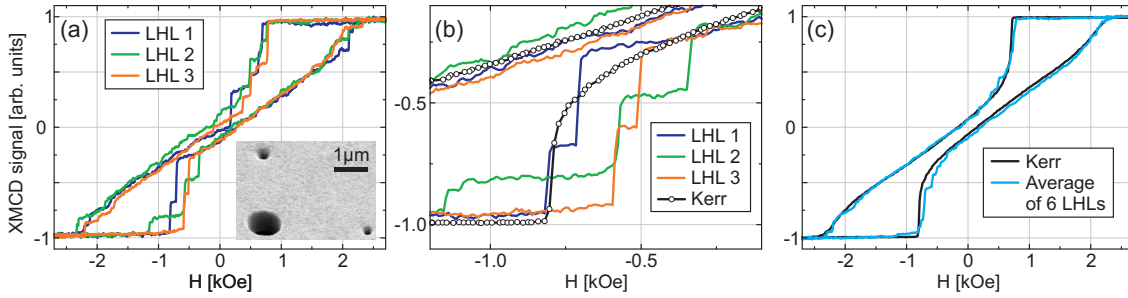


Figure 3.23: (a) XMCD local hysteresis loops measured at the Co edge on the AF-coupled sample. The inset illustrates the reduced sample region and the references defined by the FTH-mask. (b) Enlarged nucleation region compared to a macroscopic MOKE measurement. (c) The average of 6 LHLs compared to a macroscopic hysteresis obtained by MOKE. The magnetic field values for the MOKE measurement were scaled by 10% to compensate for sample position uncertainty and field calibration errors.

the previous section a smooth local magnetic reversal of Co/Pd multilayers was observed for a sputter deposition pressure of 3 mTorr. Only an increased pressure of 6 mTorr caused stepped LHLs. It seems that the introduction of the central AF-coupled Co/Ni stack causes a similar steplike magnetic reversal for the present sample at low deposition pressure. In Fig. 3.23(c) the average of 6 LHLs is plotted. In the graph the steps are almost lost and as a result the average hysteresis loop compares better to a macroscopic MOKE measurement than each of the individual LHLs on its own. That means the sudden magnetization jumps in the AF-coupled sample are irreproducible as for the 6 mTorr sample in the previous section. An interesting difference between the stepped LHLs of these two samples is that for the 6 mTorr sample the increased defect concentration causes not only a stepped local reversal, but has a significant impact on the general shape of the hysteresis. Remanent saturation and increased coercivity is observed. In contrast, the stepped LHLs of the present AF-coupled sample have kept a remanent domain state and the corresponding low coercivity of a Co/Pt multilayer with a high number of repeats [Hel07].

Obviously the underlying mechanism of the stepped loops is different for the AF-coupled sample as compared to the 6 mTorr sample from the previous section. An explanation is the introduction of the Co/Ni stack. This stack features different magnetic properties compared to the two Co/Pt stacks. Especially its smaller number of repeats causes a different intrinsic domain width. That means at the Co/Pd-Co/Ni interfaces, where the different magnetic systems are brought to contact, frustration is to be expected as it is not possible for both types of stacks to reach their preferred magnetic configuration simultaneously.

For the LHLs shown in Fig. 3.23 corresponding images can be recorded to illustrate the domain formation corresponding to the local magnetization jumps. This procedure is illustrated in Fig. 3.24. An initial magnetic field sweep from -2.7 kOe to 2.7 kOe drives the sample into the uniform magnetized state (iv). Note that this LHL exhibits more

noise as it is recorded behind the beamline focus of the UE52-SGM beamline to allow for the recording of additional Fourier transform holograms at the same time. At the end of the initializing field sweep the first image in Fig. 3.24 confirms the absence of any domains within the FOV at 2.7 kOe. During the proceeding along the descending hysteresis branch the magnetic field sweep is paused for Co-edge FTH recording. The first interruption is made directly after encountering the first magnetization jump at 0.73 kOe leaving the magnetic field applied. The corresponding hologram reconstruction reveals the initial domain nucleation within the field of view. The descending loop is continued in this fashion recording ten domain pattern along the hysteresis loop. For the data analysis the parts of the descending hysteresis branch are stitched together. All holograms are recorded with an overall exposure time of 1200 s except for the last two images at -2.53 kOe and -2.7 kOe where the exposure time was halved due to time constraints. All hologram reconstructions are compiled in Fig. 3.25 with prominent domain pattern changes marked by the circles.

The second (0.73 kOe) and third (0.45 kOe) domain configuration do correspond to the first two prominent steps in the local hysteresis. They illustrate the initial appearance of domains in the FOV and the growth of a distinct domain “branch”. Afterwards the steps become less pronounced and the magnetic reversal proceeds in a more continuous fashion, i.e. the contraction of stripe domains to bubble domains, which are finally annihilated. Nevertheless, in the images it can be observed that the reversal often happens by domain growth at a specific location. Examples for this observation are marked in the figure. This behavior corresponds to the magnetization jumps on the LHLs which already indicate the presence of spin-flip avalanches on the investigated length scale during the reversal process. Finally, the last image recorded at -2.7 kOe reveals a small bubble domain, which resists the reversal at the applied field value.

As in the previous section a set of independent magnetic states is recorded at the coercive point. Ten of such independent states are measured in remanence where the AF-coupled sample exhibits a zero net magnetization. In between each domain state the magnetic history is erased with a magnetic field of 7 kOe. All domain states are recorded at the Co edge with an overall exposure time of 320 s per difference hologram. This series is presented in Fig. 3.26(a) together with the enlarged average image shown in panel (b). For a normalization of each separate domain state to the interval ranging from 0 (black) to 1 (white), the average image exhibits a z-scaling from 0.2 up to 0.9. The average sample magnetization obtained from the sum-images is 0.52 indicating that, indeed, the coercive point of the AF-coupled sample is found close to remanence.

As before the pure magnetic information is extracted from the images in Fig. 3.26 by threshold binarization. An example is given in panels (a) and (b) of Fig. 3.27. The sum of all ten measured, binarized images of the remanent magnetic state is shown in Fig. 3.27(c). This image exhibits a black and white contrast over the full range from zero to one. As comparison, the same statistical analysis is performed as for the 3 mTorr and 6 mTorr samples in the previous section. Square regions with an edge length of 25 pixels such as the one illustrated in Fig. 3.27(d) are chosen randomly from a binarized MFM image of the AF-coupled sample. The overall FOV of the MFM image is $(20 \mu\text{m})^2$, the area

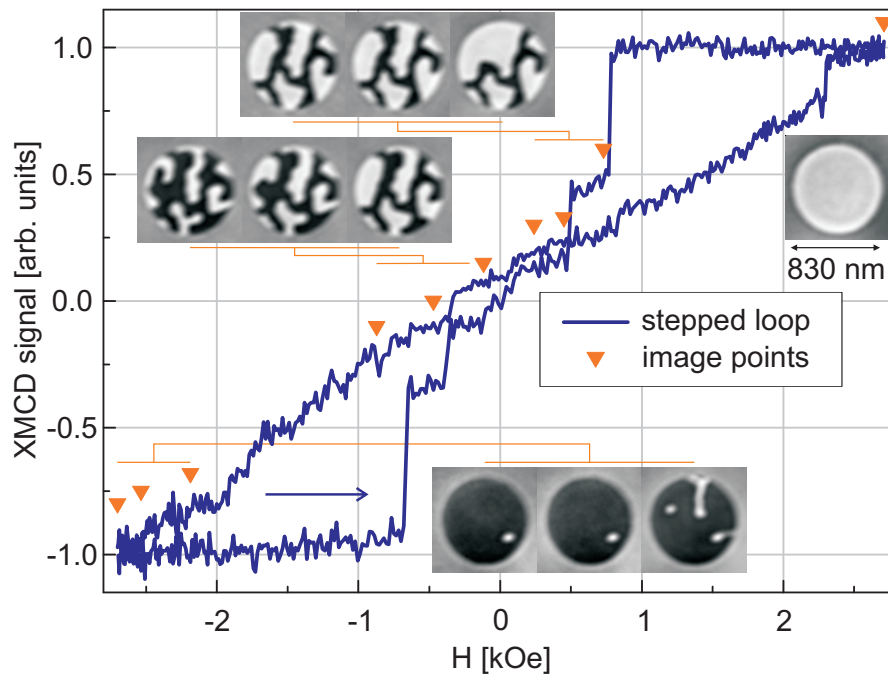


Figure 3.24: XMCD local hysteresis loop at the Co edge on the AF-coupled sample measured in holography setup geometry. Additional FTH images are recorded along the branch starting at 2.7 kOe to image the steplike magnetization inversion.

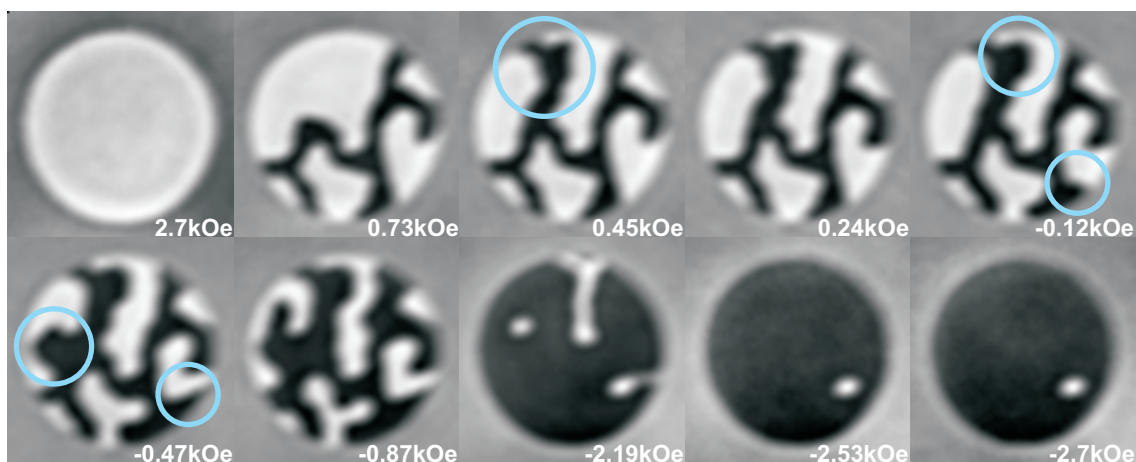


Figure 3.25: Magnified FTH images recorded along the stepped hysteresis loop for the AF-coupled sample. The circles mark prominent domains developing in avalanches.

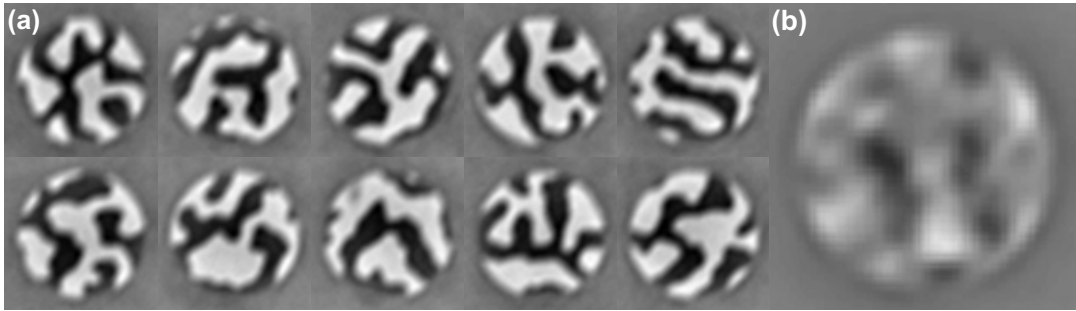


Figure 3.26: (a) Ten remanent domain configurations of the AF-coupled sample after saturation with 7kOe. (b) The z-scale of the average image ranges from 0.2 to 0.9.

chosen for the analysis corresponds to $(0.975 \mu\text{m})^2$. The threshold for the binarization of the MFM image was chosen such that the average magnetization of the MFM image resembles the value of 0.52 determined from the hologram reconstructions in Fig. 3.26. In Fig. 3.27(e) the sum of ten of such randomly chosen states is presented. The contrast in this single-sum image ranges from zero to one as well. This fact indicates already that a number of ten uncorrelated magnetic states is not sufficient to reduce the contrast in their sum-image.

To visualize the contrast development the sum of up to 500 randomly chosen magnetic states is calculated. Hereby, the calculation is repeated 50 times for each data point to obtain the mean value and the standard deviation of the minimum and maximum z-values. The reduction of the contrast is plotted in Fig. 3.27(f). For a high number of independent magnetic states added up the contrast in the resulting image converges towards the average magnetization, here 0.52. The black vertical line marks the value for the sum of ten magnetic states, the corresponding expected extreme z-values are 0.01 and 1.0. That means from the low number of only ten independent states recorded no definite visualization of locations with preferred magnetization orientation can be drawn.

It is reasonable that ten independent magnetic states are not sufficient for clear identification of possible pinning sites. In the previous section the higher numbers 24 and 30 of magnetic states have been found as too low for that purpose. Following the contrast development in Fig. 3.27(f) a number of magnetic states on the order of 100 appears appropriate. For such a high number of magnetic states the expected contrast in the image sum has converged sufficiently towards the average magnetization. As a result, it would be possible to reliably identify locations with a preferred magnetization orientation by z-values that fall significantly out of the envelope determined in Fig. 3.27(f).

In conclusion the combination of magnetometry measurements with x-ray techniques results in a thorough picture of the AF-coupled multilayer sample. The strong demagnetization fields of the Co/Pt stacks generate the typical lateral labyrinth domain pattern. At the same time the introduction of an intermediate antiferromagnetic-coupled Ru(9)/[Co(4)/Ni(10)]₂/Co(4)/Ru(9) stack generates a vertical ferrimagnetic structure.

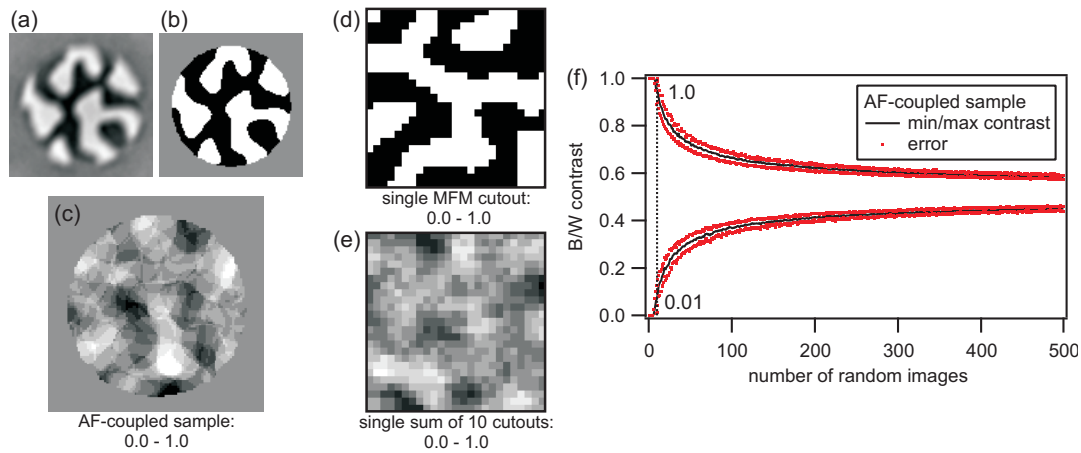


Figure 3.27: (a) Exemplary measured magnetic state, which is binarized in (b). (c) Resulting image sum of ten binary magnetic states. (d) Randomly chosen region of interest from an MFM image and (e) a single sum of ten of such states. (f) Development of the extreme z-values for an image sum consisting of up to 500 separate states chosen from the MFM image.

This coexistence results in a stable ferrimagnetic labyrinth domain pattern in remanence that could be directly imaged. Element-specific hysteresis loops reveal a triple inversion of the intermediate Co/Ni stack during external magnetic field sweeps. Furthermore, local hysteresis loops reveal a steplike behavior, although plain Co/Pd stacks sputtered at the same deposition pressure exhibit smooth LHLs. Therefore, the intermediate AF-coupled stack can be considered to introduce artificial pinning sites that prevent a uniform domain growth. A possible source for the steplike reversal in the investigated system is the conflicting effect of the different intrinsic domain widths for the Co/Ni and Co/Pt stacks in conjunction with the strong AF-coupling. Both conditions cannot be optimized at the same time, which leads to magnetic frustration. Additional future measurements systematically varying the sample's growth parameters are necessary for confirmation. Finally, the LHLs and the imaged domain configurations are irreproducible. It is thus concluded that these introduced defects do not trigger RPM for the investigated sample.

In summary, in this section it was shown that the reduction of the field of view to a size of less than ten domains can reveal additional information on the microscopic reversal behavior of Co/Pd and Co/Pt ML films. The exchange of an area-resolving detector with a photodiode and the positioning of the sample in the beamline focus allow to measure fast local hysteresis loops on layered magnetic systems. A transition from smooth LHLs towards stepped loops with sudden magnetization jumps was observed to be triggered by an increased defect concentration. These steps are interpreted in terms of Barkhausen noise. A similar stepped reversal behavior was found in a similar Co/Pt system but caused by the introduction of an intermediate AF-coupled Co/Ni interlayer even at low deposition

pressure. An interesting difference between the samples featuring stepped loops is that an increase of the defect concentration causes a significant change of macroscopic coercivity and nucleation onset while the AF-coupled interlayer seems to preserve these features. Thus, one gains access to two adjustment parameters which allow to tailor the reversal behavior in Co/Pt and Co/Pd multilayers.

An important next step would be to be able to trigger a reproducible local reversal in such systems. A further increase of the defect concentration was demonstrated to achieve this transition and add RPM. Because of the constant reduction of the bit size in magnetic storage devices reproducible switching on small length scales is important to ensure the stability of the stored information. A proposed route on this path is the introduction of patterned media to generate small and reproducible magnetic bits [Mos02].

3.4 Soft X-ray Rotating Beamstop

Small-angle x-ray scattering patterns exhibit a strong q -dependence proportional to a power law, while typical detectors used today (CCD cameras) are characterized by a limited dynamic range and comparably long readout times on the order of seconds. That is why experimental setups for the measurement of x-ray scattering patterns often feature a beamstop. This device blocks the high-intensity part in the center of the scattering pattern. In this way longer exposures are possible before detector saturation. As a result, the signal in the high- q region, which corresponds to higher resolution, can be collected faster. A beamstop optimized for the collection of x-ray scattering patterns would exhibit a q -dependent absorption profile extending over the whole detector area to compensate for the quick drop of such patterns towards high momentum transfer. Ideally, the absorption profile reproduces the inverse function of the scattering pattern's envelope, such that a recorded scattering pattern exhibits a flat intensity distribution.

In this section the concept of a rotating wire used to generate a q -dependent absorption profile is discussed and demonstrated. For rotation periods faster than the detectors exposure time such a rotating wire generates a smooth absorption profile which decreases with the distance from the center of rotation with r^{-1} . The realization of such a beamstop for soft x-ray experiments requires vacuum compatibility at fast rotation speeds. To prove the feasibility of the concept, a prototype of an electromotor was designed and manufactured, which fulfills the above requirements. Stability disadvantages of a simple rotating wire were identified in a performance test and compensated by the fabrication of a stable beamstop plate featuring a star-like structure. Finally, a Fourier transform hologram was recorded using the beamstop prototype and successfully reconstructed. The analysis of the experimental data shows the expected r^{-1} absorption profile.

3.4.1 Beamstops in X-ray Imaging Experiments

For scattering experiments at a given λ the diffraction-limited resolution increases with the maximum collected scattering angle ϑ or in-plane momentum transfer q (see Sec. 2.1). At

the same time, the radial integration of the diffracted intensity $I(q)$ typically depends on the absolute value q obeying a power law ($I(q) \sim q^{-a}$) [SBT04]. As a result, the strength of the scattering signal quickly decreases for a high momentum transfer and may cover several orders of magnitude for low and high q depending on the experimental setup parameters such as wavelength λ , sample-detector distance L and detector size D . Present soft x-ray charge-coupled device (CCD) detectors are characterized by a limited dynamic range, which is typically on the order of 10^3 – 10^4 analog to digital units (ADUs), and a readout time on the order of seconds. The bright center, the Airy disk, of x-ray scattering patterns generated by apertures such as holographic masks and directly transmitted radiation can easily saturate the x-ray detector and require a readout before reaching saturation. As a result, repeated exposures are necessary for an x-ray diffraction pattern in order to build up a sufficient signal in the high- q region by summation of the intensity patterns. Hereby, the readout time of the detector, which may significantly exceed the exposure time, hinders a quick data acquisition. This problem is common for many types of x-ray scattering experiments like small-angle x-ray scattering (SAXS), coherent diffraction imaging (CDI), and Fourier transform holography (FTH). Here, the situation is described in the context of FTH.

To address the problem a beamstop is often integrated into experimental setups (see Fig. 2.2). The purpose of such a device is to block the bright center of x-ray scattering patterns. Thus, a longer exposure time is possible, less readout cycles are required, and a certain level of signal in the high- q region is built up faster. Several approaches for beamstop implementation do exist. Thin stable wires or bars can be moved into the beam blocking the Airy disk, but at the same time large parts of the diffraction pattern. For scattering experiments that directly analyze the scattered intensity in reciprocal space missing data can often be tolerated. Experiments with the goal to invert the scattering pattern to an image might suffer strongly from missing data. Consequently, one tries to minimize the obstruction of desired scattering outside of the Airy disk. The beamstop used in this thesis for the magnetic-imaging experiments consists of a drop of vacuum-compatible epoxy glue on a 10- μm -thick, gold-coated tungsten wire mounted on a translatable frame. The wire is thinner than one CCD pixel allowing for a successful hologram reconstruction even if the area blocked by the wire remains untreated. For hard x-rays a drop of gold on a translatable x-ray window can be used.

X-ray pulses from free-electron lasers carry sufficient energy to evaporate material. For such experiments the usage of a blocking structure may be impossible. An alternative approach is to selectively transmit only the beam with $q > 0$ towards the detection system. In Ref. [Cha07] the scattering signal is reflected onto a CCD by a multilayer mirror. This mirror features a bore in the center, which is aligned to the center of the scattering and thus transmits the bright central intensity without detection. Alternatively, x-ray detectors consisting of several CCD chips leaving a dead area in the center for the high-intensity part are manufactured.

While the blocking of the central part of scattering patterns is advantageous to save time, the missing data creates artifacts in the image reconstructions because the information on

the blocked spatial frequencies is lost. The loss of this data can be tolerated if these spatial frequencies do not correspond to the actual structure sizes of the investigated sample. This is true for the Airy disk itself, but not necessarily for scattering at higher q . On the other hand, even if no sample information is lost to the beamstop, sharp intensity differences produced by the beamstop shadow result in strong artifacts calculating the Fourier transform, if not treated correctly. A softening of the sharp edge, e.g. by multiplication with a Gaussian smoothed mask of zeros, is often sufficient to suppress strong modulations created by this edge. Alternatively, one can record the blocked Airy disk separately and use this information to fill in the missing data in the high- q hologram.

A different beamstop concept is explored in Ref. [Sch07b]. A radial Gaussian absorption profile is created by Pt deposition of concentric circles on a silicon nitride membrane with the help of a focused ion beam. This device attenuates the bright central scattering instead of totally blocking it. Again the q -dependent absorption ensures that the exposure time of the detector is not limited by a few very bright pixels.

3.4.2 A Rotating Wire as Soft X-ray Beamstop

The concept of a q -dependent beamstop is very promising. The intensity of recorded scattering patterns drops quickly with q and faster data acquisition can be expected from a compensation via an adapted absorption profile. The main idea for the present section is to realize a q -dependent absorption profile with the help of a rotating wire with a rotation period small compared to the detector exposure time. The focus of such a device lies not in preserving the Airy disk information of a scattering pattern as for the approach by Schlotter [Sch07b]. A rotating wire creates a circular blocked area similar to the beamstop approaches discussed in the introduction. It is important to note that if the rotation is fast enough, no support is obscuring parts of the scattering pattern. In addition, the absorption of the remaining diffraction pattern is stronger in the bright, low- q region which allows for longer exposure times.

To derive a formula for the absorption profile of a rotating wire it is sufficient to consider the obscured area at rest. It will be shown later in this section that a simple wire suffers from bending upon fast rotation and directly reflects light onto the detector. Because of this the more stable star-like structure shown in Fig. 3.28 was fabricated for the experiment. Because of this, the geometrical consideration for the derivation of the absorption profile is adapted for this structure. For the derivation an detector ring element with radius r and thickness dr is considered as illustrated in the figure. A simple wire with thickness b blocks an area of $2bdr$ on the considered detector ring approximating the intersections as rectangles. The star-like structure that can be described as intersection of three spokes blocks an area of $3bdr$ on the same detector ring. In general, the area obscured by a structure with k spokes is $kbdr$. At distance r the fraction of the blocked area divided by the detector ring area corresponds to the percentage of absorbed light $A(r)$

$$A(r) = \frac{kbdr}{2\pi r dr} = \frac{kb}{2\pi r}. \quad (3.11)$$

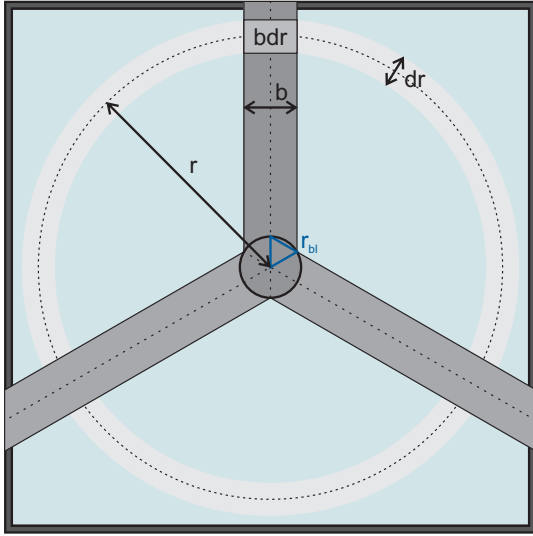


Figure 3.28: Schematic of the beamstop plate for geometrical considerations.

In the present case k equals 3. The corresponding transmission is given by $T(r) = 1 - A(r)$. Eq. 3.11 holds if the absorbing wire structure is set to rotation. For a rotation period much smaller than the CCD exposure time a smooth absorption profile over the complete detector is generated. In that case the intersection of the three spokes define a circular blocked area with zero transmission and radius r_{bl} in the center. The relation between the spoke thickness b and r_{bl} is $r_{bl} = \frac{1}{3}\sqrt{3}b \approx 0.577b$ from geometrical considerations. Thus, the complete absorption profile for a rotating structure with 3 spokes is

$$A(r) = \begin{cases} 1 & : \quad r \leq r_{bl} \\ \frac{3b}{2\pi r} & : \quad r > r_{bl} \end{cases} \quad \text{with} \quad r_{bl} = \frac{1}{3}\sqrt{3}b. \quad (3.12)$$

A prerequisite for Eq. 3.12 is that the center of the structure and the center of rotation are brought to overlap. For a different number of spokes, the formula for the blocked area r_{bl} needs to be adapted. For the case of two spokes, a simple wire, r_{bl} equals b . Here, the absorption profile $A(r)$ was derived dependent on r , which describes the distance to the center of the absorbing structure in real space. That profile is applied to the x-ray holograms described by the in-plane momentum transfer q , which is in principle a measure for the distance from the center of the hologram. To match the dimensions of the beamstop plate to the q resolution of the hologram the following relation can be used:

$$q = \frac{2\pi}{\lambda} \frac{r}{L}. \quad (3.13)$$

Note that this equation only scales the absorbing structure to the pixel size of the detector for a given experimental geometry. That means for the absorption (or transmission) profile

of the beamstop plate $A(q)$ as well as $A(r)$ always describe the same structure in the same space and do not correspond to a pair of functions of conjugated variables connected by a Fourier transform. $A(r)$ is used for general geometrical considerations while the conversion to $A(q)$ will be used in calculations with specific holograms.

To get an idea about the benefit of such a beamstop it is possible to consider the signal of a scattering pattern $S(f,t)$, which builds up collecting photons during an exposure time t for a single frame and a number of frames f . Assuming a constant photon flux the signal is growing linearly with $f \times t$, i.e. collecting 1 frame with 10s exposure is equivalent to collecting 10 frames with 1s exposure each. Furthermore, for deep-cooled CCD detectors used for exposures on the order of seconds the readout noise N of the detector is assumed to be the main noise contribution [PI11]. Since this is a normally-distributed parameter in terms of statistics, it will grow with the square root of the number of integrations f approximately independent of t . In this picture it is possible to write the measured intensity pattern $I(f,t)$ as the sum of the signal $S(f,t)$ and the noise contribution $N(f)$

$$I(f,t) = S(f,t) + N(f) = fS(t) + \sqrt{f}N. \quad (3.14)$$

From Eq. 3.14 it becomes evident that by increasing the number of integrations by a factor of f the signal to noise ratio (SNR) will increase by (only) \sqrt{f} . But the SNR will linearly improve with an increase in the exposure time per frame t , since the detector noise is (mostly) independent on t . It is thus more favorable to increase the total exposure time by extending the time t than to increase the number of integrations f . The rotating beamstop will selectively reduce the photon flux and allow for an extended exposure time per frame as its absorption profile is strongest in the bright central part of the diffraction pattern.

3.4.3 Design of the Rotating Beamstop

Soft x-rays experiments are performed under high or ultra-high vacuum conditions. The main challenge for the design of a rotating beamstop adapted to the soft x-ray regime lies in the compatibility to the experimental vacuum conditions. At the same time the rotary motion provided has to be fast compared to typical CCD detector exposure times, which are on the order of seconds. A target rotation speed of at least 10 Hz constitutes a reasonable goal.

In Fig. 3.29 photographs of the assembled rotating beamstop mounted on a custom DN-100 flange are shown. Two main components can be identified, the motor providing the rotary motion and the beamstop plate.

The motor was designed and fabricated by Günter Schindhelm and Tino Noll at the Helmholtz-Zentrum Berlin für Materialien und Energie GmbH (HZB). It is a brushless electric commutated disk (pancake) motor with a hollow rotor. The rotor and the stator are made of polyether ether ketone (PEEK) for in-vacuum compatibility. Both are connected with a 4-point hybrid rolling-element bearing by Kaydon featuring ceramic balls in a

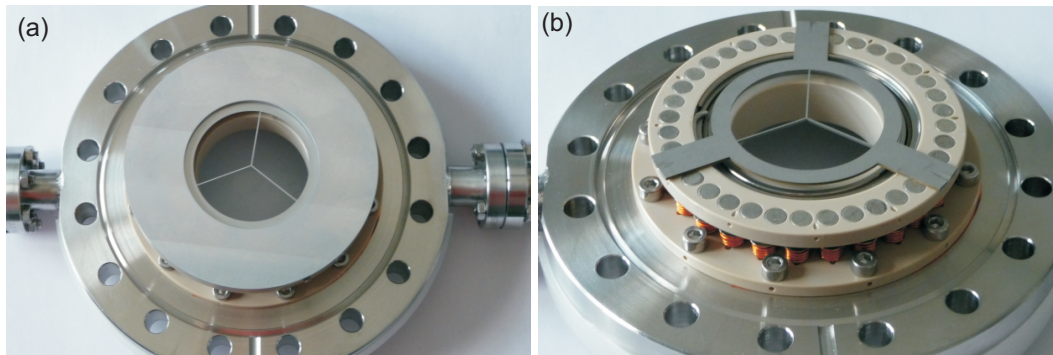


Figure 3.29: (a) Photograph of the rotating beamstop mounted on a custom DN-100 flange. In (b) the steel cap used to fix and align the absorbing structure is removed for visibility.

PEEK cage on stainless-steel races. 36 permanent magnets with alternating pole directions are integrated into the rotor on the circumference of a 76.6-mm-diameter circle. On the same circumference the stator features 27 electromagnetic coils with monolithic iron cores. These coils are cyclically connected to the three phases of the 12 V power supply in groups of nine to generate the driving field for the rotor. The connection is done in a sensorless way, i.e. one phase is used to keep track off the motor position.

During operation, a current of up to 3.6 A at 12 V was applied to the motor resulting in a maximum rotation speed of 5200 rounds per minute (rpm). The motor is controlled with the help of a serial connection over a DSUB-15 port. Percentages of the full power can be set. A copper plate thermally connects the magnet coils to the flange for heat dissipation. A PT-100 temperature sensor is integrated between the copper plate and the flange to keep track of the heat produced, especially under vacuum conditions. Fig. 3.30 shows example temperature curves measured with the beamstop rotating at different speeds at ambient pressure and under vacuum conditions.

In air, the motor can be safely operated with the full power of 3.6 A at 12 V applied exhibiting a temperature of about 50 °C. At full speed the motor rotates with an average value of 5000 rpm fluctuating with up to 200 rpm. Under high-vacuum conditions the temperature rises quickly towards 70 °C for full-speed operation due to the reduced heat dissipation. This temperature is regarded as the upper limit for the operation, i.e. full power should be avoided under vacuum for extended time periods. At 20 % the rotation of the motor is 2000 rpm (0.76 A) which corresponds to a frequency of 33 Hz. This speed is sufficiently fast to perform multiple rotations during x-ray CCD detector exposure times, which are typically larger than 1 s. In addition, at 20 % power, the operation temperature stabilizes at 45 °C. Thus, this mode of operation is used for the experiment.

It should be noted that, while all parts of the beamstop are chosen to be compatible with ultra-high vacuum (UHV, 1×10^{-9} mbar) conditions, during the experiment a slight pressure increase from below 2×10^{-7} mbar to about 3×10^{-7} mbar was observed. This

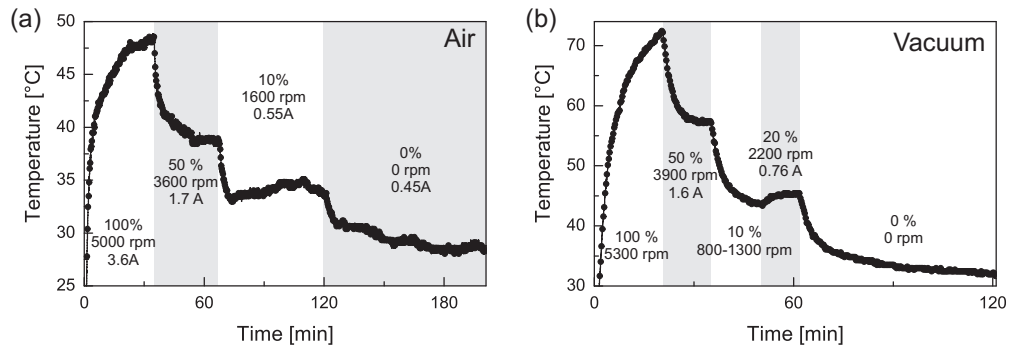


Figure 3.30: Temperature curves for the rotating beamstop operated (a) in air and (b) in high vacuum. The marked intervals indicate certain motor speed values that are given in the panel together with the corresponding rotation speeds and (if recorded) the applied currents.

pressure increase was probably caused by the heating of the Kapton cables due to ohmic resistance and a resulting gas emission from the isolation material. During one week of beamtime the base pressure turned back to its normal value below 2×10^{-7} mbar. Obviously the continuous pumping reduced the gas emission, but UHV-compatibility may not be achieved with the Kapton cables. An exchange with, for instance, diamond-like carbon (DLC) coated copper cables could establish UHV-compatibility. So far the problem was not investigated further since the established pressure, is sufficient for beamline operation with the ALICE experimental chamber.

In order to allow scattering light to pass, the motor is designed with a circular opening of 42.5 mm in the rotor. Different absorbing structures can be mounted using either the mounting holes in the rotor itself or an additional steel cap (visible in Fig. 3.29(a)). Initial experiments were performed with a Tantalum (Ta) wire of 500 μm diameter and a Kapton wire of 1 mm diameter. Both wires are shown mounted on the rotating beamstop at rest in panel (a) and (c) of Fig. 3.31, respectively. The x-ray holograms are generated at the Co-L_3 edge by the magnetic 3 mTorr sample from Sec. 3.3, which serves here as a test sample. Starting the rotation of the beamstop reveals the following problems. In panel (b) of Fig. 3.31 a hologram is shown recorded with 4.5 s exposure time and the Ta wire rotating at a speed of 2800 rpm, i.e. the wire performs about 210 rotations during the hologram recording. First, it becomes evident that the diameter of the circular blocked area corresponds to only 25 % of the Ta wires thicknesses. This fact indicates an imperfect alignment of the wire with respect to the rotational axis and/or a bending of the wire under operation. Second, the round shape of the wire reflects light directly on the CCD detector. Due to the rotation of the Ta wire an isotropic background is created, which totally overwhelms the scattering. Apart from the Airy disk nothing of the hologram is recognizable in Fig. 3.31(b). In addition, some strong reflections can be observed as straight lines in panel (b), which support the hypothesis of irreproducible wire bending.

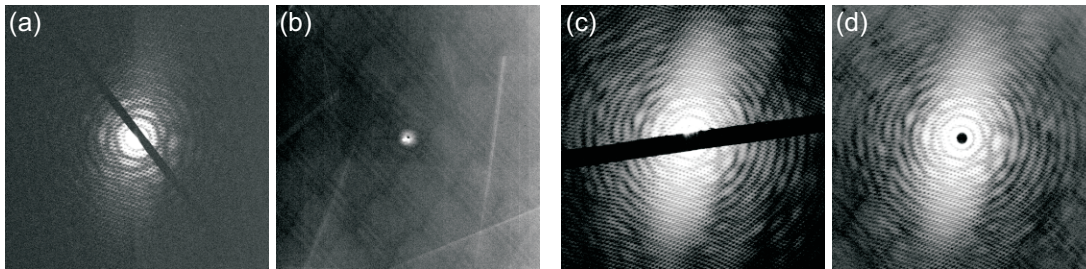


Figure 3.31: Rotating beamstop with a $500\ \mu\text{m}$ Ta wire (a) at rest and (b) rotating and a $1\ \text{mm}$ Kapton wire (c) at rest and (d) rotating. The scattering patterns are recorded at an energy of $781\ \text{eV}$ and at $2800\ \text{rpm}$ speed of beamstop rotation. The exposure times for the panels (a) to (d) are $15\ \text{s}$, $4.5\ \text{s}$, $1000\ \text{s}$ and $3000\ \text{s}$.

In comparison the $1\ \text{mm}$ Kapton wire performs better. The diameter of the blocked area corresponds to 60% of the wires thickness measured on the CCD. That means the wire is more stable and better aligned to the axis of rotation. As a result and because of the thick wire, the direct reflection of x-rays on the detector is strongly reduced. In Fig. 3.31(d) no straight lines of direct reflection are observable and the hologram is clearly recognizable over the isotropic background. Still, an increased background is observed.

As a solution, the already mentioned stable plate with a star-like structure was manufactured by spark eroding out of a 1-mm -thick steel plate. Instead of a wire, it features three spokes of $430\ \mu\text{m}$ thickness with a deviation of $\pm 5\ \mu\text{m}$ separated by 120° to avoid deformation during rotation (Fig. 3.29(b)). In Fig. 3.32(a) and (b) the front and back side of the spokes' intersection region is magnified. The cross-section of the beamstop plate narrows towards the back side to a thickness of $80\ \mu\text{m}$. The narrowing cross-section together with the flat surface facing the x-ray beam minimize directly on the detector reflected light as illustrated in panel (c) of Fig. 3.32.

In panel (d) the calculated absorption profile according to Eq. 3.12 is illustrated. For a spoke thickness b of $430\ \mu\text{m}$ r_{bl} is $248\ \mu\text{m}$. At a distance of $1\ \text{mm}$ from the center of rotation 20% of the scattering patterns intensity is absorbed. In Fig. 3.32(a) it can be observed that the 120° corners exhibit a certain roundness, which results in a blocked area larger than derived. The two yellow circles correspond to radii of $248\ \mu\text{m}$ and $260\ \mu\text{m}$, respectively. The latter value is correct for the manufactured plate. A correction is generated for the absorption profile of the beamstop plate by radial integration of a binarized microscopy image and added to the calculated one in Fig. 3.32 (d). The beamstop plate is held on the rotor by a steel cap, which is fixed and adjusted using three set screws. In this way, the center of the beamstop plate can be adjusted to the rotational axis of the motor.

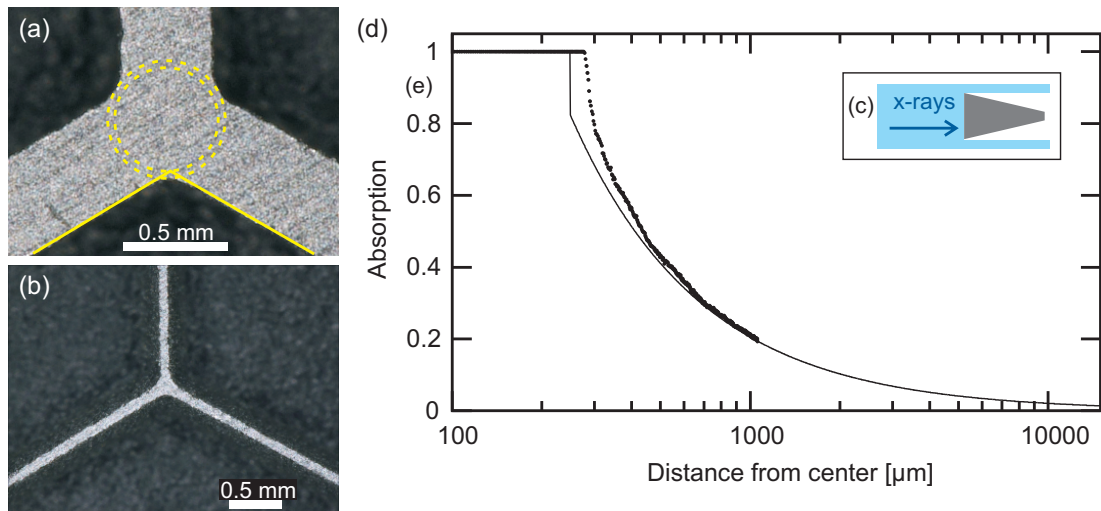


Figure 3.32: (Microscopy images by courtesy of Stephanie Lemke.) (a) Front side and (b) back side of the beamstop plate. (c) The cross-section of the plate narrows towards the back side to avoid reflection on the detector. (d) Calculated absorption profile according to Eq. 3.12 (line) with a correction introduced by manufacturing deviations (solid circles).

3.4.4 Performance of the Device

Fourier transform holography featuring the rotating beamstop is performed at 175 eV (7.1 nm) to demonstrate the expected r^{-1} absorption profile. The sample consists of a diatom skeleton ensemble surrounded by four reference apertures described in Ref. [Gue09] and is located 350 mm behind the focus of the UE52-SGM undulator beamline. The CCD camera is positioned 410 mm downstream of the sample defining a diffraction-limited resolution of 210 nm. The readout time for a full-chip exposure is 4.2 s. The rotating beamstop is located 110 mm in front of the detector.

Fig. 3.33(a) and (b) compare the scattering patterns of the diatom sample with the rotating beamstop operational and at rest. The hologram in Fig. 3.33(a) was recorded by integration of 200 frames with an exposure time of 3 s each and the beamstop rotating at ~ 2000 rpm. For Fig. 3.33(b) the maximum exposure time before detector saturation was set to $1.2 \text{ s} \times 200$ frames. At rest the rotating beamstop works like a wire blocking the bright center of the hologram plus large parts of the desired scattering. As a solution a second hologram is recorded with the same exposure parameters but with the beamstop position shifted by about 60° . For the further discussion and comparison these two holograms with the beamstop at rest are patched together to obtain a complete Fourier transform hologram without the influence of the spokes.

The longer exposure time applicable for the hologram recorded with the operating rotating beamstop already indicates the effect of the radial absorption profile. Considering an identical integrated exposure time of $f \times t = 600 \text{ s}$ the recording of the first hologram

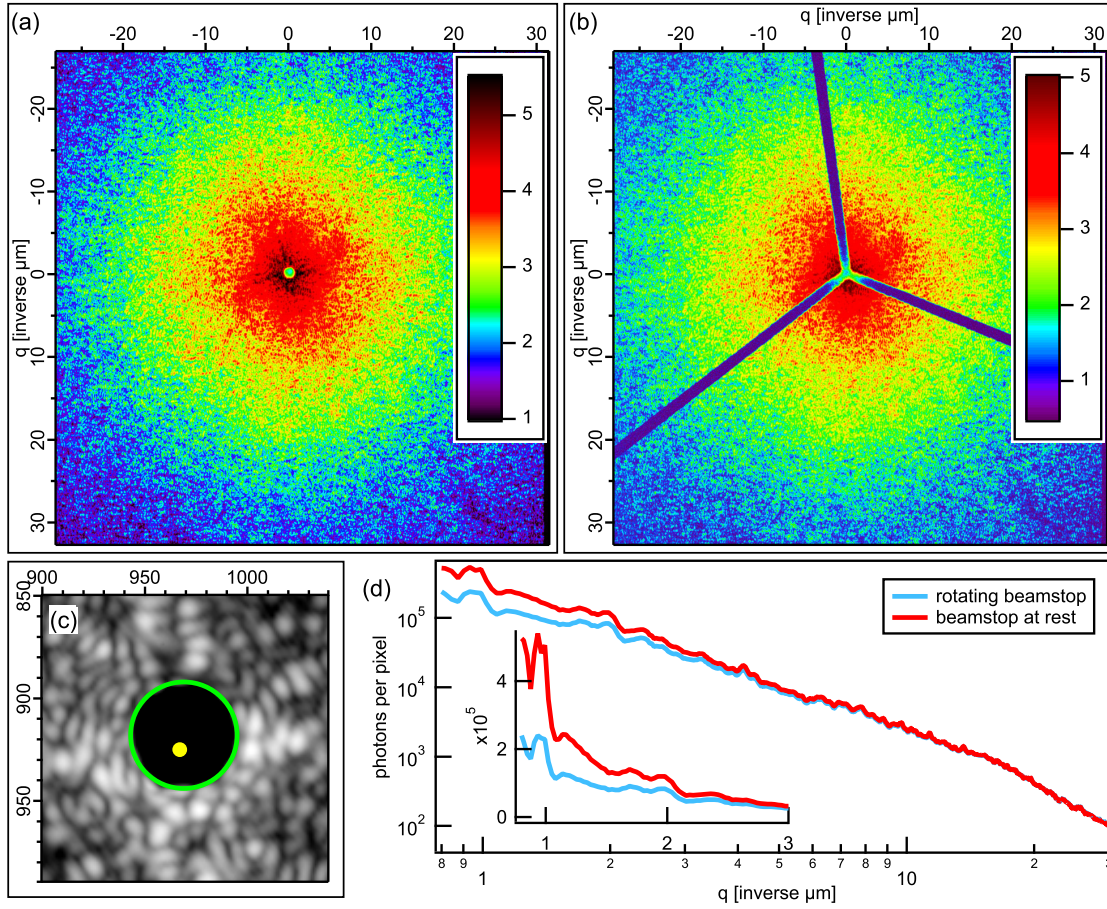


Figure 3.33: X-ray holograms recorded with the beamstop (a) rotating and (b) at rest. (c) The enlarged center region reveals an offset between the center of rotation and $q = 0$. (d) Radial integrations around $q = 0$ on logarithmic scale. The inset emphasizes the high-absorption region for low momentum transfer on a linear scale.

in Fig. 3.33(a) requires $200(3\text{ s} + 4.2\text{ s}) = 1440\text{ s}$ including the CCDs readout time, whereas the recording with the second exposure parameters corresponding to Fig. 3.33(b) would last $500(1.2\text{ s} + 4.2\text{ s}) = 2700\text{ s}$. In other words, the rotating beamstop allows to collect the same amount of photons in the high- q region in almost half the time. Note that at the same time the hologram recorded with the operating rotating beamstop exhibits a reduced level of readout noise as less detector readouts were required.

In Fig. 3.33(b) the thickness of the spokes measured between the center values of the rising and falling flank corresponds to 44 pixels which equals $594\text{ }\mu\text{m}$. The green circle in Fig. 3.33(c) has a diameter of 52 pixels or $702\text{ }\mu\text{m}$. Both values are significantly larger than b and r_{b1} as they were measured directly on the beamstop plate. The reason is that

the absorbing structure is projected onto the detector and consequently appears enlarged. A structure of size b located 300 mm behind the sample, which acts as the scattering source, appears enlarged by a factor of $410 \text{ mm}/300 \text{ mm} \approx 1.367$ on a detector located 410 mm behind the sample. Here, in the small-angle regime, the sine and tangent of the considered angle are identified with the angle. With that correction the measured value of $b = 430 \text{ }\mu\text{m}$ corresponds to $588 \text{ }\mu\text{m}$, which fits the value derived from the hologram within one pixel. For the blocked area of $2r_{\text{bl}} = 560 \text{ }\mu\text{m}$ diameter an obscured area of $765 \text{ }\mu\text{m}$ diameter is expected in the detector plane. The diameter of the green circle in Fig. 3.33(c) of $702 \text{ }\mu\text{m}$ stays below that value, which indicates a slight imperfection in the overlap of the beamstop plate center with the motor's center of rotation C_{rot} .

For further analysis C_{rot} at pixel coordinates (969, 918) needs to be distinguished from the symmetry center of the hologram $q = 0$ at (967, 925). In Fig. 3.33(c) C_{rot} is identified with the middle of the green circle, while $q = 0$ is marked by the yellow dot. Keeping this deviation in mind, radially integrated intensity curves around $q = 0$ for the hologram with rotating and resting beamstop are shown in panel (d) on a logarithmic scale. For comparison, the profile of the patched hologram with the beamstop at rest is multiplied with 1.25 to consider the different exposure time, as well as with 1.056, to correct for the lower monitor signal, which corresponds to the decreasing current in the storage ring. With these corrections the high- q tails of the profiles are well overlapping. In contrast, as seen in the inset of Fig. 3.33(d) the rotating beamstop clearly reduces the central intensity of the scattering pattern as intended.

To correct for the displacement of C_{rot} and $q = 0$, the hologram with the rotating beamstop is divided pixel by pixel by the patched hologram resulting from the two recordings with the beamstop at rest. Hereby the latter is scaled with the same factor of 1.32 compensating for the difference in exposure time and the decreasing storage ring current. The resulting two-dimensional quotient describes the transmission profile of the rotating beamstop and removes any scattering information. This profile is radially integrated around C_{rot} . To consider the absorption instead of the transmission the resulting profile is subtracted from 1. This function is shown in Fig. 3.34. A fit of the data ranging from $q = 1.8 \text{ }\mu\text{m}^{-1}$ to $q = 15 \text{ }\mu\text{m}^{-1}$ yields the following parameters: $A = 0.663 \pm 0.002$, $y_0 = -0.0282 \pm 0.0007$ and $\text{pow} = -1.028 \pm 0.005$ for a fit function of the form: $f(x) = Ax^{\text{pow}} + y_0$. Below $q = 1.8 \text{ }\mu\text{m}^{-1}$ the scattering signal is blocked by the beamstop, especially for the patched hologram with the beamstop at rest. Above $q = 15 \text{ }\mu\text{m}^{-1}$ the noise contained in the holograms starts to influence the fraction.

The values for the errors of the fit parameters are sufficiently small to indicate that the measured function is well approximated by a power function. However, these errors consider only the mathematical approximation of the absorption profile. In Fig. 3.34 the measured transmission profile is compared to two theoretical predictions for a spoke thickness of $b = 430 \text{ }\mu\text{m}$ which is the measured thickness of the beamstop plate and $b = 594 \text{ }\mu\text{m}$ which is the corresponding thickness projected on the CCD. It appears that for lower q the derived curve follows the trend of the $b = 594 \text{ }\mu\text{m}$ graph, but afterwards approaches the x-axis too fast. This becomes evident as well in the fit parameter y_0 ,

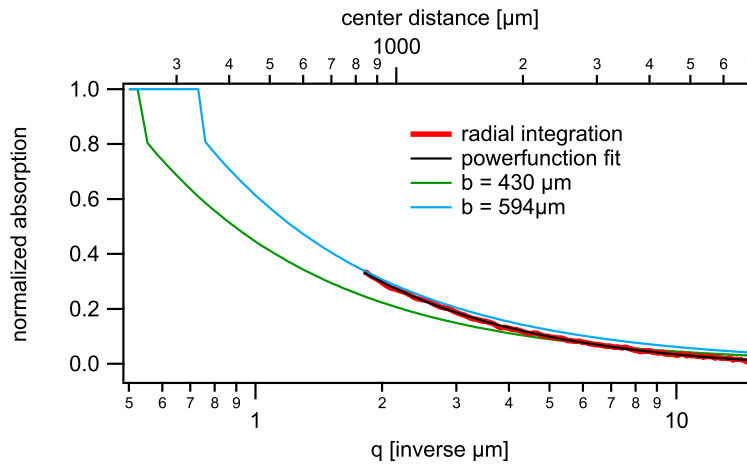


Figure 3.34: Radial integration of the quotient of the holograms shown in Fig. 3.33(a) and the patched version of Fig. 3.33(b). The resulting curve follows a r^{-1} dependency. Calculated absorption profiles for $b = 430 \mu\text{m}$ and $b = 594 \mu\text{m}$ are shown for comparison.

which takes a value below 0. That value falls out of the interval of physical reasonable results. In addition, although a value of -1.028 for the exponent pow approximates the r^{-1} expectation quite well it does not overlap with -1 within its uncertainty interval. Obviously another error needs to be considered.

For the analysis presented above it is necessary to determine the exact background of the diffraction patterns. Unfortunately, for this experiment only general dark images are available for subtraction from the diffraction patterns. A small area of the CCD remained shaded during the experiment and this area was used to improve the adjustment of the holograms base line to zero. However, the dark current remains an unknown for this experiment. Calculating the ratio of two holograms can easily introduce deviations if the dark current is not removed correctly from the diffraction patterns. Thus, the unknown dark current of the detector is held responsible for the deviation of the measured absorption profile from the theoretical prediction. If the dark current is exactly known, the measured absorption profile is expected to match the calculated prediction better. From the analysis so far it can be said that, in principle, the absorption profile of the rotating beamstop can be reproduced if the geometry of the experiment is known. Thus, a correction curve for recorded diffraction pattern can be calculated.

Such a correction is important for the direct analysis (in reciprocal space) of the scattering pattern itself as, for instance, for SAXS experiments. In contrast, the main goal in x-ray FTH is to obtain a real-space image of the sample. The question arises how the modification of the hologram by the rotating beamstop affects the reconstruction of the hologram. The following analysis shows that the effect on the real-space image is negligible, at least for the setup parameters from above. In Sec. 2.3 Eq. 2.17 already illustrated that the hologram $H(\mathbf{q})$ is recorded in the far-field as the magnitude squared

of the Fourier transformation of the sample function $s(\mathbf{r})$ describing the specimen and the references. The reconstruction is performed by an inverse Fourier transform, which yields the autocorrelation (Patterson) map P of the sample function

$$\begin{aligned} H(\mathbf{q}) &= \mathcal{F}^* \{s(\mathbf{r})\} \mathcal{F} \{s(\mathbf{r})\} \\ P &= \mathcal{F}^{-1} \{H(\mathbf{q})\} = s^*(-\mathbf{r}) * s(\mathbf{r}). \end{aligned} \quad (3.15)$$

The rotating beamstop directly affects the hologram in reciprocal space. Its transmission profile $T(q) = 1 - A(q)$ is multiplied to $H(\mathbf{q})$. Similar to the hologram reconstruction itself the multiplication in reciprocal space leads to a convolution of the Fourier transforms in real space

$$\mathcal{F}^{-1} \{T(q)H(\mathbf{q})\} = \mathcal{F}^{-1} \{T(q)\} * \mathcal{F}^{-1} \{H(\mathbf{q})\}. \quad (3.16)$$

The second term corresponds to the original hologram reconstruction yielding the already discussed Patterson map P . This reconstruction is modified by the convolution with the Fourier transform of the rotating beamstop's transmission profile $\mathcal{F}^{-1} \{T(q)\}$. The central part of this term is shown in 3.35(a) on a logarithmic z-scale. The two-dimensional transmission profile was generated for the corrected thickness b of 594 μm (44 pixels) corresponding to the setup geometry. The central pixel dominates the pattern by more than two orders of magnitude. This sharp, rapidly decreasing (i.e. delta-like) peak function of the Fourier transform is caused by the smoothly increasing transmission profile of the beamstop profile. As this function is convolved with the original hologram reconstruction, a minimal effect of the rotating beamstop on the hologram reconstruction is therefore expected. Note that this calculation is not dependent on the energy of the incident radiation but on the beamstop profile only. The calculation is also valid for the reconstruction of magnetic holograms, where the same term is convolved to the reconstruction of a difference hologram obtained from x-rays with opposite circular helicities.

As corroboration hologram reconstructions are compared in Fig. 3.35(b) and (c) generated by the 600-nm-diameter reference of the two holograms recorded with the beamstop rotating and at rest. For the reconstruction the data matrix is centered and zero-padded into a 4096×4096 pixel matrix after dark current subtraction. The two reconstructions shown each consist of 650×650 pixels. The sharp edges at the circumference of the blocked circular area are Gaussian smoothed to avoid strong modulations created by the abrupt intensity change. Since absorption is the dominant contrast for the diatom object, the real part of the reconstruction is shown. An artifact has been removed from both images, which originates from a preferred direction in the used CCD dark images and manifests itself in a localized spot of about 10 pixels with extreme z-values. For that the z-values are adjusted to the surrounding pixels. Afterwards a Gaussian convolution filter is applied to a 16×16 pixels region containing the distortion. Both reconstructions are virtually identical, i.e. although the transmission profile of the rotating beamstop is easily calculable and can be multiplied to the hologram for correction, its effect on the hologram reconstruction is negligible for the setup parameters used here.

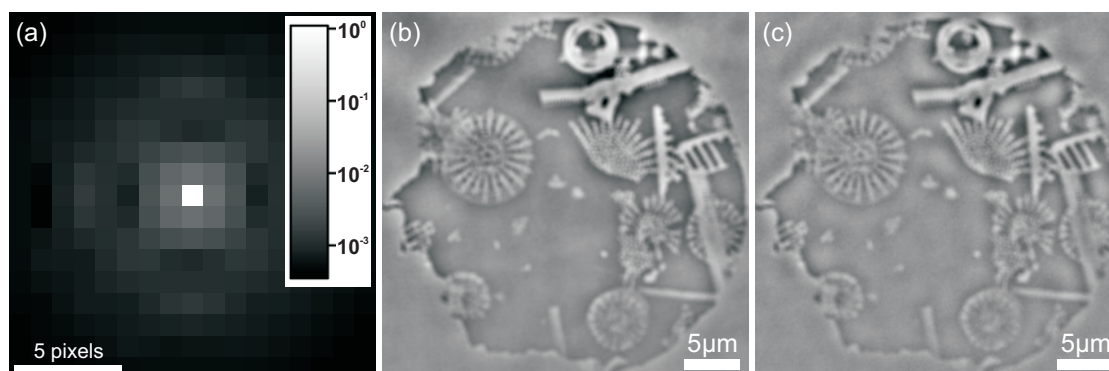


Figure 3.35: Reconstructions: (a) The Fourier transform of the 2D transmission profile generated by the rotating beamstop according to Eq. 3.12 on a logarithmic z -scale. This pattern is convolved to the hologram reconstruction. The central pixel dominates the pattern by two orders of magnitude. As a result, the real part of the reconstructions of the holograms from Fig. 3.33 with the rotating beamstop (b) operational and (c) at rest look close to equal.

In essence the concept, the design and the fabrication for a q -dependent beamstop was illustrated. This device serves for signal-integrating x-ray imaging and scattering experiments based on a rotating wire concept. The main advantage lies in its radial absorption profile, which suppresses the bright low- q region stronger than the desired high- q area and therefore shortens the overall exposure time. Furthermore, due to the movement of the beamstop, no supporting material absorbs scattered radiation. Given that the geometric parameters of the beamstop are known, its absorption profile can be calculated and applied to the x-ray scattering pattern, which is especially important for direct scattering analysis. However, for the application to imaging experiments, the disturbance introduced by the q -dependence of one rotating wire-like beamstop turns out to be negligible for the hologram reconstruction.

3.4.5 Future Improvements of the Rotating Beamstop

This section illustrates the realization of a q -dependent beamstop based on a rotating structure. The rotating beamstop has advantages compared to a standard beamstop setup, but requires an increased instrumentation effort, which needs to be justified. The main goal for such a beamstop strategy is to flatten the recorded diffraction patterns, which are typically following a power law [SBT04]. In this way the scattered intensity is evenly distributed over the detector area and thus the possible exposure time before detector saturation is maximized.

To reach that goal the absorbing structure can be modified. A rotating wire of thickness b defines an absorption profile $A(q)$ which decreases with q^{-1} . However, for the modification of the hologram the transmission profile $T(q) = 1 - A(q)$ needs to be considered, thus

$T(q) \sim 1 - q^{-1}$. Because of the subtraction from 1 the resulting transmission profile is not ideally suited to compensate the envelope of the scattering pattern. To obtain proportionality to a power function it is necessary to directly define the transmission profile of the rotating structure.

The general form of these transmission profiles is illustrated in Fig. 3.36(a) for comparison. All functions are arbitrarily scaled such that a transmission of 1 is approached at a distance $r = 14\text{ mm}$ from the center of rotation, which corresponds to half of the size of the CCD chip used in the experiments. Note again that for the absorption profile r and q describe its dimensions in the same space and are connected by the linear relation from Eq. 3.13. The blue curve illustrates the transmission of a rotating wire, i.e. it corresponds to the presented experiment. As shown in this section this transmission profile successfully reduces the central intensity but increases fast towards unity. The red and green curve correspond to $T(r) \sim r$ and $T(r) \sim r^2$, respectively. Both are better adapted to the intensity envelope of an x-ray hologram.

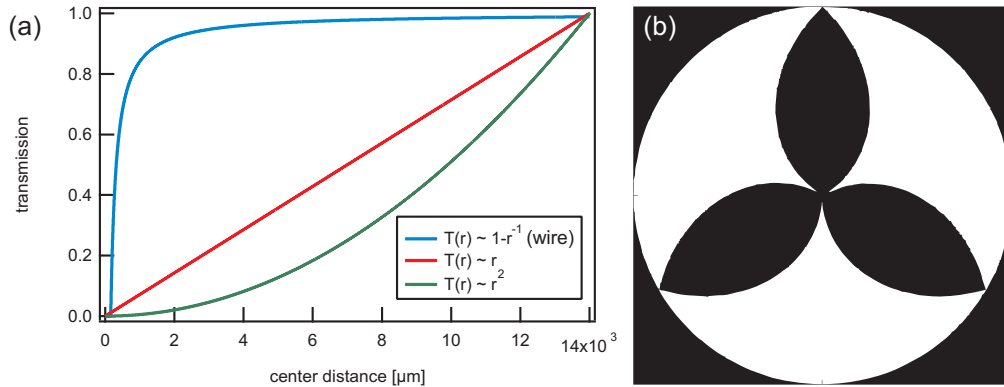


Figure 3.36: (Beamstop plate layout by courtesy of Jan Geilhufe.) (a) Exemplary transmission profiles for a rotating wire (blue), and plates with quadratically (red) and cubically (green) increasing open area. (b) Exemplary layout for a beamstop plate that generates a quadratic transmission profile upon rotation. The white and black regions correspond to transmitted and blocked light, respectively.

Such functions can be directly defined by the opening of a modified beamstop plate. In Fig. 3.36(b) a layout is shown that realizes a quadratic increase of the open area with increasing r . Note that such a beamstop plate generates the linear transmission profile corresponding to the red curve in panel (a) because of the division with the circumference at each r . In principle any function can be generated by the design of a suitable beamstop plate, limited of course by the capability to manufacture the fine details of the structure. Thus, the beamstop function can be adjusted to the scattering of a specific sample, which might exhibit a varying q -dependency.

Another option worth to be followed is to combine several rotating beamstops in serial operation. Given that the rotational axes are on one line the transmission profiles of the

different beamstops multiply

$$T_{\text{tot}}(q) = T_1(q) T_2(q) \dots T_m(q) = \prod_{i=1}^m T_i(q). \quad (3.17)$$

The appeal of such a setup is, that by adjusting the rotational speed of the individual beamstops it is possible to change the overall transmission profile in-situ, which is advantageous for soft x-ray experiments carried out under vacuum conditions. Considering two beamstops equipped with the beamstop plate featuring three spokes shown in Fig. 3.28. If both beamstops are operated at different rotation speed and the resulting beat frequency is still fast compared to the detector exposure time, the transmission profiles multiply according to Eq. 3.17. In the case of identical absorbing structures, one obtains the squared transmission profile of a single beamstop. Now if the beamstops are operated at the same speed, they act like a single beamstop with six spokes. Thus, it is possible to significantly influence the overall transmission profile.

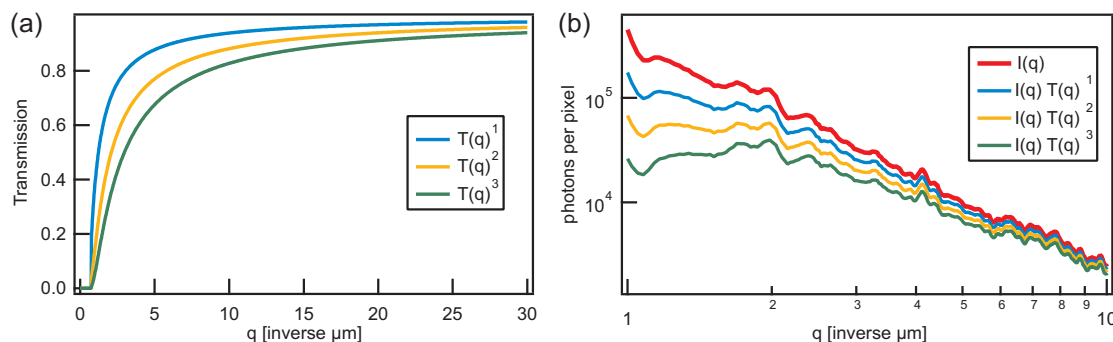


Figure 3.37: (a) The theoretically calculated transmission profile of the rotating beamstop, squared and cubed. (b) The radially integrated hologram of Fig. 3.33 multiplied with the transmission profiles from (a).

This behavior is illustrated based on the calculated transmission profile of the three-spokes beamstop plate with $b = 594 \mu\text{m}$ from Fig. 3.34. Fig. 3.37(a) illustrates the resulting transmission profiles for the case of one, two and three serial rotating beamstops. In panel (b) these transmission profile are multiplied to the radially integrated intensity of the diatom sample taken from Fig. 3.33(d). The resulting intensity distributions are further reduced for low q while the effect on high- q information is minimized, i.e. the scattered intensity is further flattened.

The serial-operation approach is compatible with the beamstop plates directly generating a transmission profile proportional to a power function (Fig. 3.36). For example, the combination of two beamstops with linear and quadratic transmission profile allows to in-situ switch the total transmission profile between powers of two and three. Thus, one obtains an elegant way to adjust the q -dependency of the rotating beamstop. Both possibilities suggested here are subject to further exploration in future x-ray FTH experiments.

4 Ultrafast Sequential X-ray Imaging

The experiments presented in the previous chapter were all performed at undulator beam-lines of a third generation synchrotron source. These sources have been the first x-ray light sources providing sufficient brilliance to extract a significant coherent flux. Consequently, third generation synchrotrons have stimulated experiments based on coherence properties in the x-ray regime such as x-ray photon correlation spectroscopy (XPCS) [Shp07], coherent diffraction imaging (CDI) [Mia99], inline [Ros07; Ros09b] or Fourier transform holography (FTH) [Eis04].

However, synchrotrons compare to an intrinsic coherent light source like a mercury lamp to a laser in the optical regime. Coherence filtering is performed at a high loss of photon flux, making coherence experiments feasible but inefficient. X-ray free-electron lasers (XFELs), the fourth generation of accelerator driven x-ray sources, provide orders of magnitude more photons compressed in pulses of femtosecond duration. With these photons featuring a high degree of transverse coherence, new possibilities are open for coherent x-ray experiments.

This chapter presents an imaging approach that is capable of imaging a specimen twice within an ultrashort time period. A soft x-ray “split-and-delay” unit provides femtosecond x-ray pulses in close succession. After sample interaction the two resulting holograms are superimposed on one detector. Reference multiplexing maps the information about the pulse timing to a spatial information in the hologram. The reconstruction separates the individual images which can be unambiguously assigned to a recording time.

4.1 Motivation — The “Molecular Movie”

Microscopy allows to directly explore the surrounding microcosm. Since the first glimpse into the nanoworld, microscopy techniques have been constantly improved to resolve increasingly smaller structures. As a result, present microscopy techniques have conquered the regime of atomic resolution as, for example, scanning transmission electron microscopy (STEM) or scanning tunneling microscopy (STM) [BDK02; Bin82]. Besides this quest for high resolution another goal exists, to record movies of dynamic processes. For that a sequence of images in fast, snapshot-like illumination is required. In this way, it becomes possible to capture the dynamics of a specimen and gain information about its temporal evolution, e.g. its transition from a certain ground state to another final state.

In the optical regime and on macroscopic length scales such transitions are easily followed by high-speed cameras. For example, in reference [XZN05] a high-speed video camera images the splashing of a drop of liquid on a smooth surface with several thousands of

images per second. Xe et al. found that dependent on the pressure of the surrounding gas, the splashing can be completely suppressed. At the first glance this result is very counterintuitive to everyday experience.

Such experiments underpin the importance of dynamic imaging, which becomes even more important in the nanoworld where dynamics often take place in a counterintuitive manner. Because of the small sizes and distances considered, the dynamics at this length scale may happen on quite a faster time scale compared to the macroscopic world. On the atomic level the time scale set by atomic motion can be on the order of femtoseconds. Some examples for such processes as, for instance, the breaking of chemical bonds are given in the introductions of Refs. [DM10; Dwy06]. In fact, for longer wavelengths like in the optical regime, this ultrafast time regime can be accessed by lasers providing pulses of femtosecond length and below [Buc07; Gou07]. Unfortunately, with decreasing wavelength the intensity of such short pulses decreases quickly, which prevents ultrafast imaging.

That means atomic resolution and ultrashort pulses are separately available by different experimental techniques. The ultimate goal for the study of atomic dynamics can then be considered as the combination of imaging with atomic resolution in femtosecond exposures and this goal has been described as the recording of a “molecular movie”. Significant progress in this direction has been made in recent years by electron diffraction techniques [DM10; Dwy06].

4.1.1 X-ray Free-Electron Lasers

An alternative probe carrying the potential to combine high resolution with ultrashort pulses is constituted by x-rays, which are a complementary probe to electrons with different interaction strength and scattering mechanisms. According to Eq. 3.1 with shorter wavelength it becomes increasingly difficult to operate a coherent source. The absence of reflecting materials for the realization of resonators as well as the incompatibility with optical lenses aggravate the problem.

A technical solution lies in free-electron lasers (FELs) invented and realized in the 1970s [Mad71; Dea77]. As the name suggests in this device the electrons are not confined within a resonator. Instead an FEL is realized with the help of a brilliant electron bunch traveling along an undulator, similar to a third generation synchrotron. In contrast to synchrotrons, the undulator for a free-electron laser tends to be much longer, especially in the x-ray regime. While several FELs are under operation today, only two of them provide (soft) x-ray light, the free-electron laser in Hamburg (FLASH) [Ack07], Germany and the Linac Coherent Light Source (LCLS) [Emm10] in Stanford, USA. The undulator at FLASH consists of three 4.5-m-long segments and generates radiation in the single-nm regime. LCLS reaches down to 1.2 Å featuring an undulator consisting of 33 segments with 3.42 m length each. Two of the undulators for the European XFEL-project in Hamburg, Germany, which is scheduled to be operational in 2014, are designed to be longer than 200 m.

A high-density electron bunch, typically containing a number of electrons N_e higher than 1×10^9 is injected into that undulator. Due to the high charge-density the electrons start

to interact with their own radiation field in the long undulator. Spontaneous emission, present in every undulator, acts as a seed and begins to influence the surrounding electron density. Depending on their phase, electrons within the bunch are either accelerated or decelerated. This process results in an increasing longitudinal modulation of the electron bunch as it is propagating along the undulator length, the so-called microbunching occurs. The increased ordering of the electrons causes their spontaneous radiation emitted to be more in phase, which results in a further increased electron modulation again. This feedback loop is called spontaneous amplification by stimulated emission (SASE).

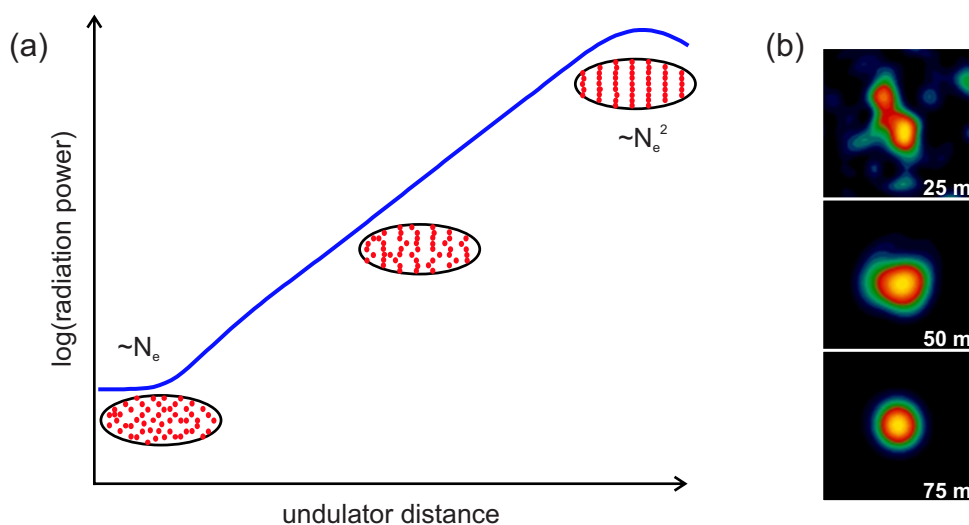


Figure 4.1: (Reproduced from Ref. [HK07].) (a) Electron-microbunching in an XFEL undulator. Due to the longitudinal ordering the electrons radiate in phase, which results in an increase of the radiation power by a factor of N_e upon saturation. (b) GENESIS simulation of the angular LCLS radiation profile at given positions along the undulator. Each image illustrates the angular distribution from ± 0.004 mrad in both dimensions.

Fig. 4.1(a) illustrates the microbunching within an XFEL undulator. Note that the number of microbunches created by SASE is typically on the order of several thousand. Due to their increased longitudinal ordering, traveling along the undulator, the electrons radiate more and more in phase. Consequently, the generated electromagnetic field is more coherently amplified and the radiation power grows exponentially with the propagated undulator distance. Upon saturation the radiation power is proportional to the number of electrons squared instead the number of electrons as for synchrotron undulator radiation. The peak brightness for XFELs is about ten orders of magnitude higher than for third generation synchrotrons.

The SASE process affects the coherence properties of the generated radiation as well. In Fig 4.1(b) a GENESIS simulation [Rei99] of the angular distribution of the LCLS radiation is illustrated at different positions along the undulator. Multiple transverse modes are excited at the beginning. The fundamental mode has its highest intensity on the electron

beam axis, which is in contrast to the competing modes. Thus, the fundamental mode features superior overlap with the electron beam and a faster growth rate. Approaching the saturation regime the fundamental mode usually dominates the others and the FEL beam exhibits almost full transverse coherence (“mode cleaning”) [HK07; SDR08].

In essence x-ray free-electron lasers provide pulses with femtosecond duration and unprecedented peak brightness. With these parameters XFELs are a suitable source for the capture of dynamics on the atomic scale. In addition, the generated light features a very high degree of coherence in the transverse direction, which favors coherence-based experiments as CDI and FTH [Cha06; Bar08; Mar08; Gü11]. Beyond these two fourth generation sources operational, further XFEL-facilities are planned as, for instance, the Spring-8 Compact SASE Source (SCSS) in Japan and the European XFEL in Germany.

4.2 Sample Concept and Setup

Free-electron lasers store huge amounts of energy in single pulses of femtosecond duration. As a tradeoff the time to generate another pulse compares large to synchrotron sources. The repetition rate of FLASH and LCLS is on the order of 100 Hz [Ack07; Emm10]. For the European XFEL a repetition rate of 30 000 Hz¹ is planned. Still, in these cases the repetition rate is not sufficient to resolve ultrafast dynamics. To address this problem “split-and-delay” units have been built, which are capable to cut one ultrashort x-ray pulse in two and apply a femtosecond delay between the resulting two beams [Mit05; Mit08; Ros09a].

With the problem of the generation of highly intense and ultrashort pulses in close succession principally solved, the spatially resolved detection of the scattering pattern remains a problem. Assuming a temporal pulse spacing of 10 fs, the speed of light limits the distance over which the information of the first pulse can be transferred away from the detector to 3 μm before the second pulse arrives. This distance is on the order of the size of a single detector pixel only. A readout of present 2D pixelated detectors required for 2D imaging is thus not possible in between the arrival of the two pulses. Expressed in a photography analogy, there is just not enough time to wind the photographic film to the next frame to get ready for the second exposure.

One possibility is to use two separate detectors for the recording of two pulses within a femtosecond period. This concept necessitates that the two probing x-ray pulses are incident on the sample with an included angle, which allows for an angular separation of the two scattering patterns. In Fig. 4.2 the experimental scenario for CDI or FTH with two separate detectors is sketched schematically. The maximum detected scattering angle in each scattering pattern is ϑ and the associated diffraction-limited resolution

¹ According to the technical design report of the European XFEL [Alt07] the linac will be capable of producing 10 RF pulses per second. Each of these pulses will be 600 μs long and may contain up to 3000 electron bunches with a minimum spacing of 200 ns.

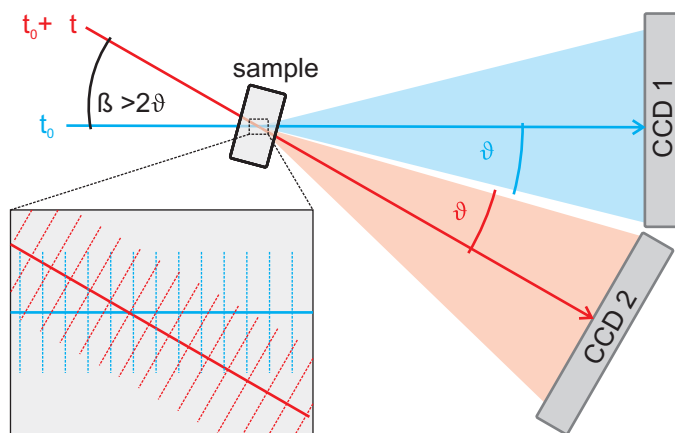


Figure 4.2: Ultrafast imaging using two separate detectors: high resolution necessitates the recording of large scattering angles. Consequently, the recorded images include a spatial and temporal parallax.

$\lambda/\sin \vartheta$. Consequently, an angle of $\beta > 2\vartheta$ has to be included between the beams to avoid overlap and to allow for an angular separation of the two diffraction patterns. High spatial resolution requires the collection of a large scattering angle. For example, at FLASH, which is a soft x-ray FEL featuring a fundamental wavelength in the single-nm regime ($\lambda_{\text{fundamental}} > 5 \text{ nm}$)¹, a scattering angle of $\vartheta = 15^\circ$ at a wavelength λ of 32 nm was collected in Ref. [Cha06]. For this high- q collection the detector has to be brought closely to the sample to a distance of few centimeters.

Even if technically feasible, the inclusion of such a large associated angle β of 30° introduces an undesired spatial and temporal parallax between the two recorded images: propagating through the sample the wavefronts of the two beams include β as well, as illustrated in the inset of Fig. 4.2. The resulting two different projections of the sample recorded, are considered as spatial parallax. In addition, for large angles, the illumination time difference experienced at a certain point within the sample becomes a function of the position of that point within the sample. In other words, due to the included angle β the time delay Δt between the two pulses varies for different sample positions, a temporal parallax is present.

A reduction of the wavelength of the incident light allows to achieve the same momentum-transfer at a smaller angle β . Still, even at a wavelength λ of 1 Å, the ultimate goal of a molecular movie would require a prohibitively high scattering angle ϑ of 30° , as $\sin \vartheta = 0.5$ for 2 Å resolution and would still require an included angle β of 12° for a resolution level of 1 nm.

The detection of two images, generated by subsequent x-ray pulses with intermediate,

¹ Today FLASH reaches 4.12 nm (see <http://flash.desy.de/> retrieved on October, 21th 2011).

femtosecond spacing is non-trivial. Nevertheless, a holographic imaging concept allows to solve this problem. FTH is capable of recording multiple independent images of the same object during a single exposure with the help of multiple references [Sch06]. For sequential x-ray imaging, two holograms generated by consecutive x-ray pulses on the sample are superimposed and recorded on the same detector in one readout cycle. During the hologram reconstruction individual images of the object are disentangled due to the specific holographic geometry. Thereby, the information about the pulse arrival is mapped to a spatial information in the hologram reconstruction.

4.2.1 Concept and Sample Design for Time-resolved X-ray FTH

Fourier transform holography featuring reference multiplexing has been successfully demonstrated with x-rays [Sch06] and is routinely applied in experiments today [Pfa11; Gü10; Pfa10a]. The images found by different reference waves are completely independent, which opens different experimental possibilities. First, if the shape and size of the references is approximately equal, the images can be summed up to increase the signal-to-noise (SNR) ratio in an integrated picture. For this picture the SNR scales with the square root of the number N of individual images ($\text{SNR}_N \sim \sqrt{N}\text{SNR}$) [Sch06]. This simultaneous recording of multiple images is advantageous for specimen sensitive to radiation damage. Second, in a multiplexed imaging experiment references of different sizes can deliver high-intensity, low-resolution and low-intensity, high-resolution images at the same time. In this way these counteracting properties can be tuned to an optimum value.

For sequential x-ray imaging multiple references are used to image an object at different points in time. The idea is to define the illumination functions of two consecutive x-ray pulses such that each one exposes the object, but different references. In the resulting hologram reconstruction each of the individual object images corresponds to the point in time when its reference has been illuminated. Due to the spatial separation of the images during the hologram reconstruction the coherent diffraction patterns can be superimposed on the detector without the need for intermediate readout. Therefore, this concept allows for ultrashort sequential image creation without the introduction of a significant additional spatial or temporal parallax.

In section 2.3 the image formation for one reference has been derived. For sequential x-ray imaging a sample structure is used featuring many references. Therefore, the image formation formalism is generalized for the case of multiple references. In addition, illumination parameters are introduced that consider shaded reference apertures. In accordance with Eq. 2.15 the sample function $s(\mathbf{r})$ with n reference contributions can be written as

$$s(\mathbf{r}) = o(\mathbf{r}) + \sum_{k=1}^n b_k \delta(\mathbf{r} - \mathbf{r}_k). \quad (4.1)$$

Here, a parameter b_k is introduced for each reference aperture defining the illumination, more precisely the magnitude and phase of the exit surface wave, at this point. Throughout

this thesis b_k is considered to take only the binary values 1 or 0, i.e. switch the contribution of a particular reference ‘on’ or ‘off’. Generally, b_k can have any complex value to define stronger or weaker illumination with a certain phase. All values b_k of a multiplexed hologram geometry can be combined in the illumination vector $\mathbf{b} = (b_1 \ b_2 \ \dots \ b_n)$. Similar to section 2.3 the Patterson map P is given by the autocorrelation of $s(\mathbf{r})$

$$\begin{aligned}
P &= s^*(-\mathbf{r}) * s(\mathbf{r}) = o^*(-\mathbf{r}) * o(\mathbf{r}) \\
&+ \sum_{k=1}^n \left(\underbrace{b_k o^*(-\mathbf{r}) * \delta(\mathbf{r} - \mathbf{r}_k)}_{P_k^*} + b_k^* \underbrace{\delta(-\mathbf{r} - \mathbf{r}_k) * o(\mathbf{r})}_{P_k} \right) + \sum_{k,l=1}^n b_{kl} \delta_{kl}(\mathbf{r}) \\
&= o^*(-\mathbf{r}) * o(\mathbf{r}) + \sum_{k=1}^n (b_k P_k^* + b_k^* P_k) + \sum_{k,l=1}^n b_{kl} \delta_{kl}(\mathbf{r}).
\end{aligned} \tag{4.2}$$

Again, the autocorrelation of the object function forms in the center of the Patterson map. As could be expected, n complex conjugated twin-images of the object are obtained forming at the positions $\pm \mathbf{r}_k$, which are designated as (sub)images P_k and P_k^* of the hologram reconstruction. Note the illumination coefficient b_k for each subimage that can suppress its contribution. The n^2 autocorrelation and cross-correlation terms formed between references can be thought of the sum over a reference matrix with elements $\delta_{kl}(\mathbf{r})$. The corresponding illumination matrix with elements b_{kl} is formed by the outer product of the illumination vector with itself, containing all the product combinations:

$$\delta_{kl}(\mathbf{r}) = \delta(-\mathbf{r} - \mathbf{r}_k) * \delta(\mathbf{r} - \mathbf{r}_l) \quad \text{and} \quad b_{kl} = b_k^* b_l. \tag{4.3}$$

The reference autocorrelations all appear in the center of the hologram reconstruction. Reference cross-correlation terms form at the positions $\pm(\mathbf{r}_k - \mathbf{r}_l)$. These positions have to be taken into consideration during the design of the holographic sample arrangement to avoid overlap with the subimages P_k^* and P_k . The illumination parameter products b_{kl} suppress reference cross-correlations if one of the contributing apertures is shaded.

Fig. 4.3 (a) illustrates the multiplexed sample configuration with $n = 12$ references designed for the use in this work. The object $o(\mathbf{r})$ is inspired by the ‘‘Brandenburg Gate’’ (BG) one of the landmarks of the capital of Germany, Berlin. This object is surrounded by twelve references, which are located on the circumferences of four circles in groups of three. The reference apertures are numbered from top-left to bottom-right throughout this chapter. In panel (b) the calculated magnitude of the corresponding Patterson map is illustrated. All twelve subimage pairs reconstruct without overlap with the faintly visible reference cross-correlations. Six of these reference cross-correlations are magnified in the inset in panel (b) generated by the convolution of the reference pairs (4,6), (7,9), (6,8), (10,11), (3,4), (5,7) from left to right. To illustrate the image formation the subimages created by the references at \mathbf{r}_4 and \mathbf{r}_{12} have been highlighted (blue) as well as one of the cross-correlations between the reference apertures located at \mathbf{r}_{10} and \mathbf{r}_{11}

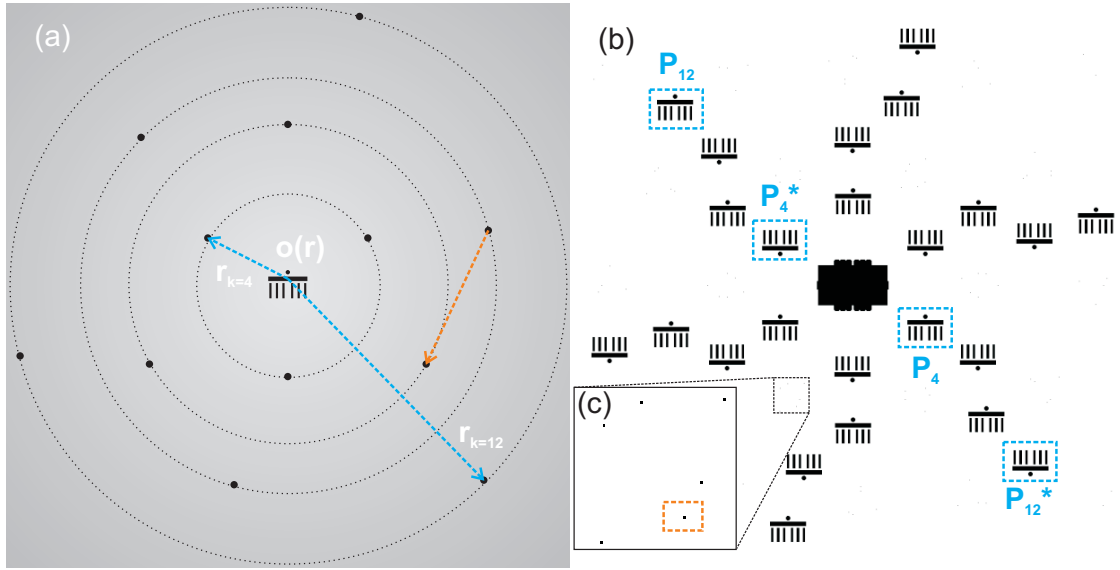


Figure 4.3: Sample layout: (a) The object, an aperture shaped like the Brandenburg Gate (BG), is imaged by twelve references. (b) Autocorrelation of the sample layout. The inset (c) magnifies an autocorrelation region containing the following six reference cross-correlations from left to right: (4,6), (7,9), (6,8), (10,11), (3,4), (5,7).

(orange). In addition, the relative orientation of these participating apertures is marked in the holography sample layout in panel (a). The goal for this sample arrangement is to illuminate the object and different references on its left-hand and the right-hand side with consecutive x-ray pulses.

4.2.2 Experimental Setup at FLASH

The experiment was conducted at beamline BL3 of the free-electron laser in Hamburg (FLASH) facility, Germany [Ack07]. Fig. 4.4 illustrates the setup. FLASH provided unfocused, parallel pulses with a wavelength λ of 23.5 nm (52.7 eV). The pulse duration is estimated to be 30 fs [Mit09] at a repetition rate of 5 Hz. The mean pulse energy was 14 μJ , which corresponds to an average of 1.7×10^{12} photons per pulse. These were transported by BL3 with a transmission of $\sim 70\%$.

A soft x-ray autocorrelator (AC) serves as additional optical element that produces the desired pulse pattern. The schematic layout of the AC is given in Fig. 4.5(a). This device shears off one half of each incident FLASH pulse with the help of a beamsplitting (BS) mirror under an incidence angle of 3° [Mit05; Mit08]. The two created beam halves propagate through different optical paths. These paths are defined by additional water-cooled mirrors fabricated from silicon and featuring a carbon coating. Under an angle of 6° the mirrors exhibit a reflectivity of more than 80% in the range between 40 eV and 200 eV. As a result, the overall transmission of the soft x-ray autocorrelator in this energy

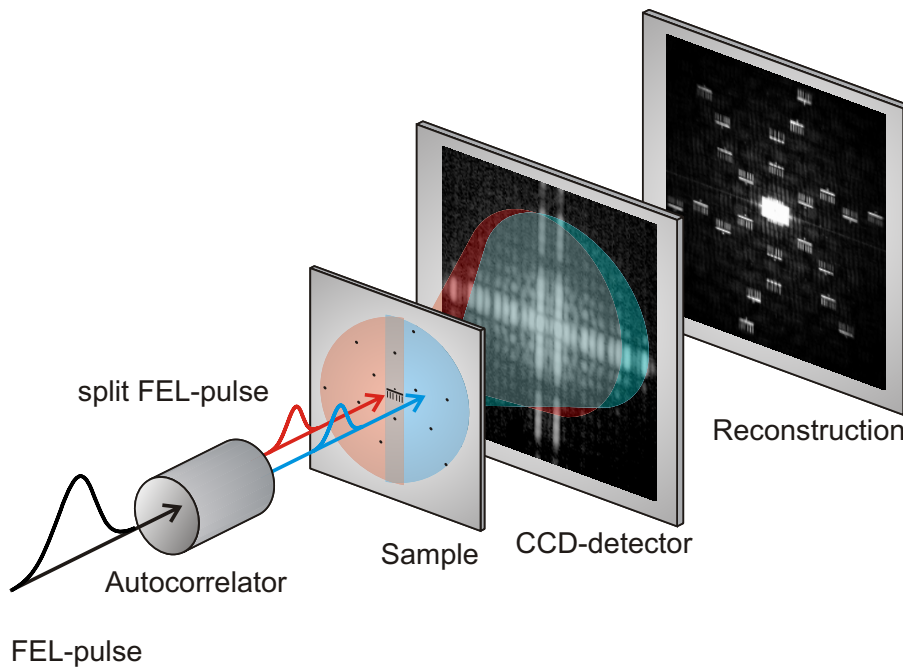


Figure 4.4: The experimental setup at FLASH for sequential x-ray imaging.

regime lies between 40 % and 60 %. The variable branch of the AC features a translation stage that can establish time delays from -3 ps up to 20 ps between the two half-beams. Under stable thermal conditions the step size for the time delay is 0.04 fs [Mit08]. The lateral separation of the split beams at the exit of the AC was adjusted to ~ 1 mm. The

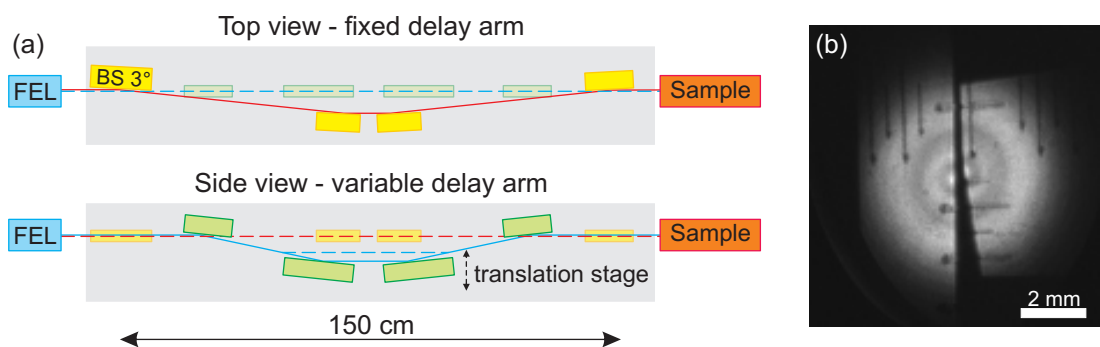


Figure 4.5: (a) Schematic layout of the autocorrelator device illustrating the beamsplitter mirror (BS) and the two optical branches. (b) The split FLASH pulse on a fluorescence screen. The lines visible are markers on the screen for size measurements.

two beams are brought to overlap at the sample, which is located 90 cm downstream of the AC. The resulting opening angle of 0.06° was determined by spatial constraints in the FLASH experimental hall. In future experiments, this parallax can easily be reduced by an increased AC-sample distance. Fig. 4.5(b) shows the split FLASH pulse on a fluorescence screen. Beyond its delay capabilities, the autocorrelator allows to steer the directions of the emerging half-pulses.

The holography sample reproduces the aperture arrangement described in Fig. 4.3 and is fabricated as an aperture structure in a 5- μm -thick NiFe foil. The stylized version of the Brandenburg Gate magnified in Fig. 4.6(a) has a size of $72\ \mu\text{m} \times 50\ \mu\text{m}$. Its smallest features are the six 3.2- μm -wide columns. The object is surrounded by twelve 2.5- μm -diameter references (Fig. 4.6(b)) arranged in groups of three on four circles with radii of 170 μm , 294 μm , 382 μm , and 512 μm . This foil has been patterned via the direct LIGA process¹ [HZBb]. A positive resist (AZ9260) on a silicon substrate is exposed to ultraviolet radiation passing through a chromium photomask manufactured by electron-beam lithography. After the exposure the photo-resist is developed and the voids are electroplated with a NiFe alloy to a thickness of 5 μm . In the last step, the foil is removed from the substrate.

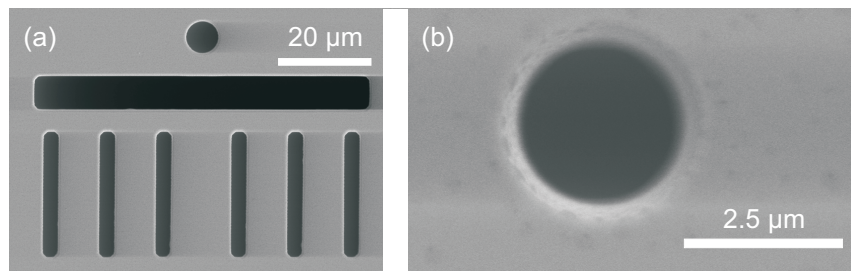


Figure 4.6: Scanning electron microscopy images of (a) the object and (b) an example reference aperture of the sample for the sequential imaging experiment.

The hologram is detected in the far-field, 102 cm downstream of the sample, by a Princeton Instruments PI-MTE in-vacuum charged-coupled device (CCD) camera, which was thermoelectrically cooled to -50°C . The detector features 2048×2048 pixels of $(13.5\ \mu\text{m})^2$ size. At the given photon energy of 52.7 eV the CCD camera exhibits a quantum efficiency of 41 %. The setup parameters define a maximum detectable in-plane momentum transfer q of $3.6\ \mu\text{m}^{-1}$, the corresponding diffraction-limited resolution is 1.7 μm .

¹ german acronym for: *Lithographie, Galvanik, Abformung*

4.3 Results and Discussion

4.3.1 Single-shot Reconstruction

In a first experiment the complete sample structure is illuminated with one of the split half-beams created by the AC, while the second optical branch is blocked i.e. the setup corresponds to a standard FTH geometry.

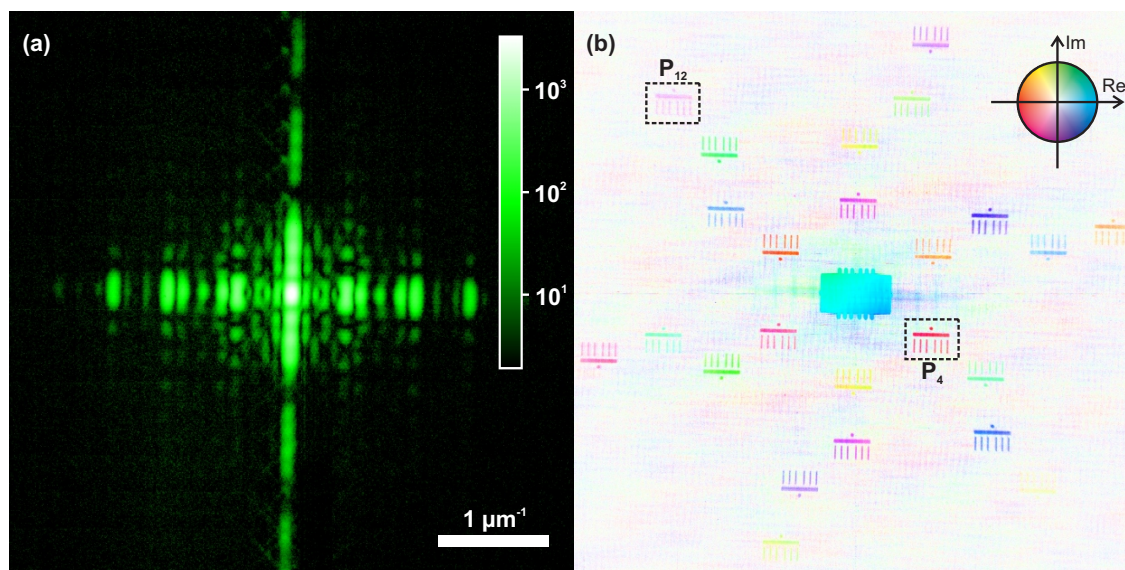


Figure 4.7: (a) The hologram recorded with a single FLASH pulse up to a momentum transfer of $2.5 \mu\text{m}^{-1}$. About 1.3×10^7 photons are contained distributed as given by the logarithmic color scale. (b) The hologram reconstruction with the magnitude encoded in intensity and the phase encoded in hue. The marked subimages corresponding to the references number 4 and 12 are magnified in Fig. 4.8.

The center region up to an in-plane momentum transfer of $2.5 \mu\text{m}^{-1}$ of the resulting hologram is shown in Fig. 4.7(a) on a logarithmic color scale. The complete pattern features scattering information up to $q = 3.6 \mu\text{m}^{-1}$ and contains about 1.3×10^7 photons. The dominant features are the stripes along the vertical and horizontal directions caused by the straight features of the BG-sample along the Cartesian axes. The exposure time of the CCD was set to 150 ms to ensure the recording of single pulses only, which were supplied with 200 ms spacing. A beamstop protecting the CCD camera could be omitted without saturating single pixels.

Fig. 4.7(b) shows the corresponding complex-valued hologram reconstruction with the magnitude encoded in saturation and the phase encoded in hue. In this reconstruction all twelve twin-image pairs of the object are clearly visible and the overall Patterson map looks equal to the simulation in Fig. 4.3. Note that in FTH the phase relative to a certain reference aperture is recorded. That means, subimages created by references with equal

distance to the object, i.e. located on the same circles, are supposed to show similar phase values. This behavior is observed with slight deviations that can originate, for instance, from phase variations within the beam or from the sample not being aligned normal to the incident beam.

Fig. 4.8 magnifies the magnitude of the brightest (P_4) and the faintest (P_{12}) subimages as they are marked in Fig. 4.7. For both the Brandenburg Gate object with all features is clearly recognizable. The reference creating the subimage P_{12} is located at the edge of the sample structure where the beam is weaker. As a result, less photons have been transmitted through that aperture and the generated subimage exhibits a reduced signal-to-noise ratio. Still the object is identified.

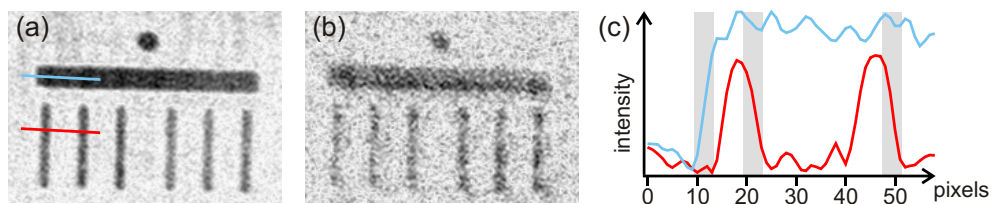


Figure 4.8: Magnifications of the subimages (a) P_4 and (b) P_{12} as marked in Fig. 4.7. (c) Line scans through P_4 along the two lines in (a).

In panel (c) two line scans through the subimage P_4 are plotted along the lines illustrated in panel (a). The gray-shaded areas mark certain rising edges. Each of them is 4 pixels wide, which corresponds to $1.7 \mu\text{m}$ in the hologram reconstruction. That value fits well with the calculated diffraction-limited resolution set by the detector size and the experimental geometry. In reference [Sch07b] the resolution limit set by a circular reference aperture is estimated by convolution with a step function and a value of about 70 % of the reference diameter is found as result. Using this value, the convolution of the BG object with a $2.5\text{-}\mu\text{m}$ -diameter reference aperture yields a resolution of $1.7 \mu\text{m}$ as well. The reference diameter and the maximum momentum transfer recordable in this geometry are thus well matched to each other in the experiment.

4.3.2 Two-beam “Movie”

For the two-image “movie” the autocorrelator cuts each incident FLASH pulse in halves. The relative time delay between the pulses is set arbitrarily to $\Delta t = 50 \text{ fs}$. The two halves of the split FLASH beam are steered onto the sample such that each half-beam illuminates the BG object plus the reference apertures on the left-hand or right-hand side of the object. Note again that this beam alignment can be done with a minimum included angle of 0.06° between the two beams, given by the exit mirror positions in the AC and the distance to the sample. The adjustment is illustrated in panel (a) and (b) in Fig. 4.9. In the first case only the fixed branch of the autocorrelator is used for sample illumination, while for the latter case only the variable arm transmits light. The corresponding holograms are each recorded integrating over 100 FLASH pulses with an exposure time of 150 ms. Since

FLASH was operated with 200 ms pulse spacing this procedure results in an integrated exposure over 75 pulses. The remaining 25 pulses are incident on the closed CCD shutter. The complete holograms in Fig. 4.9(a) and (b) contain 4.9×10^8 and 3.5×10^8 photons, respectively.

The corresponding hologram reconstructions reveal the familiar BG subimages. Not all twelve subimages are present because of the partial illumination of the reference apertures. The positions for visible upside-down subimages of the BG are highlighted in blue for the fixed delay branch and in red for the variable delay branch. The upside-down subimages form at $+\mathbf{r}_k$, that means from their appearance one can directly derive the illumination of the sample. For visualization, a semicircle illustrates the illumination function in the sample arrangement as well as in the hologram reconstructions. References number 4–12 are illuminated for the fixed-branch exposure, whereas for the variable-branch exposure light is transmitted for references number 1–7. Considering a binary illumination that only states a reference as being shaded or transparent the illumination vectors $\mathbf{b}(t_0)$ and $\mathbf{b}(t_1)$ are

$$\mathbf{b}(t_0) = (0\ 0\ 0\ 1\ 1\ 1\ 1\ 1\ 1\ 1\ 1\ 1\ 1) \quad \text{and} \quad \mathbf{b}(t_1) = (1\ 1\ 1\ 1\ 1\ 1\ 1\ 0\ 0\ 0\ 0\ 0). \quad (4.4)$$

Here, the two exposures have been designated with t_0 for the fixed AC-branch marked in blue and $t_1 = t_0 + \Delta t$ for the variable-delay branch marked in red. The time delay Δt is on the order of seconds as different pulses have been used for image generation. For both reconstructions a subimage that can only be found in one reconstruction i.e. that is created by a single-exposed reference, is magnified: P_9 for t_0 and P_3 for t_1 .

Now, for sequential imaging with ultrashort delay the experiment is repeated with both AC-branches set to transmission. Fig. 4.9(c) illustrates the resulting two-beam hologram recorded integrating over the 75 FLASH pulses and containing 9.4×10^8 photons. The center of each hologram can easily be identified by the intense, forward scattered beam. Their lateral separation on the detector chip is 92 pixels (1.242 mm), which corresponds to an offset of $\Delta \mathbf{q} = 0.33 \mu\text{m}^{-1}$ on the momentum-transfer scale. Each hologram encodes spatial information on the sample up to the rim of the CCD camera, which corresponds to a momentum transfer of $q = 3.6 \mu\text{m}^{-1}$, i.e. the two hologram are entirely overlapping.

In the reconstruction the appearance of all twelve BG twin-images is observed. Since the illumination functions are known for the two half-beams, it is possible to unambiguously assign each of the BG subimages to one or the other of the incident half-pulses. The situation becomes obvious when examining the holograms and their reconstructions with one AC-branch blocked from panel (a) and (b) again. Note, that these additional images are helpful for the assignment of the subimages in the two-beam reconstruction, but are not required for the hologram reconstruction itself. This fact is very important for destructive and therefore non-repetitive single-shot imaging.

In Fig. 4.9(c) all subimages of the BG-sample look similar. The setup parameters for the experiment — a wavelength λ of 23.5 nm and a sample-CCD distance of ~ 1 m resulting in $1.7 \mu\text{m}$ diffraction-limited resolution plus the unfocused beam of 5 mm diameter

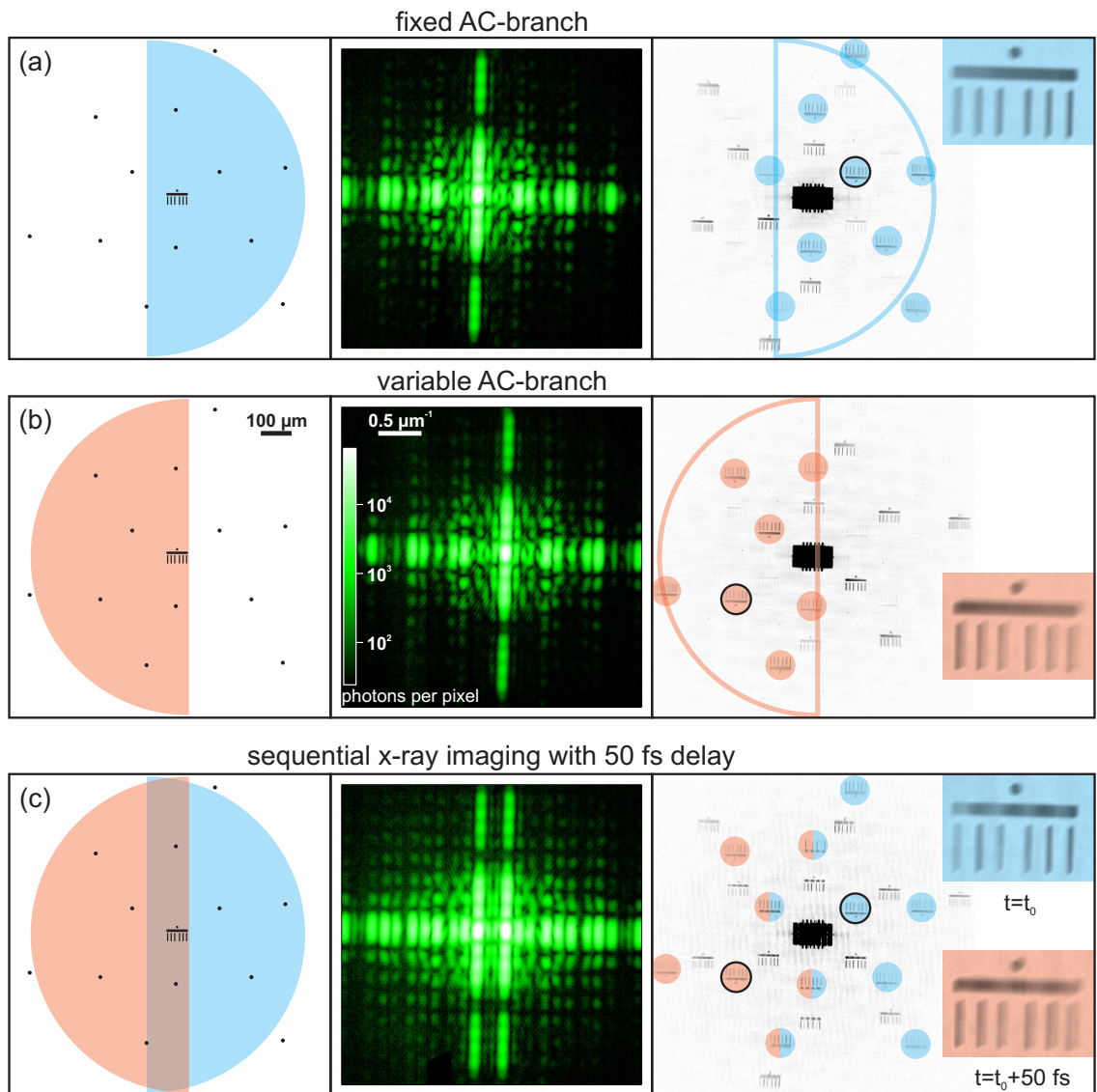


Figure 4.9: Two-image “movie”: Each panel shows from left to right the schematic illumination function, the recorded hologram on logarithmic color scale and the magnitude of the resulting hologram reconstruction. In panel (a) the variable branch of the autocorrelator is blocked and the fixed branch transmits light whereas in panel (b) the situation is vice versa. Since both branches only partially illuminate the reference apertures, different BG subimages are observed in the reconstruction. These subimages and the corresponding illumination function are marked in red and blue, respectively. In panel (c) sequential x-ray imaging is presented: both optical branches transmit light with an adjusted time delay of 50 fs. The scattering patterns are superimposed on the detector, but the subimages are disentangled during the hologram reconstruction. The subimages can be assigned to a creating pulse and therefore to a recording time.

— did neither allow for high-resolution nor for destructive dynamic imaging. Therefore, the experiment focuses on ultrafast, sequential imaging with moderate resolution and with a static sample. Nevertheless, in the reconstruction of the two-beam hologram in Fig. 4.9 the images marked in red can be unambiguously assigned as being recorded 50 fs after the images marked in blue. The two magnified subimages P_9 and P_3 constitute an ultrafast two-image “movie” of the object acquired within the same detector exposure. The reconstruction of the single-pulse hologram in Fig. 4.7 demonstrates that one split FLASH pulse is sufficient for successful hologram reconstruction with the experimental parameters used here. In fact, single-pulse holography would result in images with superior quality as discussed in a later section. Unfortunately, this experiment could not be carried out due to beamtime constraints at FLASH.

For now it is important to put on record that the combination of Fourier transform holography featuring sample multiplexing with an XFEL-compatible soft x-ray beamsplitter allows for the recording of two independent images within an ultrafast time delay.

4.3.3 Comparison to Complementary Ultrafast X-ray Techniques

Since the start of operation of the FLASH facility different x-ray imaging approaches have been performed with the goal to access the ultrafast dynamics regime [Bar10]. All of them feature different advantages and limitations which are shortly put into context in this section.

The basic proof for the feasibility of ultrafast x-ray imaging at XFEL sources has been provided by Chapman et al. [Cha06]. A single FLASH pulse evaporated a nanostructured Si_3N_4 membrane. Still, from the recorded scattering pattern the artificial pattern etched into the membrane could be reconstructed by iterative phase retrieval. This experiment demonstrated that, even if the sample does not survive the strong XFEL radiation, the light-matter interaction takes place on a faster time scale than the adjacent explosion of the sample. Thus, the information about the sample is collected before.

The logical consequence of this experiment is to apply an external pump and use the XFEL pulse to probe the dynamics of the resulting change. This approach was demonstrated by Barty et al. [Bar08]. An optical laser producing the same pulse pattern as FLASH [WKT05] and synchronized better than 1 ps destroyed artificial structures on Si_3N_4 membranes. The resulting explosion was captured by a FLASH pulse and the corresponding images were reconstructed with the help of CDI achieving a spatial resolution of 50 nm. The time resolution of 10 ps was determined by the pulse width of the optical laser.

Pump-probe CDI is capable to capture one image following sample dynamics started by an external trigger. For the creation of a time series this experimental approach relies on identical samples exhibiting repetitive dynamics. That means the technique is well-suited for the observation of triggered, repetitive phenomena. In contrast, the sequential x-ray imaging approach discussed here, collects two images on one identical sample. In addition, the two x-ray pulses in close succession allow to follow untriggered phenomena. Thus,

this complementary experimental approach focuses on the investigation of non-repetitive phenomena like e.g. equilibrium fluctuations.

Another ultrafast imaging approach has been presented by Chapman et al. at FLASH with a version of Newton’s “dusty mirror” experiment [Cha07]. In this experiment an XFEL pulse is incident on single polystyrene particles of 140 nm diameter, triggering their explosion. The light scattered by one particles as well as the directly transmitted light are reflected back to the sample position for a second interaction. A second scattered wave is created by the exploding particle and interferes with the wave created during the first interaction. The “time-delay hologram” contains information on the expansion of the exploding particle on the femtosecond time scale. This approach shares the capability of sequential x-ray imaging to record a time series on one sample and investigate untriggered phenomena. However, it constitutes a difference image of the object without the possibility to generate independent images and is thus complementary to sequential x-ray imaging.

To summarize the chapter so far, the FTH capability of reference multiplexing allows to record two independent time frames on one sample in close succession. The resulting imaging approach can access ultrafast dynamics on the femtosecond time scale. The focus of the technique lies in the investigation of non-repetitive and untriggered dynamics. With these unique selling points sequential femtosecond x-ray imaging finds its application among other ultrafast imaging techniques.

4.4 Details of Image Formation and Artifacts

The hologram reconstruction of the two-beam hologram in Fig. 4.9 exhibits some special properties, which are caused by the superposition of two coherent diffraction patterns. The most prominent feature is the strong horizontal modulation on subimages created by double-exposed references. In Fig. 4.10 this modulation is clearly visible in the magnitude of the subimage P_6 . For a better understanding of the image formation in the two-beam hologram reconstruction the corresponding mathematical equations are derived in this section. A simulation of the observed properties completes the calculation. In addition, the effect of the SASE source on the imaging process is discussed.

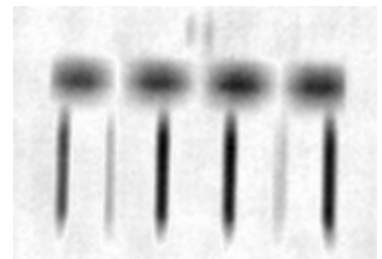


Figure 4.10: Magnification of the subimage generated by the double-exposed reference at r_6 .

4.4.1 Coherent vs. Incoherent Hologram Superposition

The two-beam hologram is a superposition of two holograms separated in time by the delay Δt and shifted in \mathbf{q} -space by $\Delta \mathbf{q}$. For each of those holograms different references are illuminated to generate different subimages, which correspond to different recording times in the experiment. That means the illumination vector depends on t as different apertures are illuminated at the different times ($\mathbf{b} = \mathbf{b}(t)$). The same is true for the object

function ($o(\mathbf{r}) = o_t(\mathbf{r})$) which may exhibit changes during the time interval Δt due to the interaction with the first pulse, an additional external pump pulse or by untriggered equilibrium fluctuations.

It is important to distinguish an incoherent from a coherent superposition. In the first case the intensities of the two holograms are superimposed, while for the latter case the amplitudes of the holograms have to be summed up generating additional interference terms.

First, the incoherent case is considered, i.e. the intermediate time delay Δt is larger than the coherence time τ_c of the FLASH pulse. The resulting Patterson map P_{in} is calculated as the superposition of two intensity patterns obtained at the times t_0 and t_1 . These patterns are recorded on the same detector in one exposure and are separated by a shift in \mathbf{q} -space. Analogous to Eq. 2.17 where the basic image formation for one Fourier transform hologram is illustrated, the sample function $s(\mathbf{r})$ (see Eq. 4.1 for the definition with multiple references) and its correspondent in reciprocal space $S(\mathbf{q})$ are used to calculate P_{in}

$$\begin{aligned} P_{\text{in}} &= \mathcal{F}^{-1} \left\{ |S_{t_0}(\mathbf{q})|^2 + |S_{t_1}(\mathbf{q} - \Delta\mathbf{q})|^2 \right\} \\ &= \mathcal{F}^{-1} \left\{ |S_{t_0}(\mathbf{q})|^2 \right\} + e^{i\Delta\mathbf{q}\mathbf{r}} \mathcal{F}^{-1} \left\{ |S_{t_1}(\mathbf{q})|^2 \right\} \\ &= s_{t_0}^*(-\mathbf{r}) * s_{t_0}(\mathbf{r}) + e^{i\Delta\mathbf{q}\mathbf{r}} [s_{t_1}^*(-\mathbf{r}) * s_{t_1}(\mathbf{r})] . \end{aligned} \quad (4.5)$$

Eq. 4.5 leads to the sum of two autocorrelations of the sample functions corresponding to the times t_0 and t_1 , respectively. One of the two autocorrelations, here t_1 , exhibits an additional phase factor $e^{i\Delta\mathbf{q}\mathbf{r}}$, which results from the fact that only one of the two superimposed holograms can be centered at $q = 0$ for the Fourier transformation. Following the Fourier shift theorem the uncentered reconstruction contribution is multiplied by a phase factor corresponding to the center displacement $\Delta\mathbf{q}$. Note, that this phase factor can be transferred to the other autocorrelation corresponding to t_0 if the Fourier transformation is performed with the hologram part belonging to t_1 in the center. Thus, the mathematical description is symmetric for the two pulses. Eq. 4.5 is expanded further by inserting the expressions for the sample function from Eq. 4.1 to visualize the effect on the subimages $P_k(t)$:

$$\begin{aligned} P_{\text{in}} &= o_{t_0}^*(-\mathbf{r}) * o_{t_0}(\mathbf{r}) + \sum_{k=1}^n [b_k(t_0)P_k^*(t_0) + b_k^*(t_0)P_k(t_0)] + \sum_{k,l=1}^n b_{kl}(t_0)\delta_{kl}(\mathbf{r}) \\ &+ e^{i\Delta\mathbf{q}\mathbf{r}} \left(o_{t_1}^*(-\mathbf{r}) * o_{t_1}(\mathbf{r}) + \sum_{k=1}^n [b_k(t_1)P_k^*(t_1) + b_k^*(t_1)P_k(t_1)] + \sum_{k,l=1}^n b_{kl}(t_1)\delta_{kl}(\mathbf{r}) \right) . \end{aligned} \quad (4.6)$$

The image terms of interest are again designated with $P_k(t)$. The object is reconstructed up to n times for each recording time. Keep in mind that the illumination coefficients $b_k(t)$

may suppress subimages for shaded references. In dependence on the illumination scheme defined by the alignment of the two half-beams one can identify different reconstruction scenarios for the subimages P_k . (i) A reference is illuminated by pulse t_0 only: this reference creates a subimage pair of the object at the recording time t_0 . (ii) A reference is illuminated by pulse t_1 only: this reference creates an image of the object at recording time t_1 . The image is modulated by a phase factor $e^{i\Delta\mathbf{q}\mathbf{r}}$, which results from the displacement $\Delta\mathbf{q}$ between the center of the Fourier transformation and the center of the hologram ($q = 0$). This phase factor will not show up in the magnitude of the reconstruction and can be shifted to the other hologram part by adequate centering. (iii) A reference is illuminated by both pulses: in this special case the object-images corresponding to t_0 and t_1 are superimposed at the same position in the Patterson map. In addition, the superimposed subimages suffer from the phase factor modulation caused by the displacement of the hologram part recorded at t_1 from the center of the Fourier transformation.

Eq. 4.6 describes the general case of an incoherent two-beam hologram superposition. The specific case of the sequential imaging experiment presented in Fig. 4.9 is obtained by inserting the illumination vectors $\mathbf{b}(t_0)$ and $\mathbf{b}(t_1)$ from Eq. 4.4

$$P = o_{t_0}^*(-\mathbf{r}) * o_{t_0}(\mathbf{r}) + \sum_{k=4}^{12} [P_k^*(t_0) + P_k(t_0)] + \sum_{k,l=4}^{12} b_{kl}(t_0)\delta_{kl}(\mathbf{r}) + e^{i\Delta\mathbf{q}\mathbf{r}} \left[o_{t_1}^*(-\mathbf{r}) * o_{t_1}(\mathbf{r}) + \sum_{k=1}^7 [P_k^*(t_1) + P_k(t_1)] + \sum_{k,l=1}^7 b_{kl}(t_1)\delta_{kl}(\mathbf{r}) \right]. \quad (4.7)$$

A closer look at the image terms forming by convolution with the k^{th} reference serves for a better understanding of the image formation in a two-beam hologram. Remember that the k^{th} reference generates two subimages at the positions $\pm\mathbf{r}_k$. Focusing on the upright subimage at $-\mathbf{r}_k$ only and omitting all other terms Eq. 4.6 becomes the following expression:

$$P_{\text{in}} = \dots + b_k(t_0)P_k^*(t_0) + \overline{b_k^*(t_0)P_k(t_0)} + b_k(t_1)e^{i\Delta\mathbf{q}\mathbf{r}}P_k^*(t_1) + \overline{b_k^*(t_1)e^{i\Delta\mathbf{q}\mathbf{r}}P_k(t_1)} + \dots \quad (4.8)$$

As the sample consists of open apertures, absorption is the main contrast mechanism, which allows to focus on the magnitude of the Patterson map. The magnitude squared is obtained by multiplying the Patterson map with its complex conjugate. Since the sample arrangement has been defined such that no overlapping of subimage terms with other correlation terms occurs, the Patterson map consists of undisturbed localized functions. The only overlap is observed in the central part of the Patterson map, where all autocorrelations terms form. This means, calculating the magnitude squared, the subimage term forming at $-\mathbf{r}_k$ yields non-zero terms only for the multiplication with terms forming at the same position in the Patterson map. These are again only the two

terms identified in Eq. 4.8:

$$\begin{aligned}
|P_{\text{in}}|^2 &= \dots + \left[b_k(t_0)P_k^*(t_0) + b_k(t_1)e^{i\Delta\mathbf{q}\mathbf{r}}P_k^*(t_1) \right] \left[b_k(t_0)P_k(t_0) + b_k(t_1)e^{-i\Delta\mathbf{q}\mathbf{r}}P_k(t_1) \right] + \dots \\
&= \dots + b_k(t_0)^2P_k(t_0)^2 + b_k(t_0)b_k(t_1)e^{-i\Delta\mathbf{q}\mathbf{r}}P_k^*(t_0)P_k(t_1) \\
&\quad + b_k(t_1)b_k(t_0)e^{i\Delta\mathbf{q}\mathbf{r}}P_k^*(t_1)P_k(t_0) + b_k(t_1)^2P_k(t_1)^2 + \dots .
\end{aligned} \tag{4.9}$$

Up to four terms contribute to the magnitude of the subimage forming at position $-\mathbf{r}_k$. Beyond the quadratic subimage terms corresponding to the two recording times, two mixed contributions are observed each modulated by $e^{\pm i\Delta\mathbf{q}\mathbf{r}}$. For the case of a single-exposed reference, i.e. either $b_k(t_0)$ or $b_k(t_1)$ is equal to zero, one obtains the quadratic term corresponding to t_0 or t_1 only. This fact is important as it proves that the sequential imaging approach produces correct subimages for single-exposed reference similar to Eq. 2.19. For the case of double-exposed references all four terms do contribute yielding the superposition of the object at both recording times plus the modulation by $e^{i\Delta\mathbf{q}\mathbf{r}}$. That means in general double-exposed references do not generate clear subimages of the object.

In the experiment presented here the sample did not exhibit a change in time. Assuming a static sample ($P_k(t_0) = P_k(t_1) = P_k$), Eq. 4.9 can be further simplified to

$$\begin{aligned}
|P_{\text{in}}|^2 &= \dots + 2(P_k)^2 + (P_k)^2 \left[e^{-i\Delta\mathbf{q}\mathbf{r}} + e^{i\Delta\mathbf{q}\mathbf{r}} \right] + \dots \\
&= \dots + 2(P_k)^2 + (P_k)^2 [2 \cos(\Delta\mathbf{q}\mathbf{r})] + \dots \\
&= \dots + (P_k)^2 [2 + 2 \cos(\Delta\mathbf{q}\mathbf{r})] + \dots .
\end{aligned} \tag{4.10}$$

At this point the magnitude squared is still considered. The square root yields the magnitude of a subimage P_k for a static sample created by a double-exposed reference

$$|P_{\text{in}}| = \dots + P_k \sqrt{2 + 2 \cos(\Delta\mathbf{q}\mathbf{r})} + \dots . \tag{4.11}$$

For this special case of an identical object at both recording times a subimage term P_k is modulated by a square root factor, which oscillates between 0 and 2 depending on the $\cos(\Delta\mathbf{q}\mathbf{r})$ term.

This behavior is visualized in Fig. 4.11(a,b). For this simulation two sample arrangements are generated reproducing the illumination scheme of the two-beam experiment in Fig. 4.9. In addition, a slight change is introduced to the object simulating different states at t_0 and t_1 : the dot above the BG is exchanged with the letters ‘‘R’’ and ‘‘L’’ marking the right-hand and left-hand references as illuminated. This change helps to visualize the different contributions to a certain subimage. For an incoherent two-beam hologram the magnitudes squared of the Fourier transforms of both sample patterns are added with and without a displacement $\Delta\mathbf{q}$ in Fourier space. The corresponding reconstructions, again by the application of a Fourier transform, can be found in the upper row. The single-exposed

reference at \mathbf{r}_{11} and the double-exposed reference at \mathbf{r}_6 have been magnified.

The first thing to put on record is that in accordance with Eq. 4.9 a single-exposed reference generates a clear subimage P_k , that is free from artifacts independent of a present $\Delta\mathbf{q}$ -shift. Second, without a $\Delta\mathbf{q}$ -shift the $\cos(\Delta\mathbf{q}\mathbf{r})$ term in Eq. 4.11 is equal to 1 and the square root reduces to 2. As a result, the superposition of the object at t_0 and t_1 is found at the k th position in the Patterson map. This case is illustrated in panel (a): For the double-exposed references 4–7 the BG subimages appear brighter by a factor of two, except for the sample difference at the marking letters. Third, if the $\Delta\mathbf{q}$ -shift is present, the modulation by the phase factor $e^{i\Delta\mathbf{q}\mathbf{r}}$ is observed in the magnitude of the reconstruction and modulates double-exposed subimages as visible in panel (b).

In Fig. 4.11 a coherent superposition of the diffraction in the two-beam hologram is simulated as well. Such a superposition would be encountered if Δt is chosen such that the two pulses arrive within the longitudinal coherence time ($\Delta t < \tau_c$). For the case of a coherently superimposed two-beam hologram the amplitudes instead of the intensities of the two hologram parts are summed up resulting in

$$\begin{aligned}
P_{\text{coh}} &= \mathcal{F}^{-1} \left\{ |S_{t_0}(\mathbf{q}) + S_{t_1}(\mathbf{q} - \Delta\mathbf{q})|^2 \right\} \\
&= \mathcal{F}^{-1} \left\{ [S_{t_0}(\mathbf{q}) + S_{t_1}(\mathbf{q} - \Delta\mathbf{q})]^* [S_{t_0}(\mathbf{q}) + S_{t_1}(\mathbf{q} - \Delta\mathbf{q})] \right\} \\
&= \mathcal{F}^{-1} \left\{ S_{t_0}^*(\mathbf{q}) + S_{t_1}^*(\mathbf{q} - \Delta\mathbf{q}) \right\} * \mathcal{F}^{-1} \left\{ S_{t_0}(\mathbf{q}) + S_{t_1}(\mathbf{q} - \Delta\mathbf{q}) \right\} \\
&= \left[s_{t_0}^*(-\mathbf{r}) + e^{i\Delta\mathbf{q}\mathbf{r}} s_{t_1}^*(-\mathbf{r}) \right] * \left[s_{t_0}(\mathbf{r}) + e^{i\Delta\mathbf{q}\mathbf{r}} s_{t_1}(\mathbf{r}) \right] \\
&= \underbrace{s_{t_0}^*(-\mathbf{r}) * s_{t_0}(\mathbf{r}) + e^{i\Delta\mathbf{q}\mathbf{r}} s_{t_1}^*(-\mathbf{r}) * e^{i\Delta\mathbf{q}\mathbf{r}} s_{t_1}(\mathbf{r})}_{P_{\text{in}}} \\
&\quad + s_{t_0}^*(-\mathbf{r}) * e^{i\Delta\mathbf{q}\mathbf{r}} s_{t_1}(\mathbf{r}) + e^{i\Delta\mathbf{q}\mathbf{r}} s_{t_1}^*(-\mathbf{r}) * s_{t_0}(\mathbf{r}).
\end{aligned} \tag{4.12}$$

Eq. 4.12 contains the autocorrelations of the sample functions corresponding to t_0 and t_1 as in the derivation for the incoherent superposition. Consequently, one can substitute these terms with P_{in} . In addition, the cross-correlations of the two sample functions are observed. As before Eq. 4.12 is expanded by insertion of the sample function $s(\mathbf{r})$

$$\begin{aligned}
P_{\text{coh}} &= P_{\text{in}} + o_{t_0}^*(-\mathbf{r}) * e^{i\Delta\mathbf{q}\mathbf{r}} o_{t_1}(\mathbf{r}) + e^{i\Delta\mathbf{q}\mathbf{r}} o_{t_1}^*(-\mathbf{r}) * o_{t_0}(\mathbf{r}) \\
&\quad + \sum_{k=1}^n \left[b_k(t_1) e^{i\Delta\mathbf{q}\mathbf{r}_k} P_k^*(t_0) + b_k^*(t_0) e^{i\Delta\mathbf{q}(\mathbf{r}+\mathbf{r}_k)} P_k(t_1) \right] + \sum_{k,l=1}^n b_{kl}(t_0, t_1) \delta'_{kl}(\mathbf{r}) \\
&\quad + \sum_{k=1}^n \left[b_k(t_0) e^{i\Delta\mathbf{q}(\mathbf{r}-\mathbf{r}_k)} P_k^*(t_1) + b_k^*(t_1) e^{-i\Delta\mathbf{q}\mathbf{r}_k} P_k(t_0) \right] + \sum_{k,l=1}^n b_{kl}(t_1, t_0) \delta''_{kl}(\mathbf{r}).
\end{aligned} \tag{4.13}$$

In this equation one finds the mixed coefficients

$$\begin{aligned}
\delta'_{kl}(\mathbf{r}) &= \delta(-\mathbf{r} - \mathbf{r}_k) * e^{i\Delta\mathbf{q}\mathbf{r}} \delta(\mathbf{r} - \mathbf{r}_l) & \text{and} & & b_{kl}(t_0, t_1) &= b_k^*(t_0) b_l(t_1), \\
\delta''_{kl}(\mathbf{r}) &= e^{i\Delta\mathbf{q}\mathbf{r}} \delta(-\mathbf{r} - \mathbf{r}_k) * \delta(\mathbf{r} - \mathbf{r}_l) & \text{and} & & b_{kl}(t_1, t_0) &= b_k^*(t_1) b_l(t_0).
\end{aligned} \tag{4.14}$$

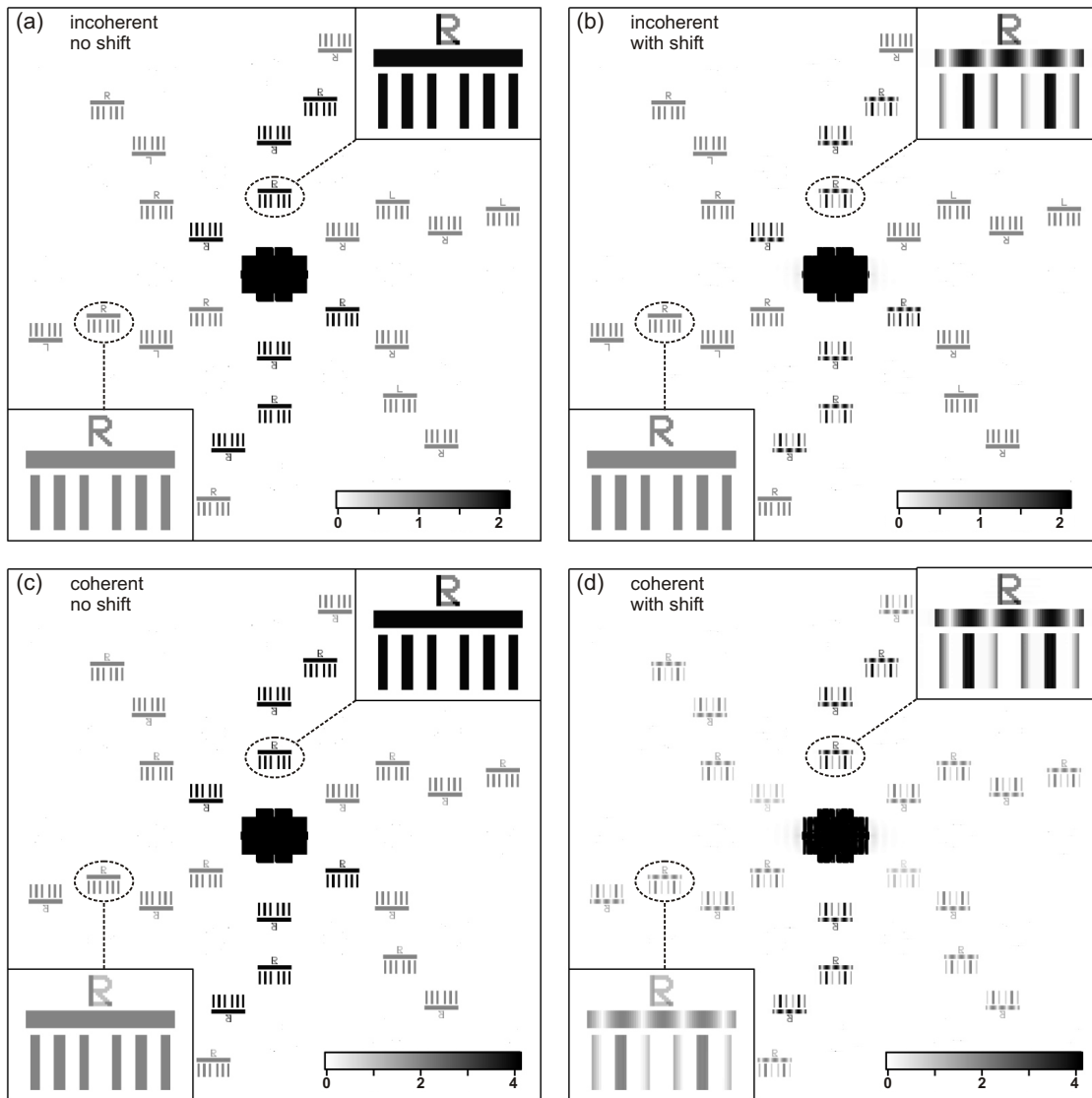


Figure 4.11: Reconstructions of simulated holograms illustrating the incoherent (upper row) and coherent (lower row) superposition of a two-beam hologram. The left reconstructions assume a superposition at the same spot on the detector, whereas the right column includes a shift by $\Delta\mathbf{q}$. In addition, for each reconstruction the single-exposed subimage P_{11} and the double-exposed subimage P_6 are magnified.

In Eq. 4.13 subimages are found corresponding to the object at time t_0 , $P_k(t_0)$, multiplied with illumination coefficients corresponding to recording time t_1 , $b_k(t_1)$, and vice versa due to the cross-correlations of the sample functions $s_{t_0}(\mathbf{r})$ and $s_{t_1}(\mathbf{r})$. These occur in addition to the subimages already described by P_{in} . That means that already every single-exposed reference produces subimages of the object at *both* recording times superimposed at the same location. Furthermore, at least one of these superimposed subimages is not only modulated by a phase factor dependent on $\Delta\mathbf{q}\mathbf{r}$ but also on $\Delta\mathbf{q}\mathbf{r}_k$. This behavior is illustrated in the lower panels (c) and (d) of Fig. 4.11. Note the intensity scale, which is increased up to a value of 4. All subimages reveal the letter “L” and “R” superimposed above the BG, non-regarding the fact whether they are single- or double-exposed. Consequently, all subimages exhibit the horizontal modulation if $\Delta\mathbf{q}$ is non-zero. The additional \mathbf{r}_k -dependence of the modulating phase factors becomes evident in panel (d) for the double-exposed reference at \mathbf{r}_4 . The subimage P_4 appears much fainter.

The main conclusion to put on record is that for a coherent overlap of the sequential holograms no clear subimages are produced in the reconstruction. That means the experimental approach is limited in the sense that the time delay range shorter than the coherence time of the FEL pulse is not accessible without the artifacts derived above. Complementary techniques that apply an external trigger to a specimen as for instance pump-probe coherent diffraction imaging [Bar08] do not suffer from such a directly evident limitation. Since the pulses originate from different sources they can be overlapped at the sample without interference. However, regarding the physical information that can be extracted from the sample, the limiting factor in terms of time resolution is given by the pulse length. This is finally the length of the XFEL pulses for both techniques.

At the same time, the difference in image formation for the coherent and incoherent hologram superposition provides a tool to accurately measure the coherence time of the incident FEL pulses. Once the autocorrelator is aligned, each reference is known to be single- or double illuminated. The significant change of the complete hologram reconstruction, in particular the onset of the horizontal modulation on single-exposed subimages, for a $\Delta t < \tau_c$ clearly marks the coherent regime. The fact that apertures that have been illuminated separately at the different recording times actually do generate cross-correlations provides another indicator. Reference cross-correlations for the references \mathbf{r}_k and \mathbf{r}_l form at the positions $\pm(\mathbf{r}_k - \mathbf{r}_l)$. If the references are illuminated at t_0 and t_1 , respectively, the corresponding cross-correlation can only be observed for a time delay within the coherence time. Since the time delay is known and can be adjusted with the help of the autocorrelator, systematic Δt -dependent scans for the features above are possible. In this way, it is not only possible to tune the sequential-imaging approach to its shortest limit, but also to determine the coherence time of the source. Interference measurements of the direct FLASH beam to directly determine the temporal overlap have been performed at ~ 10 m autocorrelator-detector distance for fringe visibility [Mit08]. In contrast, the holographic approach of sequential x-ray imaging can significantly reduce the required distance. Here, by a factor of ten.

4.4.2 Image Artifacts

In section 4.1.1 self-amplified stimulated emission (SASE) has been described as the intrinsic mechanism of FEL radiation. SASE is a statistical process starting from noise. Fluctuations in the electron bunch randomly produce locations with an increased electron concentration, which act as seed for the microbunching process. As a result, each individual FLASH pulse carries an uncertainty about its energy, its pointing direction and its precise timing. The two-beam hologram and the two holograms recorded with partially blocked autocorrelator shown in Fig. 4.9 have been recorded integrating over 75 FLASH pulses. The determination of the exact pulse timing is not necessarily required in the experiment, since the AC splits each incident pulse with the identical delay Δt . In contrast, the energy jitter and the spatial deviations of the beam introduce artifacts in the hologram reconstruction which are analyzed in detail in this section.

Energy jitter

In Fourier transform holography the light's energy as well as the sample-CCD distance L influence the \mathbf{q} -sampling of the recorded hologram and thus the pixel resolution of the object in the hologram reconstruction. In practice that means at fixed sample-detector distance L , an energy change of the incident light directly transfers to a position shift of the subimages P_k in the hologram reconstruction.

Third generation synchrotron beamlines equipped with monochromators typically do have energy resolutions better than three orders of magnitude [HZBa]. At FLASH the energy width $\Delta\lambda/\lambda$ is $\sim 1\%$ for averaged pulses [Ack07]. This energy uncertainty is responsible for a noticeable displacement of the subimages in the hologram reconstruction. This shift $\Delta\mathbf{r}_k$ corresponds to the direction and the magnitude of the reference-object vector. That means the subimage smears out along the direction of \mathbf{r}_k with $\Delta\mathbf{r}_k = \mathbf{r}_k \cdot \Delta\lambda/\lambda$. This effect is discussed in detail in Ref. [Pfa10a], where it has also been observed to be present in FTH reconstructions from single FLASH pulses. The reason has been found in multiple modes that can be contained within a single SASE pulse [Fru09]. Here, diffraction patterns are recorded integrating over 75 FLASH pulses, which strongly amplifies the smearing.

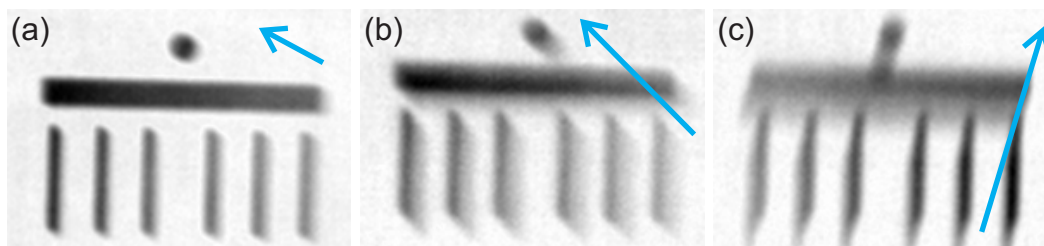


Figure 4.12: Magnifications of the subimages (a) P_4 , (b) P_2 and (c) P_8 from the sequential imaging setup in Fig. 4.9. The images are taken from the setup with one of the optical arms of the AC blocked. The blue arrows indicate the direction and the distance towards the center of the reconstruction.

In Fig. 4.12 three subimages are magnified featuring an increasing distance from the hologram center. P_4 and P_2 are taken from the reconstruction of the integrated exposure recorded through the variable branch of the AC (Fig. 4.9(b)), while P_8 corresponds to the fixed branch (Fig. 4.9(a)). The blue arrows indicate the direction and the distance to the hologram center by their pointing direction and length, respectively. The increase of the subimage displacement with increasing reference-object distance due to the energy jitter in an integrated exposure is clearly apparent.

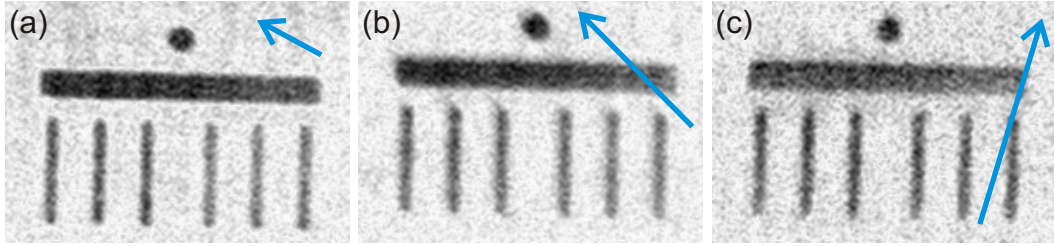


Figure 4.13: The subimages (a) P_4 , (b) P_2 and (c) P_8 from a single-shot hologram reconstruction generated by one FLASH pulse with defined energy do not show the smearing along r_k .

As comparison, in Fig. 4.13 the same subimages are magnified obtained from the single-shot hologram reconstruction from Fig. 4.7. In a single pulse the bunch energy is much better defined and, as a result, all three subimages exhibit a reduced smearing due to a reduced energy uncertainty. Naturally, the single-pulse reconstruction exhibits a lower SNR than the integrated exposure.

Spatial jitter

The FLASH pulses do not only exhibit a spectral distribution, but may also differ in their pointing direction. While for most cases the illuminated spot on the sample is reproducible, for individual pulses the illumination vector may change significantly¹. This change of the illumination function for different pulses affects holograms recorded by integration over several pulses.

In Fig. 4.14 the subimage P_9 is enlarged for all three autocorrelator settings from the two-beam “movie” experiment from Fig. 4.9. Panel (a) and (b) correspond to the scenarios where one of the optical branches of the autocorrelator has been blocked, respectively. This reference is considered single-exposed by the pulse t_0 (blue). Nevertheless, the reconstruction in panel (b) reveals a faint, but clearly recognizable, subimage corresponding to the recording time t_1 . In fact, as fewer pulses did contribute to that subimage the smearing due to the spectral broadening just derived is less pronounced. It seems that

¹ In the following section an example is given how much the illumination for certain FLASH pulses can differ for identically recorded holograms (compare Fig. 4.15(a,b)).

some of the 75 FLASH pulses did illuminate that reference and contribute to the Patterson map for time t_1 . In the context of the mathematical equations that makes subimage P_9 a double-exposed one with a illumination coefficient $b_9(t_1)$ greater than 0 but much smaller than 1. As a consequence, the subimage in Fig. 4.14(c), which illustrates the two-beam “movie” case, exhibits a faint horizontal modulation originating from the $\Delta\mathbf{q}$ -shift.

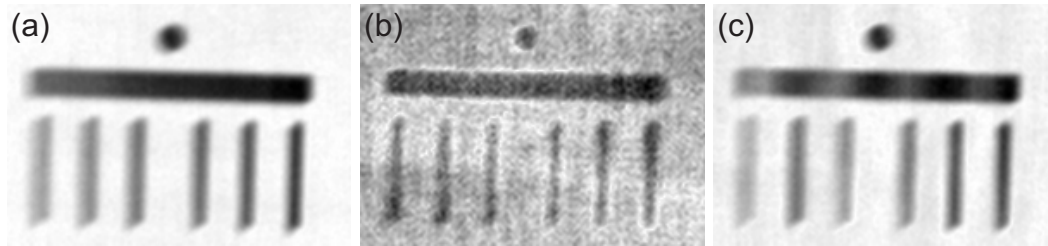


Figure 4.14: Magnification of the subimage P_9 from the sequential imaging setup with (a) the variable and (b) the fixed AC-branch blocked. In (b) the intentionally shaded reference at \mathbf{r}_9 transmits sufficient light for a recognizable subimage. (c) Due to this light leakage the horizontal $\Delta\mathbf{q}$ modulation is faintly visible in the two-beam hologram reconstruction.

Taking a closer look at the subimages from Fig. 4.9 reveals this modulation with varying strength on most subimages. Due to the spatial jitter of the FLASH pulses, in principle, all references have been double-exposed during the two-beam experiment.

Theoretically, there could be another explanation for the observation of the faint horizontal modulation: in the previous section it was derived that a (partially) coherent superposition of the two-beam hologram parts can also generate the $\Delta\mathbf{q}$ -modulation on every subimage, single- or double-exposed. A time delay of 50 fs should exceed the pulse length and thus the coherence time of the FLASH pulse. However, multiple modes have been found to be present in single FLASH pulses, which might prolong these values [Mit08; Ack07; Fru09]. In that case of a partly coherent hologram superposition it would be possible to observe reference cross-correlations corresponding to single-exposed references illuminated at different times. This is not the case, which supports the theory of a incoherent hologram superposition with light leakage through intentionally shaded apertures. However, the location of such coherent reference cross-correlations would be in the high- q region of the Patterson map, where this small signal approaches the noise level.

In essence it is very likely that the faint horizontal modulation in Fig. 4.14(c) originates from the spatial jitter of different FLASH pulses. But since the experiment was performed at a time delay nominally just outside of the estimated 30 fs pulse duration of the unmonochromatized FLASH beam [Mit08; Ack07], a slightly longer pulse duration and thus partly coherent superposition cannot be completely ruled out.

Artificial two-beam hologram

In order to support the equations derived in Sec. 4.4.1 and illustrate the FTH image quality without the artifacts resulting from the integration over FLASH pulses, a two-beam

exposure is simulated on the basis of single-pulse data.

In Fig. 4.15(a) the magnitude of the single-shot hologram reconstruction from Fig. 4.7 recorded with only one AC-branch is shown again. All reference apertures are exposed by the FLASH pulse generating the twelve BG twin-images. Panel (b) illustrates the reconstruction of a single-shot hologram from the same exposure series, but with different sample illumination. Obviously, only the lower half of the sample arrangement was exposed by this particular FLASH pulse. The illumination vector for the second hologram is $\mathbf{b} = (1\ 0\ 1\ 0\ 1\ 0\ 1\ 0\ 0\ 1\ 0\ 1)$. The corresponding hologram contains 5.6×10^6 photons, which is roughly the half of the 1.3×10^7 photons contained in the hologram of the fully illuminated sample generating the reconstruction in panel (a).

The holograms corresponding to these two reconstruction can serve as input data for a simulated two-beam exposure. In Fig. 4.15(c) the sum of the two holograms is calculated. The partially illuminated hologram is shifted by 92 pixels along the horizontal, which fits to the $\Delta\mathbf{q}$ -shift observed in the actual two-beam experiment. Note, that this shift is created artificially to investigate its effects. In reality both holograms are recorded through the same branch of the AC one after the other. That means that no included parallax β or shift $\Delta\mathbf{q}$ is present and that the superposition is totally incoherent.

This calculated two-beam hologram is reconstructed in Fig. 4.15(d). Designating the two holograms as t_0 and t_1 (with a time delay of several seconds in between), Eq. 4.6 can be applied leading to

$$P = \sum_{k=1}^{12} [P_k^*(t_0) + P_k(t_0)] + e^{i\Delta\mathbf{q}\mathbf{r}} \left(\sum_{\substack{k=1,3,5, \\ 7,10,12}} [P_k^*(t_1) + P_k(t_1)] \right) + \dots \quad (4.15)$$

omitting the object's autocorrelation and reference cross-correlation terms for clarity. All subimages that are visible in panel(b) are double-exposed in panel (d) and exhibit the horizontal modulation caused by the artificially applied $\Delta\mathbf{q}$ -shift. Although, both single FLASH pulses feature probably a slightly different energy, the resulting Patterson map appears much sharper and the artifacts originating from the pulse integration did vanish: the smearing along \mathbf{r}_k is missing as well as the horizontal modulation on all subimages due to light leaking through shaded reference apertures. Furthermore, in this reconstruction the fact that double-exposed references generate a brighter subimage is apparent as was derived in Eq. 4.11.

Thus, the reconstruction in Fig. 4.15(d) corresponds to a clear data set recorded by a single split pulse and illustrates in a clearer way the image formation in a reconstructed two-beam hologram that was derived in this chapter. Sequential x-ray imaging generates correct images as in standard FTH if the illumination of the holographic sample is properly controlled.

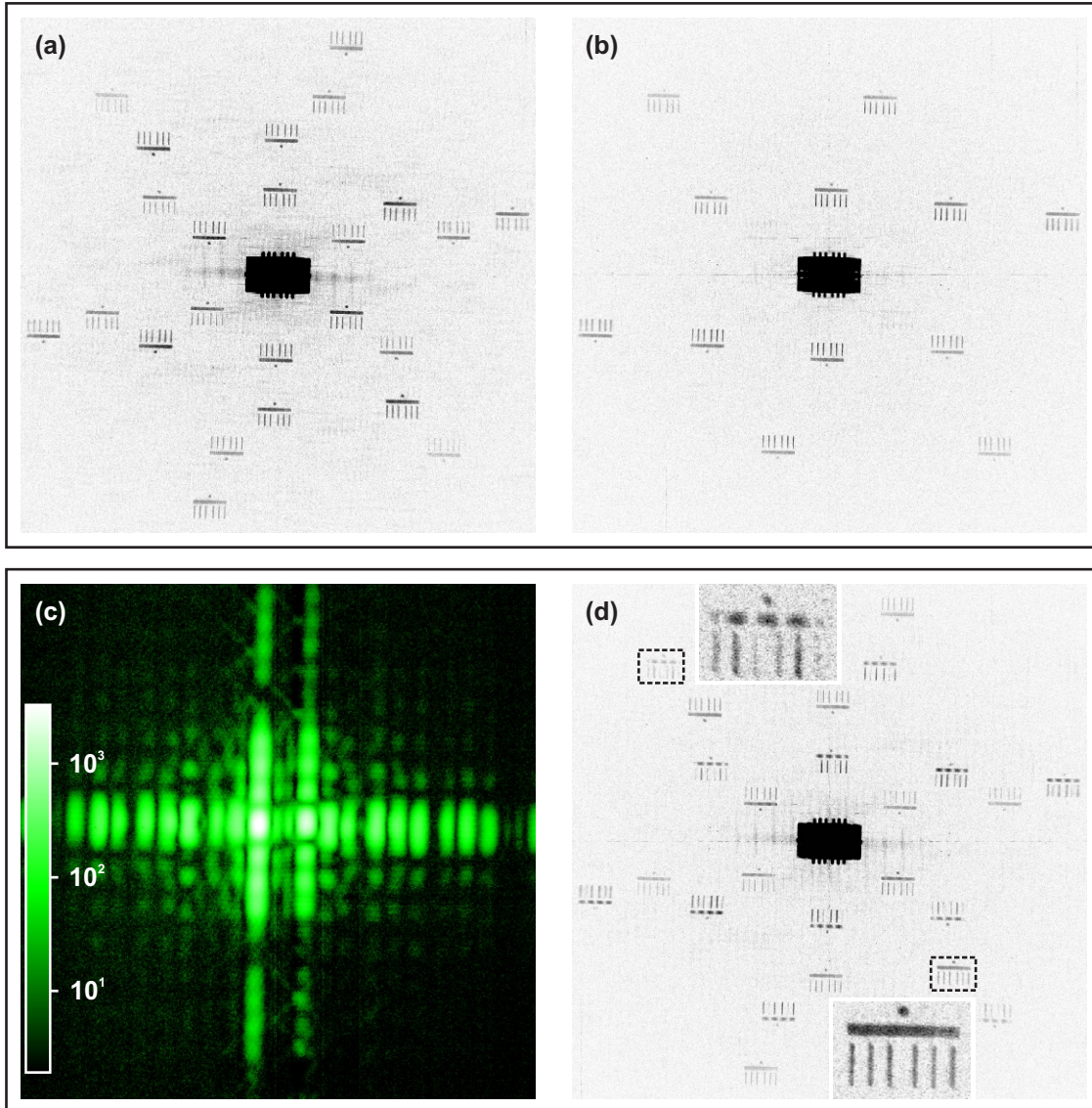


Figure 4.15: (a) Magnitude of the single-shot FTH reconstruction from Fig. 4.7. In (b) only a part of the references is illuminated despite identical sample alignment. (c) The sum of the holograms creating (a) and (b) including an artificial Δq -shift simulates a single-shot two-beam hologram, which is reconstructed in (d). The subimages P_4 and P_{12} are magnified for comparison.

4.5 Future Perspectives

In this section the opportunity is taken to speculate about the development of sequential x-ray imaging. The scaling to high resolution is discussed as well as the recording of multiple time frames. Finally, the topic of a numerical separation of a superimposed diffraction pattern is touched.

4.5.1 Scaling to High Resolution

The standard resolution routinely achieved with Fourier transform holography at synchrotron sources is well below 50 nm [Eis04; Gü10; Pfa11]. Here, ultrafast, sequential x-ray imaging is presented at a moderate resolution of 1.7 μm , dictated by the setup parameters. With x-ray focusing accompanied by equivalent downscaling of the holographic mask it will be straightforward to drive the resolution of sequential x-ray imaging towards the FTH standard of below 50 nm as long as the split beams can be prepared with sufficiently sharp rising edges. However, following the path towards the ultimate goal of a “molecular movie” it is well worth to discuss the scaling possibilities of two-beam holography.

The wavefront-splitting autocorrelator [Mit05; Mit08] constitutes a key device for the presented sequential imaging approach as it allows for the creation of x-ray pulses with a controllable femtosecond time delay and the option for a spatial adjustment of the emerging half-beams. The AC consists of several mirrors for geometrical splitting of the incident light and manipulation of the split pulses. This device performs well in the soft x-ray regime provided by FLASH, where it allows, for example, to observe non-linear effects and accurately determine the pulse length of the source [Mit09]. The first step to increase the potential spatial resolution is to increase the energy of the imaging light. Generally, away from resonances, the reflectivity of x-rays decreases with an increase in energy. For compensation x-ray reflection is performed under small incidence angles. In the AC all incidence angles do not exceed 6° , which makes the device rather large (~ 1.5 m). In order to keep the transmission through the device acceptable for higher x-ray energies, an AC based on the same concept requires further reduced incidence angles. This fact makes the technical realization of a similar high-energy x-ray AC technically challenging as smaller incidence angles cause a further increase of the mirror sizes and thus of the complete device. Nevertheless, a follow-up of the autocorrelator used in the present experiment is planned by the group of Prof. H. Zacharias from the university of Münster and supported by the BMBF under FKZ:05K10PM2¹.

An alternate approach was demonstrated by Roseker et al. who designed a hard x-ray “split-and-delay line” based on eight perfect silicon(511) crystals [Ros09a]. Two wedge-shaped crystals are used in Laue geometry for the beam splitting and successive recombination. The other six crystals serve as mirrors in symmetric Bragg geometry. This device exhibits a throughput of 0.6% at 8.39 keV and can apply time delays of up

¹ Private communication with Prof. H. Zacharias

to 2.62 ns in steps of 7 fs. Thus, an approach to split and delay hard x-rays has been demonstrated.

Another obstacle to overcome for resolution improvement of sequential x-ray imaging is the production of sufficiently small reference structures. The size of the reference is one of the resolution-limiting factors in Fourier transform holography. At the same time FTH is, in principle, fully compatible with the application of iterative phase retrieval methods to improve the resulting spatial resolution below the reference size and towards the diffraction limit [Sta08]. However, for the treatment of the superimposed two-beam hologram presented in Fig. 4.9 no phase retrieval algorithm exists so far. Therefore, one has to rely on the manufacturing of suitable small references alone. With decreasing wavelength a gold film needs to be thicker than the standard $\sim 1 \mu\text{m}$, which means pinholes will probably not provide the desired few-nm resolution for sequential x-ray imaging in the near future.

The problem of small reference production can be addressed by Babinet's principle, which states that complementary structures create identical diffraction patterns. That means that instead of pinholes nanoparticles can create a spherical reference wave, too. The feasibility of this approach has already been demonstrated [Sta08; He03]. In contrast to the pinhole production, nanoparticles made of heavy, x-ray absorbing materials are commercially available in sizes down to 2 nm today. Nanoparticles at such small sizes exhibit a weak total scattering cross-section with increasing x-ray energy. This is a problem for holography, as the reference wave will become weak for a smaller reference-particle size. The low scattering signal can be compensated by massively parallel imaging. Uniformly redundant arrays (URAs) represent an optimized, densely packed arrangement of reference structures. Recently, single-shot imaging at FLASH has been successfully demonstrated using URAs [Mar08]. The substitution of single pinholes with URAs is completely compatible with the presented sequential x-ray imaging technique and the combination of nanoparticles in URA arrangement is envisioned as a promising approach to push FTH resolution at XFELs to the few-nm range.

An alternative approach towards high-resolution lies in the replacement of pinhole apertures with extended apertures. This approach has been suggested first by Podorov et al. [PPP07]. Guizar-Sicairos et al. have generalized the technique under the name of Holography with Extended Reference by Autocorrelation Linear Differential Operator (HERALDO) [GSF07]. The main idea is to exploit apertures with sharp corners such as slits, triangles or rectangles as references. Normally, the shape of these references is convolved with the object. In a simple picture, directional derivatives along the edges of these references ensure that only the corners of the reference structures contribute to the image formation. Mathematically, different realizations of this algorithm exist operating in real or reciprocal space. Note that for all practical realizations the algorithm is non-iterative. The hope for this imaging technique is that extended structures featuring sharp corners are easier to produce than small-diameter pinholes. The HERALDO technique has been successfully demonstrated with visible light [GSF08] as well as with soft x-rays provided by synchrotron radiation and a laser-based table-top source [GS10; Gau10]. A

recent paper demonstrated sub-pinhole resolution for HERALDO [Zhu10]. Upon suitable placement of the extended reference structures the HERALDO approach is compatible with the sequential x-ray imaging technique discussed and thus constitutes a possible way to scale the method to high resolution.

4.5.2 Multiple Timeframes

The presented sequential x-ray imaging approach exploits the optical splitting of an x-ray pulse into two pulses, which are then delayed and used separately for imaging. Fourier transform holography encodes the individual images in one hologram. In principle, this concept can be extended to more than two frames of a time lapse movie encoded simultaneously. Regarding the holography part of the experiment, the sequential imaging sample used here generates twelve independent images. In general, multiple-image encoding in a single hologram has been demonstrated [Pfa10a; Gü10; Sch06]. The challenge lies in defining the corresponding illumination scheme.

In principle, multiple pulses could be generated by combining several x-ray beamsplitters in serial operation to subsequently split already split pulses. However, one single x-ray autocorrelator itself constitutes already a complicated experimental device. Furthermore, the associated optical transmission loss caused by the multiple reflections limits this possibility to a few temporal frames.

Approaches exist to directly define the electron bunch in an FEL via the use of slotted foils [Emm04]. So far the concept has been proposed to reduce the FEL pulse length. In principle, a foil with several slots could be used to directly split an FEL-pulse into several smaller parts [Emm04]. This technique avoids the optical losses of an autocorrelator series and can generate separate fs x-ray pulses with inter-pulse spacings in the fs regime. If the trajectories of these pulses through the undulator could be controlled to generate x-ray pulses with slightly different pointing directions, the resulting illumination would be compatible with sequential x-ray imaging. This approach could enable “movies” of untriggered dynamics with a higher number of temporal frames.

4.5.3 Separation of the Diffraction Patterns

In this thesis sequential imaging is demonstrated at a moderate resolution of 1.7 μm . If the approach is scaled to higher resolution, the scenario may arise that the resolution limit set by the reference size cannot keep up with the diffraction-limited resolution set by the recording geometry. In that case for standard FTH the possibility exists to apply additional phase retrieval algorithms and improve the image resolution below the reference structure size towards the diffraction limit as demonstrated in Ref. [Sta08]. So far such algorithms do not exist for the superimposed two-beam hologram.

As an outlook to this chapter, the discussion is started about the possibility to separate a superimposed two-beam hologram and extract the individual diffraction patterns created by the different pulses. The motivation for such a separation is twofold. First, phase

retrieval algorithms could then be applied to the two individual holograms and separately improve their resolution. Second, if two superimposed coherent diffraction patterns can be reliably separated analytically, the sequential imaging approach may be performed in conjunction with coherent diffraction imaging (CDI) alone. The disentanglement of the images corresponding to the different recording times would then not rely on the holographic references. Such an approach can be advantageous if the preparation of references is not feasible and one has to rely on, for instance, particle beams as in Ref. [Bog08]. So far the concept for the two-beam hologram separation can only be demonstrated with simulated data, free from noise and artifacts. Nevertheless, this section already illustrates one strategy which might be worth to be pursued.

The idea is to make use of the mathematical properties of the coherent diffraction patterns which are: (i) the centers ($q = 0$) of the individual holograms are known and (ii) each individual hologram is point symmetric to that center under the approximation that the object is either a pure amplitude or phase object. Here, the information about the center could easily be derived directly from the superimposed hologram as no beamstop was employed (see Fig. 4.9 again). If the center information is not directly available it is possible to make use of the hologram's point symmetry to determine the center pixel. However, the point symmetry of a scattering pattern cannot be taken for granted. The investigated specimen may exhibit a phase contrast that produces an asymmetric scattering pattern. In addition, noise (e.g. originating from the detector) contributes to the breaking of the point symmetry of the hologram. In that case, the separation approach presented here does not work.

The hologram separation is demonstrated based on the computer-generated hologram corresponding to the incoherent superposition of two diffraction patterns including a $\Delta\mathbf{q}$ -shift from Fig. 4.11(b). Here, the object exhibits pure absorption contrast. The corresponding simulated hologram is visualized in Fig. 4.16.

This diffraction pattern serves as intensity input data $I(\mathbf{q})$ that is subject to the separation. The two Airy disks clearly mark the positions of the two hologram centers. Two smaller rectangular matrices of equal size $H_0(\mathbf{q})$ and $H_1(\mathbf{q} + \Delta\mathbf{q})$ are defined around these centers that will build up the symmetric part of $I(\mathbf{q})$ to that specific center. $H(\mathbf{q})$ is the “double-exposed” sum of $H_0(\mathbf{q})$ and $H_1(\mathbf{q} + \Delta\mathbf{q})$ for the iteration. $R(\mathbf{q})$ is the residuum of $H(\mathbf{q})$ subtracted from the original dataset $I(\mathbf{q})$. The loop body of the algorithm consists of the following five steps illustrated in pseudo-code:

1. $H(\mathbf{q}) = H_0(\mathbf{q}) + H_1(\mathbf{q} + \Delta\mathbf{q})$,
2. $R(\mathbf{q}) = I(\mathbf{q}) - H(\mathbf{q})$,
3. $H_0(\mathbf{q}) = \frac{1}{2} [H_0(\mathbf{q}) + R(\mathbf{q})]$ and
 $H_1(\mathbf{q} + \Delta\mathbf{q}) = \frac{1}{2} [H_1(\mathbf{q} + \Delta\mathbf{q}) + R(\mathbf{q} + \Delta\mathbf{q})]$,
4. $H_0(\mathbf{q}) = \frac{1}{2} [H_0(\mathbf{q}) + S \cdot H_0(\mathbf{q})]$ and
 $H_1(\mathbf{q} + \Delta\mathbf{q}) = \frac{1}{2} [H_1(\mathbf{q} + \Delta\mathbf{q}) + S \cdot H_1(\mathbf{q} + \Delta\mathbf{q})]$,

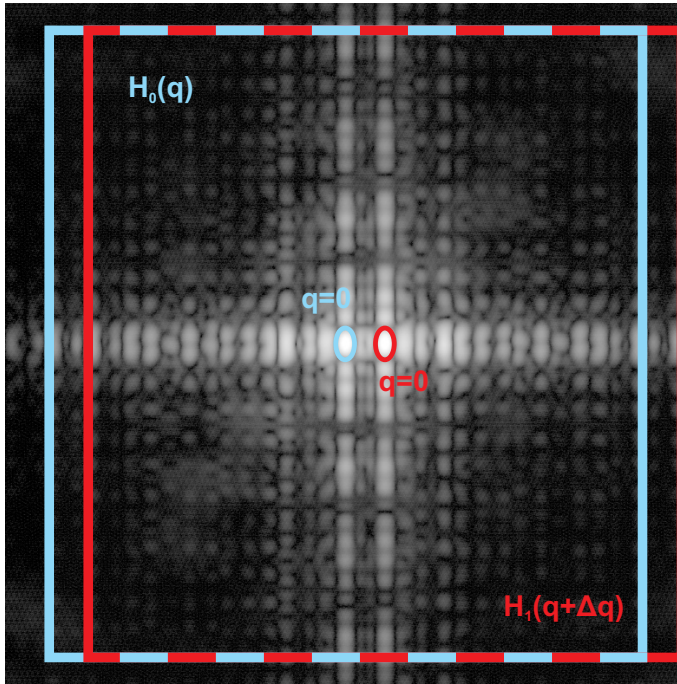


Figure 4.16: The simulated two-beam hologram which corresponds to the reconstruction in Fig. 4.11(b) on a logarithmic intensity scale. The separation algorithm exploits the point symmetry to the centers of the two individual holograms.

5. $H_0(\mathbf{q}) = \max(0, H_0(\mathbf{q}))$ and
 $H_1(\mathbf{q} + \Delta\mathbf{q}) = \max(0, H_1(\mathbf{q} + \Delta\mathbf{q}))$.

Any operation between one of the smaller matrices ($H_0(\mathbf{q})$ or $H_1(\mathbf{q} + \Delta\mathbf{q})$) and one of the other matrices is always understood such that, depending on the output, either the missing data at the corresponding edges is padded with zeros or only the corresponding part of the bigger matrices is considered. In the first step the iterating two-beam hologram $H(\mathbf{q})$ is calculated as the sum of the two individual holograms $H_0(\mathbf{q})$ and $H_1(\mathbf{q} + \Delta\mathbf{q})$. Since the latter are both initialized with zeros, $H(\mathbf{q})$ consists of zeros for the first iteration. Consequently, the comparison of $H(\mathbf{q})$ with the input data $I(\mathbf{q})$ in the second step shifts the complete input dataset to the residuum $R(\mathbf{q})$. The third step mixes each of the separate holograms with their part of the residuum matrix, i.e. for the first iteration $H_0(\mathbf{q})$ and $H_1(\mathbf{q} + \Delta\mathbf{q})$ are just the corresponding part of $I(\mathbf{q})$. In the fourth step S is the symmetry operator mirroring $H_0(\mathbf{q})$ and $H_1(\mathbf{q} + \Delta\mathbf{q})$ at their centers. In other words, both matrices are added with their correspondent rotated by 180° around its center, respectively. Finally, all negative values in $H_0(\mathbf{q})$ and $H_1(\mathbf{q} + \Delta\mathbf{q})$ are set to zero and the next iteration loop starts. Due to the fourth step $H_0(\mathbf{q})$ and $H_1(\mathbf{q} + \Delta\mathbf{q})$ built up the point symmetric part of the original intensity pattern around the corresponding center.

The iteration algorithm was implemented in MATLAB. In the example 200 iterations successfully extract the two hologram parts visualized in Fig. 4.17(a) and (b). Remember that for the simulation in Fig. 4.11 the object was slightly changed for each of the two superimposed hologram parts to clarify their contribution in the resulting superimposed

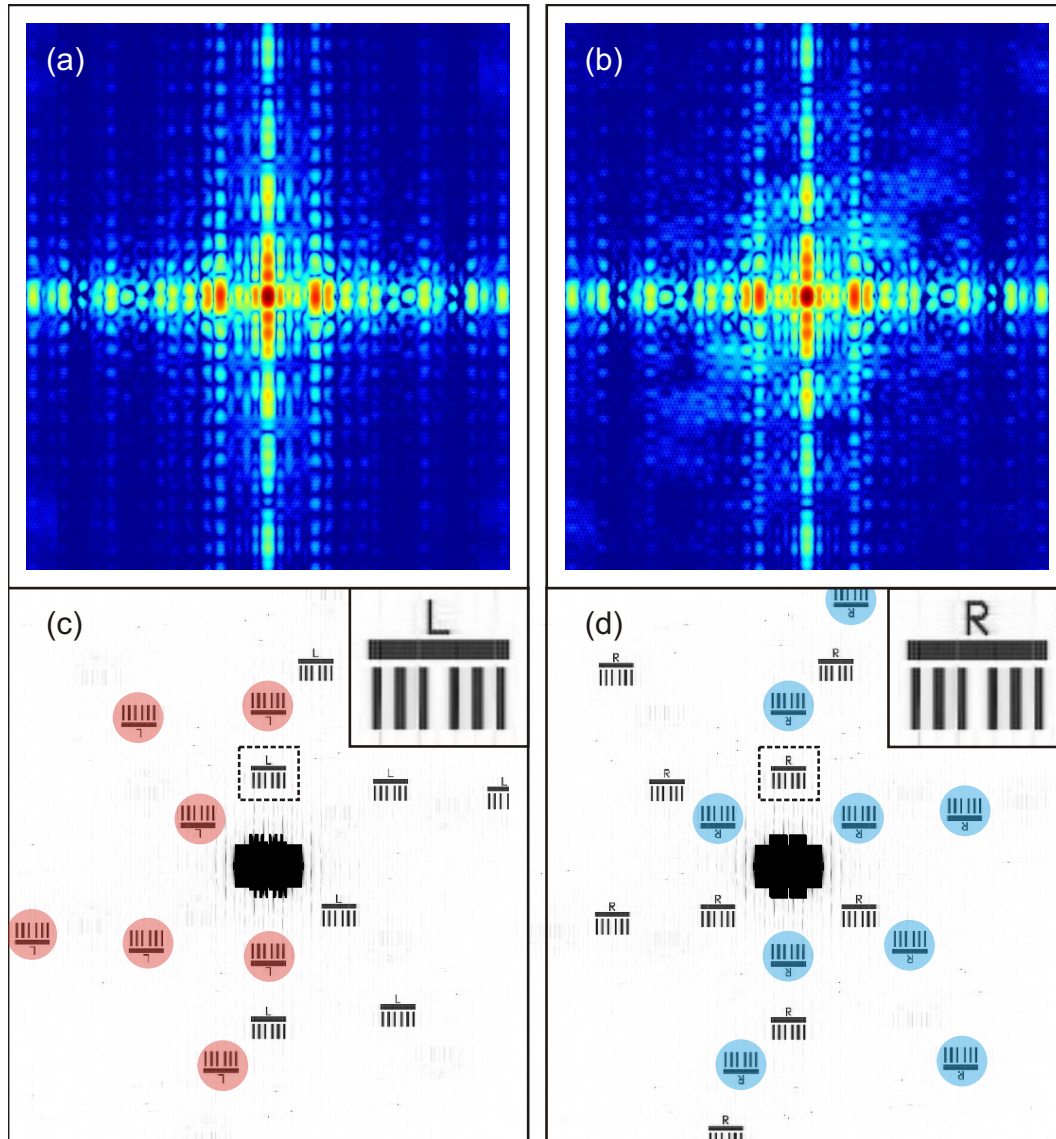


Figure 4.17: Upon sufficient symmetry a two-beam hologram can be separated. Panel (a) and (c) illustrate the two hologram parts extracted from Fig. 4.16 on logarithmic color scale. The reconstructions in panel (b) and (d) reveal only object subimages corresponding to one “recording pulse”. For clarity, the insets magnify the double-exposed reference number 6.

reconstruction. In panel (c) and (d) the two reconstructions of the extracted holograms clearly exhibit only one type of BG subimages: either the one marked by the letter “L” or the letter “R”, respectively. Even the double exposed-references number 4–7 give a clear, artifact-free image of the object. These subimages are found in both hologram reconstructions.

This relatively simple algorithm is capable to separate a simulated dataset with perfect symmetry, free from noise or other artifacts. On the other hand the algorithm fails if it is applied in its current form to the real experimental data shown in Fig. 4.9. In so far the presented approach can be considered as being a first step towards a successful separation of superimposed holograms. Improvements could be made by eliminating the artifacts from real data, as well as transferring the hologram to a finer matrix for sub-pixel centering. Another possibility might be to introduce additional constraints in the real-space reconstruction itself and develop some kind of combined phase retrieval. If the illumination is sufficiently well known, the shaded references are known and, consequently, the corresponding region in the Patterson map can be zeroed. Switching back and forth between Fourier and real space might lead to a unique solution. However, this last approach applies only for FTH and not for experiments without reference waves.

The detailed exploration of the numerical approach for the separation of a superimposed scattering pattern is beyond the scope of this thesis and subject for future work. The sketched approach might contribute to the quest for ultrafast *and* high-resolution imaging, which constitutes a challenge up to the present date.

5 Summary and Outlook

In 2004, Eisebitt et al. demonstrated a practical solution to make lensless Fourier transform holography compatible with the short wavelength of soft x-rays [Eis04]. As a result, this imaging method reaches a high spatial resolution below 50 nm (see for example [Pfa11]) while being capable to penetrate materials and provide information on buried layers. Soft x-ray FTH benefits from the many absorption edges in this energy range, which allow for element-specific imaging at resonances and the utilization of additional contrast mechanisms like, for instance, XMCD contrast. Furthermore, x-ray FTH is a lensless photon-in photon-out technique and thus provides a flexible sample environment. These facts allow for the application of high external magnetic fields and the experimental realization of such fields. Because of these properties x-ray FTH has quickly developed to a reliable x-ray imaging technique used in material science studies, especially in the area of nanomagnetism. In this field of research x-ray FTH has unique selling features, in particular, if the scientific experiment requires the simultaneous combination of the properties mentioned above. At the same time, the methodology of x-ray FTH has been constantly pushed forward to access new sample systems and improve the images provided. As a part of this process, in this thesis method refinements in conjunction with applications are presented.

In Sec. 3.2 temperature-dependent x-ray FTH was performed between 150 K and 350 K. Temperature changes may introduce drift into the setup and make the experiment challenging. Here, x-ray FTH benefits from the integrated mask-sample design, which ensures a rigid coupling of the holographic mask and the specimen and rules out relative drift between these two elements. The movement of the complete sample structure during hologram recording can be tolerated up to the amount of the pixel size of the x-ray detector, which is on the order of 10 μm . The element-specific imaging of soft x-ray FTH allowed to distinguish the magnetic configurations of a dipolar-coupled magnetically hard/soft multilayer system [Hau08]. In this way, it was possible to follow the replication of a domain state trapped in the hard stack into the soft one. In two studies, this replication was triggered by (i) an externally applied magnetic field at 150 K as well as (ii) by thermal activation during a heating cycle of the sample to room temperature. It was found that without fine-tuning of the additional driving force of the external magnetic field the matching between replicated and original domain state is higher for pure temperature-induced domain replication. The comparison of the switching onset in the soft stack in the two replication experiments is in line with the strength of stray fields of the hard stack, which are responsible for the replication process. Coupled magnetic thin films are subjects of interest as they allow detailed studies of the different coupling mechanisms between the

layers and carry potential for the development of spintronic devices. At the same time, the number of experimental methods allowing for a separate imaging of the magnetic stacks in a coupled system in a flexible magnetic and temperature environment is very limited. The experimental setup in its current state would allow for a temperature range from 4.2 K up to ~ 400 K. Future temperature-dependent x-ray FTH experiments would benefit from an improved setup designed to extend the accessible temperature range and minimize the drift of the integrated sample structure.

Another aspect of x-ray holography was emphasized in Sec. 3.3. Beyond its imaging capabilities, the microscopic field of view of the FTH-mask provides valuable information itself. The confinement to a microscopic part of the specimen generates sensitivity to domain wall jumps in fast, integrating hysteresis measurements. More precisely, the onset of spin-flip avalanches has been observed in local hysteresis loops depending on the sputter-deposition pressure [Gü08] as well as on the introduction of an AF-coupled interlayer [Hel11]. In both cases the onset of the steplike magnetic reversal was attributed to an increased concentration of magnetically active pinning sites. The results suggest different domain wall pinning mechanisms for the two sample systems. In particular, a magnetostatic mechanism is feasible for the AF-coupled system, but more systematic studies are needed to corroborate this hypothesis. Irrespective of the microscopic mechanism it is important to note that the impact of the two types of defects on the macroscopic hysteresis loop is different. Thus, the increase of the defect concentration and the introduction of AF-coupled interlayers generate different degrees of freedom to artificially tune material properties. In this study, the integrated mask-sample design allowed for additional domain images and thus to search for possible pinning sites within the *identical* sample region. Finally, due to the element specificity and penetration depth of x-rays, it was possible to directly image the anticorrelation of antiferromagnetically coupled multilayers, i.e. to observe a magnetic checkerboard state [Hel11].

These two experiments are exemplary to illustrate the development of x-ray holography to an established x-ray imaging technique at synchrotron sources with unique properties. In both cases new aspects of the imaging technique itself have been used providing new insight into the magnetic reversal behavior of multilayers with perpendicular anisotropy.

Beyond its present capabilities the method of x-ray Fourier transform holography has been further developed in this work. In Sec. 3.4 a beamstop concept based on a rotating wire was demonstrated. Such a beamstop generates a q -dependent absorption profile adapted to the strong q -dependence of x-ray scattering patterns and allows for longer exposure times. The prototype of a fast vacuum-compatible electromotor featuring a hollow rotor was illustrated from the design and manufacturing phase to its performance in initial experiments. This device provides the rotary motion for the beamstop. Standard wires mounted as absorbing structures were found to be subject to bending during operation and reflected light onto the detector due to their curved surface. Consequently, a stable beamstop plate was manufactured by spark eroding. The absorption profile for this structure followed the predicted q^{-1} dependence. Typical scattering patterns exhibit a

stronger q -dependence than q^{-1} . Design suggestions are made for better adapted beamstop plates directly generating the matching transmission profiles. Another interesting option discussed is the serial operation of several beamstops, which allows an in-situ control of the transmission profile.

In the x-ray regime laser-like sources known as x-ray free-electron lasers have recently begun to deliver photon beams of unprecedented peak brightness compressed into femtosecond pulses. Lensless imaging concepts based on coherence hold great potential at these devices as they do not rely on optical elements, which are subject to destruction in the highly intense XFEL beam, but on the high coherent photon flux characteristic for these sources. Consequently, methods like x-ray CDI and FTH have been transferred to and improved for free-electron lasers [Mar08; Bar08; Cha07; Pfa10b; Gü11]. A main goal of research at x-ray free-electron lasers is to follow ultrafast dynamics at the nanoscale. X-ray FTH provides a high spatial resolution and is compatible with single-shot XFEL imaging [Mar08; Pfa10b]. In addition, FTH can be performed in conjunction with reference multiplexing [Sch06], i.e. it is possible to generate several *independent* images from one pulse of light.

In chapter 4 an experimental approach was demonstrated, which allows to record an ultrafast image *sequence* from one XFEL pulse based on FTH reference multiplexing and a split-and-delay line. This autocorrelator was used to split an XFEL pulse, apply a time delay, and adjust the resulting two half-beams such that both illuminate the object aperture but different reference apertures. The recorded hologram contains the superimposed information of both light-sample interactions. Nevertheless, during the hologram reconstruction the different subimages were successfully disentangled. Each subimage was assigned to a point in time depending on which half-beam illuminated that reference aperture. Thus, the temporal information on the object at the two times was successfully mapped to a spatial information in the hologram reconstruction. That means with FTH it is possible to record an image sequence of one object exposed to two XFEL pulses in femtosecond succession. In contrast to pump-probe measurements applying an external pump, it is also possible to follow equilibrium fluctuations with two x-ray probes. This new experimental imaging approach is well-suited for the new x-ray sources and constitutes an important step in conquering the regime of ultrafast dynamics at the nanoscale with x-rays. Accompanying single-shot reconstructions proved the feasibility of ultrafast image-sequence recording at an adjustable femtosecond time delay. For a thorough understanding of the data in such a two-beam hologram the different image formation for a time delay within or outside of the XFELs coherence time was discussed. It was found that the coherence time sets a lower limit for the accessible time delay. Furthermore, the effect of the FELs jitter in space and energy on the hologram reconstruction was investigated with emphasis on hologram recording.

A next step for the near future would be to improve the moderate spatial resolution in the experiment towards the standard resolution of present multi-shot x-ray FTH experiments at storage ring sources. Complex reference schemes have been identified as a possible way

to push the resolution of sequential imaging even further, in particular the concept of uniformly redundant arrays (URAs) appears very promising [Mar08]. Another approach worth to be followed is the disentanglement of the superimposed scattering patterns without relying on reference beams at all. A possible way exploiting the symmetry properties of scattering patterns is sketched at the end of chapter 4. Such a separation would directly enable the resolution improvement of ultrafast sequential x-ray imaging via iterative phase retrieval and allow for the investigation of additional sample systems without references such as injected particle beams.

Bibliography

- [AIK72] S. Aoki, Y. Ichihara, and S. Kikuta, “X-Ray Hologram Obtained by Using Synchrotron Radiation”, *Jpn. J. Appl. Phys.* **11**, 1857–1857 (1972), DOI: [10.1143/JJAP.11.1857](https://doi.org/10.1143/JJAP.11.1857), (cit. on p. 2).
- [Ack07] W. Ackermann, G. Asova, V. Ayvazyan, A. Azima, N. Baboi, J. Baehr, V. Balandin, B. Beutner, A. Brandt, A. Bolzmann, et al., “Operation of a free-electron laser from the extreme ultraviolet to the water window”, *Nat. Photon.* **1**, 336–342 (June 2007), DOI: [10.1038/nphoton.2007.76](https://doi.org/10.1038/nphoton.2007.76), (cit. on pp. 2, 80, 82, 86, 101, 103).
- [Alb05] M. Albrecht, G. Hu, A. Moser, O. Hellwig, and B. D. Terris, “Magnetic dot arrays with multiple storage layers”, *J. Appl. Phys.* **97**, 103910 (2005), DOI: [10.1063/1.1904705](https://doi.org/10.1063/1.1904705), (cit. on p. 30).
- [Alt07] M. Altarelli, R. Brinkmann, M. Chergui, W. Decking, B. Dobson, S. Düsterer, G. Grübel, W. Graeff, H. Graafsma, J. Hajdu, et al., *The European X-Ray Free-Electron Laser*, tech. rep., Notkestrasse 85, 22607 Hamburg, Germany: DESY XFEL Project Group, European XFEL Project Team, Deutsches Elektronen-Synchrotron, Member of the Helmholtz Association, July 2007, (cit. on p. 82).
- [Att00] D. Attwood, “Soft X-Rays and Extreme Ultraviolet Radiation: Principles and Applications”, Cambridge University Press, 2000, (cit. on pp. 6, 7, 10, 11, 20, 21).
- [Awa10] N. Awaji, K. Nomura, S. Doi, S. Isogami, M. Tsunoda, K. Kodama, M. Suzuki, and T. Nakamura, “Large Area Imaging by Fourier Transform Holography Using Soft and Hard X-rays”, *Appl. Phys. Ex.* **3**, 085201 (2010), DOI: [10.1143/APEX.3.085201](https://doi.org/10.1143/APEX.3.085201), (cit. on p. 14).
- [BDK02] P. E. Batson, N. Dellby, and O. L. Krivanek, “Sub-angstrom resolution using aberration corrected electron optics”, *Nature* **418**, 617–620 (Aug. 2002), (cit. on p. 79).
- [Bal07] V. Baltz, A. Marty, B. Rodmacq, and B. Dieny, “Magnetic domain replication in interacting bilayers with out-of-plane anisotropy: Application to *Co/Pt* multilayers”, *Phys. Rev. B* **75**, 014406 (Jan. 2007), DOI: [10.1103/PhysRevB.75.014406](https://doi.org/10.1103/PhysRevB.75.014406), (cit. on p. 30).

- [Bar08] A. Barty, S. Boutet, M. J. Bogan, S. Hau-Riege, S. Marchesini, K. Sokolowski-Tinten, N. Stojanovic, R. Tobey, H. Ehrke, A. Cavalleri, et al., “Ultrafast single-shot diffraction imaging of nanoscale dynamics”, *Nat. Photon.* **2**, 415–419 (July 2008), DOI: [10.1038/nphoton.2008.128](https://doi.org/10.1038/nphoton.2008.128), (cit. on pp. 82, 93, 100, 115).
- [Bar10] A. Barty, “Time-resolved imaging using x-ray free electron lasers”, *Journal of Physics B: Atomic, Molecular and Optical Physics* **43**, 194014 (2010), (cit. on p. 93).
- [Ber98] G. Bertotti, “Hysteresis in Magnetism”, Academic Press, Inc., 1998, 558, (cit. on p. 43).
- [Bin82] G. Binnig, H. Rohrer, C. Gerber, and E. Weibel, “Surface Studies by Scanning Tunneling Microscopy”, *Phys. Rev. Lett.* **49**, 57–61 (1 July 1982), DOI: [10.1103/PhysRevLett.49.57](https://doi.org/10.1103/PhysRevLett.49.57), (cit. on p. 79).
- [Bog08] M. Bogan, W. Benner, S. Boutet, U. Rohner, M. Frank, A. Barty, M. Seibert, F. Maia, S. Marchesini, S. Bajt, et al., “Single Particle X-ray Diffractive Imaging”, *Nano Lett.* **8**, 310–316 (2008), DOI: [10.1021/nl072728k](https://doi.org/10.1021/nl072728k), (cit. on p. 109).
- [Bro92] F. J. A. den Broeder, E. Janssen, W. Hoving, and W. B. Zeper, “Perpendicular Magnetic-Anisotropy and Coercivity of Co/Ni Multilayers”, English, *IEEE Trans. Magn.* **28**, 2760–2765 (Sept. 1992), DOI: [10.1109/20.179619](https://doi.org/10.1109/20.179619), (cit. on p. 54).
- [Buc07] P. H. Bucksbaum, “The Future of Attosecond Spectroscopy”, *Science* **317**, 766–769 (2007), DOI: [10.1126/science.1142135](https://doi.org/10.1126/science.1142135), eprint: <http://www.sciencemag.org/content/317/5839/766.full.pdf>, (cit. on p. 80).
- [But09] T. Butz, “Fouriertransformation für Fußgänger”, Vieweg+Teubner, 2009, (cit. on pp. 132, 133).
- [CXR] CXRO, The Center for X-ray Optics, URL: <http://www-cxro.lbl.gov/>, (cit. on p. 140).
- [Cha06] H. N. Chapman, A. Barty, M. J. Bogan, S. Boutet, M. Frank, S. P. Hau-Riege, S. Marchesini, B. W. Woods, S. Bajt, W. H. Benner, et al., “Femtosecond diffractive imaging with a soft-X-ray free-electron laser”, *Nat. Phys.* **2**, 839–843 (Dec. 2006), DOI: [10.1038/nphys461](https://doi.org/10.1038/nphys461), (cit. on pp. 82, 83, 93).
- [Cha07] H. N. Chapman, S. P. Hau-Riege, M. J. Bogan, S. Bajt, A. Barty, S. Boutet, S. Marchesini, M. Frank, B. W. Woods, W. H. Benner, et al., “Femtosecond time-delay X-ray holography”, *Nature* **448**, 676–679 (Aug. 2007), DOI: [10.1038/nature06049](https://doi.org/10.1038/nature06049), (cit. on pp. 63, 94, 115).
- [Cow98] R. P. Cowburn, D. K. Koltsov, A. O. Adeyeye, and M. E. Welland, “Probing submicron nanomagnets by magneto-optics”, *Appl. Phys. Lett.* **73**, 3947–3949 (1998), DOI: [10.1063/1.122945](https://doi.org/10.1063/1.122945), (cit. on p. 44).

- [DM10] R. J. Dwayne Miller, R. Ernstorfer, M. Harb, M. Gao, C. T. Hebeisen, H. Jean-Ruel, C. Lu, G. Moriena, and G. Sciaini, “Making the molecular movie: first frames”, *Acta Crystallogr. A* **66**, 137–156 (Mar. 2010), DOI: [10.1107/S0108767309053926](https://doi.org/10.1107/S0108767309053926), (cit. on p. 80).
- [DP99] M. Donahue and D. Porter, *OOMMF User’s Guide, Version 1.0*, tech. rep., Gaithersburg, MD: National Institute of Standards and Technology, Sept. 1999, (cit. on p. 42).
- [DZ06] G. Durin and S. Zapperi, “The Barkhausen effect”, *The Science of Hysteresis* **2**, 181–267 (2006), (cit. on p. 48).
- [Dav04] J. E. Davies, O. Hellwig, E. E. Fullerton, G. Denbeaux, J. B. Kortright, and K. Liu, “Magnetization reversal of Co/Pt multilayers: Microscopic origin of high-field magnetic irreversibility”, *Phys. Rev. B* **70**, 224434 (Dec. 2004), DOI: [10.1103/PhysRevB.70.224434](https://doi.org/10.1103/PhysRevB.70.224434), (cit. on p. 45).
- [Dea77] D. A. G. Deacon, L. R. Elias, J. M. J. Madey, G. J. Ramian, H. A. Schwettman, and T. I. Smith, “First Operation of a Free-Electron Laser”, *Phys. Rev. Lett.* **38**, 892–894 (Apr. 1977), DOI: [10.1103/PhysRevLett.38.892](https://doi.org/10.1103/PhysRevLett.38.892), (cit. on p. 80).
- [Dwy06] J. R. Dwyer, C. T. Hebeisen, R. Ernstorfer, M. Harb, V. B. Deyirmenjian, R. E. Jordan, and R. Dwayne Miller, “Femtosecond electron diffraction: ‘making the molecular movie’”, *Phil. Trans. R. Soc. A* **364**, 741–778 (Mar. 2006), DOI: [10.1098/rsta.2005.1735](https://doi.org/10.1098/rsta.2005.1735), (cit. on p. 80).
- [Eis03] S. Eisebitt, M. Lörger, W. Eberhardt, J. Lüning, J. Stöhr, C. T. Rettner, O. Hellwig, E. E. Fullerton, and G. Denbeaux, “Polarization effects in coherent scattering from magnetic specimen: Implications for x-ray holography, lensless imaging, and correlation spectroscopy”, *Phys. Rev. B* **68**, 104419 (Sept. 2003), DOI: [10.1103/PhysRevB.68.104419](https://doi.org/10.1103/PhysRevB.68.104419), (cit. on p. 26).
- [Eis04] S. Eisebitt, J. Lüning, W. F. Schlotter, M. Lörger, O. Hellwig, W. Eberhardt, and J. Stöhr, “Lensless imaging of magnetic nanostructures by X-ray spectro-holography”, *Nature* **432**, 885–888 (Dec. 2004), DOI: [10.1038/nature03139](https://doi.org/10.1038/nature03139), (cit. on pp. 2, 12, 14, 21, 79, 106, 113).
- [Emm04] P. Emma, K. Bane, M. Cornacchia, Z. Huang, H. Schlarb, G. Stupakov, and D. Walz, “Femtosecond and Subfemtosecond X-Ray Pulses from a Self-Amplified Spontaneous-Emission-Based Free-Electron Laser”, *Phys. Rev. Lett.* **92**, 074801 (Feb. 2004), DOI: [10.1103/PhysRevLett.92.074801](https://doi.org/10.1103/PhysRevLett.92.074801), (cit. on p. 108).
- [Emm10] P. Emma, R. Akre, J. Arthur, R. Bionta, C. Bostedt, J. Bozek, A. Brachmann, P. Bucksbaum, R. Coffee, F.-J. Decker, et al., “First lasing and operation of an angstrom-wavelength free-electron laser”, *Nat. Photon.* **4**, 641–647 (Sept. 2010), DOI: [nphoton.2010.176](https://doi.org/10.1038/nphoton.2010.176), (cit. on pp. 2, 80, 82).

- [Fer08] A. Fert, “Nobel Lecture: Origin, development, and future of spintronics”, *Rev. Mod. Phys.* **80**, 1517–1530 (Dec. 2008), DOI: [10.1103/RevModPhys.80.1517](https://doi.org/10.1103/RevModPhys.80.1517), (cit. on p. 29).
- [Fru09] U. Fruhling, M. Wieland, M. Gensch, T. Gebert, B. Schütte, M. Krikunova, R. Kalms, F. Budzyn, O. Grimm, J. Rossbach, et al., “Single-shot terahertz-field-driven X-ray streak camera”, *Nat Photon* **3**, 523–528 (Sept. 2009), DOI: [10.1038/nphoton.2009.160](https://doi.org/10.1038/nphoton.2009.160), (cit. on pp. 101, 103).
- [Gü08] C. M. Günther, F. Radu, A. Menzel, S. Eisebitt, W. F. Schlotter, R. Rick, J. Lüning, and O. Hellwig, “Steplike versus continuous domain propagation in Co/Pd multilayer films”, *Appl. Phys. Lett.* **93**, 072505 (2008), DOI: [10.1063/1.2968305](https://doi.org/10.1063/1.2968305), (cit. on pp. 14, 48, 114).
- [Gü10] C. M. Günther, O. Hellwig, A. Menzel, B. Pfau, F. Radu, D. Makarov, M. Albrecht, A. Goncharov, T. Schrefl, W. F. Schlotter, et al., “Microscopic reversal behavior of magnetically capped nanospheres”, *Phys. Rev. B* **81**, 064411 (Feb. 2010), DOI: [10.1103/PhysRevB.81.064411](https://doi.org/10.1103/PhysRevB.81.064411), (cit. on pp. 14, 84, 106, 108).
- [Gü11] C. M. Günther, B. Pfau, R. Mitzner, B. Siemer, S. Roling, H. Zacharias, O. Kutz, I. Rudolph, D. Schondelmaier, R. Treusch, et al., “Sequential femtosecond X-ray imaging”, *Nat Photon* **5**, 99–102 (Feb. 2011), DOI: [10.1038/nphoton.2010.287](https://doi.org/10.1038/nphoton.2010.287), (cit. on pp. 82, 115).
- [GNZ03] J. Grabis, A. Nefedov, and H. Zabel, “Diffractometer for soft x-ray resonant magnetic scattering”, *Rev. Sci. Instrum.* **74**, 4048–4051 (2003), DOI: [10.1063/1.1602932](https://doi.org/10.1063/1.1602932), (cit. on p. 28).
- [GS10] M. Guizar-Sicairos, D. Zhu, J. R. Fienup, B. Wu, A. Scherz, and J. Stöhr, “Holographic x-ray image reconstruction through the application of differential and integral operators”, *Opt. Lett.* **35**, 928–930 (2010), (cit. on p. 107).
- [GSF07] M. Guizar-Sicairos and J. R. Fienup, “Holography with extended reference by autocorrelation linear differential operation”, *Opt. Exp.* **15**, 17592–17612 (2007), (cit. on p. 107).
- [GSF08] M. Guizar-Sicairos and J. R. Fienup, “Direct image reconstruction from a Fourier intensity pattern using HERALDO”, *Opt. Lett.* **33**, 2668–2670 (2008), DOI: [10.1364/OL.33.002668](https://doi.org/10.1364/OL.33.002668), (cit. on p. 107).
- [Gab48] D. Gabor, “A New Microscopic Principle”, *Nature* **161**, 777–778 (1948), DOI: [10.1038/161777a0](https://doi.org/10.1038/161777a0), (cit. on pp. 1, 12).
- [Gau10] D. Gauthier, M. Guizar-Sicairos, X. Ge, W. Boutu, B. Carré, J. R. Fienup, and H. Merdji, “Single-shot Femtosecond X-Ray Holography Using Extended References”, *Phys. Rev. Lett.* **105**, 093901 (Aug. 2010), DOI: [10.1103/PhysRevLett.105.093901](https://doi.org/10.1103/PhysRevLett.105.093901), (cit. on p. 107).

- [Gid98] S. Gider, B.-U. Runge, A. C. Marley, and S. S. P. Parkin, “The Magnetic Stability of Spin-Dependent Tunneling Devices”, *Science* **281**, 797–799 (1998), DOI: [10.1126/science.281.5378.797](https://doi.org/10.1126/science.281.5378.797), (cit. on p. 31).
- [Goo00] J. W. Goodman, “Statistical Optics”, *Wiley Classics Library*, John Wiley & Sons, Inc., 2000, (cit. on p. 10).
- [Goo05] J. W. Goodman, “Introduction to Fourier Optics”, Roberts & Co Publ., 2005, (cit. on pp. 1, 14).
- [Gou07] E. Goulielmakis, V. S. Yakovlev, A. L. Cavalieri, M. Uiberacker, V. Pervak, A. Apolonski, R. Kienberger, U. Kleineberg, and F. Krausz, “Attosecond Control and Measurement: Lightwave Electronics”, *Science* **317**, 769–775 (2007), DOI: [10.1126/science.1142855](https://doi.org/10.1126/science.1142855), eprint: <http://www.sciencemag.org/content/317/5839/769.full.pdf>, (cit. on p. 80).
- [Gra05] J. Grabis, “Soft X-ray resonant scattering from magnetic heterostructures”, *phdthesis*, Ruhr-Universität Bochum, Fakultät für Physik und Astronomie, 2005, (cit. on p. 28).
- [Gru08] P. A. Gruenberg, “Nobel Lecture: From spin waves to giant magnetoresistance and beyond”, *Rev. Mod. Phys.* **80**, 1531–1540 (Dec. 2008), DOI: [10.1103/RevModPhys.80.1531](https://doi.org/10.1103/RevModPhys.80.1531), (cit. on p. 29).
- [Gue09] E. Guehrs, C. M. Günther, R. Könnecke, B. Pfau, and S. Eisebitt, “Holographic soft X-ray omni-microscopy of biological specimens”, *Opt. Exp.* **17**, 6710–6720 (2009), DOI: [10.1364/OE.17.006710](https://doi.org/10.1364/OE.17.006710), (cit. on pp. 14, 70).
- [Gue10] E. Guehrs, C. M. Günther, B. Pfau, T. Rander, S. Schaffert, W. F. Schlotter, and S. Eisebitt, “Wavefield back-propagation in high-resolution X-ray holography with a movable field of view”, *Opt. Exp.* **18**, 18922–18931 (Aug. 2010), DOI: [10.1364/OE.18.018922](https://doi.org/10.1364/OE.18.018922), (cit. on p. 14).
- [HGD93] B. L. Henke, E. M. Gullikson, and J. C. Davis, “X-Ray Interactions: Photoabsorption, Scattering, Transmission, and Reflection at $E = 50\text{--}30,000$ eV, $Z = 1\text{--}92$ ”, *Atomic Data and Nuclear Data Tables* **54**, 181–342 (1993), DOI: [DOI:10.1006/adnd.1993.1013](https://doi.org/10.1006/adnd.1993.1013), (cit. on p. 140).
- [HK07] Z. Huang and K.-J. Kim, “Review of x-ray free-electron laser theory”, *Phys. Rev. ST Accel. Beams* **10**, 034801 (Mar. 2007), DOI: [10.1103/PhysRevSTAB.10.034801](https://doi.org/10.1103/PhysRevSTAB.10.034801), (cit. on pp. 81, 82).
- [HMW04] H. F. Hamann, Y. C. Martin, and H. K. Wickramasinghe, “Thermally assisted recording beyond traditional limits”, *Appl. Phys. Lett.* **84**, 810–812 (2004), DOI: [DOI:10.1063/1.1644924](https://doi.org/10.1063/1.1644924), (cit. on p. 31).
- [HO05] Herbert Hopster and Hans Peter Oepen, eds., “Magnetic Microscopy of Nanostructures”, *Nanoscience and Technology*, Springer, Berlin, 2005, (cit. on p. 44).

- [HTT09] O. Hellwig, B. D. Terris, and J.-U. Thiele, “Three-Dimensional Magnetic Memory With Multi-Layer Data Storage Layers”, English (US), pat. 0154219, June 2009, (cit. on p. 29).
- [HTT11] O. Hellwig, B. D. Terris, and J.-U. Thiele, “Perpendicular magnetic recording medium and system with low-curie-temperature multilayer for heat-assisted writing and/or reading”, English (US), pat. 7862912, Jan. 2011, (cit. on p. 29).
- [HZBa] HZB, *Beamline List*, Helmholtz-Zentrum Berlin für Materialien und Energie GmbH, URL: http://www.helmholtz-berlin.de/user/photons/instrumentation/beamlines-stations_en.html, (cit. on pp. 28, 101).
- [HZBb] HZB, *Comparison of LIGA and Direct-Liga*, Helmholtz-Zentrum Berlin für Materialien und Energie GmbH, URL: http://www.helmholtz-berlin.de/forschung/grossgeraete/azm/hzb-intern/verfahren_en.html, (cit. on p. 88).
- [Har02] P. Hariharan, “Basics of Holography”, Cambridge University Press, 2002, (cit. on p. 13).
- [Hau08] T. Hauet, C. M. Günther, B. Pfau, M. E. Schabes, J.-U. Thiele, R. L. Rick, P. Fischer, S. Eisebitt, and O. Hellwig, “Direct observation of field and temperature induced domain replication in dipolar coupled perpendicular anisotropy films”, *Phys. Rev. B* **77**, 184421 (2008), DOI: [10.1103/PhysRevB.77.184421](https://doi.org/10.1103/PhysRevB.77.184421), (cit. on pp. 32, 33, 113).
- [He03] H. He, S. Marchesini, M. Howells, U. Weierstall, H. Chapman, S. Hau-Riege, A. Noy, and J. C. H. Spence, “Inversion of x-ray diffuse scattering to images using prepared objects”, *Phys. Rev. B* **67**, 174114 (May 2003), DOI: [10.1103/PhysRevB.67.174114](https://doi.org/10.1103/PhysRevB.67.174114), (cit. on p. 107).
- [Hel03a] O. Hellwig, G. P. Denbeaux, J. B. Kortright, and E. E. Fullerton, “X-ray studies of aligned magnetic stripe domains in perpendicular multilayers”, *Physica B: Condensed Matter* **336**, 136–144 (Aug. 2003), DOI: [10.1016/S0921-4526\(03\)00282-5](https://doi.org/10.1016/S0921-4526(03)00282-5), (cit. on p. 45).
- [Hel03b] O. Hellwig, T. L. Kirk, J. B. Kortright, A. Berger, and E. E. Fullerton, “A new phase diagram for layered antiferromagnetic films”, *Nat. Mater.* **2**, 112–116 (Feb. 2003), (cit. on pp. 53, 54).
- [Hel06] O. Hellwig, S. Eisebitt, W. Eberhardt, W. F. Schlotter, J. Lüning, and J. Stöhr, “Magnetic imaging with soft x-ray spectroholography”, *Proceedings of the 50th annual conference on magnetism and magnetic materials*, vol. 99, 8, AIP, 2006, 08H307, DOI: [10.1063/1.2165925](https://doi.org/10.1063/1.2165925), (cit. on p. 14).

- [Hel07] O. Hellwig, A. Berger, J. B. Kortright, and E. E. Fullerton, “Domain structure and magnetization reversal of antiferromagnetically coupled perpendicular anisotropy films”, *J. Magn. Magn. Mater.* **319**, 13–55 (Dec. 2007), DOI: [10.1016/j.jmmm.2007.04.035](https://doi.org/10.1016/j.jmmm.2007.04.035), (cit. on pp. 45, 53, 54, 57).
- [Hel11] O. Hellwig, C. M. Günther, F. Radu, A. Menzel, W. F. Schlotter, J. Lüning, and S. Eisebitt, “Ferrimagnetic stripe domain formation in antiferromagnetically-coupled Co/Pt–Co/Ni–Co/Pt multilayers studied via soft x-ray techniques”, *Appl. Phys. Lett.* **98**, 172503 (2011), DOI: [10.1063/1.3583454](https://doi.org/10.1063/1.3583454), (cit. on pp. 14, 54, 114).
- [IMM99] R. S. Indeck, M. W. Muller, and R. E. Morley Jr., “Method and apparatus for fingerprinting and authenticating various magnetic media”, pat. 5920628, July 1999, (cit. on p. 53).
- [IMO99] R. S. Indeck, M. W. Muller, and J. A. O’Sullivan, “Method for precompensating signals for magnetic media noise”, pat. 5959794, Sept. 1999, (cit. on p. 53).
- [Igo] *IGOR Pro Manual*, 6.21, WaveMetrics, Inc., PO Box 2088 Lake Oswego OR 97035 USA, Nov. 2010, (cit. on pp. 40, 50).
- [KCS03] D.-H. Kim, S.-B. Choe, and S.-C. Shin, “Direct Observation of Barkhausen Avalanche in Co Thin Films”, *Phys. Rev. Lett.* **90**, 087203 (Feb. 2003), DOI: [10.1103/PhysRevLett.90.087203](https://doi.org/10.1103/PhysRevLett.90.087203), (cit. on p. 48).
- [KS04] D.-H. Kim and S.-C. Shin, “Intermittency of Barkhausen avalanche in Co nanothin films”, *The 9th Joint MMM/Intermag Conference*, vol. 95, 11, AIP, 2004, 6971–6973, DOI: [10.1063/1.1688638](https://doi.org/10.1063/1.1688638), (cit. on p. 48).
- [Kik72] S. Kikuta, S. Aoki, S. Kosaki, and K. Kohra, “X-ray holography of lensless Fourier-transform type”, *Opt. Commun.* **5**, 86–89 (1972), DOI: [DOI:10.1016/0030-4018\(72\)90005-3](https://doi.org/10.1016/0030-4018(72)90005-3), (cit. on p. 2).
- [Kis07] N. S. Kiselev, I. E. Dragunov, U. K. R. Iler, and A. N. Bogdanov, “Exchange shift of stripe domains in antiferromagnetically coupled multilayers”, *Appl. Phys. Lett.* **91**, 132507 (2007), DOI: [10.1063/1.2793626](https://doi.org/10.1063/1.2793626), (cit. on p. 54).
- [Lö04] M. Lörger, “Coherent Soft X-Ray Magnetic Scattering and Lensless Imaging”, *PhD Thesis*, Technical University of Berlin, School of Mathematics and Natural Sciences, Mar. 2004, (cit. on p. 26).
- [LC96] S. W. Lovesey and S. P. Collins, “X-ray Scattering and Absorption by Magnetic Materials”, *Oxford Series on Synchrotron Radiation 1*, Oxford University Press, 1996, (cit. on pp. 6, 23, 24, 137).
- [LU63] E. N. Leith and J. Upatnieks, “Wavefront Reconstruction with Continuous-Tone Objects”, *J. Opt. Soc. Am.* **53**, 1377–1381 (1963), (cit. on pp. 1, 13).

- [LU64] E. N. Leith and J. Upatnieks, “Wavefront Reconstruction With Diffused Illumination and Three-Dimensional Objects”, *J. Opt. Soc. Am.* **54**, 1295–1300 (1964), (cit. on p. 1).
- [Len01] B. Lengeler, “Coherence in X-ray physics”, *Naturwissenschaften* **88**, 249–260 (June 2001), DOI: [10.1007/s001140100221](https://doi.org/10.1007/s001140100221), (cit. on pp. 11, 20, 21).
- [Lug64] A. Lugt, “Signal detection by complex spatial filtering”, *IEEE Trans Inform Theo* **10**, 139–145 (Apr. 1964), DOI: [10.1109/TIT.1964.1053650](https://doi.org/10.1109/TIT.1964.1053650), (cit. on pp. 1, 13).
- [Mad71] J. M. J. Madey, “Stimulated Emission of Bremsstrahlung in a Periodic Magnetic Field”, *J. Appl. Phys.* **42**, 1906–1913 (1971), DOI: [10.1063/1.1660466](https://doi.org/10.1063/1.1660466), (cit. on p. 80).
- [Mai60] T. H. Maiman, “Stimulated Optical Radiation in Ruby”, *Nature* **187**, 493–494 (1960), DOI: [10.1038/187493a0](https://doi.org/10.1038/187493a0), (cit. on p. 1).
- [Mar08] S. Marchesini, S. Boutet, A. E. Sakdinawat, M. J. Bogan, S. Bajt, A. Barty, H. N. Chapman, M. Frank, S. P. Hau-Riege, A. Szoke, et al., “Massively parallel X-ray holography”, *Nat. Photon.* **2**, 560–563 (Sept. 2008), DOI: [10.1038/nphoton.2008.154](https://doi.org/10.1038/nphoton.2008.154), (cit. on pp. 82, 107, 115, 116).
- [McN92] I. McNulty, J. Kirz, C. Jacobsen, E. H. Anderson, M. R. Howells, and D. P. Kern, “High-Resolution Imaging by Fourier Transform X-ray Holography”, *Science* **256**, 1009–1012 (1992), DOI: [10.1126/science.256.5059.1009](https://doi.org/10.1126/science.256.5059.1009), eprint: <http://www.sciencemag.org/cgi/reprint/256/5059/1009.pdf>, (cit. on pp. 2, 12, 14, 27).
- [Men96] Q. Meng, W. P. van Drent, J. C. Lodder, and T. J. A. Popma, “Curie temperature dependence of magnetic properties of CoNi/Pt multilayer films”, *J. Magn. Magn. Mater.* **156**, 296–298 (1996), DOI: [DOI:10.1016/0304-8853\(95\)00875-6](https://doi.org/10.1016/0304-8853(95)00875-6), (cit. on p. 32).
- [Mer05] H.-C. Mertins, S. Valencia, A. Gaupp, W. Gudat, P. Oppeneer, and C. Schneider, “Magneto-optical polarization spectroscopy with soft X-rays”, *Appl. Phys. A* **80**, 1011–1020 (Feb. 2005), DOI: [10.1007/s00339-004-3129-5](https://doi.org/10.1007/s00339-004-3129-5), (cit. on p. 134).
- [Mia99] J. Miao, P. Charalambous, J. Kirz, and D. Sayre, “Extending the methodology of X-ray crystallography to allow imaging of micrometre-sized non-crystalline specimens”, *Nature* **400**, 342–344 (July 1999), (cit. on pp. 12, 21, 79).
- [Mit05] R. Mitzner, M. Neeb, T. Noll, N. Pontius, and W. Eberhardt, “An x-ray autocorrelator and delay line for the VUV-FEL at TTF/DESY”, *Ultrafast X-Ray Detectors, High-Speed Imaging, and Applications*, ed. by Stuart Kleinfelder, Dennis L. Paisley, Zenghu Chang, Jean-Claude Kieffer, and Jerome B. Hastings, vol. 5920, 1, San Diego, CA, USA: SPIE, 2005, 59200D, DOI: [10.1117/12.617304](https://doi.org/10.1117/12.617304), (cit. on pp. 82, 86, 106).

- [Mit08] R. Mitzner, B. Siemer, M. Neeb, T. Noll, F. Siewert, S. Roling, M. Rutkowski, A. A. Sorokin, M. Richter, P. Juranic, et al., “Spatio-temporal coherence of free electron laser pulses in the soft x-ray regime”, *Opt. Express* **16**, 19909–19919 (2008), DOI: [10.1364/OE.16.019909](https://doi.org/10.1364/OE.16.019909), (cit. on pp. 82, 86, 87, 100, 103, 106).
- [Mit09] R. Mitzner, A. A. Sorokin, B. Siemer, S. Roling, M. Rutkowski, H. Zacharias, M. Neeb, T. Noll, F. Siewert, W. Eberhardt, et al., “Direct autocorrelation of soft-x-ray free-electron-laser pulses by time-resolved two-photon double ionization of He”, *Phys. Rev. A* **80**, 025402 (Aug. 2009), DOI: [10.1103/PhysRevA.80.025402](https://doi.org/10.1103/PhysRevA.80.025402), (cit. on pp. 86, 106).
- [Mos02] A. Moser, K. Takano, D. T. Margulies, M. Albrecht, Y. Sonobe, Y. Ikeda, S. Sun, and E. E. Fullerton, “Magnetic recording: advancing into the future”, *J. Phys. D* **35**, R157–R167 (2002), (cit. on pp. 31, 62).
- [PI11] Princeton-Instruments, *PI-MTE: 2048B*, Data Sheet, 2011, (cit. on pp. 66, 131).
- [PPP07] S. G. Podorov, K. M. Pavlov, and D. M. Paganin, “A non-iterative reconstruction method for direct and unambiguous coherent diffractive imaging”, *Opt. Express* **15**, 9954–9962 (Aug. 2007), DOI: [10.1364/OE.15.009954](https://doi.org/10.1364/OE.15.009954), (cit. on p. 107).
- [Pag06] D. Paganin, “Coherent x-ray optics”, *Oxford Series on Synchrotron Radiation* 6, Oxford University Press, 2006, (cit. on pp. 6, 16).
- [Par91] S. S. P. Parkin, “Systematic variation of the strength and oscillation period of indirect magnetic exchange coupling through the 3d, 4d, and 5d transition metals”, *Phys. Rev. Lett.* **67**, 3598–3601 (Dec. 1991), DOI: [10.1103/PhysRevLett.67.3598](https://doi.org/10.1103/PhysRevLett.67.3598), (cit. on p. 29).
- [Pfa10a] B. Pfau, C. M. Günther, S. Schaffert, R. Mitzner, B. Siemer, S. Roling, H. Zacharias, O. Kutz, I. Rudolph, R. Treusch, et al., “Femtosecond pulse x-ray imaging with a large field of view”, *New J. Phys.* **12**, 095006 (Sept. 2010), DOI: [10.1088/1367-2630/12/9/095006](https://doi.org/10.1088/1367-2630/12/9/095006), (cit. on pp. 8, 84, 101, 108).
- [Pfa10b] B. Pfau, C. M. Günther, R. Könnecke, E. Guehrs, O. Hellwig, W. F. Schlotter, and S. Eisebitt, “Magnetic imaging at linearly polarized x-ray sources”, *Opt. Express* **18**, 13608–13615 (June 2010), DOI: [10.1364/OE.18.013608](https://doi.org/10.1364/OE.18.013608), (cit. on pp. 14, 115).
- [Pfa11] B. Pfau, C. M. Günther, E. Guehrs, T. Hauet, H. Yang, L. Vinh, X. Xu, D. Yaney, R. Rick, S. Eisebitt, et al., “Origin of magnetic switching field distribution in bit patterned media based on pre-patterned substrates”, *Appl. Phys. Lett.* **99**, 062502 (Aug. 2011), DOI: [DOI:10.1063/1.3623488](https://doi.org/10.1063/1.3623488), (cit. on pp. 14, 84, 106, 113).
- [Pfa12] B. Pfau, “Magnetic scattering at coherent x-ray sources”, *PhD Thesis (in preparation)*, Technical University Berlin, 2012, (cit. on p. 134).

- [Pie03] M. S. Pierce, R. G. Moore, L. B. Sorensen, S. D. Kevan, O. Hellwig, E. E. Fullerton, and J. B. Kortright, “Quasistatic x-ray speckle metrology of microscopic magnetic return-point memory”, *Phys. Rev. Lett.* **90**, 175502 (May 2003), DOI: [10.1103/PhysRevLett.90.175502](https://doi.org/10.1103/PhysRevLett.90.175502), (cit. on pp. 44, 45, 53).
- [Pie05] M. S. Pierce, C. R. Buechler, L. B. Sorensen, J. J. Turner, S. D. Kevan, E. A. Jagla, J. M. Deutsch, T. Mai, O. Narayan, J. E. Davies, et al., “Disorder-induced microscopic magnetic memory”, *Phys. Rev. Lett.* **94**, 017202 (Jan. 2005), DOI: [10.1103/PhysRevLett.94.017202](https://doi.org/10.1103/PhysRevLett.94.017202), (cit. on pp. 44, 45, 53).
- [Pie07] M. S. Pierce, C. R. Buechler, L. B. Sorensen, S. D. Kevan, E. A. Jagla, J. M. Deutsch, T. Mai, O. Narayan, J. E. Davies, K. Liu, et al., “Disorder-induced magnetic memory: Experiments and theories”, *Phys. Rev. B* **75**, 144406 (2007), DOI: [10.1103/PhysRevB.75.144406](https://doi.org/10.1103/PhysRevB.75.144406), (cit. on pp. 43–45, 53).
- [RB04] U. K. Rößler and A. N. Bogdanov, “Synthetic metamagnetism – magnetic switching of perpendicular antiferromagnetic superlattices”, *J. Magn. Magn. Mater.* **269**, L287–L291 (Mar. 2004), (cit. on p. 54).
- [RBD06] B. Rodmacq, V. Baltz, and B. Dieny, “Macroscopic probing of domain configurations in interacting bilayers with perpendicular magnetic anisotropy”, *Phys. Rev. B* **73**, 092405 (Mar. 2006), DOI: [10.1103/PhysRevB.73.092405](https://doi.org/10.1103/PhysRevB.73.092405), (cit. on pp. 30, 31, 33).
- [Rei99] S. Reiche, “GENESIS 1.3: a fully 3D time-dependent FEL simulation code”, *Nucl. Instr. Meth. Phys. Res. A* **429**, 243–248 (June 1999), (cit. on p. 81).
- [Ros07] A. Rosenhahn, R. Barth, X. Cao, M. Schürmann, M. Grunze, and S. Eisebitt, “Vacuum-ultraviolet Gabor holography with synchrotron radiation”, *Ultramicroscopy* **107**, 1171–1177 (2007), DOI: [DOI:10.1016/j.ultramicroscopy.2007.01.010](https://doi.org/10.1016/j.ultramicroscopy.2007.01.010), (cit. on p. 79).
- [Ros09a] W. Roseker, H. Franz, H. Schulte-Schrepping, A. Ehnes, O. Leupold, F. Zontone, A. Robert, and G. Grübel, “Performance of a picosecond x-ray delay line unit at 8.39 keV”, *Opt. Lett.* **34**, 1768–1770 (2009), DOI: [10.1364/OL.34.001768](https://doi.org/10.1364/OL.34.001768), (cit. on pp. 82, 106).
- [Ros09b] A. Rosenhahn, F. Staier, T. Nisius, D. Schäfer, R. Barth, C. Christophis, L.-M. Stadler, S. Streit-Nierobisch, C. Gutt, A. Mancuso, et al., “Digital In-line Holography with femtosecond VUV radiation provided by the free-electron laser FLASH”, *Opt. Exp.* **17**, 8220–8228 (2009), DOI: [10.1364/OE.17.008220](https://doi.org/10.1364/OE.17.008220), (cit. on p. 79).
- [SBT04] Q. Shen, I. Bazarov, and P. Thibault, “Diffractive imaging of nonperiodic materials with future coherent X-ray sources”, *J. Syn. Rad.* **11**, 432–438 (Sept. 2004), DOI: [10.1107/S0909049504016772](https://doi.org/10.1107/S0909049504016772), (cit. on pp. 8, 63, 75).

- [SDR08] P. Schmüser, M. Dohlus, and J. Rossbach, “Ultraviolet and Soft X-Ray Free-Electron Lasers: Introduction to Physical Principles, Experimental Results, Technological Challenges”, vol. 229, *Springer Tracts in Modern Physics*, Springer-Verlag Berlin Heidelberg, 2008, 220, (cit. on p. 82).
- [SF64] G. W. Stroke and D. G. Falconer, “Attainment of high resolutions in wavefront-reconstruction imaging”, *Phys. Lett.* **13**, 306–309 (1964), DOI: [DOI:10.1016/0031-9163\(64\)90022-8](https://doi.org/10.1016/0031-9163(64)90022-8), (cit. on p. 1).
- [SN09] S. Streit-Nierobisch, D. Stickler, C. Gutt, L.-M. Stadler, H. Stillrich, C. Menk, R. Fromter, C. Tieg, O. Leupold, H. P. Oepen, et al., “Magnetic soft x-ray holography study of focused ion beam-patterned Co/Pt multilayers”, *J. Appl. Phys.* **106**, 083909 (2009), DOI: [10.1063/1.3246724](https://doi.org/10.1063/1.3246724), (cit. on pp. 14, 133).
- [SS06] J. Stöhr and H. C. Siegmann, “Magnetism - From Fundamentals to Nanoscale Dynamics”, Springer-Verlag Berlin, 2006, (cit. on pp. 6, 22–24, 137, 141).
- [Sas94] S. Sasaki, “Analyses for a planar variably-polarizing undulator”, *Nuclear Instruments and Methods in Physics Research Section A: Accelerators, Spectrometers, Detectors and Associated Equipment* **347**, 83–86 (1994), DOI: [DOI:10.1016/0168-9002\(94\)91859-7](https://doi.org/10.1016/0168-9002(94)91859-7), (cit. on pp. 21, 27).
- [Sch06] W. F. Schlotter, R. Rick, K. Chen, A. Scherz, J. Stöhr, J. Lüning, S. Eisebitt, C. Günther, W. Eberhardt, O. Hellwig, et al., “Multiple reference Fourier transform holography with soft x rays”, *Appl. Phys. Lett.* **89**, 163112 (Oct. 2006), DOI: [10.1063/1.2364259](https://doi.org/10.1063/1.2364259), (cit. on pp. 16, 84, 108, 115).
- [Sch07a] A. Scherz, W. F. Schlotter, K. Chen, R. Rick, J. Stöhr, J. Lüning, I. McNulty, C. Günther, F. Radu, W. Eberhardt, et al., “Phase imaging of magnetic nanostructures using resonant soft x-ray holography”, *Phys. Rev. B* **76**, 214410 (2007), DOI: [10.1103/PhysRevB.76.214410](https://doi.org/10.1103/PhysRevB.76.214410), (cit. on p. 134).
- [Sch07b] W. F. Schlotter, “Lensless Fourier Transform Holography With Soft X-rays”, *PhD Thesis*, Stanford University, 2007, (cit. on pp. 27, 64, 90).
- [Sch68] A. L. Schawlow, “Laser Light”, *Sci. Am.* **219**, 120 (1968), (cit. on p. 20).
- [Sch83] G. Schütz, E. Zech, E. Hagn, and P. Kienle, “Anisotropy of x-rays and spin dependence of the photoabsorption of circularly polarized soft x-rays in magnetized Fe”, *Hyperfine Interactions* **16**, 1039–1042 (1 1983), DOI: [10.1007/BF02147415](https://doi.org/10.1007/BF02147415), (cit. on p. 21).
- [Sch87] G. Schütz, W. Wagner, W. Wilhelm, P. Kienle, R. Zeller, R. Frahm, and G. Materlik, “Absorption of circularly polarized x rays in iron”, *Phys. Rev. Lett.* **58**, 737–740 (Feb. 1987), DOI: [10.1103/PhysRevLett.58.737](https://doi.org/10.1103/PhysRevLett.58.737), (cit. on pp. 21, 25).

- [Sen01] F. Senf, F. Eggenstein, U. Flechsig, R. Follath, S. Hartlaub, H. Lammert, T. Noll, J. S. Schmidt, G. Reichardt, O. Schwarzkopf, et al., “Performance of the first undulator beamline U49-1-SGM at BESSY II”, *Nucl. Instr. Meth. Phys. Res. A* **467-468**, 474–478 (July 2001), DOI: [10.1016/S0168-9002\(01\)00372-2](https://doi.org/10.1016/S0168-9002(01)00372-2), (cit. on p. 27).
- [Shp07] O. G. Shpyrko, E. D. Isaacs, J. M. Logan, Y. Feng, G. Aeppli, R. Jaramillo, H. C. Kim, T. F. Rosenbaum, P. Zschack, M. Sprung, et al., “Direct measurement of antiferromagnetic domain fluctuations”, *Nature* **447**, 68–71 (May 2007), DOI: [doi:10.1038/nature05776](https://doi.org/10.1038/nature05776), (cit. on pp. 12, 21, 79).
- [Sta08] L.-M. Stadler, C. Gutt, T. Autenrieth, O. Leupold, S. Rehbein, Y. Chushkin, and G. Grübel, “Hard X Ray Holographic Diffraction Imaging”, *Phys. Rev. Lett.* **100**, 245503 (2008), DOI: [10.1103/PhysRevLett.100.245503](https://doi.org/10.1103/PhysRevLett.100.245503), (cit. on pp. 17, 107, 108).
- [Sti10] D. Stickler, R. Frömter, H. Stillrich, C. Menk, C. Tieg, S. Streit-Nierobisch, M. Sprung, C. Gutt, L.-M. Stadler, O. Leupold, et al., “Soft x-ray holographic microscopy”, *Appl. Phys. Lett.* **96**, 042501 (2010), DOI: [10.1063/1.3291942](https://doi.org/10.1063/1.3291942), (cit. on p. 14).
- [Str65] G. W. Stroke, “Lensless Fourier-Transform Method for Optical Holography”, *Appl. Phys. Lett.* **6**, 201–203 (1965), DOI: [10.1063/1.1754131](https://doi.org/10.1063/1.1754131), (cit. on pp. 1, 13).
- [THH08] J.-U. Thiele, T. Hauet, and O. Hellwig, “Design of Co/Pd multilayer system with antiferromagnetic-to-ferromagnetic phase transition”, *Appl. Phys. Lett.* **92**, 242502 (2008), DOI: [10.1063/1.2946654](https://doi.org/10.1063/1.2946654), (cit. on p. 53).
- [TMF03] J.-U. Thiele, S. Maat, and E. E. Fullerton, “FeRh/FePt exchange spring films for thermally assisted magnetic recording media”, *Appl. Phys. Lett.* **82**, 2859–2861 (2003), DOI: [10.1063/1.1571232](https://doi.org/10.1063/1.1571232), (cit. on p. 31).
- [Tie10a] C. Tieg, E. Jiménez, J. Camarero, J. Vogel, C. Arm, B. Rodmacq, E. Gautier, S. Auffret, B. Delaup, G. Gaudin, et al., “Imaging and quantifying perpendicular exchange biased systems by soft x-ray holography and spectroscopy”, *Appl. Phys. Lett.* **96**, 072503 (2010), DOI: [10.1063/1.3291111](https://doi.org/10.1063/1.3291111), (cit. on p. 14).
- [Tie10b] C. Tieg, R. Frömter, D. Stickler, S. Hankemeier, A. Kobs, S. Streit-Nierobisch, C. Gutt, G. Grübel, and H. P. Oepen, “Imaging the in-plane magnetization in a Co microstructure by Fourier transform holography”, *Opt. Express* **18**, 27251–27256 (Dec. 2010), DOI: [10.1364/OE.18.027251](https://doi.org/10.1364/OE.18.027251), (cit. on p. 14).
- [Tie10c] C. Tieg, R. Frömter, D. Stickler, H. Stillrich, C. Menk, S. Streit-Nierobisch, L.-M. Stadler, C. Gutt, O. Leupold, M. Sprung, et al., “Overcoming the field-of-view restrictions in soft x-ray holographic imaging”, *Journal of Physics: Conference Series* **211**, 012024 (2010), (cit. on p. 14).

- [VP04] F. van der Veen and F. Pfeiffer, “Coherent x-ray scattering”, *J. Phys. Condens. Matter* **16**, 5003–5030 (2004), DOI: [10.1088/0953-8984/16/28/020](https://doi.org/10.1088/0953-8984/16/28/020), (cit. on pp. 10, 21).
- [WKT05] I. Will, G. Koss, and I. Templin, “The upgraded photocathode laser of the TESLA Test Facility”, *Nucl Instr Meth A* **541**, 467 (2005), DOI: [DOI: 10.1016/j.nima.2004.12.007](https://doi.org/10.1016/j.nima.2004.12.007), (cit. on p. 93).
- [WW65] J. T. Winthrop and C. R. Worthington, “X-ray microscopy by successive Fourier transformation”, *Phys. Lett.* **15**, 124–126 (Mar. 1965), (cit. on pp. 1, 13).
- [Wie05] S. Wiebel, J.-P. Jamet, N. Vernier, A. Mougín, J. Ferré, V. Baltz, B. Rodmacq, and B. Dieny, “Domain decoration in dipolar coupled ferromagnetic stacks with perpendicular anisotropy”, *Appl. Phys. Lett.* **86**, 142502 (2005), DOI: [10.1063/1.1897845](https://doi.org/10.1063/1.1897845), (cit. on p. 31).
- [XZN05] L. Xu, W. W. Zhang, and S. R. Nagel, “Drop Splashing on a Dry Smooth Surface”, *Phys. Rev. Lett.* **94**, 184505 (May 2005), DOI: [10.1103/PhysRevLett.94.184505](https://doi.org/10.1103/PhysRevLett.94.184505), (cit. on p. 79).
- [ZFDS04] I. Zutic, J. Fabian, and S. Das Sarma, “Spintronics: Fundamentals and applications”, *Rev. Mod. Phys.* **76**, 323–410 (Apr. 2004), DOI: [10.1103/RevModPhys.76.323](https://doi.org/10.1103/RevModPhys.76.323), (cit. on p. 29).
- [Zha10] F. Zhang, Z. Y. Liu, X. Y. Han, B. Xu, H. L. He, D. L. Yu, and Y. J. Tian, “Magnetization reversal of the hard stack in antiferromagnetically coupled soft and hard Co/Pt multilayer stacks: Exploring via minor-loop measurements on the soft stack”, *J. Appl. Phys.* **107**, 123902 (2010), DOI: [10.1063/1.3340525](https://doi.org/10.1063/1.3340525), (cit. on pp. 30, 31).
- [Zhu10] D. Zhu, M. Guizar-Sicairos, B. Wu, A. Scherz, Y. Acremann, T. Tyliczszak, P. Fischer, N. Friedenberger, K. Ollefs, M. Farle, et al., “High-Resolution X-Ray Lensless Imaging by Differential Holographic Encoding”, *Phys. Rev. Lett.* **105**, 043901 (July 2010), DOI: [10.1103/PhysRevLett.105.043901](https://doi.org/10.1103/PhysRevLett.105.043901), (cit. on p. 108).

A Practical Reconstruction of Fourier Transform Holograms

The data acquired in an x-ray FTH experiment typically differs from an ideal dataset without artifacts. For example, often only a certain part of the complete physical information is accessible and the missing part needs to be compensated. In addition, the experimental measurement process contributes noise, which is superimposed to the recording. Artifacts originating from such contributions need to be removed from the experimental data or compensated in the reconstruction.

In theory, for FTH a single Fourier transform is sufficient to reconstruct the hologram and obtain the sample image. In practice the image quality can be improved by the suppression or complete removal of noise and artifacts. This appendix shortly illustrates possible data treatment for x-ray holograms as it was performed in this thesis. The goal is not to present a quantitative treatment of the hologram artifacts but to give an idea about their influence in the reconstruction and to sketch possible ways for removal.

For FTH it is important to distinguish between magnetic samples for which in most cases the *difference* of two holograms with opposite circular polarization is recorded from holograms relying on absorption or phase contrast. For the latter usually only one type of polarization is used. The resulting differences for the data treatment are given in the text.

Dark Current Subtraction

Charge-coupled device (CCD) cameras as they are used in the presented experiment exhibit readout noise as well as a certain dark current. For an operating temperature of -40°C this results in a random intensity pattern with a typical intensity distribution on the order of 100 analog-to-digital units (ADUs) and a standard deviation on the order of 5 ADUs¹ for the readout of the shaded CCD chip [PI11]. This background can be subtracted from recorded holograms to correct the zero-intensity baseline. For that purpose, usually the average of about ten of such patterns is recorded for a specific exposure time. This procedure may also remove permanent straylight, which might be present in the experimental chamber. Note that for difference holograms of magnetic samples the non-zero baseline as well as constant stray light contributions are automatically removed by the subtraction of two holograms.

¹ An analysis of exemplary dark files recorded with a Roper PI-MTE resulted in a mean value of 195 ADUs and a σ of 3.7. (Private communication with Jan Geilhufe.)

Beamstop Treatment

In Sec. 3.4 the necessity for beamstops was discussed as well as possible implementations. These devices are used to block the high-intensity Airy disk as well as residual transmitted x-rays. As a result, the central data around $q = 0$ is missing in the hologram. While the information loss corresponding to large structures is mostly tolerable, the artificial edge created by the sudden jump from maximum to zero intensity causes additional modulations in the hologram reconstruction by Fourier transformation. These might obstruct the object image in the hologram reconstruction. These modulations can be suppressed by multiplication of a smooth two-dimensional function, which cuts out the beamstop. For this purpose a Gaussian smoothed circle with zeros is appropriate as well as a radial symmetric Fermi function. In principle any two-dimensional function approximating the possibly irregular shape of the beamstop can be employed. A circle has the advantage that its shape is adapted to the scattering rings of the usually circular object aperture. The width of the junction from zero to one depends on the hologram. Values between 1 and 10 pixels have been found to work well. Usually the problem is less severe for difference holograms as the overall intensity is already reduced.

The missing central data might be a problem, especially for non-magnetic samples where often the magnitude of the reconstruction is considered. In such cases a possibility is to separately record the Airy disk and patch it into the high- q hologram. Ideally this procedure is performed with a smooth mask as described above.

Zeropadding and Centering

Zeropadding means that the data matrix representing the recorded hologram is embedded into a larger matrix of zeros. This is done for two reasons. First, an increase of the pixel number in reciprocal space corresponds to a higher sampling of the object function in real space. In other words, the pixel number of the object image is artificially increased. Note that this procedure does not improve the real resolution of the image. Second, the Fourier transform assumes periodic functions. Setting all pixel values at the edges of the hologram to zero favors the periodic boundary conditions for the Fourier transformation.

At the same time, zeropadding can be used to center the hologram for the reconstruction. A displacement between the center of the physical hologram at $q = 0$ and the center of the matrix as it is assumed by the Fourier transformation algorithm leads to an additional phase factor according to the Fourier shift theorem (see for example [But09]). In the reconstruction such a shift results in a periodic modulation with a periodicity corresponding directly to the distance and direction between the two centers. One possibility to solve this issue is to embed the data matrix into the larger matrix such that the center of the hologram and the center for the Fourier transformation do coincide. Note that most Fourier transform algorithms assume the center in one of the four corners of the matrix whereas the physical hologram is usually recorded with $q = 0$ close to the middle of the CCD chip. Alternatively, it is possible to remove the modulation caused by the center

displacement after the Fourier transform is performed. The resulting phase factor can be calculated and removed from the hologram reconstruction. The effect of this procedure is demonstrated, for instance, in [SN09]. Direct compensation of the generated modulation has the advantage that, as equivalent operation, the hologram centering can be performed with sub-pixel resolution. Another advantage is that the Fourier transform has to be performed only once. In contrast, a centering of the hologram in real space is easier to perform. It is possible to combine both methods, i.e. to center a hologram roughly in reciprocal space and later compensate any remaining modulation resulting from center displacement with a calculated phase factor. If only the magnitude of the hologram reconstruction is of interest, the centering procedure can be completely omitted as the phase factor originating from center displacement does usually not affect the magnitude.

Window Function

Window functions are used to ensure a smooth junction toward zero at the edges of a signal subject to Fourier transformation. There are several functions fulfilling this requirement all of which feature different characteristics. A comparison can be found in [But09]. For FTH window functions are important if the measured signal is still strong at the edges of the CCD chip. In this case a sharp edge is created when the hologram matrix is embedded into a matrix of zeros during zeropadding. The signal resembles a two-dimensional step function with the size of the CCD chip, i.e. a bright square contained in a larger square of zeros. The Fourier transformation yields a sinc function with strong and sharp streaks emerging from the center. These might obstruct the image in the hologram reconstruction. The radial-symmetric window function ensures a smooth junction of the data matrix towards zero at the edges and thus a distortion-free zeropadding.

Window functions are usually not necessary for magnetic difference holograms as the subtraction of two holograms ensures intensity values close to zero at the edges of the data matrix. For none of the magnetic holograms in this thesis the application of a window function was required. The case is different for the diatom sample shown in Sec. 3.4, which was imaged utilizing absorption contrast. This sample scatters strongly resulting in a strong signal at the edges of the CCD chip. For this hologram a Blackmann-Harris window function for -72 db suppression [But09] was used with a radius of 1750 pixels.

Fourier Transformation

At this point the hologram is sufficiently prepared for the Fourier transformation. Most mathematical programs are capable to perform this operation on a discrete two-dimensional data matrix. The Fourier transformation is a complex operation resulting in magnitude and phase. For holograms recorded with one polarization of the light both parts can be evaluated corresponding to the contrast mechanisms of absorption and phase, respectively.

For magnetic FTH the difference of two holograms with opposite circular polarization is recorded. Because of the subtraction the charge scattering contained within both

holograms cancels out while the magnetic contrast is enhanced. However, the magnetic information is contained in a single-helicity hologram, too. That means the real-space difference of the two separate hologram reconstructions can be evaluated also and often provides magnetic images of similar quality. Since the magnitudes can be used for this operation no centering is required. This method can thus be used for quick data evaluation, e.g. at the beamline. Usually, the final evaluation is performed by reconstruction of the hologram difference in reciprocal space.

Another question is, which part of the Fourier transformation of such a difference hologram is to be evaluated. The magnetic information can be contained either in the real or in the imaginary part of the reconstruction according to the exact x-ray energy used in the experiment as demonstrated in Ref. [Sch07a]. In Fig. A.1 the contrast in the difference-hologram reconstruction is illustrated that arises from two oppositely orientated perpendicular-anisotropy magnetic areas. For the simulation the strongly photon-energy-dependent magnetic dichroism in the optical constants at the Co- L_3 resonance taken from [Mer05] has been used. The magnetic contrast in the hologram reconstruction is rotated through the complex plane for different photon energies, here, around the Co- L_3 resonance. On resonance at 781.1 eV the complete magnetic contrast is contained in the real part of the hologram reconstruction. Away from the resonance the magnitude of the contrast starts to decrease. At the same time the imaginary part starts to increase along the positive or negative axis depending on a positive or negative deviation from the resonance, i.e. a magnetic contrast inversion of the imaginary part of the reconstruction is observed for photon energies above and below the resonance.

Often the exact x-ray energy providing full magnetic contrast is unknown and the magnetic information is spread among both complex parts of the reconstruction. By application of a phase factor it is possible to rotate the magnetic contrast and shift it to the real or imaginary part. Bastian Pfau discusses this issue in detail in his PhD-thesis and describes the optimum measurement signal of a magnetic image with maximized contrast as signed magnitude [Pfa12].

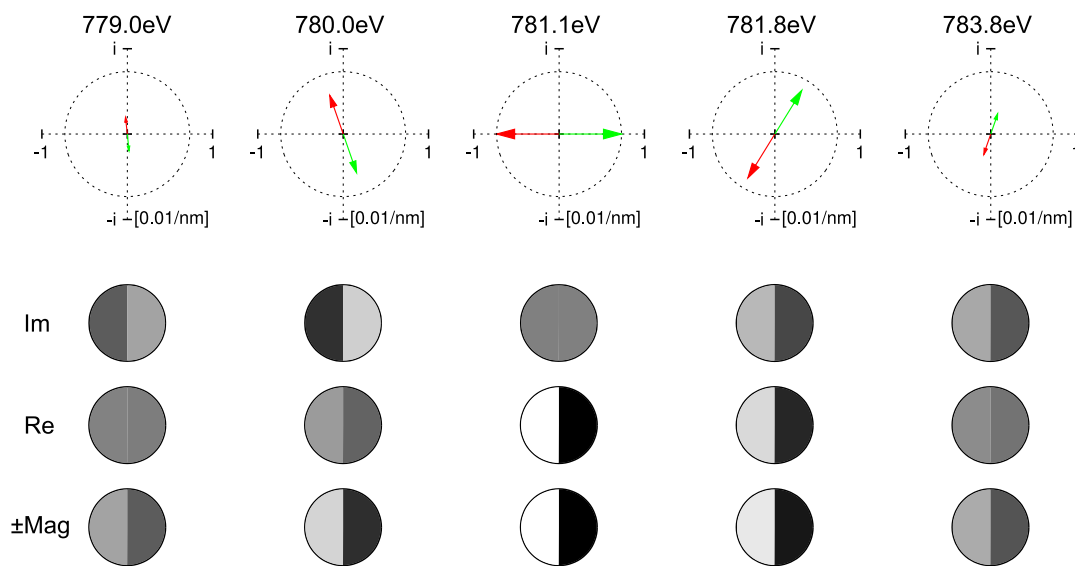


Figure A.1: (Courtesy of Bastian Pfau.) Simulated contrast for the two orientations of perpendicular-anisotropy magnetic domains in the reconstruction of a difference hologram. The upper row visualizes the magnetic contrast in the complex plane given in units of 0.01 per nm of Co-layer thickness. Below the resulting black & white contrast for the imaginary and the real parts as well as for the signed magnitude is illustrated. The latter is suggested as optimized measurement signal for hologram reconstructions.

B Resonant Magnetic Scattering with Soft X-rays

The theory of scattering and absorption of electromagnetic waves in matter is comprehensively summarized in text books, for instance by S.W. Lovesey [LC96] or J. Stöhr & H.C. Siegmann [SS06]. The notation in this appendix strongly follows the one from the latter book and summarizes the most important equations in a very shortened form focusing on scattering in the soft x-ray regime.

The processes of absorption and scattering are described by their cross-sections which are both derived uniformly from the complex *scattering length* $f(\mathbf{q}, E)$ in the following ways:

$$\left(\frac{d\sigma}{d\Omega}\right)^{\text{scat}} = |f(\mathbf{q}, E)|^2, \quad (\text{B.1})$$

$$\sigma^{\text{abs}} \sim \text{Im} \{f(\mathbf{q}, E)\}. \quad (\text{B.2})$$

The total scattering cross-section for a scattering process σ^{scat} is obtained by angular integration of the *differential scattering cross-section* $d\sigma/d\Omega$. Eq. B.2 is also known as the optical theorem, which is valid in the long-wavelength limit.

Non-resonant Scattering

The simplest case to consider is the scattering of an electromagnetic plane wave with fields

$$\mathbf{E}(\mathbf{r}, t) = \boldsymbol{\epsilon} E_0 e^{-i(\omega t - \mathbf{k} \cdot \mathbf{r})} \quad (\text{B.3})$$

$$\mathbf{B}(\mathbf{r}, t) = \frac{1}{c} (\mathbf{k}_0 \times \boldsymbol{\epsilon}) E_0 e^{-i(\omega t - \mathbf{k} \cdot \mathbf{r})} \quad (\text{B.4})$$

from a single electron with charge $-e$ and spin \mathbf{s} . Linear polarization is assumed and the unit polarization vector $\boldsymbol{\epsilon}$ chosen along the \mathbf{E} -vector. Upon interaction, in a first step the charge and spin of the electron are set in motion creating an oscillating electric and magnetic dipole moment, which in a second step reradiates an electromagnetic wave. That means two scattering processes for charge and spin scattering do exist and one can define two polarization-dependent scattering lengths f_e and f_s for these processes. Scattering channels originating from spin-orbit coupling are neglected here. It is important to note, that a phase shift of π for charge scattering and of $\pi/2$ for spin scattering exists between the incident and scattered fields. Furthermore, charge scattering maintains the light polarization while spin scattering causes a polarization rotation. The scattering

length for charge scattering of one free electron is defined as

$$f = f_e(\boldsymbol{\epsilon}, \boldsymbol{\epsilon}') = r_0 \boldsymbol{\epsilon} \cdot \boldsymbol{\epsilon}' \quad (\text{B.5})$$

with $r_0 = e^2/4\pi\epsilon_0 m_e c^2 = 2.82 \times 10^{-6}$ nm being the classical electron radius (or Thomson scattering length), and $\boldsymbol{\epsilon}'$ the unit polarization vector of the scattered radiation. Calculating the magnitude squared followed by angular integration according to Eq. B.1 yields the total scattering cross-section σ_e for one electron

$$\sigma_e = \frac{8\pi}{3} r_0^2 = 0.665 \times 10^{-28} \text{ m}^2 = 0.665 \text{ barn} . \quad (\text{B.6})$$

σ_e is called the Thomson cross-section. The scattering length for the spin scattering f_s is

$$f_s(\boldsymbol{\epsilon}, \boldsymbol{\epsilon}') = -i r_0 \frac{\hbar\omega}{m_e c^2} \mathbf{s} \cdot (\mathbf{k}_0 \times \boldsymbol{\epsilon}) \times (\mathbf{k}'_0 \times \boldsymbol{\epsilon}') \quad (\text{B.7})$$

resulting in the cross-section

$$\sigma_s = \frac{\sigma_e}{4} \left(\frac{\hbar\omega}{m_e c^2} \right)^2 . \quad (\text{B.8})$$

The two cross-sections σ_e and σ_s take the same value for an energy $\hbar\omega = 2m_e c^2 = 1.022$ MeV. Below that energy, and especially for soft x-rays, σ_s is orders of magnitude smaller than σ_e . Consequently, spin scattering is omitted from this point.

That means the scattering of soft x-rays at a free electron is described by the scattering length $f = r_0 \boldsymbol{\epsilon} \cdot \boldsymbol{\epsilon}'$. For all scenarios beyond a single free electron the scattering length f is modified by multiplication of the *scattering factor* $F(\mathbf{q}, E)$, which describes all additional contributions. Thus, the general form of the scattering length is

$$f(\mathbf{q}, E) = r_0 (\boldsymbol{\epsilon} \cdot \boldsymbol{\epsilon}') F(\mathbf{q}, E) . \quad (\text{B.9})$$

$F(\mathbf{q}, E)$ can depend on the momentum transfer \mathbf{q} and the light's energy E according to the effects considered in the scattering process. As a result, it may consist of quite some complicated terms. Some examples are given below.

The next step to consider after single-electron scattering is the scattering from an atom with a multitude of electrons. The total scattered amplitude is taken as the sum of the scattering amplitudes of the individual electrons. Interference between these individual scattering amplitudes that might occur is taken into account by the *atomic form factor* $F^0(\mathbf{q})$, the Fourier transform of the number density of the electrons in the atomic volume

$$F^0(\mathbf{q}) = -\frac{1}{e} \int \rho(r) e^{i\mathbf{q} \cdot \mathbf{r}} \text{d}r . \quad (\text{B.10})$$

This form factor is multiplied to the scattering length according to Eq. B.9, i.e. the scattering factor becomes the atomic form factor ($F(\mathbf{q}, E) = F^0(\mathbf{q})$) and the non-resonant scattering length of an atom takes the form

$$f_{\text{atom}} = f(\mathbf{q}) = r_0 (\boldsymbol{\epsilon} \cdot \boldsymbol{\epsilon}') F^0(\mathbf{q}). \quad (\text{B.11})$$

The scattering length is angle-dependent because of the scattering factors dependence on the momentum transfer \mathbf{q} . Consequently, this dependence is found in the differential scattering cross-section

$$\left(\frac{d\sigma}{d\Omega} \right)_{\text{atom}}^{\text{scat}} = r_0^2 |\boldsymbol{\epsilon} \cdot \boldsymbol{\epsilon}'|^2 |F^0(\mathbf{q})|^2 = \frac{3}{8\pi} \sigma_e |\boldsymbol{\epsilon} \cdot \boldsymbol{\epsilon}'|^2 |F^0(\mathbf{q})|^2. \quad (\text{B.12})$$

In the soft x-ray regime the wavelength is on the order of 1 nm or above, which means it is larger than the typical distances between atoms in matter. As a result, all electrons scatter in phase and the form factor becomes equal to the number of electrons ($F^0(\mathbf{q}) = Z$). Furthermore, approximately only forward scattering happens, i.e. \mathbf{q} is small and $\boldsymbol{\epsilon} = \boldsymbol{\epsilon}'$.

Resonant Scattering

The different electrons in the shells of an atom (core and valence electrons) have different binding energies. Resonance effects are to be expected if the light's energy corresponds to these characteristic energies. For example, a core electron is excited into a higher empty state and decays afterwards to its initial state (elastic resonant scattering). Within a semi-classical picture these effects are considered in a further modification of the scattering factor $F(\mathbf{q}, E)$

$$F(\mathbf{q}, E) = F^0(\mathbf{q}) + \underbrace{F'(E)}_{\text{refractive}} - i \underbrace{F''(E)}_{\text{absorptive}} \stackrel{\text{small } \mathbf{q}}{=} \underbrace{Z + F'(E)}_{f_1(E)} - i \underbrace{F''(E)}_{f_2(E)}. \quad (\text{B.13})$$

$F^0(\mathbf{q})$ is again the atomic form factor derived by Fourier transformation of the scattering atom's electron number density distribution. The anomalous factors $F'(E)$ and $F''(E)$ originate from the semi-classical description of a multielectron atom as collection of harmonic oscillators each with binding energy E_n and resonance widths Δ_n . Solving the equation of motion of a forced harmonic oscillator yields the energy-dependent resonance factors $F_n(E)$ for each binding energy E_n

$$F_n(E) = \frac{E^2}{E^2 - E_n^2 + iE\Delta_n} \approx 1 + F'_n(E) - iF''_n(E). \quad (\text{B.14})$$

For $\Delta_n \ll E_n$ the resonance factors $F_n(E)$ can be approximated with $F'_n(E)$ and $F''_n(E)$ as illustrated in Eq. B.14. $F'_n(E)$ is associated with the refractive and $F''_n(E)$ with the absorptive contribution to the scattering. These factors have the following form:

$$F'_n(E) = \frac{E_n^2(E^2 - E_n^2)}{(E^2 - E_n^2)^2 + (E\Delta_n)^2} \quad \text{and} \quad F''_n(E) = \frac{E_n}{\Delta_n} \frac{(\Delta_n/2)^2}{(E - E_n)^2 + (\Delta_n/2)^2}. \quad (\text{B.15})$$

For illustration, both are plotted in Fig. B.1 for a resonance at $E_n = 778$ eV and a width $\Delta_n = 5$ eV.

This formalism considers the resonant process with one particular core shell with binding energy E_n . If the photon energy is tuned to that value, the atomic response is dominated by that particular shell. The other (non-resonant) shells will contribute a constant background, which is already considered by the form factor $F^0(\mathbf{q})$. Thus, the resonant differential atomic scattering cross-section becomes

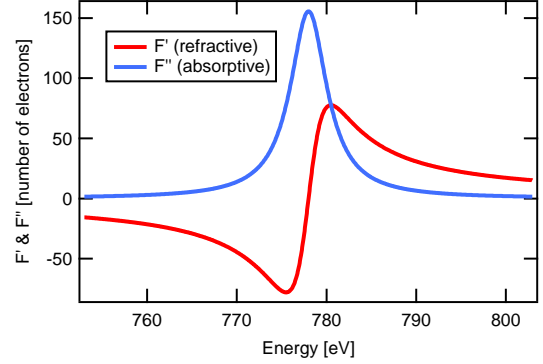


Figure B.1: The resonance factors F' and F'' .

$$\left(\frac{d\sigma}{d\Omega} \right)_{\text{res}}^{\text{scat}} = |f(\mathbf{q}, E)|^2 = r_0^2 |\boldsymbol{\epsilon} \cdot \boldsymbol{\epsilon}'|^2 \left| F^0(\mathbf{q}) + F'(\mathbf{q}) - iF''(E) \right|^2. \quad (\text{B.16})$$

Again, for forward scattering, which is valid for soft x-rays ($\lambda \geq 1$ nm), the form factor is identified with the electron number Z as above. For this energy range the tabulated *Henke-Gullikson factors* [CXr; HGD93] with $f_1 = Z + F'(E)$ and $f_2 = F''(E)$ can be consulted for practical use as already indicated in Eq. B.13 describing the general elastic resonant scattering factor $F(\mathbf{q}, E)$. Under this condition the differential scattering cross-section becomes

$$\left(\frac{d\sigma}{d\Omega} \right)_{\text{res}, \mathbf{q}=0}^{\text{scat}} = r_0^2 \left\{ [Z + F'(E)]^2 + [F''(E)]^2 \right\} = r_0^2 \left\{ [f_1(E)]^2 + [f_2(E)]^2 \right\}. \quad (\text{B.17})$$

At this point the semi-classical picture (one-electron picture or active electron approximation) reaches its limits. The problem remains that the atom consists of several electrons that are not passive during the absorption or scattering process. The complete picture of magnetic elastic resonant scattering is only accessible with the help of quantum-mechanics. The description is done by transition matrix elements, which correspond to transitions directly from an initial state $|i\rangle$ to a final state $|f\rangle$ (first order process) or via an intermediate virtual state $|n\rangle$ (second order process). The states $|i\rangle$ and $|f\rangle$ contain an electron and a photon part. It turns out that x-ray absorption is described by the first-order process while resonant x-ray scattering corresponds to a second-order process. The derivation of the *elastic resonant magnetic scattering factor* in this sense is considered too long for this

summary and only the final result is given. The details can be found again in the book by Stöhr & Siegmann [SS06]. The scattering factor for elastic resonant magnetic scattering $F(\mathbf{q}, E)$ has the general form

$$F(\hbar\omega) = \frac{\hbar\omega^2\alpha_f\mathcal{R}^2}{2cr_0} \left[\underbrace{(\boldsymbol{\epsilon}'^* \cdot \boldsymbol{\epsilon}) G_0}_{\text{charge}} + \underbrace{i(\boldsymbol{\epsilon}'^* \times \boldsymbol{\epsilon}) \cdot \hat{\mathbf{m}} G_1}_{\text{XMCD}} + \underbrace{(\boldsymbol{\epsilon}'^* \cdot \hat{\mathbf{m}})(\boldsymbol{\epsilon} \cdot \hat{\mathbf{m}}) G_2}_{\text{XMLD}} \right] \quad (\text{B.18})$$

with

$$G_0 = \sum_n \frac{|\langle a | C_{+1}^{(1)} | n \rangle|^2 + |\langle a | C_{-1}^{(1)} | n \rangle|^2}{(\hbar\omega - E_R^n) + i(\Delta_n/2)}, \quad (\text{B.19})$$

$$G_1 = \sum_n \frac{|\langle a | C_{-1}^{(1)} | n \rangle|^2 - |\langle a | C_{+1}^{(1)} | n \rangle|^2}{(\hbar\omega - E_R^n) + i(\Delta_n/2)}, \quad (\text{B.20})$$

$$G_2 = \sum_n \frac{2|\langle a | C_0^{(1)} | n \rangle|^2 + |\langle a | C_{-1}^{(1)} | n \rangle|^2 + |\langle a | C_{+1}^{(1)} | n \rangle|^2}{(\hbar\omega - E_R^n) + i(\Delta_n/2)}. \quad (\text{B.21})$$

Here \mathcal{R} is the radial dipole matrix element with the shell and subshell quantum numbers $\{n, c\}$ and $\{n', l\}$ of the initial and final states

$$\mathcal{R} = \langle R_{n',l}(r) | r | R_{n,c}(r) \rangle = \int_0^\infty R_{n',l}^*(r) R_{n,c}(r) r^3 dr. \quad (\text{B.22})$$

The terms $|\langle a | C_q^{(1)} | n \rangle|^2$ are dipole matrix elements of the Racah spherical tensors. Racah spherical tensors operators are defined as

$$C_m^{(l)} = \sqrt{\frac{4\pi}{2l+1}} Y_{l,m}(\theta, \phi). \quad (\text{B.23})$$

with $Y_{l,m}(\theta, \phi)$ being the spherical harmonics. α_f is the fine-structure constant. The important information upon examination of Eq. B.18 is that the three terms G_0, G_1, G_2 are multiplied with terms showing different dependencies on the polarization ($\boldsymbol{\epsilon}, \boldsymbol{\epsilon}'$) and magnetization orientation of the sample $\hat{\mathbf{m}}$. An interpretation of Eq. B.18 is given in the main text.

Publications

Publications Resulting from the Work Described in this Thesis

Parts of this thesis have already been published in the following articles. Several figures used in this thesis are similar versions or are based on the same datasets as in these publications, namely the figures with numbers 3.7, 3.8, 3.10, 3.11, 3.14, 3.15, 3.17, 3.18, 3.21, 3.22, 3.23, 3.24, 3.26, 4.3, 4.4, 4.5, 4.6, 4.7, 4.9, 4.11, and 4.15.

- C. M. Günther, B. Pfau, R. Mitzner, B. Siemer, S. Roling, H. Zacharias, O. Kutz, I. Rudolph, D. Schondelmaier, R. Treusch and S. Eisebitt “Sequential femtosecond X-Ray imaging” *Nature Photonics* **5**, 99 (2011).
<http://dx.doi.org/10.1038/nphoton.2010.287>
- O. Hellwig, C. M. Günther, F. Radu, A. Menzel, W. F. Schlotter, J. Lüning and S. Eisebitt “Ferrimagnetic stripe domain formation in AF-coupled Co/Pt-Co/Ni-Co/Pt multilayers observed via soft x-ray techniques” *Applied Physics Letters* **98**, 172503 (2011).
<http://dx.doi.org/10.1063/1.3583454>
- C. M. Günther, F. Radu, A. Menzel, S. Eisebitt, W. F. Schlotter, R. Rick, J. Lüning, and O. Hellwig “Steplike versus continuous domain propagation in Co/Pd multilayer films” *Applied Physics Letters* **93**, 072505 (2008).
<http://dx.doi.org/10.1063/1.2968305>
- T. Hauet, C. M. Günther, B. Pfau, M. E. Schabes, J.-U. Thiele, R. L. Rick, P. Fischer, S. Eisebitt, and O. Hellwig “Direct observation of field and temperature induced domain replication in dipolar coupled perpendicular anisotropy films” *Physical Review B* **77**, 184421 (2008).
<http://dx.doi.org/10.1103/PhysRevB.77.184421>
- C. M. Günther, T. Noll, G. Schindhelm, J. Geilhufe, B. Pfau, E. Guehrs, O. Kutz, and S. Eisebitt “Rotating beamstop for soft x-rays” *in preparation*.

Publications in Peer-reviewed Journals

- B. Pfau, C. M. Günther, E. Guehrs, T. Hauet, H. Yang, L. Vinh, X. Xu, D. Yaney, R. Rick, S. Eisebitt, and O. Hellwig “Origin of magnetic switching field distribution in bit patterned media based on pre-patterned substrates” *Applied Physics Letters* **99**, 062502 (2011).
<http://dx.doi.org/10.1063/1.3623488>
- B. Pfau, C. M. Günther, S. Schaffert, R. Mitzner, B. Siemer, S. Røling, H. Zacharias, O. Kutz, I. Rudolph, R. Treusch, and S. Eisebitt “Femtosecond pulse x-ray imaging with a large field of view” *New Journal of Physics* **12**, 095006 (2010).
<http://dx.doi.org/10.1088/1367-2630/12/9/095006>
- E. Guehrs, C. M. Günther, B. Pfau, T. Rander, S. Schaffert, W. F. Schlotter, and S. Eisebitt “Wavefield back-propagation in high-resolution X-ray holography with a movable field of view” *Optics Express* **18**, 18922 (2010).
<http://dx.doi.org/10.1364/OE.18.018922>
- B. Pfau, C. M. Günther, R. Könnecke, E. Guehrs, O. Hellwig, W. F. Schlotter, and S. Eisebitt “Magnetic imaging at linearly polarized x-ray sources” *Optics Express* **18**, 13608 (2010).
<http://dx.doi.org/10.1364/OE.18.013608>
- C. Gutt, S. Streit-Nierobisch, L.-M. Stadler, B. Pfau, C. M. Günther, R. Könnecke, R. Frömter, A. Kobs, D. Stickler, H. P. Oepen, R. R. Fäustlin, R. Treusch, J. Feldhaus, E. Weckert, I. A. Vartanyants, M. Grunze, A. Rosenhahn, T. Wilhein, S. Eisebitt, and G. Grübel “Single-pulse resonant magnetic scattering using a soft x-ray free-electron laser” *Physical Review B* **81**, 100401 (2010).
<http://dx.doi.org/10.1103/PhysRevB.81.100401>
- C. M. Günther, O. Hellwig, A. Menzel, B. Pfau, F. Radu, D. Makarov, M. Albrecht, A. Goncharov, T. Schrefl, W. F. Schlotter, R. Rick, J. Lüning, and S. Eisebitt “Microscopic reversal behavior of magnetically capped nanospheres” *Physical Review B* **81**, 064411 (2010).
<http://dx.doi.org/10.1063/1.2968305>
- C. Gutt, L.-M. Stadler, S. Streit-Nierobisch, A. P. Mancuso, A. Schropp, B. Pfau, C. M. Günther, R. Könnecke, J. Gulden, B. Reime, J. Feldhaus, E. Weckert, I. A. Vartanyants, O. Hellwig, F. Staier, R. Barth, M. Grunze, A. Rosenhahn, D. Stickler, H. Stillrich, R. Frömter, H. P. Oepen, M. Martins, T. Nisius, T. Wilhein, B. Faatz, N. Guerassimova, K. Honkavaara, V. Kocharyan, R. Treusch, E. Saldin, S. Schreiber, E. A. Schneidmiller, M. V. Yurkov, S. Eisebitt, and G. Grübel “Resonant magnetic scattering with soft x-ray pulses from a free-electron laser operating at 1.59 nm” *Physical Review B* **79**, 212406 (2009).
<http://dx.doi.org/10.1103/PhysRevB.79.212406>

-
- A. Rosenhahn, F. Staier, T. Nisius, D. Schäfer, R. Barth, C. Christophis, L.-M. Stadler, S. Streit-Nierobisch, C. Gutt, A. Mancuso, A. Schropp, J. Gulden, B. Reime, J. Feldhaus, E. Weckert, B. Pfau, C. M. Günther, R. Könnecke, S. Eisebitt, M. Martins, B. Faatz, N. Guerassimova, K. Honkavaara, R. Treusch, E. Saldin, S. Schreiber, E. A. Schneidmiller, M. V. Yurkov, I. Vartanyants, G. Grübel, M. Grunze, and T. Wilhein “Digital In-line Holography with femtosecond VUV radiation provided by the free-electron laser FLASH” *Optics Express* **17**, 8220 (2009).
<http://dx.doi.org/10.1364/OE.17.008220>
- E. Guehrs, C. M. Günther, R. Könnecke, B. Pfau, and S. Eisebitt “Holographic soft X-ray omni-microscopy of biological specimens” *Optics Express* **17**, 6710 (2009).
<http://dx.doi.org/10.1364/OE.17.006710>
- A. P. Mancuso, A. Schropp, B. Reime, L.-M. Stadler, A. Singer, J. Gulden, S. Streit-Nierobisch, C. Gutt, G. Grübel, J. Feldhaus, F. Staier, R. Barth, A. Rosenhahn, M. Grunze, T. Nisius, T. Wilhein, D. Stickler, H. Stillrich, R. Frömter, H.-P. Oepen, M. Martins, B. Pfau, C. M. Günther, R. Könnecke, S. Eisebitt, B. Faatz, N. Guerassimova, K. Honkavaara, V. Kocharyan, R. Treusch, E. Saldin, S. Schreiber, E. A. Schneidmiller, M. V. Yurkov, E. Weckert, and I. A. Vartanyants “Coherent-Pulse 2D Crystallography Using a Free-Electron Laser X-Ray Source” *Physical Review Letters* **102**, 035502 (2009).
<http://dx.doi.org/10.1103/PhysRevLett.102.035502>
- T. Hauet, C. M. Günther, O. Hovorka, A. Berger, M.-Y. Im, P. Fischer, T. Eimüller, and O. Hellwig “Field driven ferromagnetic phase nucleation and propagation in antiferromagnetically coupled multilayer films with perpendicular anisotropy” *Applied Physics Letters* **93**, 042505 (2008).
<http://dx.doi.org/10.1063/1.2961001>
- A. Scherz, W. F. Schlotter, K. Chen, R. Rick, J. Stöhr, J. Lüning, I. McNulty, C. Günther, F. Radu, W. Eberhardt, O. Hellwig, and S. Eisebitt “Phase imaging of magnetic nanostructures using resonant soft x-ray holography” *Physical Review B* **76**, 214410 (2007).
<http://dx.doi.org/10.1103/PhysRevB.76.214410>
- W. F. Schlotter, J. Lüning, R. Rick, K. Chen, A. Scherz, S. Eisebitt, C. M. Günther, W. Eberhardt, O. Hellwig, and J. Stöhr “Extended field of view soft x-ray Fourier transform holography: toward imaging ultrafast evolution in a single shot” *Optics Letters* **32**, 3110 (2007).
<http://dx.doi.org/10.1364/OL.32.003110>
- G. Wernicke, J. Frank, H. Gruber, M. Dürr, A. Langner, S. Eisebitt, C. Günther, L. Bouamama, S. Krüger, and A. Hermerschmidt “Applications of the high-resolution optical reconstruction of digital holograms” *Proceedings of the SPIE — Practical*

Holography XX: Materials and Applications **6136** 61360Q (2006).
<http://dx.doi.org/10.1117/12.651622>

- W. F. Schlotter, R. Rick, K. Chen, A. Scherz, J. Stöhr, J. Lüning, S. Eisebitt, C. Günther, W. Eberhardt, O. Hellwig, and I. McNulty “Multiple reference Fourier transform holography with soft x rays” *Applied Physics Letters* **89**, 163112 (2006).
<http://dx.doi.org/10.1063/1.2364259>

Acknowledgment of the Work of Others

The x-ray holography experiments presented in this thesis were performed at the BESSY-II synchrotron in Berlin, Germany and the free-electron laser FLASH in Hamburg, Germany. The success of the experimental work at such large-scale facilities depends on the combined effort of scientists, who are acknowledged here:

The experiments on magnetic samples in Sec. 3.2 and Sec. 3.3 were performed in collaboration with Olav Hellwig and Thomas Hauet from Hitachi GST who fabricated all magnetic thin films and provided the characterization measurements by magnetometry and MFM. Both participated in the x-ray holography measurements of these samples together with Andreas Menzel, Florin Radu, Stefan Eisebitt and the author of this thesis. The nanostructuring of the FTH-mask by FIB was performed at the SSRL by Ramon Rick and Bill Schlotter. The estimate of the magnetic stray field value by OOMMF simulation in Sec. 3.2.4 was provided by Jyoti Mohanty.

The initial concept of a rotating beamstop presented in Sec. 3.4 resulted from discussions between Pierre Thibault and Stefan Eisebitt. Tino Noll and Günter Schindhelm were responsible for the design and fabrication of the in-vacuum electromotor. The diatom sample visible in Fig. 3.35 used for performance testing of the rotating beamstop was provided by Erik Gührs who also participated in the synchrotron beamtime for that project together with Bastian Pfau, Stefan Eisebitt and the author. Oliver Kutz fabricated the beamstop plate and the sample for the sequential x-ray imaging approach, both according to the design of the author.

The author is responsible for the conceptual idea of sequential x-ray imaging presented in chapter 4. The AC was provided, adjusted and operated by the group of Prof. Helmut Zacharias from the University Münster, in particular Rolf Mitzner, Sebastian Roling and Björn Siemer. The iterative approach for the separation of a superimposed diffraction pattern from Sec. 4.5.3 results from inspiring discussions between Michael Leitner and the author. The conduction of the experiment at FLASH and the data interpretation is a result of the combined work of Rolf Mitzner, Bastian Pfau, Stefan Eisebitt and the author.

For all of the above experiments the author of this thesis contributed significantly to the preparation and conduction of the x-ray holography measurements as well as their analysis and interpretation. In particular, all reconstructions of holograms are the original work of the author.

Stephanie Lemke, Stefan Schaffert, Jan Geilhufe and Bastian Pfau contributed images to this thesis as stated in the captions of Fig. 3.2, Fig. 3.32, Fig. 3.36, and Fig. A.1. Bastian Pfau, Stefan Schaffert, Erik Gührs and Jan Geilhufe are all members of the group of Stefan Eisebitt that aim for the degree of PhD.

Acknowledgments

This thesis is based on the knowledge resulting from the scientific work as a PhD student at the former BESSY GmbH, which is now part of the Helmholtz-Zentrum Berlin. During that time I had the opportunity to work at a scientific large-scale facility together with motivated people that I would like to thank.

Stefan Eisebitt took the role of the supervisor throughout my PhD. Maybe the most important lesson I learned from him is to get connected with other scientists and get the right people into the boat for a successful experiment. He has the ability to explain physical details in a simple way and thus can inspire people toward new ideas.

Bastian Pfau did accompany me during my PhD and through countless beamtimes. He catches on problems very fast, either in physics or anything else, and comes up with a solution. It is always a good choice to rely on him and I value his advice very high.

Erik Gührs was the first reinforcement for Stefan's group during my PhD. He quickly learned about synchrotron night shifts and was a most welcome support for the performance of experiments. In return he showed me that there are more samples to investigate than magnetic multilayers.

Since then Stefan's group did certainly grow. I really enjoy working with the members of the group as well as spending time besides physics, now and in the future.

At the beginning of my PhD I had the opportunity to visit Hitachi GST in San José, California. *Olav Hellwig* did not only act as my local supervisor and introduced me to the mysteries of magnetic-multilayer sputtering, but took me into his home. Thanks to him most of my spare time was packed with outdoor activities. The rest was taken care of by *Thomas Hauet* who took me on his culinary exploration tours around the area.

I am thankful for the selfless support of *Rolf Mitzner* who totally abandoned sleep after his beamtime shift and kept the autocorrelator going for us. If nothing else worked, the alignment of the mirrors did.

Tino Noll is a design engineer from the bottom of his heart. It seems he always finds a way to fulfill different specifications from several scientists at the same time, and to add some Kevlar rope somewhere. His door is always open for anyone searching inspiration.

I would like to thank *Wolfgang Eberhardt* for giving me the opportunity to take part in a synchrotron research group and for taking the time and responsibility that come with reviewing this thesis.

Finally, I am deeply indebted to my family and friends and, in particular, my partner. During the writing of this thesis all of them showed great understanding and have patiently put aside matters of all kinds to give me the time I needed so much and that I owe to them now.